JOURNAL OF APPLIED PHYSICS

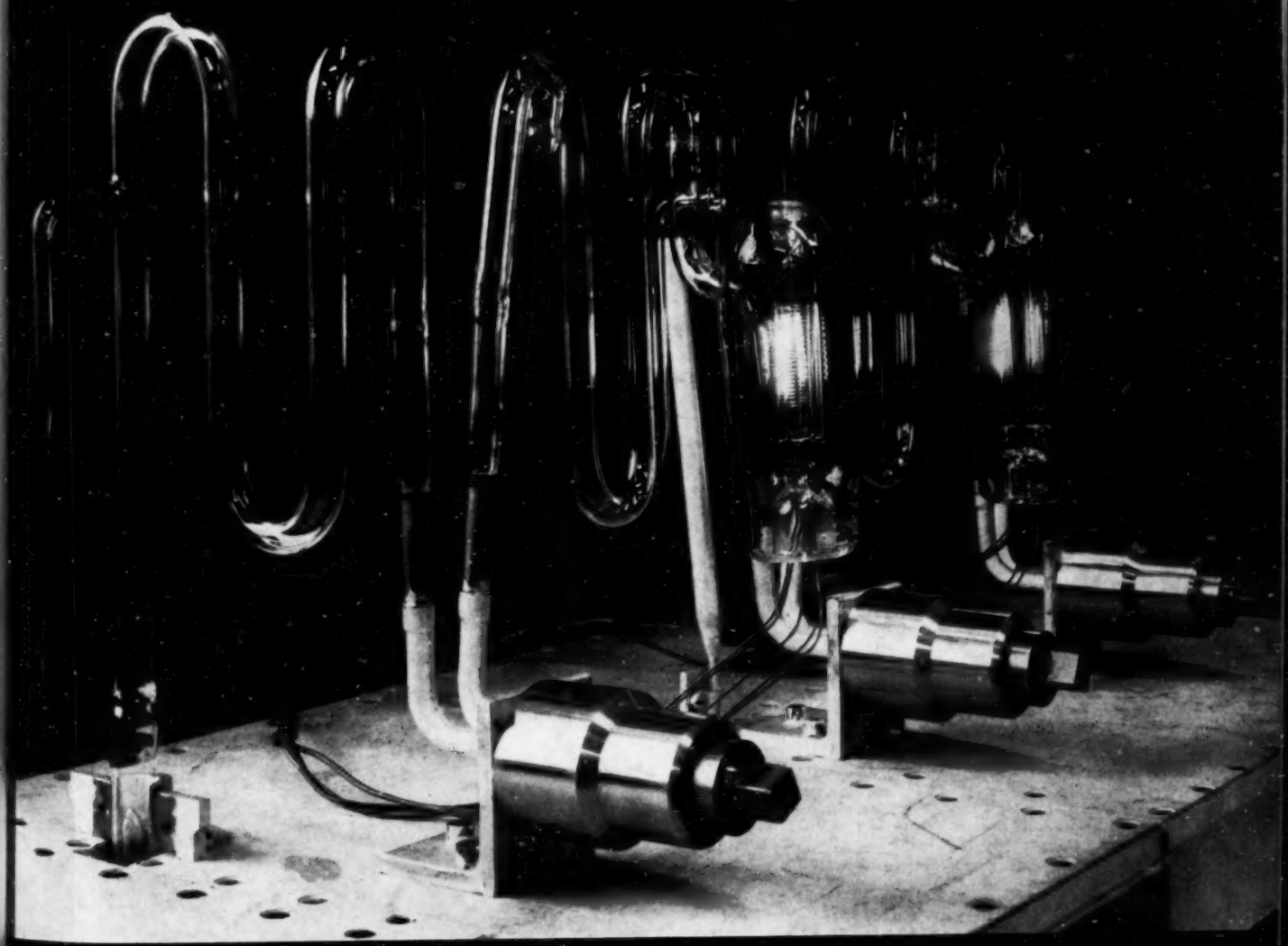

JOURNAL OF APPLIED PHYSICS

Vol. 24, No. 7 JULY, 1953

In This Issue

	Page
Nonequilibrium Thermodynamics Newman A. Hall	819
Experiments on Radiation by Fast Electron Beams H. Motz, W. Thon, and R. N. Whitehurst	826
Theorem on the Impedance-Transforming Properties of Reactive Networks Leo Storch	833
Experimental Verification of the Metal-Strip Delay-Lens Theory Seymour B. Cohn	839
Equivalence of Optimum Transducers and Sufficient and Most Efficient Statistics Glenn W. Preston	841
Transmission of Electromagnetic Waves through Pairs of Parallel Wire Grids Willice E. Groves	845
Starting Currents in the Backward-Wave Oscillator L. R. Walker	854
New Developments in the Production and Measurement of Ultra High Vacuum D. Alpert	860
Convection Currents in Porous Media. V. Variational Form of the Theory F. T. Rogers, Jr.	877
Probe Studies of Energy Distributions and Radial Potential Variations in a Low Pressure Mercury Arc R. M. Howe	881
Certain Problem in Heat Conduction Henry Zatzkis	895
Potential Analog Network Synthesis for Arbitrary Loss Functions Ernest Shiu-jen Kuh	897
Matrix Solution of Equations of the Mathieu-Hill Type Louis A. Pipes	902
Relaxation Distribution Function of Polyisobutylene in the Transition from Rubber-like to Glass-like Behavior John D. Ferry, Lester D. Grandine, Jr., and Edwin R. Fitzgerald	911
Helix Impedance Measurements Using an Electron Beam D. A. Watkins and A. E. Siegman	917
Consolidation Around Pore Pressure Meters G. de Josselin de Jong	922
Reflection of Sound in the Ocean from Temperature Changes Richard R. Carhart	929
On the Statistical Theory of Detection of a Randomly Modulated Carrier W. M. Stone	935
New Method for Continuous Viscosity Measurement. General Theory of the Ultra-Viscoson Wilfred Roth and Stanley R. Rich	940
Letters to the Editor:	
Comments on "The Dirac Delta Function and the Summation of Fourier Series" Erich R. Berger	951
Measurements of Stacking Faults in Cold-Worked Alpha Brass B. E. Warren and E. P. Warekois	951
Limitation of the Reversion Method W. J. Cunningham	952
Crossed Electron Beam Technique for Displaying Short Pulses Paul D. Coleman and Murray D. Sirkis	952
On Damage to Specimens by Shadowing Bombardment. I. Experiment K. Tokuyasu	953
On Damage to Specimens by Shadowing Bombardment. II. Calculation K. Tokuyasu	954
X-Ray Transmission Studies of Large Imperfect Crystals George L. Rogosa and Guenter Schwarz	954
Contour Lines on the Shadowed Side in the Electron Microscope K. Tokuyasu	956
Dielectric Constant Measurements at 8.6-mm Wavelength Paul Hertel, Jr., A. W. Straiton, and C. W. Tolbert	956
Effect of Biaxial Orientation on the Ultimate Strength and Crazing of Linear Polymers C. C. Hsiao and J. A. Sauer	957
Method of Determining Electrical Resistivities at Low Temperatures David C. Baird and Willard S. Boyle	958
Radiation Fields of a Horizontal Dipole in a Semi-Infinite Dissipative Medium James R. Wait	958
Deduction of the Maximum Torsional Stress in a Shaft with Notches Sennosuke Momma	959
Polystyrene and Lucite Rod Antennas Giswalt von Trentini	960
Surface Wave Propagation over a Coated Conductor with Small Cylindrical Curvature in Direction of Travel Kazuo Horiuchi	961
Effect of Particle Size on Magnetic Loss Tangent of Obstacle Type Artificial Dielectrics J. M. Kelly and J. O. Stenoien	962
Effect of Neutron Bombardment Upon the Magnetic Susceptibility of Several Pure Oxides J. D. McClelland and J. J. Donoghue	963
Erratum:	
Growth of Cadmium Sulfide Crystals M. E. Bishop and S. H. Liebson	963
Announcements	964
Index to Advertisers	xxx

ELMER HUTCHISSON,
Editor

EARLE C. GREGG,
Assistant Editor

Board of Editors
RAY E. BOLZ
LYLE D. BORST
WALLACE J. ECKERT
ROBERT D. HEIDENREICH
LEONARD B. LOEB
W. JAMES LYONS
LOUIS A. PIPES
ROMAN SMOLUCHOWSKI
W. R. SMYTHE

Publication of the
American
Institute of Physics

OFFICERS
GEORGE R. HARRISON,
Chairman
GEORGE B. PEGRAM,
Treasurer

GOVERNING BOARD
J. W. BUCHTA
KARL K. DARROW
G. J. DIENES
S. A. GOUDSMIT
GEORGE R. HARRISON
FREDERICK V. HUNT
DEANE B. JUDD
HUGH S. KNOWLES
C. C. LAURITSEN
WILLIAM F. MEGGERS
PHILIP M. MORSE
BRIAN O'BRIEN
GEORGE B. PEGRAM
I. I. RABI
DUANE ROLLER
FREDERICK SEITZ
WILLIAM SHOCKLEY
RICHARD M. SUTTON
J. H. VAN VLECK
MARK W. ZEMANSKY

Consultant on Printing
MELVIN LOOS

ADMINISTRATIVE STAFF
HENRY A. BARTON,
Director
WALLACE WATERFALL,
Executive Secretary
THEODORE VORBURGER,
Advertising Manager
RUTH F. BRYANS,
Publication Manager
BETTY H. GOODFRIEND,
Assistant Secretary
EILEEN B. NEUBERGER,
Circulation Manager
KATHRYN SETZE
Assistant Treasurer

The JOURNAL OF APPLIED PHYSICS, published monthly at Prince and Lemon Sts., Lancaster, Pa., is devoted to physics in its role as the science basic to other natural sciences and to the arts and industries. Previous to 1937 this publication was known as PHYSICS. The JOURNAL OF APPLIED PHYSICS publishes editorials and reviews, as well as technical papers of applied physics. Articles appearing in it are indexed regularly, according to their field, by Physics Abstracts, Chemical Abstracts, Engineering Index, Inc., Industrial Arts Index, etc.

Manuscripts should be submitted to Elmer Hutchisson, Editor, Case Institute of Technology, Cleveland 6, Ohio. Unless otherwise stated, submission of a manuscript is a representation that it has been neither copyrighted, published, nor submitted for publication elsewhere. The authors' institutions are requested to pay a **publication charge** of $8 per page which, if honored, entitles them to 100 reprints without further charge. Instructions will be sent with galley proofs.

Subscriptions, renewals, and orders for back numbers should be addressed to the American Institute of Physics, 57 East 55 Street, New York 22, New York.

Subscription Price	U.S. and Canada	Elsewhere
To members of the American Institute of Physics and Affiliated Societies	$10.00	$11.00
To all others	12.00	13.00

Back Number Prices

Yearly back number rate when complete year is available: $14.00. Single copies: $1.25 each.

Changes of address should be sent to the American Institute of Physics; **corrected proofs** should be sent to the Publication Manager, American Institute of Physics. **Advertising rates** supplied on request. Orders, advertising copy, and cuts should be sent to the American Institute of Physics.

Entered as second class matter January 22, 1937, at the Post Office at Lancaster, Pennsylvania, under the Act of March 3, 1879. Accepted for mailing at the special rate of postage provided for in paragraph (d-2), section 34.40, P. L. & R. of 1948, authorized May 2, 1932.

Journal
of
Applied Physics

Volume 24, Number 7 July, 1953

Nonequilibrium Thermodynamics

NEWMAN A. HALL
University of Minnesota, Minneapolis, Minnesota
(Received January 13, 1953)

The foundations and implications of the concepts essential to the thermodynamic analysis of nonequilibrium systems are investigated. Following a review of the background developments in irreversible thermodynamics the concept of thermostatic isolation is introduced. This provides a conceptual device whereby a thermostatic state may be established for any nonequilibrium system and a means of justifying extended use of basic relations of classical thermodynamics or thermostatics.

The conventional development of the form of entropy production is outlined. This in general is the sum of extrinsic entropy production and intrinsic entropy production. The former occurs as the sum of products of generalized diffusion effects and property gradients and is the result of interactions with discrete adjacent systems. The latter occurs as the sum of products of generalized affinities and generalized reaction rates and is the result of interaction between geometrically coincident overlapping systems. Between the diffusion effect and gradients of extrinsic entropy production generally occur linear relations with phenomenological coefficients subject to the Onsager reciprocal relations. The intrinsic entropy production occurs as a relaxation phenomenon developed from the first-order relaxation between the affinity and the displacement of the reaction from equilibrium.

The relation of the ultimate limits of applicability of thermodynamics to the uncertainty in establishing thermostatic state under conditions of microscopic fluctuations is discussed.

IN the development and application of thermodynamics much has depended on the precision and comprehensiveness of the postulates and principles on which the structure of analysis is based. The significance of the contributions of Clausius, Helmholtz, Gibbs, Carathéodory, and Keenan has been their concern that an unambiguous description of the analytical model be set forth. This concern has established the logic of thermodynamics with sufficient firmness so that further developments may be made with confidence.

The structure of thermodynamics which has arisen contains certain severe limitations, however, when applied critically to actual physical phenomena. These limitations are associated primarily with questions of equilibrium and continuity. While classical thermodynamics admits the existence of nonequilibrium states, it provides definitive information only when the system or medium is in equilibrium or can be subdivided into subsystems in equilibrium.

Likewise any encounter with the microscopic structures of molecular discontinuities effectively removes thermodynamics as a useful tool.

In spite of these difficulties the formal procedures of classical thermodynamics have been applied with success in many cases where a strict logic would prohibit their use. This is unsatisfactory primarily in that without a firm basis for such an extension, a critical analysis is impossible. A very familiar example of current interest is the thermodynamic analysis of shock waves. By virtue of both of the limitations mentioned, the principles of thermodynamics should not be applicable. Yet to some extent the results of such an analysis appear to be useful.

The most popular alternate to thermodynamics in such cases is kinetic theory and statistical mechanics. While these theories have given much substance to thermodynamics since the time of Gibbs there are two serious disadvantages. The methods of analysis are of such complexity that they should be used only when essential, and in addition, the question of the extent of validity of the thermodynamic method is set aside rather than answered.

A partial answer to the basic question has appeared in recent years as a thermodynamic theory of irreversible processes. This development was inspired by the work of De Donder[1] who was concerned with irreversible processes in chemical reaction. Later L. Onsager,[2] considering heat transfer as well as thermo-

[1] T. L. De Donder, *L'Affinité* (Paris, 1926).
[2] L. Onsager, Phys. Rev. **37**, 405 (1931); **38**, 2265 (1931).

chemical problems, set forth certain general correlations characteristic of these processes. Subsequent studies by Meixner,[3] Eckart,[4] Verschaffelt,[5] Prigogine,[6] De Groot,[7] and others developed applications to thermodiffusion, thermoelectricity, viscous flow, and heat transfer as typical irreversible processes.

This approach has been summarized more recently by three monographs by De Groot,[7] Prigogine,[6] and Haase,[8] which are essentially equivalent in initial premises and major aspects of exposition. In each case the basic Gibbs relation between entropy, internal energy, specific volume, and chemical potentials (Eq. 18) is assumed valid in the extended domain of action of irreversible processes. This provides a device whereby a formal application of classical thermodynamics may be made and the direct quantitative effects of irreversibility on the thermodynamic state evaluated. The principal elements of this theory have also been summarized by Prigogine[9] and by Denbigh.[10]

In general the potential usefulness of such an extension of thermodynamics lies in its ability to put many phenomena on a common basis and thereby establish more firmly their possible interrelation and the more fundamental aspect of their own nature, and also the possibility of providing quantitative criteria of the boundary between continuum thermodynamics and discrete theories such as statistical mechanics.

These objectives have been attained in part and it is intended in these remarks to explain more fully certain fundamental questions and to suggest some of the areas where uncertainties remain.

Before extending the domain of classical thermodynamics it is well to review certain of its own fundamental concepts. The most essential is that of equilibrium. A system in thermodynamic equilibrium is one such that if it is isolated from all external influences, its state remains unchanged. Classical thermodynamics makes quantitative statements with reference only to such equilibrium states. For this reason it has been appropriately proposed to refer to this theory as thermostatics.

Associated directly with the concept of equilibrium is that of reversible processes. A process is reversible if the system undergoing the process is at all times in a state of thermodynamic equilibrium. Thus an adiabatic reversible compression or expansion is one such that if the process is instantaneously terminated and the system isolated no further change of state will occur. Similarly reversible heat transfer will occur in a system where work is being transferred at the same time so as to maintain an isothermal state. Again isolation of the system will leave it unchanged and in an equilibrium state.

So long as a system is in thermodynamic equilibrium there is no uncertainty in referring to its state or properties. However, in extending thermostatics to irreversible thermodynamics, there exists a critical uncertainty. As typified by temperature, the fundamental properties of a system are defined conceptually in terms of equilibrium correlation or effectively by thermodynamic coincidence with reference measurement standards. The so-called zeroth law of thermodynamics[11] which establishes the temperature concept states that two systems in thermal equilibrium with a third are in thermal equilibrium with each other. In this respect it is as essential to have an equilibrium condition to define temperature as it is to have geometric coincidence to define distance.

Not only is it essential to have equilibrium from a conceptual viewpoint but also from a critical experimental standpoint as well. It is only to the extent that a thermometer is in true thermal equilibrium that an unambiguous temperature can be determined. If the system whose temperature was to be determined consisted of two portions, A and B, separated by an adiabatic barrier, it is clear that if the local temperatures of A and B differed, the temperature readings could be either that of A or B depending on whether the thermometer was in contact with A or B. Also, if the thermometer were in thermal contact with both A and B, the very nature of the thermometer itself would determine the temperature. In any case where a temperature gradient exists, the same difficulty provides one element of uncertainty in experimental measurements.

The same type of conceptual and experimental question arises in cases where gradients or discontinuities in other properties such as concentration or velocity occur.

The establishment of a satisfactory definition of state accordingly requires either some new procedure of physical coincidence in order to obtain properties under nonequilibrium conditions or some method whereby the nonequilibrium condition during the irreversible processes can be associated with an equivalent equilibrium state.

The latter is proposed as more useful and effective. An irreversible process is maintained together with an implied nonequilibrium state because of the action of some influence external to the system. If such influences are removed, isolating the system, it will proceed spontaneously to a state of thermodynamic equilibrium.

[3] J. Meixner, Ann. Physik **35**, 701 (1939); **36**, 105 (1939); **39**, 333 (1941); **40**, 165 (1941); **41**, 409 (1942); **43**, 244 (1943).
[4] C. Eckart, Phys. Rev. **58**, 267, 269 (1940).
[5] J. E. Vershcaffelt, Bull. classe sci. Acad. roy. Belg. **28**, 436, 455, 476, 490 (1942); **30**, 330 (1944); **34**, 126 (1948).
[6] I. Prigogine, *Étude thermodynamique des phénomènes irréversibles* (Liège, 1947).
[7] S. R. De Groot, *Thermodynamics of Irreversible Processes* (North Holland Publishing Company, Amsterdam, 1951).
[8] R. Hasse, Z. Naturforsch. **6a**, 420, 522 (1951).
[9] I. Prigogine, Appl. Mechanics Rev. **5**, 193 (1952).
[10] K. G. Denbigh, *The Thermodynamics of the Steady State* (Methuen & Company, London, 1951).
[11] J. H. Keenan and A. H. Shapiro, Mech. Eng. **V**, 915 (1947).

The properties of this resulting equilibrium state may then be defined as the properties of the original nonequilibrium system. Specifically these may be termed the thermostatic properties. To be satisfactory this definition must be consistent with the principles of thermostatics and with accepted terminology in relation to experimental techniques.

The correlation with thermostatics is certainly satisfactory since no other direct criteria regarding nonequilibrium states exist. Furthermore the usual procedure in experimental observations is to search for a condition where equilibrium conditions are approximated either by controlling the environment or, where gradients are unavoidable, by reducing the size of the instrumentation. In either case the ultimate in experimental procedure either of extensive or differential uniformity would measure properties coincident with those of the thermostatic state.

In addition to resolving the question of state in irreversible processes the thermostatic properties provide a useful device for thermodynamic analysis of extensive systems where property gradients are known to occur. In effect the thermostatic properties provide a thermodynamic average in such cases.

For example, a substantial amount of engineering analysis in fluid motion involves the assumption of one-dimensional flow. The conventional procedure is to apply standard equations as if no radial gradients occurred. The same result can be attained, but on a more rigorous basis, if the properties used in the one-dimensional analysis are the thermostatic properties for a section across the stream tube of differential length. Thus in the case of constant area flow thermostatic isolation is obtained by an adiabatic frictionless transition from the real flow with cross stream gradients to uniform thermostatic flow. The thermostatic state is then determined by the relations

$$w=\rho_s A V_s=\int \rho V dA, \tag{1}$$

$$F=p_s A+\frac{1}{g_c}wV_s=\int pdA+\frac{1}{g_c}\int \rho V^2 dA, \tag{2}$$

$$wh^0=wh_s+\frac{1}{2g_c}wV_s^2=\int \rho V h dA+\frac{1}{2g_c}\int \rho V^3 dA, \tag{3}$$

where the thermostatic properties h_s, p_s, and ρ_s are also related by an equation of state. These four equations are sufficient to determine the thermostatic state for any initial distribution.

For laminar isothermal flow in a circular pipe of a constant density fluid, this analysis gives the following thermostatic properties:

$$V_s=V_M, \tag{4}$$

$$\rho_s=\rho, \tag{5}$$

$$p_s=p+\frac{1}{3g_c}\rho V_M^2, \tag{6}$$

$$h_s=h+\frac{1}{2g_c}V_M^2, \tag{7}$$

$$u_s=u+\frac{1}{6g_c}V_M^2. \tag{8}$$

These results follow directly from the local parabolic velocity distribution

$$V=2V_M[1-(r^2/a^2)]. \tag{9}$$

The local thermostatic properties for a differential element will be the local thermodynamic properties as conventionally used. There is no significance in referring to an internal distribution as in the case just discussed. Furthermore, while a differential system may be formally defined from a thermodynamic viewpoint, the actualities of microscopic physical structure impose severe practical limitations. The thermodynamic system at all times must be sufficiently large that it is not affected by microscopic statistical fluctuations. Under normal circumstances the number of molecules in a gas, say, is sufficiently large that differentials may approach the infinitesimal limit to satisfy mathematical requirements and still remain above the fluctuation range. However, if an extreme degree of irreversibility occurs, there will exist property gradients of sufficient magnitude that an attempt to analyze detail behavior as in a shock wave or a flame front will require reference to differentials small enough that the fluctuation limit is reached.

In the domain where statistical fluctuations are significant the concept of thermostatic state fails, as the state is no longer unique. The procedure of thermostatic isolation for the system would establish properties dependent on random statistical fluctuations in addition to the conventional thermodynamic environment. Thus, thermodynamic analysis would no longer be applicable. This circumstance can be developed quantitatively to provide criteria for the limits of thermodynamics in irreversible processes.

The conceptual procedure of thermostatic isolation which stops any interaction between the system and any other system in contact has particular significance when two or more systems occupy the same space. This occurs, for example, when several radiation fields of different temperatures occupy a volume which may also contain a gas at a still different temperature. The same situation occurs in the phenomena of thermal relaxation of a gas where the two systems are the

internal or vibration system and the external or translation rotation system. In a reacting chemical mixture the two sets of chemical species comprise the systems; although on thermostatic isolation any diffusion gradient is to disappear while the reaction is to be frozen, maintaining a difference in free energy between the systems.

In each of these cases the discontinuity or gradient which gives rise to the irreversible action is not spatial but is distributive and intrinsic. The irreversible interaction is essentially local and unless external influences are involved will proceed as a transient. The terminal state of such a transient when external factors are absent or removed is frequently identified as the state of thermodynamic equilibrium for the resulting combined system. This equilibrium must be carefully distinguished from the equilibrium involved in the thermostatic isolation of the component system.

Since any thermostatic property is defined with reference to an equilibrium state, any principle of thermodynamics stated implicitly in terms of equilibrium states may be applied, in general, without qualification, provided thermostatic properties are used consistently. The first law of thermodynamics defines the property internal energy by the relation

$$dU = dQ - dW, \tag{10}$$

assuming heat and work to be known. According to reference 11, equally satisfactory statements express internal energy in terms of work and an adiabatic process or heat and a no-work process.

The second law similarly defines entropy as a property by the relation

$$ds = dQ/T, \tag{11}$$

where the system is closed and the process is reversible. This is somewhat analogous to the definition of internal energy in terms of heat transferred during a no-work process. A further implication of the second law is that for an adiabatic process

$$ds \geq 0 \tag{12}$$

also analogous to defining internal energy in terms of work transferred in an adiabatic process. The increase of entropy implied is due to irreversibility taking place and can be expressed in terms of a rate of irreversible entropy production σ. Thus

$$ds = \sigma dt. \tag{13}$$

Combining these specialized expressions, the general expression for entropy corresponding to Eq. (10) for internal energy is

$$ds = (dQ/T) + \sigma dt. \tag{14}$$

The second law states that

$$\sigma \geq 0. \tag{15}$$

The nature of the entropy production σ is the primary concern of the theory of irreversible thermodynamics.

The two terms in the entropy equation (14) are frequently identified separately[6,7,10] as the external entropy transport,

$$ds_e = dQ/T, \tag{16}$$

and the internal entropy production,

$$ds_i = \sigma dt. \tag{17}$$

Neither of these is a property differential unless associated respectively with reversible or adiabatic processes in the same way that dQ and dW do not represent property differentials in general.

For any closed system the rate of entropy production may be determined from Eq. (14) by knowing the heat transferred together with the thermostatic state at successive time intervals. The entropy change ds follows from the differential change in thermostatic state corresponding to the time change dt.

In the more general case of an open multicomponent system additional factors are involved in determining entropy transport and production. The statements of the first and second law, Eqs. (10) and (15), are still applicable. In addition, the general theory of thermostatics of equilibrium thermodynamics provides the Gibbs relation

$$Tds = dU + dW_r - \sum_k \mu_k dm_k, \tag{18}$$

where dW_r is the reversible work. In general, this may be expressed as the sum of products of generalized forces and generalized displacements

$$dW_r = \sum_n F_n dX_n. \tag{19}$$

The forces F_n will be intensive quantities such as pressure, elastic stress, or electric or magnetic potential. The displacements will be extensive quantities such as volume, displacement, or charge. The most familiar form for simple mechanical-chemical fluid systems is

$$dW_r = pdV. \tag{20}$$

The Gibbs relation is one between thermostatic properties and accordingly may be applied to irreversible processes provided the thermostatic state at any time is determinate.

To illustrate the structure of the entropy production for continuous systems the intrinsic form of the Gibbs relation Eq. (18) may be applied to the limited case of a fluid multicomponent system in which the component systems interact according to a set of chemical reactions and in which the only reversible work is that of the form Eq. (20). This is a rather specialized type of system but includes a larger number of common phenomena.

In this case the Gibbs relation for unit mass assumes the form

$$Tds = du + pdv - \sum_k \mu_k dc_k, \tag{21}$$

where c_k is the concentration

$$c_k = m_k/m. \tag{22}$$

The internal energy is changed according to the first law Eq. (10) by the action of (a) heat transfer and (b) work transfer. The concentration is changed by the action of (a) mass transfer and (b) chemical reaction.

Since the general thermodynamics of a fluid system involves accelerated flow, it is convenient to apply Eq. (21) to a volume of fluid following the mean motion. In this case

$$T\frac{ds}{dt} = \frac{du}{dt} - \frac{p}{\rho^2}\frac{d\rho}{dt} - \sum_k \mu_k \frac{dc_k}{dt}, \tag{23}$$

where the time derivative is taken along the path of mean motion.

The flow of heat in such a convective field can be described by a vector $\mathbf{q}$ which gives the heat flow rate per unit area. Applying this to a differential unit volume the rate of heat addition will be

$$\rho\frac{dQ}{dt} = -\nabla\cdot\mathbf{q}. \tag{24}$$

This can be obtained by direct consideration of the heat flow across the differential volume boundaries or by use of Gauss' theorem.

The work transfer will be that caused by surface forces, external forces, and acceleration. The surface forces comprise the net effect of the normal pressure p and the stress tensor τ.

These result in a net work transfer from their action on the surface of the fluid element, consequently, the rate of surface work transfer is

$$\rho\frac{dW_s}{dt} = \nabla\cdot(p\mathbf{v}) - \nabla\cdot(\tau\cdot\mathbf{v}). \tag{25}$$

The external forces and acceleration, however, act on the fluid element as a whole, so the resulting rate of work transfer is

$$\rho\frac{dW_e}{dt} + \rho\frac{dW_a}{dt} = -\rho\mathbf{F}_e\cdot\mathbf{v} + \rho\frac{d\mathbf{v}}{dt}\cdot\mathbf{v}. \tag{26}$$

The general equation of motion for such a fluid element as expressed by the Navier-Stokes equation is

$$\rho\frac{d\mathbf{v}}{dt} = \rho\mathbf{F}_e - \nabla p + \nabla\tau. \tag{27}$$

Consequently, the total rate of work transfer per unit volume is

$$\begin{aligned}\rho\frac{dW}{dt} &= \nabla\cdot(p\mathbf{v}) - \nabla\cdot(\tau\cdot\mathbf{v}) - \rho\mathbf{F}_e\cdot\mathbf{v} + \rho\frac{d\mathbf{v}}{dt}\cdot\mathbf{v} \\ &= \nabla\cdot(p\mathbf{v}) - \nabla\cdot(\tau\cdot\mathbf{v}) - \nabla p\cdot\mathbf{v} + \nabla\tau\cdot\mathbf{v} \\ &= p\nabla\mathbf{v} - (\tau\cdot\nabla)\mathbf{v}.\end{aligned} \tag{28}$$

The equation of continuity for the fluid element is

$$\frac{d\rho}{dt} + \rho\nabla\mathbf{v} = 0, \tag{29}$$

so that

$$\rho\frac{dW}{dt} = -\frac{p}{\rho}\frac{d\rho}{dt} - (\tau\cdot\nabla)\cdot\mathbf{v}. \tag{30}$$

Combining the rate of heat and work transfer according to the first law, Eq. (10), the rate of internal energy change is given by

$$\rho\frac{du}{dt} = -\nabla\cdot\mathbf{q} + \frac{p}{\rho}\frac{d\rho}{dt} + (\tau\cdot\nabla)\cdot\mathbf{v}. \tag{31}$$

The rate of change of concentration may be shown[7] by considering the two factors of mass transfer and chemical reaction to be given by

$$\rho\frac{dc_k}{dt} = -\nabla\cdot\mathbf{m}_k + \sum_j \nu_{kj}\cdot\xi_j, \tag{32}$$

where $\mathbf{m}_k$ is a vector mass velocity describing the selective flow of certain of the components relative to the mean motion, ν_{kj} is the product of the chemical reaction stoichiometric coefficient and the molecular weight, and ξ_j is the reaction rate of the jth chemical reaction.

Combining Eqs. (23), (31), and (32) the total rate of change of entropy is given by

$$\begin{aligned}T\rho\frac{ds}{dt} &= -\nabla\cdot\mathbf{q} + (\tau\cdot\nabla)\cdot\mathbf{v} \\ &\quad + \sum_k \mu_k\nabla m_k - \sum_k \mu_k \sum_j \nu_{kj}\xi_j.\end{aligned} \tag{33}$$

In dividing this into entropy production and entropy transport, it should be observed that in applying the first law as given by Eq. (10) to the unit volume of fluid in an open system the thermal effects of mass transfer have been included in the term dq. Thus the heat flow vector $\mathbf{q}$ includes the transport of energy across the fluid element boundary resulting from diffusion as well as conduction. This vector energy transport, characterizing action at a surface and not within a volume, is locally reversible and contains effects only other than work transfer. Accordingly, the corresponding entropy vector transport will be indicated by the Gibbs relation Eq. (18) omitting the terms derived from work transport. Thus the entropy flow vector is

$$\mathbf{s} = \frac{\mathbf{q} - \sum_k \mu_k\mathbf{m}_k}{T}, \tag{34}$$

and the corresponding net reversible entropy transport

per unit volume is the negative divergence

$$\rho\frac{ds_e}{dt}=-\nabla\cdot\mathbf{s}=-\nabla\cdot\frac{\mathbf{q}-\sum_k \mu_k\mathbf{m}_k}{T}. \tag{35}$$

The rate of entropy production per unit volume follows from Eqs. (33), (34), and (35) as

$$\begin{aligned}T\rho\sigma&=T\rho\frac{ds}{dt}-T\rho\frac{ds_e}{dt}\\&=(\boldsymbol{\tau}\cdot\nabla)\cdot\mathbf{v}+\sum_j A_j\dot{\xi}_j\\&\quad-\mathbf{q}\cdot\nabla\ln T-T\sum_k\mathbf{m}_k\cdot\nabla\frac{\mu_k}{T}_k.\end{aligned} \tag{36}$$

The affinity of the chemical reactions A_j is also the negative of the free-energy difference between reactants and products

$$A_j=-\sum_k \nu_{kj}\mu_k=-\Delta F_j. \tag{37}$$

This development of the entropy production is representative of more general forms.[6–8,10] In all cases it appears that it can be presented as a sum of terms, each corresponding to a different effect and each occurring as the product of two terms which can be identified as causes and effects. The effects are sometimes termed thermodynamic fluxes and the causes, thermodynamic forces.[7]

The items making up the entropy production may be divided into two general classes. The first class comprises those associated with transport phenomena and occurs essentially as the product of a diffusion effect such as shear stress, heat or mass, and the gradient of the property correlated with this diffusion. As these all involve an interaction of the system with the surroundings by virtue of the gradients, the total effect may be termed the extrinsic entropy production σ_e. In general,

$$\sigma_e=\sum_m D_m\cdot\nabla P_m. \tag{38}$$

In the foregoing development

$$\begin{aligned}&D_1=\boldsymbol{\tau}/T\rho, \quad P_1=\mathbf{v}\\&D_2=-\mathbf{q}/T\rho, \quad P_2=\ln T\\&D_k=\mathbf{m}_k/\rho, \quad P_k=\mu_k/T.\end{aligned} \tag{39}$$

The second class is represented in the above development by the term dependent on the rate of the chemical reaction. As described earlier the chemical reaction is not controlled primarily by any external gradient but rather by the intrinsic free-energy differential between the reactants and products in the system. Accordingly, the resulting effect may be termed the intrinsic entropy production. Not included in the analytical formulation but causing the same type of intrinsic entropy production are the phenomena of thermal relaxation of gases and interaction between radiation fields and gases referred to earlier.

If several of these effects occur, the total intrinsic entropy production σ_i can be expressed as a sum of products where in this case a generalized affinity corresponds to the thermodynamic force and a generalized rate to the thermodynamic flux.

While the entropy production may be formulated and classified in this very general manner, the central problem of nonequilibrium thermodynamics remains the complete description of the several factors involved. Beyond the type of general development presented above, the basic principles of thermostatics can provide no information.

In the case of extrinsic entropy production, phenomenological principles propose certain very general linear relations. These are of the form

$$D_m=\sum_r \gamma_{mr}\nabla P_r. \tag{40}$$

These include such familiar relations as Fourier's law for heat transfer, Ficks' law for diffusion and Newton's law for viscosity. The coefficients γ_{mr} generalize such terms as the thermal conductivity, coefficient of viscosity, etc.

The implications of the linear relation Eq. (40), comprise most of the recent expositions on irreversible thermodynamics. In particular the phenomenological coefficients γ_{mr} appear to obey the Onsager relation[2,7,10]

$$\gamma_{mr}=\gamma_{rm}, \tag{41}$$

which have simplified implications in regard to coupling of irreversible actions.[7,10]

The linear relations Eq. (40), however, represent empirical approximations. If the coefficients are given a more general definition,

$$\gamma_{mr}=\partial D_m/\partial\nabla P_r, \tag{42}$$

there is reason to expect that they may themselves depend on the gradients in a manner analogous to the way specific heat defined as a differential still depends on temperature. Furthermore, with this more general definition it is uncertain whether the Onsager relations remain valid.

The intrinsic entropy production requires a different approach as indicated by the complexity of chemical kinetic theories. Attempts to relate the generalized affinities and rates by linear relation of the type have had limited success[6,7] with any range of usefulness being limited to a very restricted neighborhood of the equilibrium for the combined systems.

A more promising approach is that followed customarily for thermal relaxation of gases which introduces a relaxation time to characterize the essential transient character of the action. This approach has been applied

to the case of chemical reaction rates recently[12] with promise that it may be very generally applicable. Reference may be made to this treatment of Kirkwood and Crawford to observe the general type of formulation which may be made. A recent study by Meixner[13] suggests that intrinsic entropy production may give rise to certain dynamic effects in fluid motion of a type essentially different from those associated with the extrinsic entropy production correlated with viscosity.

In summary, it appears that the concept of thermostatic isolation provides a means whereby the concept of state dependent on thermodynamic equilibrium may be extended to nonequilibrium systems. Furthermore, such nonequilibrium systems are differentiated from the corresponding equilibrium systems by the occurrence of entropy production. This may be extrinsic and dependent on generalized diffusions and gradients or intrinsic and dependent on generalized affinities and rates. The limitations on the applicability of thermodynamic analysis appear to be associated with the uniqueness of the thermostatic state as it may be affected by microscopic statistical fluctuations. The investigation of this limitation and of the structure of entropy production remains as central problems for the thermodynamics of nonequilibrium systems.

NOTATION

A Cross-section area—one-dimensional flow
a Cross-section radius—one-dimensional flow
$A_j = -\Delta F_j$ Affinity—multicomponent system
C_k Concentration—multicomponent system
D_k Diffusion effect
F Thrust functions—one-dimensional flow
F_n Generalized force for reversible work
$\mathbf{F}_e$ External body force field
g_c Gravitational conversion factor
h_a Enthalpy
h_s Thermostatic enthalpy
h^0 Stagnation enthalpy
m Mass of fluid element
m_k Mass of component in fluid element
$\mathbf{m}_k$ Mass vector velocity of component
P_k Property—extrinsic entropy production
p Pressure
p_s Thermostatic pressure—one-dimensional flow
Q Heat
$\mathbf{q}$ Heat flow vector
r Radial position—one-dimensional flow
S Entropy
S_e External entropy—as entropy transport
S_i Irreversible or internal entropy—from entropy production
s Specific entropy
$\mathbf{s}$ Entropy flow vector
T Temperature
t Time
U Internal energy
u Specific internal energy
u_s Thermostatic internal energy—one-dimensional flow
V Volume
v Velocity—one-dimensional flow
v_s Thermostatic velocity—one-dimensional flow
v_M Average velocity—one-dimensional flow
$\mathbf{v}$ Vector velocity
W Work
W_r Reversible work
W_e External work
W_a Kinetic work
W_s Surface work
w Mass flow rate—one-dimensional flow
X_n Generalized displacement—reversible work
γ_{mn} Phenomenological coefficients
μ_k Component chemical potential
ν_{kj} Stoichiometric coefficients
ρ Density
ρ_s Thermostatic density
σ Entropy production rate
τ Stress tensor
$\dot{\xi}$ Reaction rate

[12] J. G. Kirkwood and B. L. Crawford, J. Phys. Chem. **56**, 1048 (1952).
[13] J. Meixner, Z. Physik. **131**, 456 (1952).

Experiments on Radiation by Fast Electron Beams*

H. Motz, W. Thon, and R. N. Whitehurst
Microwave Laboratory, Stanford University, Palo Alto, California
(Received October 27, 1952)

The results of some experiments on millimeter wave and light generation by means of an undulator are described. After a brief survey of the theoretical background the design of a magnet system is discussed. An experiment is described in which a 100-Mev electron beam from the Stanford linear accelerator passed through the undulator. Light radiated by the beam was observed and the plane of polarization determined. A small linear accelerator with good bunching action was used for an experiment on millimeter wave generation. At a beam energy of 3 Mev, radiation in a wavelength band below 1.9 millimeters was observed. A peak power output of the order of one watt was obtained. Millimeter waves generated in the accelerator tube were also observed.

I. INTRODUCTION

THEORETICAL investigations have shown[1–4] that under certain conditions radiation ranging from millimeter waves to visible light is emitted by electrons in accelerated motion in the energy range of a few Mev to, say, 100 Mev. In particular, sinusoidal orbits were investigated in detail,[3] and the power level obtainable in the millimeter range from electrons with an energy of a few Mev seemed promising. In this paper the results of some preliminary experiments on millimeter wave and light generation are presented.

While the light generation experiments are of purely academic interest, the millimeter wave experiments may have some practical importance. In this case it is possible to bunch the electron beam so that groups of electrons radiate coherently. It was shown[3] that the power level may be higher by a factor of the order of a million as compared to noncoherent radiation and that a peak power of the order of kilowatts may be obtainable in practice. The first experimental attempts reported in this paper resulted in a power output in excess of one watt in the millimeter wave range. This result, although it falls far short of what is ultimately hoped for, is yet encouraging in view of the general situation in this field.[5] Klein *et al.*[6] report a power output of the order of milliwatts from magnetron harmonics at about 1-mm wavelength, and other methods give comparable results.

II. THEORETICAL BACKGROUND

1. The Undulator

Electrons passing through a magnetic field, the direction of which alternates in space along the electron path, describe a periodic orbit in a plane perpendicular to that of the field. We call the arrangement a magnetic undulator (Fig. 1). It was shown[3] that electrons moving in a sinusoidal orbit radiate electromagnetic waves of angular frequency,

$$\omega = 2\pi v/l_0[1-(v\cos\theta)/c], \tag{1}$$

depending on the angle θ which the wave normal makes with the axis of the undulator. Here l_0 is the space period of the magnetic flux distribution and v the axial electron velocity. This formula is valid as long as $evBl_0/m_0c^2$ is small compared to unity. For larger values of this quantity harmonics of the fundamental frequency (1) will appear with increasing intensity. The foregoing formula applies to an infinitely long undulator and to radiation in free space. If the electron beam is confined by a wave guide of transverse dimensions comparable with the wavelength of the radiation the various modes of wave-guide propagation have to be considered.

2. Calculation of Frequency Spectrum Radiated in a Wave Guide

The radiation emitted by the electrons in a wave guide may be calculated by considering, at first, an observer riding with the electrons. Such an observer sees the space period l_0 of the undulator shortened by Lorentz contraction. Such an observer therefore sees the electron carry out oscillations of angular frequency

$$\omega' = 2\pi v/l_0(1-\beta^2)^{\frac{1}{2}} \tag{2}$$

in a plane perpendicular to the magnetic-field direction.

The field modes propagated in a guide of rectangular cross section depend on z' and t' according to the relation

$$E', H' \sim \exp(-i\gamma'_{m,n}|z'|+i\omega' t'), \tag{3}$$

where

$$\gamma_{m,n}'^2 = (k')^2 - \frac{m^2\pi^2}{a^2} - \frac{n^2\pi^2}{b^2}, \quad k' = \frac{\omega'}{c}, \tag{4}$$

$$m=0, 1, 2, 3\cdots, \; n=0, 1, 2, 3\cdots, \; m+n\neq 0,$$

* The work reported herein was performed under a contract between Stanford University and the U. S. Office of Naval Research.

[1] V. L. Ginsburg, Bull acad. sci. U.S.S.R. Sér. phys. **11**, 165 (1947).
[2] P. D. Coleman, Ph.D. thesis, Physics Department, Massachusetts Institute of Technology, 1951.
[3] H. Motz, J. Appl. Phys. **22**, 527 (1951).
[4] K. Landecker, Phys. Rev. **86**, 852 (1952).
[5] J. R. Pierce, Phys. Today **3**, 24 (1950).
[6] Klein, Loubser, Nethercot, and Townes, Rev. Sci. Instr. **23**, 78 (1952).

and a, b, $(a>b)$ are the dimensions of the guide cross section.

The coordinates z',t' of the observer moving with an electron are related to the coordinates z, t of an observer in the laboratory frame of reference by the Lorentz transformations

$$z'=(z-vt)/(1-\beta^2)^{\frac{1}{2}},\ t'=(t-\beta z/c)/(1-\beta^2)^{\frac{1}{2}}. \quad (5)$$

Hence, in the laboratory frame of reference for $z>vt$ the fields will depend on z, t according to the relation

$$E,\ H\sim \exp[i(\gamma'_{m,n}+\beta k')z/(1-\beta^2)^{\frac{1}{2}} + i(\gamma'_{m,n}\beta+k')ct/(1-\beta^2)^{\frac{1}{2}}]. \quad (6)$$

In this system the propagation constants and frequencies are given by

$$\gamma_{m,n}=2\pi/\lambda_{m,n}=(\gamma'_{m,n}+\beta k')/(1-\beta^2)^{\frac{1}{2}}, \quad (7a)$$

$$k_{m,n}=\omega_{m,n}/c=(\gamma'_{m,n}\beta+k')/(1-\beta^2)^{\frac{1}{2}}. \quad (7b)$$

It is clear that the radiation in an infinitely long guide would have a line spectrum with one line corresponding to every undegenerated mode of propagation.

3. The Orbits

The kinetic energy of an electron is given by the relativistic formula

$$E=m_0c^2[1/(1-\beta^2)^{\frac{1}{2}}-1], \quad (8)$$

while the radius of curvature ρ of the electron path in a magnetic field B is given by

$$e\rho B=m_0v/(1-\beta^2)^{\frac{1}{2}}, \quad (9)$$

where m_0 is the rest mass. Combining these equations we find the relation between the radius of curvature and the energy

$$B\rho=(E^2+1.02E)^{\frac{1}{2}}10^4/3, \quad (10)$$

where E is the kinetic energy expressed in Mev.

Let the orbit be expressed in Cartesian coordinates y,z. Then

$$1/\rho=(d^2y/dz^2)/[1+(dy/dz)^2]^{\frac{1}{2}}. \quad (11)$$

The differential equation

$$Af(z)=(d^2y/dz^2)/[1+(dy/dz)^2]^{\frac{1}{2}} \quad (12)$$

is satisfied by the electron path $y(z)$. Here

$$B=B_Mf(z) \quad (13)$$

is the flux distribution, and $f(z)$ is a periodic function of unit maximum amplitude which specifies the wave form, and

$$A=3B_M/10^4(E^2+1.02E)^{\frac{1}{2}}. \quad (14)$$

Equation (12) can be integrated and yields

$$u(z_2)/[1+u^2(z_2)]^{\frac{1}{2}}-u(z_1)/[1+u^2(z_1)]^{\frac{1}{2}} = -A\int_{z_1}^{z_2} f(z)dz, \quad (15)$$

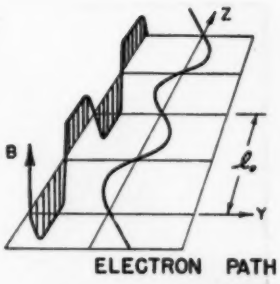

FIG. 1. Schematic diagram of the magnetic undulator.

where $u=dy/dz$. This equation can be integrated once more, and leads to the relation

$$y(z_2)-y(z_1)=\int_{z_1}^{z_2} F(z)/[1-F^2(z)]^{\frac{1}{2}}dz, \quad (16)$$

where

$$F(z)=u(z)/[1+u^2(z)]^{\frac{1}{2}}. \quad (16a)$$

Let $u(z_2)=0$ at a point $z=z_2$ where $df/dz=0$, and let $z=z_1$ be a point where $f=0$. Then, if $f(z)$ is periodic and contains odd harmonics only, the same is true for $y(z)-y(z_1)$.

If it is desired to impose $u(z_2)=0$ at a position $z=z_2$, it is only necessary to make

$$u(z_1)/[1+u^2(z_1)]^{\frac{1}{2}}=A\int_{z_1}^{z_2} f(z)dz, \quad (17)$$

i.e., to determine the injection angle at $z=z_1$ by means of Eq. (17).

As a particular case, it is interesting to consider the path in a sinusoidal flux distribution,

$$B=B_M\cos[2\pi(z-z_2)/l_0]. \quad (18)$$

The orbit is then given by

$$y=a\ln\{aA\cos(z-z_2)/a + [1-(aA)^2\sin^2(z-z_2)/a]^{\frac{1}{2}}\}/(1+aA), \quad (19)$$

where $a=l_0/2\pi$. This is a curve resembling a sine curve, i.e., for values of B and E contemplated in this paper the harmonic content is low. A maximum of this curve occurs at $z=z_2$. Then the question arises as to how to inject the electrons into a finite undulator in order to obtain the periodic orbit given by Eq. (19) for $z>z_2$. The solution is, of course, obtained by means of Eq. (17). It is preferable to inject the electrons parallel to the z axis. The flux distribution preceding the position $z=z_2$ must in this case be adjusted so as to make

$$\int_{-\infty}^{z_2} f(z)dz=0, \quad (20)$$

and this condition is independent of the electron energy.

FIG. 2. The magnetic undulator partially assembled.

III. GENERAL CONSTRUCTION OF THE UNDULATOR

1. The Design

Equation (29) of reference 3 shows that the radiation intensity is proportional to the square of the magnetic-field strength. It is therefore desirable to pass the electrons through a magnetic field with as high an amplitude of field reversal along the beam as can be obtained. Since a number of permanent magnets were available, it was decided to fit a special arrangement of pole pieces to an array of these magnets.

Figure 2 shows this array. Long steel bars cover each set of pole faces. These bars are slotted and teeth are seated horizontally in the slots. The figure shows the upper double set of teeth, and it is seen that they are staggered so as to bring the right-hand set in between the left-hand set. A second double set of teeth comes from below, staggered the opposite way. Vertical gaps are thus formed between the upper and lower sets of teeth in the manner illustrated in Fig. 3. Alternate upper teeth are connected to pole faces of opposite polarity, forming pole gaps with corresponding lower teeth in such a manner that the vertical component of magnetic flux alternates along the axis of the structure.

There is, of course, a rather large amount of leakage flux. The problem of maximizing the useful flux is hardly amenable to an exact solution. Flux measurements were therefore carried out on a model, and an optimum tooth shape was determined empirically.

At the pole tips there occurs some flux fringing which introduces a horizontal component of magnetic field. It is easy to see that the horizontal component points in the same direction in all the gaps and would bend the beam upwards when the S poles are to the right of the beam. It is therefore necessary to allow sufficient overlap between the teeth such that the beam will pass through a middle portion free from horizontal field components. The optimum overlap was determined by studying the field distribution with the help of a large-scale model of the teeth in an electrolytic tank.

The complete magnet assembly carried a second set of magnets arranged symmetrically with respect to those shown in Fig. 2 in the manner indicated in Fig. 3. There were altogether 25 magnets and 50 pole gaps. The distance between pole gaps was 20 mm so that the flux density distribution had a period of 40 mm.

The electrons pass through an evacuated wave guide shown in cross section in Fig. 3. It turned out that the dimensions of standard wave guide were not suitable. A cylindrical tube was pressed into almost rectangular shape by means of a simple die. In the case of the light generation experiment we used a copper tube of inner dimensions 0.37 cm $\times$0.82 cm. For the millimeter wave experiments we used a silver guide 0.37 cm $\times$0.83 cm.

2. Accuracy of Construction

It is clear that the field should be exactly periodic in the longitudinal direction in order to lead to a periodic electron orbit. Deviations from constant spacing between adjacent teeth and changes in the amplitude of the flux density will cause perturbations of the electron orbits. If the fluctuations are cumulative they will cause a sideways drift, and the beam may eventually be lost.

Analysis of orbit perturbation was carried out by means of Eqs. (15) and (16). It was concluded that the spacings should be correct within 0.001 inch and that the flux should repeat with an accuracy of 1 percent. The latter means that the pole separations should be exact within 0.002 inch.

Deviations should, of course, preferably occur in a random sequence.

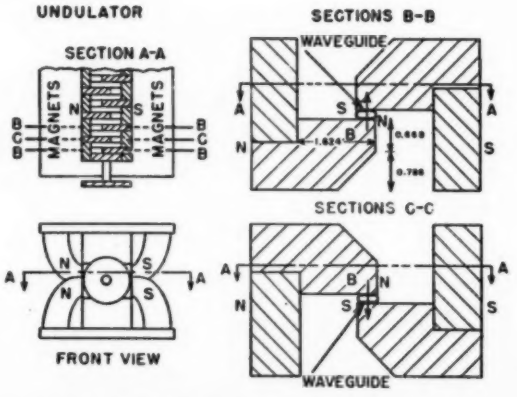

FIG. 3. Details of undulator construction.

3. Magnetic Measurements

Measurement of gap fields was carried out by means of a calibrated coil and a fluxmeter. The coil was mounted in a strip of Masonite which could slide in a brass guide shown in Fig. 2. The flux densities were averaged over one-half space period and amounted to 5600 gauss in the case of the light experiment and to 3900 gauss in the case of the millimeter wave experiment. Deviations were within 1½ percent.

4. Injection

It is easily seen that the electrons should be injected in a horizontal plane under a small angle with the axis or parallel to the axis if Eq. (20) can be satisfied. In so far as the orbit is periodic, the injection angle is repeated with the period of the alternating flux. The necessary injection angle was calculated for various energies. At the high energies required in the case of the light experiment this angle is small, and bellows inserted between the undulator guide and the electron source allowed sufficient adjustments. The whole assembly rested on a steel base plate which could be leveled by means of screws and rotated on a ball bearing situated under the first pole gap. In the case of millimeter generation the amplitude of the orbit, hence the injection angle, are larger, and the adjustments were carried out in a different way.

It was shown in Sec. II, Part 3, Eq. (20) that it is sufficient to adjust the total flux under the first pole gap to a suitable value in order to achieve satisfactory injection. The first tooth pair was made movable, and the gap separation could be adjusted by remote control.

The flux under the first tooth pair includes the flux portion in front of the undulator. Here another problem arose since this part of the flux should also be free from horizontal components arising out of flux fringing. The space immediately in front of the entrance was therefore shielded by a mild steel tube (o.d. ¾ inches, i.d. ½ inch, length 2½ inches) slipped over the wave guide.

IV. GENERATION OF VISIBLE LIGHT

1. The Basic Experiment

It follows from Eq. (1) that an electron beam with an energy 100 Mev passing through the undulator should generate visible light. Such a beam energy was available to us for a short period from the Stanford linear accelerator. The following experiment was carried out. The undulator was connected vacuumwise to the accelerator. At the exit end of the undulator the wave guide was closed by a thin glass plate (microscope cover glass). A mirror made of microscope cover slide on which silver had been evaporated was placed to intercept any light coming through the window. According to the equation

$$\theta = m_0 c^2 / E,$$

where E is the beam energy, this light would arrive under an angle of 1/200 radian. Using a selsyn drive the mirror could be rotated by remote control. At an angle of 45° with the beam the mirror would reflect the light onto the photosurface of a photomultiplier tube (Fig. 4). The photomultiplier worked into a cathode follower and a long cable to a remote oscilloscope. The γ-ray and neutron intensity near the undulator was rather large, and direct visual observation was therefore impossible. The γ-rays also caused a background signal from the photomultiplier, which was considerably reduced by careful lead shielding of the tube. We observed a pulse on the scope, corresponding to the pulsed operation of the accelerator, when the mirror was inclined 45°. The pulse disappeared when this angle was changed by a few degrees in either direction. The signal disappeared also when the electron beam was magnetically deflected and thus prevented from entering the undulator. We regard these observations as clear evidence that the undulator indeed generated a beam of light.

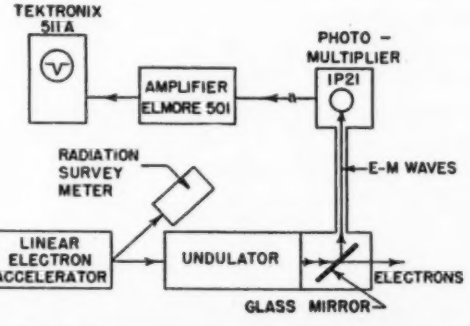

FIG. 4. Detector arrangement for light waves.

FIG. 5. Schematic diagram of polaroid experiment.

2. Polarization

The light should be polarized in a plane perpendicular to the magnetic gap field. To check on the polarization two polaroid windows were mounted on a rotating arm (Fig. 5). Alternate positions of this arm would interrupt the light beam by windows having planes of polarization perpendicular and parallel, respectively, to the gap fields. This comparison of transmitted intensities had to be made rapidly, because the beam intensity of the accelerator was not constant over longer time intervals. Moreover, if the accelerator was turned off to allow for adjustments near the target, one could not be sure to obtain the same primary electron current. The rotation of the polaroid windows was therefore remotely controlled by means of a selsyn drive.

The observed ratio of the pulse heights on the scope

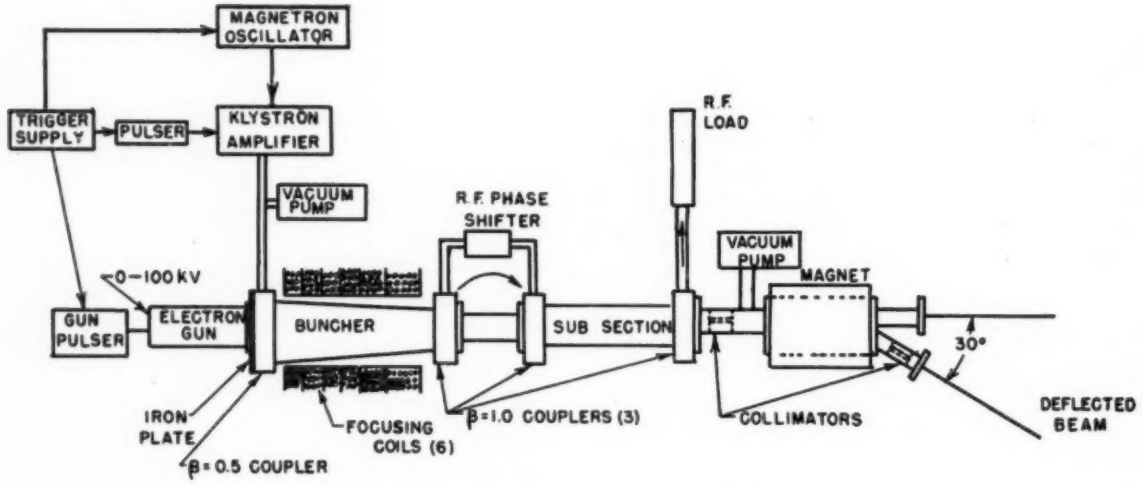

FIG. 6. Equipment outline for buncher tests.

corresponding to light passing through the two polaroid windows was 2:1 in favor of perpendicular polarization. Subtracting the background makes the evidence for polarization even stronger. A quantitative determination was not attempted.

3. Color

A qualitative experiment was also carried out concerning the color distribution of the light. An interference filter passing a band 100A wide centered on 4400A was used. Theoretically, the color of the light should range from green (5500A) to blue (3400A) in the energy range from 95 Mev to 120 Mev. The light fell on a photomultiplier 1P21, which has a sensitivity curve starting at 3000A, rising sharply to a peak at 4000A, and falling to almost zero at 7500A. We got maximum transmission at 90–95 Mev and almost no transmission at 120 Mev. We consider this as a very rough indication of agreement with theoretical predictions.

V. MILLIMETER WAVE GENERATION

1. The Electron Buncher

It has been shown that the power output of the undulator in the millimeter band can be greatly enhanced by suitable bunching of the electrons. A 3–5-Mev electron beam was used in the millimeter wave generation experiment. It was produced by a special linear accelerator, which also achieved a high degree of bunching. The design of this buncher was carried out by Mr. R. Neal and was based on some calculations by Dr. E. L. Chu. It is now used as an injection system for the Mark III Stanford linear accelerator and will be the subject of a separate publication. For our purpose suffice it to say that it is a traveling wave type of accelerator consisting of a disk-loaded structure in which the phase velocity changes from 0.5 c to approximately c over a length of 32 inches. The filling time is 0.2 microseconds. An input power up to 8 Mw is required and was obtained from a Stanford high power klystron operating at 2856 Mc/sec. Electron pulses drawn at 80 kv are obtained from a tungsten filament gun and injected into the accelerator. The gun pulse lasts 1 microsecond and is applied 0.2 microseconds after the klystron pulse.

Tests of this buncher revealed an energy spectrum of 0.2-Mev half-width at 5 Mev. The accelerator collects electrons during the full period of the traveling in the accelerator and bunches them to within 30°; and it may have been better than indicated by the foregoing numbers. Figure 6 shows a block diagram of the set-up used for testing the buncher. The buncher is followed by a standard (2-ft) accelerator section, i.e., by a uniformly disk-loaded section which obtains power coupled out of the end of the buncher through a phase shifter which allows variation of the relative phases of buncher and standard section ranging over 360°. For energy measurement purposes the beam can be magnetically deflected into a channel leading to a radiation monitor. It was necessary to insert collimators with $\frac{1}{16}$-inch clearing holes in order to obtain good energy resolution.

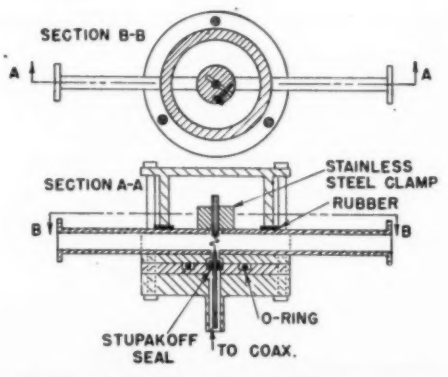

FIG. 7. Crystal detector for millimeter waves.

2. Detectors

Crystal detectors were used which could be connected to the undulator guide and evacuated so that the radiation was not intercepted by any windows (Fig. 7).

We used 0.002-in. tungsten whiskers, crimped as shown in the figure, with fine contact points etched by means of a process described in the literature.[7] Standard 10-cm crystals were remounted on a brass stem and made very satisfactory rectifiers in conjunction with the fine whiskers. The detector output was fed into a slightly modified Hewlett-Packard 450A amplifier with 3-Mc/sec band width. The modification consisted in shortening loops in the input system to reduce pick-up and replacing the input resistor by a 1000-ohm resistance, which was determined to be approximately the optimum resistance for the crystal. The detector and amplifier were placed into a carefully sealed copper box, and a long doubly shielded cable connected to a remote Tektronix oscilloscope. The shielding problem was considerable. We operated in the vicinity of the klystron pulser, which is equivalent to a 50-Mw spark transmitter. Another detector

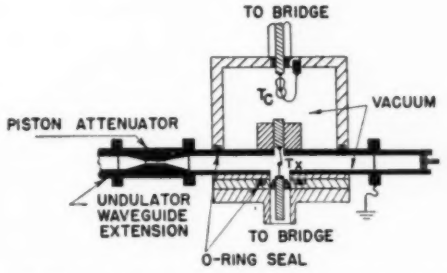

FIG. 8. Thermistor power-measurement arrangement.

arrangement consisted of two thermistors mounted in an assembly very similar to the crystal detector assembly. One thermistor of type WE D170575 (originally unmounted) was inserted in the wave guide as shown in Fig. 8. The other one, of type WED170396 (mounted in a glass bead), had similar electrical characteristics and was located near the first, in vacuum but outside the wave guide. The thermistors formed two arms of a Wheatstone bridge having a third arm with variable resistors. This bridge could be balanced (despite the fact that the thermistors are nonlinear devices); but the reading drifted because of interference picked up by the galvanometer and battery leads. The operation of the bridge was further improved by connecting one potentiometer of a ganged pair in series with each thermistor (Fig. 9). It was then possible to match the rate of change of resistance of the two thermistor arms and thus get a stable bridge. This instrument detected the heat radiated by the gun filament and was balanced and stabilized with the

[7] H. C. Torrey and C. H. Whitmer, *Crystal Rectifiers* (McGraw-Hill Book Company, Inc., New York, 1948), pp. 318–320.

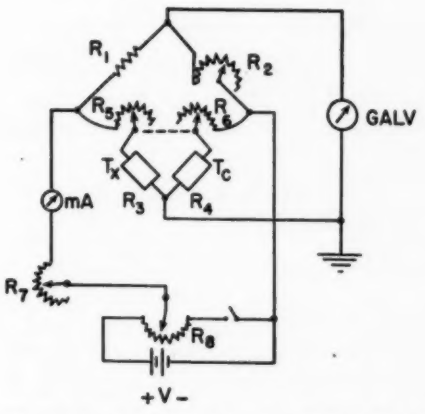

FIG. 9. Thermistor bridge circuit: $R_1=208\sim$, $R_2=133$–$201\sim$, $R_3\sim150\sim$, $R_4\sim150\sim$, $R_5=0$–$60\sim$, $R_6=0$–$60\sim$, $R_7=0$–$70\sim$, $R_8=0$–$150\sim$, $V=6$ volts.

filament running. Measurements were made by turning the gun pulse on and off.

3. Wavelength Determination

A rather crude measurement of wavelength consisted in placing various cylindrical piston attenuators between the undulator and the detector (Fig. 10). They were about 1 inch long, with diameters in the range of 0.035 inch to 0.200 inch. The figure shows an attempt to match the cylindrical holes to the rectangular wave guides by means of tapered sections. These were "hobbed" into the brass cylinders by means of steel punches. The transmission through the section in the pass region was greatly improved by making the transitions as gradual as possible.

4. Observations

For the purpose of observing millimeter waves the following arrangements were used.

(a) A set-up as illustrated in Fig. 6 was followed by the undulator. A vacuum valve connected the undulator to the magnetic deflector and allowed separate evacuation of the undulator wave guide including the detector. The undulator wave guide (internal dimensions 0.37 cm $\times$0.83 cm) was followed by a gradually tapered adapter connecting to standard RG-97/U silver guide (inside dimensions 0.568 cm $\times$0.284 cm). This guide was 10 inches long and curved upwards through 90° to connect to the crystal detector. Detector and undulator were heavily shielded by lead bricks for reasons of radiation safety (Fig. 11).

FIG. 10. Piston attenuator for wavelength estimation.

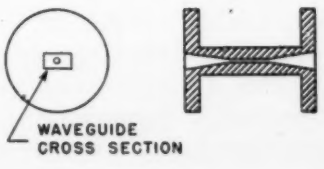

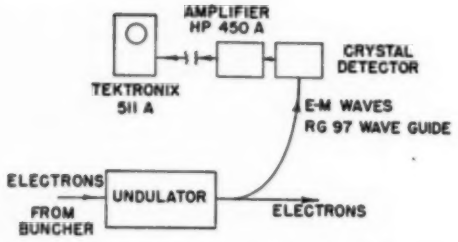

FIG. 11. Detector arrangement for millimeter waves.

Operation of this set-up produced short pulses on the scope corresponding to the pulsed operation of the buncher. Magnetic deflection of the beam in front of the undulator did not change the picture, but the pulses disappeared when a thin aluminum foil was placed across the guide or when a carbon-coated resistor strip was inserted into the guide. It was concluded that the pulses were due to a radiation of fairly short wavelength, since it passed through a piston attenuator with a cut-off wavelength of 2.7 mm. Further information about the nature of this radiation was obtained as follows: The standard accelerator section was run in phase with the buncher, then 90° out of phase leading, and also 90° out of phase lagging. In the first case, the standard section adds energy to the beam; in the other two cases it does not. However, when the standard section is leading, it should have a phase focusing and radially defocusing action, while it should be phase defocusing and radially focusing when it is lagging. In the former case the radiation was observed but not in the latter case. This is consistent with the idea that the radiation is due to radial oscillations in the fringing field of the loading disks, the field of the space harmonics. It is hard to determine the nature of these space harmonics without an exact determination of the frequency spectrum.

(b) The standard section was removed, and the distance between buncher and undulator was shortened considerably. The $\frac{1}{16}$-inch collimators were also removed. We now observed a detector signal at low beam levels which disappeared when the beam was deflected slightly. We also installed a vertical-deflection magnet, and the signal was very sensitive to its setting. At higher beam currents an increasing amount of residual signal remained after deflection, and at the highest beam currents this was predominant. Only the signal which disappeared with deflection originated in the undulator. The radiation passed through a piston attenuator with a cut-off wavelength of 1.9 mm. The signal was attenuated; but as the matching by means of tapering sections may not be effective, it is not certain whether the radiation has components with wavelengths larger than 1.9 mm. It did not pass through a piston attenuator with a lower cut-off wavelength. Theoretically, from Eq. (7), the lowest wavelength should be 0.44 mm at a beam energy of 3 Mev. The signal which did not disappear with deflection is due to radiation with a longer minimum wavelength. Some of it passed through a 2.7-mm cut-off section, but no signal passed through sections with lower cut-off. The radiation must originate in the buncher.

Measurements were made very difficult by the high level of interference from the pulse modulator. It was, however, possible to obtain fairly reliable estimates of the observed power levels.

Measurements made at Columbia University (see reference 6) indicate that a signal-to-noise ratio of unity received from a crystal corresponds to a peak power of 0.6 microwatts in the 1-mm wavelength band. Their measurements were carried out with amplifier band width of about 1 Mc/sec, and the noise voltage is of the order of microvolts. We received a signal corresponding to 50 millivolts appearing at the crystal terminals, and we concluded that the peak power of the undulator radiation might have been of the order of 10–100 watts. On the other hand, measurements with

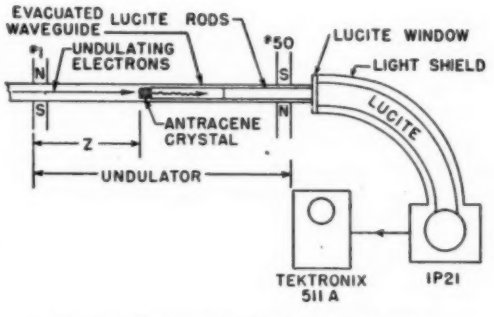

FIG. 12. Exploration of the electron beam.

our thermistor bridge indicated a peak power of 10 milliwatts. The power intercepted by the thermistor was probably a very small fraction of the incident power, however, because a crystal detector placed behind the thermistor showed no noticeable decrease of signal. If the power-interception ratio was equal to the ratio of thermistor to wave-guide cross sections, we would arrive at a peak power of 10 watts. It is thus possible to make the conservative statement that the power generation by the undulator was in excess of 1 watt.

5. Exploration of the Beam

The current in front of the undulator was measured by means of a collector electrode to be 6×10^9 electrons per pulse. To trace the beam inside the undulator wave guide is a more difficult task. The method used consisted in obtaining scintillations from an anthracene crystal, 0.7 cm long, placed in the guide. This was followed by Lucite light pipes channeling the light to the photosurface of a 1P21 photomultiplier, which in

turn was connected to a cathode follower and an oscilloscope. The arrangement is illustrated by Fig. 12. The electrons lose about 1 Mev in the crystal, and this energy is converted into light energy which is detected by the phototube. The light output is proportional to the electron current striking the crystal. In this way it was found that 90 percent of the current was lost in the first 15 cm of the undulator. We attribute this to the fact that the beam has such a large cross section that a large fraction is deflected by the horizontal component of the field arising from flux fringing and that the beam is too divergent. The result shows that a substantial increase of the power output could be obtained by improving the beam geometry.

VI. COMMENTS AND CONCLUSIONS

It will be noticed that our results are of a provisional nature and that our methods of measurement were improvisations rather than the best possible methods. This is due to the fact that both the accelerator and the buncher were available to us for a short time only. (The buncher is now used as an injection system for the Stanford linear accelerator.) It is intended to continue the work, and it is hoped to improve the measuring technique and make several important changes. Regarding measurements, it would be important to work at a larger distance from interference sources such as klystron or magnetron modulators. The beam geometry and the bunching should be improved and the energy spread within a bunch reduced.

JOURNAL OF APPLIED PHYSICS VOLUME 24, NUMBER 7 JULY, 1953

A Theorem on the Impedance-Transforming Properties of Reactive Networks

LEO STORCH
Hughes Research and Development Laboratories, Culver City, California
(Received January 19, 1953)

Complex impedance-matching problems are simplified substantially when they are studied in terms of appropriate circle transformations in the R-X impedance plane. The geometric approach yields valuable insight into the behavior of specific networks and leads to the interesting Circle-Locus Theorem which applies to any arbitrary, linear, reactive, two-terminal-pair network with lumped or distributed parameters (or a combination of both).

I. INTRODUCTION

ONE of the problems regularly encountered in communications engineering is the design of an impedance-matching network, which is to be inserted between the power source and the load. Since the principal function of such a network is to maximize the power delivered to the load, it usually will be made reactive as far as possible. That is to say, any dissipation that is present is due exclusively to the physical limitations on the Q's of coils and capacitors. Since coil Q's are of the order of 100 at radio frequencies and capacitor Q's are even much higher, it is justifiable to disregard the resistive components and to treat impedance-matching networks as purely reactive.

If a load impedance z_1 and a desired input impedance w_1 are specified,[1] both of which are located in the right-half of the impedance plane and are complex in the general case, there is an infinite number of reactive networks which can be designed to carry z_1 into w_1 at a fixed frequency. The choice of a specific network is usually guided by such relatively simple criteria as: (a) economy in the number of components; (b) convenient values for the components; (c) attenuation of the second harmonic (in case of class C amplifiers) or other undesirable frequencies.

The problem is fundamentally much more complex when the load impedance is not constant and may assume any value in a more or less well-defined area of the load-impedance plane. Such conditions frequently arise in practice, even when the operating frequency is fixed. It stands to reason that the input impedance "w" will deviate from w_1 in some manner and by varying amounts, as the load impedance "z" describes a path in the load-impedance plane with z_1 as the point of departure. But the power output drops from its maximum value when the impedance presented to the power source deviates from the optimum value w_1. For a constant-voltage generator of fixed generator impedance, the contours of constant power output are circles. The greater the diameter of a member of this family of circles, the smaller the power output which is associated with it. In the case of class C amplifiers, the contours of constant power output appear to be oval-shaped curves, which can be approximated fairly well by means of circles.

Some of the vexing questions that one faces in the course of the network design are: (a) How much dispersion in input impedance will result, with respect to the optimum value w_1, if the load impedance varies

[1] The symbol "w" will be used for input impedance rather than "z" in order to avoid cumbersome multiple subscripts.

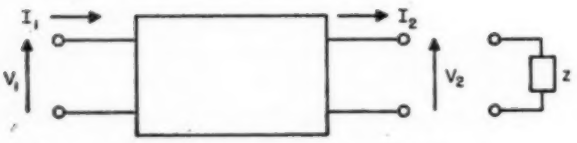

FIG. 1. The two-terminal-pair network.

over a certain area? (b) Will the input-impedance area be continuous or will it break up into several islands? (c) Will the dispersion be a function of the impedance-matching network configuration? (d) If so, how should this network be designed so that a certain load-impedance area can be compressed into the smallest possible input-impedance area, in order to achieve maximum power output? (e) Can the network be designed so as to correlate a small deviation from the nominal load impedance z_1 with a small deviation from the optimum input impedance w_1 and is such a requirement in conflict with item (d) or independent of it? Only when the network designer has the answers to such aspects of the problem readily available, is he in a position to select a network on its actual merits and to make sure that the power output will not drop below the design value under any of the possible operating conditions.

The method one would ordinarily adopt consists probably of choosing a batch of test-points in the specified load-impedance area and of investigating the behavior of one of the more commonly used networks (such as an L, a pi, or a T) by means of tedious point-by-point calculations. In the course of events, one might very likely decide to repeat all the computations for a different network, once or even several times, in the not unreasonable expectation to improve on the first set of results and to reduce the dispersion in input impedance. Although this "brute force" process is very laborious, particularly when repeated for several networks, it is motivated by expediency and it is inherently not capable of supplying a general solution. That is to say, satisfaction that an optimum solution has been reached does not lie that way.

In this paper a more general and yet compact method will be developed, which deals with contours and areas rather than points; which is simple to apply; which is geometrical in nature, and therefore stimulates intuition; and which yields a very neat solution of the several aspects of the problem which have been outlined. Although transmission-line circle diagrams have inspired the development of the geometrical interpretation of impedance transformations by reactive networks, there is no direct link. Conventional transmission-line circle diagrams[2–4] and related network diagrams[5] are based on a very specialized reference impedance z_1 which is either the iterative or the image impedance of the network, so that they are far too restrictive to be helpful here. Properties of the impedance transformation (5a) that are much wider in scope are needed to answer the questions raised in items (a) to (e), and they are the ones which are used to derive the Circle-Locus Theorem.

II. FOUR-TERMINAL NETWORKS AS IMPEDANCE TRANSFORMERS

A linear, finite, two-terminal-pair network is characterized by the pair of equations

$$V_1 = AV_2 + BI_2, \tag{1}$$

$$I_1 = CV_2 + DI_2. \tag{2}$$

The two equations express the input voltage V_1 and the input current I_1 as a linear transformation of the load voltage V_2 and load current I_2 (Fig. 1). The four "general circuit parameters" A, B, C, and D are fixed, complex numbers when the network is excited by a sinusoid of fixed frequency and has reached the steady state.[6] They are related by $AD-BC=1$ if the network obeys the reciprocity theorem, i.e., if it is passive and nondegenerate.

Let the input impedance be designated by

$$w = \frac{V_1}{I_1},$$

and let the load impedance be designated by

$$z = \frac{V_2}{I_2}.$$

Dividing (1) and (2) and making these substitutions for V_1/I_1 and V_2/I_2, it follows that

$$w = \frac{Az+B}{Cz+D}. \tag{3}$$

The input impedance "w" is a linear fractional transformation of the load impedance "z." The degenerate case $AD-BC=0$ is excluded from further consideration, since it amounts to $w=A/C=B/D$ for all values of "z." It arises only when the input terminals are not linked to the output terminals or when a permanent short circuit across the output terminals is part of the network.

The transformation (3) has many interesting properties, some of which can be forged into a tool which is valuable in the design of impedance-matching networks. Of particular interest is the subgroup of transformations characteristic of reactive networks. Equations (1) and (2) are satisfied dimensionally when A and D are numerics (i.e., ratios of two impedances), B is an impedance, and C is an admittance. The general

[2] W. Jackson and L. G. H. Huxley, J. Inst. Elec. Engrs. **91**, 105–127 (1944).
[3] H. L. Krauss, Elec. Eng. **68**, 767–774 (1949).
[4] Leo Storch, Elec. Eng. **69**, 93–94 (1950).
[5] J. Rybner, Inst. Elec. Engrs. **95**, 243–252 (1948).

[6] Massachusetts Institute of Technology Staff, *Electric Circuits* (John Wiley and Sons, Inc., New York, 1940), pp. 452–456.

circuit parameters A, B, C, D are functions of the network elements only and are independent of the terminating impedance. Since reactive networks contain only impedances of the form jX, i.e., reactances due to capacitances, self- or mutual inductances, it follows that A and D are real and that B and C are pure imaginaries. In terms of the real quantities a, b, c, and d, the general circuit parameters of reactive networks may be written as

$$A=a \tag{4a}$$

$$B=jb, \tag{4b}$$

$$C=jc, \tag{4c}$$

$$D=d; \tag{4d}$$

also,

$$ad+bc=1 \tag{4e}$$

for passive, bilateral networks.

For reactive networks, Eq. (3) takes the form

$$w=\frac{az+jb}{jcz+d}, \tag{5a}$$

where the degenerate case $ad+bc=0$ is disregarded as before.[7]

In a moment, the fact that reactive networks transform load impedances symmetrical with respect to the reactance axis into input impedances also symmetrical with respect to the reactance axis will assume significance. This statement is expressed symbolically by $w=-\bar{w}$ when $z=-\bar{z}$.[8] It can be proved by taking conjugates in (5a)

$$\bar{w}=\frac{a\bar{z}-jb}{-jc\bar{z}+d},$$

and multiplying both sides by (-1),

$$-\bar{w}=\frac{a(-\bar{z})+jb}{jc(-\bar{z})+d}. \tag{5b}$$

The recognition that neither $(-\bar{z})$ nor $(-\bar{w})$ are impedances realizable by passive networks, on account of their resistive components being negative, need not cause any apprehension. They are used merely in the course of deriving interesting results about physically realizable impedances.

[7] "Reactive network" is used from here on as a shorthand notation for "linear, finite, nondegenerate, fixed (fixed elements and fixed frequency), reactive, two-terminal-pair network." Note that "passive, bilateral," reactive networks (containing capacitances, self- and mutual inductances) are a subclass of "nondegenerate," reactive networks.

[8] The bar indicates the complex conjugate of a vector, i.e., $\bar{g}=g_1-jg_2$ when $g=g_1+jg_2$.

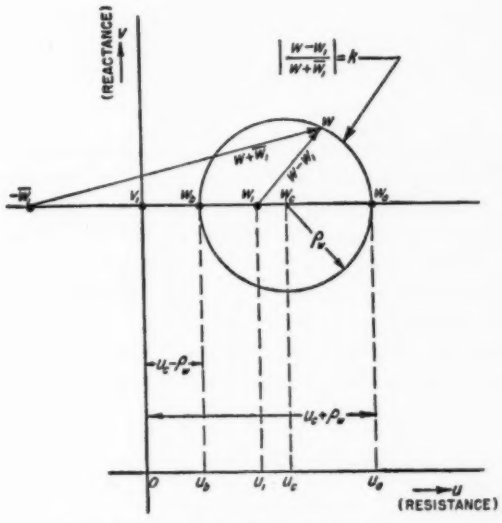

FIG. 2. The circle $|(W-W_1)/(W+\bar{W}_1)|=k$.

III. A CIRCLE-LOCUS THEOREM FOR REACTIVE NETWORKS

The transformations (3) and (5) possess the important property of transforming circles into circles; in this connection, straight lines are considered as circles of infinite radius. Consider the expression

$$(w-w_1)/(w+\bar{w}_1), \tag{6}$$

where "w" is a variable vector and w_1 and $\bar{w}_1$ are fixed vectors. Each vector is represented by a point in the plane which has the coordinates of its tip. The range of all points "w" which result in a constant magnitude of (6) forms a circle. To verify that

$$\left|\frac{w-w_1}{w+\bar{w}_1}\right|=k, \quad w_1\neq-\bar{w}_1, \tag{7}$$

is actually the equation of a circle when $0<k<\infty$, and to derive some further results, all points w_q are written in terms of their rectangular components u_q+jv_q:

$$\frac{(u-u_1)^2+(v-v_1)^2}{(u+u_1)^2+(v-v_1)^2}=k^2,$$

or

$$u^2+u_1^2+(v-v_1)^2-2u\cdot u_1\frac{1+k^2}{1-k^2}=0, \tag{8a}$$

$$\therefore \quad \left[u-u_1\cdot\frac{1+k^2}{1-k^2}\right]^2+[v-v_1]^2=\left[u_1\cdot\frac{2k}{1-k^2}\right]^2. \tag{8b}$$

This is the equation of a circle (see Fig. 2) in its familiar form, with center

$$w_c=u_c+jv_c=u_1\cdot\frac{1+k^2}{1-k^2}+jv_1, \tag{9a}$$

and radius

$$\rho_w = u_1 \cdot \frac{2k}{1-k^2}. \tag{9b}$$

In preparation for the further development, it is imperative to note that the ratio of the diameter to the resistive component of the center of the circle is completely determined by the parameter "k." Likewise, it is useful to establish a relationship between the impedance points w_a, w_b, w_c, and w_1 in Fig. 2, which have in common $v_a = v_b = v_c = v_1$.

Owing to the way w_a and w_b have been located $u_{a,b} = u_c \pm \rho_w$. Writing u_c and ρ_w in terms of (9a, 9b),

$$u_a = u_c + \rho_w = u_1 \cdot \frac{1+k}{1-k},$$

$$u_b = u_c - \rho_w = u_1 \cdot \frac{1-k}{1+k}.$$

It is convenient to define a parameter "s" which is expressed in terms of "k" only

$$s = \frac{1+k}{1-k}, \tag{10a}$$

so that

$$u_a = s \cdot u_1, \tag{10b}$$

$$u_b = u_1/s. \tag{10c}$$

Therefore, when a circle is specified as usual by means of the center and the radius, the equivalent parameters "u_1" and "s" are simply

$$u_1 = (u_a \cdot u_b)^{\frac{1}{2}}, \tag{10d}$$

$$s = \left(\frac{u_a}{u_b}\right)^{\frac{1}{2}}, \tag{10e}$$

where $u_{a,b} = u_c \pm \rho_w$ (see Fig. 2). According to (10e), the ratio of the maximum to the minimum resistive component of points on the circle is a function of "s" or "k" only. This is equivalent to the previous statement: the ratio of the diameter to the resistive component of the center of the circle is completely determined by the parameter "k."

A single restriction has been placed on the location of w_1 in (7). It must not lie on the reactance axis, i.e., w_1 must not equal $(-\bar{w}_1)$. Otherwise, the expression (7) would be trivial, since it would be satisfied by every point in the plane provided $k=1$ and by no point if $k \neq 1$. In general, if $0<k<1$, the corresponding circle lies wholly in the right half-plane if "w_1" does so, and it encloses w_1; *if* $k=1$, the circle coincides with the reactance axis; if $1<k<\infty$, the corresponding circle lies wholly in the left half-plane and encloses $(-\bar{w}_1)$.

The input-impedance circle (7) in the w plane corresponds to a load-impedance curve in the z plane. To determine the shape of this curve, substitute for w and w_1 in terms of (5a) and for $(-\bar{w}_1)$ in terms of (5b)

$$\left|\frac{w-w_1}{w-(-\bar{w}_1)}\right| = \left|\frac{\dfrac{az+jb}{jcz+d} - \dfrac{az_1+jb}{jcz_1+d}}{\dfrac{az+jb}{jcz+d} - \dfrac{-a\bar{z}_1+jb}{-jc\bar{z}_1+d}}\right|$$

$$= \left|\frac{d-jc\bar{z}_1}{d+jcz_1}\right| \cdot \left|\frac{z-z_1}{z+\bar{z}_1}\right| = k. \tag{11}$$

Since numerator and denominator are conjugate complex vectors,

$$\left|\frac{d-jc\bar{z}_1}{d+jcz_1}\right| = 1.$$

Consequently,

$$\left|\frac{w-w_1}{w+\bar{w}_1}\right| = \left|\frac{z-z_1}{z+\bar{z}_1}\right| = k. \tag{12}$$

A circle in the z plane transforms into a circle in the w plane and the parameter "k" is not modified by the transformation. In view of the relationship that "k" has been shown to control, it is now possible to state the first part of the Circle-Locus Theorem:

Theorem 1a: A load-impedance circle not having any point in common with the reactance axis is transformed by a nondegenerate, linear, finite, fixed, reactive network into an input-impedance circle which must possess the same ratio of diameter to resistive component of the impedance of the center, irrespective of the network configuration.

If the load impedance lies on a certain z circle, the input impedance must lie somewhere on the corresponding w circle. If two pairs of circles are considered of different "k" but with respect to the same z_1 and w_1, it follows from Eq. (12) that the z circle lying closer to z_1 transforms into that w circle which lies closer to w_1. As a consequence, if a load impedance lies somewhere inside a given z circle, the input impedance must lie somewhere inside the corresponding w circle and Theorem 1a can be stated in terms of enclosed circular areas as well as in terms of their perimeters.

The Circle-Locus Theorem 1a applies to any reactive network[7] of arbitrary configuration, which may possess any finite number of branches, containing elements of lumped or distributed parameters. It gives compact, definite, and precise answers to the questions about dispersion in input impedance and about differentiation between networks, which were raised in the introduction. Any reactive network[7] transforms a circular load-impedance area into a single, connected, circular input-impedance area. Irrespective of the network

configuration, all reactive networks are equivalent as far as their impedance-confining properties are concerned. This means that if a specific, reactive network transforms a given z circle area into a certain w circle area, no reactive network can be found which will transform the same z circle area so that it lies wholly inside the w circle but without filling it completely.

If a network is to link two specific circles which satisfy Theorem 1a, it must be designed in accordance with Theorem 1b, which states

Theorem 1b: The necessary and sufficient condition that a nondegenerate, linear, finite, fixed, reactive network link two specific circles (or circular areas) related as in Theorem 1a is that it should transform the load-impedance $z_1=(r_a\cdot r_b)^{\frac{1}{2}}+jx_c$ *into the input-impedance* $w_1=(u_a\cdot u_b)^{\frac{1}{2}}+jv_c$.

The meaning of the symbols is such that a parallel to the R axis which is passed through the center of the z circle intersects it in the points r_a+jx_c and r_b+jx_c and that a similar line passed through the center of the w circle intersects it in the points u_a+jv_c and u_b+jv_c.

In view of the fact that the transformation (5a) is one-to-one (univalent),[9] the proof of Theorem 1b is implicit in expression (11); also, the expressions for z_1 and w_1 in terms of certain points on the two respective circles are supported by (10d) as derived from (7). Since (5a) implies (5b), it may be deduced that any reactive network maps the right half-plane on itself. It is always possible to find reactive networks which will transform a given z_1 into any desired w_1, both lying in the right half-plane. In other words, Theorem 1b can be applied to any two circles whatsoever which possess the same ratio of diameter to resistive component of the center and lie wholly in the right-half of the impedance plane.

IV. LOCI OF CONSTANT POWER OUTPUT

The selection of a value for w_1 to achieve optimum power output depends on the properties of the power source. It is easy to show that for a constant-voltage generator E_g, of fixed internal impedance Z_g, the circle (7) or (8b) represents a locus of constant input power if $w_1=\bar{Z}_g$. Since the network is lossless by hypothesis, the corresponding load-impedance circle (12) represents a locus of constant output power, which is equal in value to the input power.

The power delivered to the network is

$$P=|I_1|^2\cdot R_{\text{input}}=\frac{E_g^2\cdot u}{|w+Z_g|^2}=\frac{E_g^2\cdot u}{|w+\bar{w}_1|^2}=\frac{E_g^2\cdot u}{(u+u_1)^2+(v-v_1)^2}.$$

Making use of (8a), the denominator is seen to be equal to $(4uu_1)/(1-k^2)$. Therefore

$$P=E_g^2\cdot\frac{1-k^2}{4u_1}=\frac{E_g^2}{u_1\left(\sqrt{s}+\frac{1}{\sqrt{s}}\right)^2}=\frac{E_g^2}{R_g\left(\sqrt{s}+\frac{1}{\sqrt{s}}\right)^2}, \tag{13a}$$

where "s" is defined by (10a) or (10e). Similarly, for a constant-current generator I_g shunted by a fixed internal impedance $Z_g=\bar{w}_1$:

$$P=I_g^2\left|\frac{\bar{w}_1}{w+\bar{w}_1}\right|^2\cdot u=I_g^2|\bar{w}_1|^2\cdot\frac{1-k^2}{4u_1}$$

$$=I_g^2|\bar{w}_1|^2\cdot\frac{1}{u_1\left(\sqrt{s}+\frac{1}{\sqrt{s}}\right)^2}=\frac{I_g^2\left(R_g+\frac{X_g^2}{R_g}\right)}{\left(\sqrt{s}+\frac{1}{\sqrt{s}}\right)^2}. \tag{13b}$$

V. APPLICATIONS OF THE CIRCLE-LOCUS THEOREM

While it is not practical to describe the various applications of the Circle-Locus Theorem and to cite typical examples, it is difficult to refrain from pointing out two important illustrations, which might not otherwise come to mind.

A. Frequency as a Variable

There are many factors which cause sizeable changes in load impedance at a fixed frequency. But at least of equal importance are the effects of frequency, both on the load impedance and on the network impedances, when the operating frequency is variable and may assume different values.

Most communications systems operate on more than one channel, some on very many. In order to study the behavior of a given matching network as a function of frequency, it is sufficient to trace merely the path of a single impedance point provided that advantage is taken of the Circle-Locus Theorem. Let it be assumed that w_1 is independent of frequency, which is usually the case when Z_g is purely resistive. Then, for a frequency "f," let the corresponding general circuit parameters of the passive, reactive network be a', b', c', and d'. It follows from (5a) and (4e) that z_1' corresponding to this frequency is given by

$$z_1'=\frac{d'w_1-jb'}{-jc'w_1+a'}. \tag{14}$$

If the permissible input-impedance circle is characterized by $s=s_a$ with respect to w_1, then the impedance points of the z circle with maximum and minimum resistive components are equal to $z_a'=r_1'\cdot s_a+jx_1'$ and

[9] Zeev Nehari, *Conformal Mapping* (McGraw-Hill Book Company, Inc., New York, 1952), p. 158.

$z_b' = r_1'/s_a + jx_1'$. Therefore, the z circle is completely determined. Since the frequency characteristics of the load, e.g., antenna, and its associated tolerance area are known, it is very easy to determine whether at this frequency the load-impedance area lies inside the permissible z circle or not. In this way, the frequency limits for each network adjustment can be determined without much effort.

The Circle-Locus Theorem is still very helpful although the problem is not a linear one any more. The movement of merely a single point z_1' as a function of frequency needs to be scrutinized and the network can be selected with the single idea in mind of steering the point z_1' in the optimum direction. Altogether, this scheme introduces remarkable simplifications in comparison to the more conventional methods, both by eliminating a mass of cumbersome calculations and by displaying boldly the essentials of the problem as well as a straightforward method of solution.

B. RF Transmission Lines as Network Links

Very often an rf transmission line is an integral link in an impedance-matching system, since the load may be situated at a considerable distance from the source of rf power. In such cases, the SWR (standing-wave ratio) is either an item of interest or its maximum value is specified. If a circular operating area has been demarcated anywhere in the right half of the load-impedance plane, the maximum SWR prevailing on an rf transmission-line link can be obtained with the help of the Circle-Locus Theorem. A little reflection will show that the maximum SWR is equal to $s_{max} = (r_a/r_b)^{\frac{1}{2}}$, provided the point z_1, as determined by the values r_a and r_b associated with the boundary circle, is transformed into the characteristic impedance R_0 of the rf transmission line. Furthermore, it is easy to show that this match of z_1 to R_0 represents optimum conditions.

It will be recalled that a constant-SWR circle of an rf transmission line has its center on the R axis and intersects it at the points σR_0 and R_0/σ, σ being equal to the SWR value.[10] The SWR is minimized, i.e., transmission is optimized, when the boundary z circle fills completely a constant-SWR circle. If z_1 as defined in Theorem 1b is transformed into R_0 by a reactive network, the boundary-circle intercepts the R axis at $s_{max} \cdot R_0$ and R_0/s_{max} by Theorem 1a. But the inverseness of these intercepts in R_0^2 has been shown to be the criterion of a constant-SWR circle. By comparison with the expressions σR_0 and R_0/σ

$$\sigma_{max} = s_{max} = \left(\frac{r_a}{r_b}\right)^{\frac{1}{2}}, \tag{14}$$

at the load terminals of the rf transmission line. Since an rf transmission line is conventionally assumed to be lossless, the SWR at any point on the line is equal to the SWR at the load terminals by Theorem 1a. Therefore, Eq. (14) represents truly the maximum SWR on the line, corresponding to the given circular load-impedance area.

This value of SWR has to be contended with when the load impedance assumes values on the boundary circle. For a load impedance z_i in the interior, the corresponding SWR is smaller and is equal to the "s" of the circle which passes through z_i in such a manner that the product of the abscissas of the points of intersection with a line through z_1 and parallel to the R axis is equal to r_1^2. This value may be determined graphically or analytically from a combination of (10a) and (8a):[11]

$$s_i + \frac{1}{s_i} = 2 \cdot \frac{1+k_i^2}{1-k_i^2} = \frac{r_i^2 + r_1^2 + (x_i - x_1)^2}{r_i \cdot r_1}. \tag{15}$$

In expositions on rf transmission lines,[12] it is usually shown that the input impedance of an arbitrary length of line lies on the same SWR circle as the load impedance, or, in other words, that an SWR circle transforms into itself. But this is only a special case of the Circle-Locus Theorem. For an SWR circle, $z_1 = R_0$. Since R_0 is the characteristic impedance of the transmission line, w_1 is also equal to R_0. When $w_1 = z_1$ in Eq. (12), then clearly the input-impedance circle and the load-impedance circle coincide since they have in common not only "k" but also the reference impedance z_1.

The Circle-Locus Theorem takes its place in the hierarchy of network theorems as a very broad generalization of this known property of rf transmission lines, generalizing from the symmetrical, distributed-parameter structure of the rf transmission line to the much wider class of arbitrary linear, reactive networks and from the single, very special reference impedance R_0 (the characteristic impedance) to any arbitrary reference impedance not lying on the reactance axis.

[10] P. H. Smith, Electronics, p. 29, Fig. 1 (January, 1939); W. R. LePage and S. Seely, *General Newtork Analysis* (McGraw-Hill Book Company, Inc., New York, 1952), Chap. 10, p. 341.

[11] Equation (8a), of course, may be expressed in terms of $z = r + jx$ rather than $w = u + jv$ without losing any of its validity.

[12] P. H. Smith, reference 10; W. R. LePage and S. Seely, reference 10.

Experimental Verification of the Metal-Strip Delay-Lens Theory*

SEYMOUR B. COHN
Stanford Research Institute, Stanford, California
(Received November 3, 1952)

In this paper a comparison is made between the index-of-refraction values measured on five metal-strip test samples and values computed from four solutions that have appeared in the literature. Three of the samples are wave-guide equivalents, and two are free-space arrays. The techniques of measurement for the two types of structures are described briefly. It has been found that all four solutions have certain ranges of validity, but that only one is reliable over the full practical range of the design parameters. This solution, derived previously by the writer, is based on a transmission-line equivalent circuit in which proximity effects are taken into account.

I. INTRODUCTION

SINCE the original treatment of the metal-strip delay-lens medium by W. E. Kock,[1] a number of other papers by various authors have appeared on this subject. At the present time four different formulas for the index of refraction of the metal-strip medium are available. The first, given by Kock, is obtained through an analogy to a molecular medium. The second, derived by this writer[2] and by Brown,[3] assumes an equivalence to a transmission line periodically loaded by shunt capacitances. The third, also derived by this writer,[2,4] utilizes a more exact shunt-loaded line taking proximity effects into account. The fourth, derived by Sharpless,[5] assumes an equivalence to a line loaded by series inductances. The agreement between these formulas is in general rather poor, and therefore experimental data that can be compared with computed values should be of interest. In this paper the results of measurements on five different test pieces are presented, and it is found that the third formula mentioned above yields the most reliable agreement between measured and computed values.

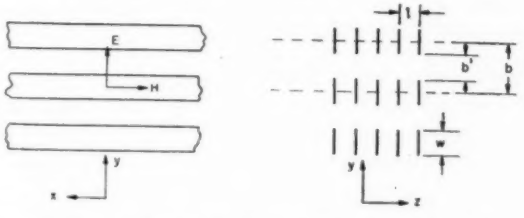

FIG. 1. Metal-strip delay structure in free space.

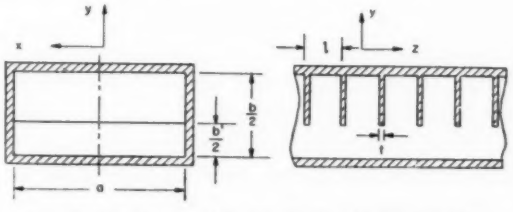

FIG. 2. Metal-strip delay structure in wave guide.

II. EXPERIMENTAL TECHNIQUES

Three of the five test structures were in rectangular wave guide, while the other two were free-space arrays. The wave-guide configuration is shown in Fig. 2. If images of the metal strips are taken in the upper and lower walls of the wave guide, an array of obstacles is obtained in the y-z plane that is identical to that in Fig. 1. It can also be shown by a simple application of the wave equation that because of the cylindrical nature of the structure parallel to the x axis the free-space formulas for η may be used for the wave-guide delay structure, if λ is taken to be the guide wavelength. The index of refraction is then defined as the guide wavelength of the uniform wave guide divided by the guide wavelength of the strip-loaded wave guide.

Each of the three wave-guide delay structures was approximately one foot in length and was constructed in 1.372 by 0.622-inch i.d. rectangular wave guide. The guide wavelength along the delay structure was measured as follows. With a signal fed into one end of the line and with a short-circuiting plate at the other, the distance between successive nulls along the line

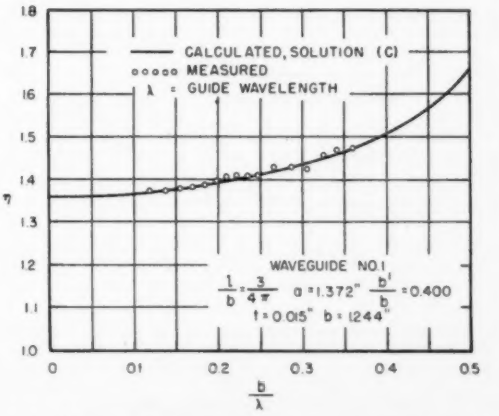

FIG. 3. Index of refraction of wave-guide test piece No. 1.

* This work was performed at the Sperry Gyroscope Company, Great Neck, New York with funds provided by the U. S. Army Signal Corps.

[1] W. E. Kock, Bell System Tech. J. **27**, 58 (1948).
[2] S. B. Cohn, J. Appl. Phys. **20**, 257–262 (1949).
[3] M. A. Brown, J. Inst. Elec. Engrs. (London) **97**, 45–47 (1950).
[4] S. B. Cohn, J. Appl. Phys. **20**, 1011 (1949).
[5] W. W. Sharpless, Proc. Inst. Radio Engrs. **39**, 1389–1393 (1951).

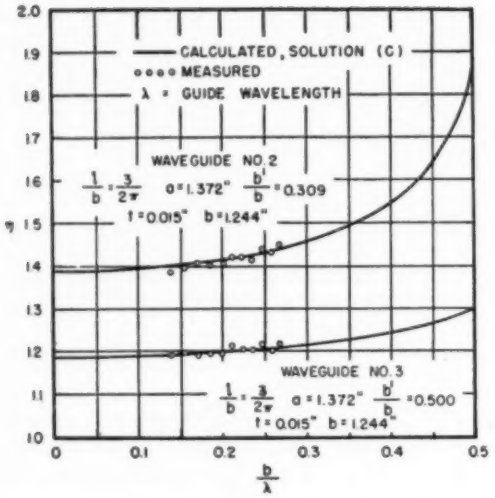

FIG. 4. Index of refraction of wave-guide test pieces No. 2 and No. 3.

was measured by means of a probe inserted through a narrow slot along the center of the broad wall opposite the strips. The guide wavelength of the unloaded line was computed from the frequency and the width of the guide. The positions of these nulls were affected somewhat by their locations relative to the nearby strips, and, therefore, the average spacing of the nulls along the entire line was used in order to improve the accuracy.

The measured points for the three wave-guide test pieces are plotted in Figs. 3 and 4. The theoretical curves were obtained from the third solution referred to above.[2,4] The parameters of the delay structure are listed in the figures. The agreement between theory and experiment is seen to be excellent in all cases. The maximum difference between the theoretical curve and the best-fitting curve through the measured points

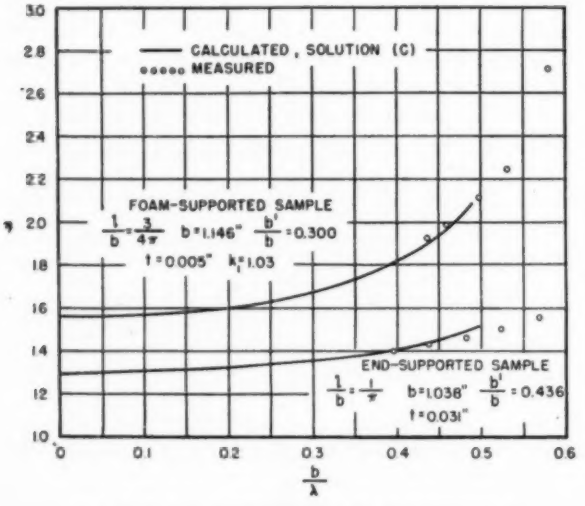

FIG. 5. Index of refraction of the Polyfoam and end-supported metal-strip arrays.

(not shown) is, respectively, 0.6, 0.7, and 0.3 percent for the three wave guides.

The free-space test pieces were approximately 12 inches square and four inches thick. They each contained about 150 strips. The index of refraction of these samples was measured by a free-space dielectrometer similar to a type described by Redheffer.[6] The particular apparatus used for the measurements and the precautions necessary to obtain accurate data have been previously discussed by the writer.[7] The first free-space test piece utilized a method of construction proposed by Kock[1] and consisted of a stack of individual slabs of Polyfoam containing brass strips 0.005 inch thick. The index of refraction of the array was affected somewhat by the dielectric constant of the Polyfoam, which was approximately 1.03. The formulas mentioned above apply to this case, however, if η is replaced by $\eta/(k_1)^{\frac{1}{2}}$ and λ by $\lambda/(k_1)^{\frac{1}{2}}$, where k_1 is the dielectric constant of the embedding medium. With these changes η remains the index of refraction relative to free space, and λ the free-space wavelength. These steps have been taken in computing values for comparison with the measured points. In the second free-space test piece,

TABLE I. Maximum differences of calculated and experimental values in percent.

Test Piece	Range of b/λ	Solutions (a)	(b)	(c)	(d)
Wave guide No. 1	0.120–0.361	8.5	13.5	0.6	3.3
Wave guide No. 2	0.139–0.268	4.2	3.0	0.7	2.4
Wave guide No. 3	0.139–0.268	0.7	1.9	0.3	0.4
Polyfoam Sample	0.436–0.493	0.4	6.1	1.8	4.5
End-Supported Sample	0.400–0.500	1.0	2.5	2.2	1.4
Maximum of all Cases		8.5	13.5	2.2	4.5

the strips were supported at their ends by a Lucite frame. Additional rigidity was provided by rods passing longitudinally through each horizontal group of strips.

The measured points for the two free-space test pieces and the theoretical curves obtained from the third solution are shown in Fig. 5. The parameters of the media are also listed there. The agreement again is very good, although not quite as close as with the wave-guide test pieces. The maximum discrepancy between the theoretical curve and the measured points was approximately two percent in each case. (Computed values for this solution are available only up to $b/\lambda = 0.5$.) Possible causes of these discrepancies are inaccuracy of measurement (which is believed to be greater in the free-space than in the wave-guide case), the presence of the rods and the relatively large thick-

[6] R. M. Redheffer, *Technique of Microwave Measurements* Radiation Laboratory Series (McGraw-Hill Book Company, Inc., New York, 1947), Vol. 11, Chap. 10, pp. 591–606.

[7] S. B. Cohn, "R-F measurements on metallic delay media," presented at the Institute of Radio Engineers National Convention, March, 1953. Accepted for publication in Proc. Inst. Radio Engrs.

ness of the strips in the edge-supported sample, and a possible slight inaccuracy of the solution for large values of b/λ.

III. COMPARISON OF THE FOUR SOLUTIONS WITH THE MEASURED DATA

Since the index-of-refraction graphs would be rendered illegible if all the computed curves were shown, Table I has been prepared listing the maximum deviation in percent between each theoretical and measured curve. Solutions (a), (b), (c), and (d) are, respectively, the four solutions mentioned in the Introduction. The range of b/λ considered is also given for each test piece. In the case of Kock's solution, his Eq. 26 was used as a high-frequency correction. A value of $\lambda_0=2w$ was selected for that formula, since it provides excellent agreement in the two cases of large b/λ. However, it will not necessarily give as good agreement in all cases of large b/λ. It is seen in Table I that solution (c) is the most reliable, the greatest discrepancy between theory and experiment being only 2.2 percent.

JOURNAL OF APPLIED PHYSICS VOLUME 24, NUMBER 7 JULY, 1953

The Equivalence of Optimum Transducers and Sufficient and Most Efficient Statistics

GLENN W. PRESTON
Research Division, Philco Corporation, Philadelphia, Pennsylvania
(Received January 23, 1953)

The problem of the design of transducers for the purpose of restoring the fidelity of a signal (which has been corrupted by noise), while preserving information in the sense of Shannon is shown to be a particular though unusual one of statistical inference and to be amendable to the methods of mathematical statistics.

Adopting the view that the inference of the approximate form of a function $s(t)$ (the signal) from the available mixture of the signal and the noise time series $n(t)$ is the natural limiting case of inference from discrete series of random variables, it is seen that the transducer under discussion is the physical analog of a "statistic"—in the sense of Fisher—and that the properties of the optimum transducer are equivalent to the statistical properties of sufficiency (preservation of information) and efficiency (maximization of fidelity).

The case of a Gaussian signal to which Gaussian noise has been added is considered in detail. Using the probability density functional of the Gaussian time series, the maximum likelihood estimate (which in this case is efficient, hence sufficient) of the signal is derived, and it's physical analog is identified as the smoothing filter of Wiener with infinite lag.

A PROBLEM of practical importance and theoretical interest in radio communications is that of deriving the characteristics of transducers which restore as far as possible the original form of signals which have been corrupted by noise during transmission.

Since communication systems are made for the purpose of conveying information (in the precise sense of Shannon and Wiener), an optimal property of all elements of a communication system, fidelity restoring transducers included, is the preserving of information.

Owing to the random nature of noise and most sources of radio interference, this problem is properly to be recognized as one of statistical inference; given the mixture of signal and noise, the fidelity restoring transducer infers the form of the original signal. Moreover, the dual optimal properties of maximization of fidelity and information preservation are entirely equivalent to the statistical attributes of "sufficiency" and "efficiency" (these terms are discussed below). This fact is of practical significance because the methods of mathematical statistics can (as demonstrated below by an example) be used to derive optimum "statistics"—in the sense of Fisher—and their physical analogs, which are the desired optimum transducers, may be identified.

In order to demonstrate by logical development the equivalence of the theory of optimum transducers and some aspects of statistical inference, we begin with the observation that a transducer is characterized by a mathematical transformation; for example, linear time invariant filters transform functions of time $f_i(t)$ into other functions of time $f_0(t)$ given by the relation

$$f_0(t)=\int_0^\infty d\tau w(\tau)f_i(t-\tau). \tag{1}$$

This linear transformation completely specifies the filter. Examples of nonlinear transformations which characterize transducers are

$$f_0(t)=f_i^v(t), \quad v=\text{constant},$$

and (2)

$$f_0(t)=\int_0^\infty d\tau_1\int_0^\infty d\tau_2 f_i(t-\tau_1)f_i(t-\tau_2)w(\tau_1,\tau_2).$$

The input to a transducer designed for fidelity improvement will be some mixture of an information bearing, hence random, time series $s(t)$ and the resultant noise and interference, also a random time series $n(t)$, while the output is intended to approximate $s(t)$. Except for the fact that we have random time series instead of random variates, and an entire function $s(t)$ is being

estimated from the observed (received) random time series instead of a single parameter, the transformation which characterizes the transducer is a statistic (particularly an estimate) in the precise sense of Fisher.[1] Ordinarily the term statistic describes a function of a finite number of observations of random variates, e.g., the arithmetic mean of the sampled values of a random variate is a statistic which is used to estimate the mean of the hypothetically infinite population of possible observations. In the present sense, the term statistic includes transformations of random functions $f(t)$, i.e., functionals: $f_0(t')$ as given by Eqs. (1) or (3) is a functional of $f_i(t)$.

Fisher[1] has also defined a sufficient statistic as an estimate of a statistical parameter which exhausts all of the information in the sample relevant to the parameter in question. Stated another way, given the estimate of the parameter computed from the sample by a sufficient statistic, then no better estimate of the parameter can be formed from a knowledge of the given sample, however detailed.

Recently Kulbach and Leibler have shown that information (in the sense of Shannon and Wiener) in a sample cannot be increased by any statistical operation, and no information is lost if, and only if, sufficient statistics are employed.[2]

In the light of the above discussion this basic result can be written; the information in a received signal, consisting of a mixture of the information bearing signal and noise; cannot be increased by any transducer and is not decreased if, and only if, the transducer is an analog of a sufficient statistic.

Now it is information which communication systems are designed to convey, and, although no transducer can increase information, some do improve "fidelity" (suitably defined), and the optimum transducer is that one which maximizes fidelity while preserving information.

Several examples of measures of fidelity are mentioned by Shannon,[3] including

$$v=\left\langle \frac{1}{T}\int_0^T dt\left[f_E(t)-f_T(t)\right]^2\right\rangle_{Av} \tag{3}$$

and

$$v=\left\langle \frac{1}{T}\int_0^T dt\left|f_E(t)-f_T(t)\right|\right\rangle_{Av}, \tag{4}$$

in which $f_E(t)$ is the estimated message signal, the transducer output, corresponding to the true message signal $f_T(t)$. The quantity v, Shannon's "evaluation function," is smaller the better the fidelity; in fact, a serviceable definition of fidelity is simply the reciprocal of v.

Fisher[1] introduced the term efficiency to measure the quantity equivalent to fidelity of statistical estimates. Fisher obtained an important result to the effect that the variance of the estimate of a statistical parameter can be no less than a quantity which depends on the underlying p.d.f. and the number of sample elements, whatever statistic is employed. He then defined the efficiency of a statistical estimate as the ratio of this lower bound to the actual variance of the estimate in question. A statistic with efficiency of unity is said to be *efficient*. We are indebted to a referee for pointing out that efficient estimates are, *a fortiori*, sufficient.[4] However, only for special cases do efficient statistics exist, although in most cases of interest a most efficient (minimum variance) estimate does exist.

It seems appropriate in connection with communication theory to widen the term most efficient to include estimates, hence transducers, which are best with respect to any given measure of fidelity, in which event the optimum transducer is, succinctly, a physical analog of a sufficient and most efficient statistic.*

When the probability density function of the random variable is known (or can be assumed) except for the statistical parameters which appear, the method of maximum likelihood can be used to produce estimates of the parameters which are efficient, when an efficient estimate exists, and sufficient. The maximum likelihood estimate of a parameter is that value which maximizes the probability density with the observed values of the random variables inserted.

For example, suppose n statistically independent measurements $X_1, X_2, \cdots, X_n$ have been made of a random variate x, whose probability density function $p(x)$ is assumed to be normal

$$p(x)=\frac{1}{(2\pi\sigma^2)^{\frac{1}{2}}}\exp\left\{-\frac{(x-\mu)^2}{2\sigma^2}\right\}, \tag{5}$$

but the mean μ and variance σ^2 are unknown and, in fact, are to be inferred from the measurements $X_1, X_2, \cdots, X_n$. The maximum likelihood estimates of μ and σ^2 are those which maximize the "likelihood"

$$\frac{1}{(2\pi\sigma^2)^{n/2}}\exp-\frac{\sum_{i=1}^{n}(X_i-\mu)^2}{2\sigma^2} \tag{6}$$

of the observed measurement. These values are found

[1] R. A. Fisher, Phil. Trans. Roy. Soc. **A222**, 309 (1921); Proc. Cambridge Phil. Soc. **22**, 700 (1925).

[2] S. Kulback and R. A. Leibler, Ann. Math. Stat. **22**, 79–87 (1951).

[3] C. E. Shannon, *The Mathematical Theory of Communication* (The University of Illinois Press, Urbana, 1944).

[4] Harold Cramer, *Mathematical Methods of Statistics* (Princeton University Press, Princeton, 1946), p. 482.

* We are reminded by a referee that Shannon[3] has shown that information is not decreased by a nonsingular transducer, all nonsingular transducers being sufficient: of course, not all sufficient transducers are nonsingular, in fact, most efficient transducers are generally singular.

to be

$$\mu=\frac{1}{n}\sum X_i$$

and

$$\sigma^2=\frac{1}{n}\sum(X_i-\mu)^2. \tag{7}$$

Thus, in this case, the maximum likelihood estimates of the mean and variance are just the sample mean and variance.

When dealing with a random time series $y(t)$, it is common practice to consider the values of the series at a set of discrete instants of time $y(t_1)$, $y(t_2)$, $y(t_3)$, etc., separated by the Nyquist interval $\tau=1/(2W)$, where W is the band width of the process.

By a Gaussian source is meant one which generates time series whose values at various discrete instants of time have the Gaussian probability density function, regardless of how closely the sampling instants are spaced. In dealing with Gaussian sources, the sampling intervals can, in fact, conveniently be reduced to zero, giving the probability density of a segment of a continuous function, i.e., *a probability density functional* (used here apparently for the first time).

The probability density functional of a segment of a Gaussian random time series $y(t)$, extending from time t_0 to t_0+T, the ensemble autocorrelation function of the process being $\psi(\tau)$, is proportional to

$$\exp\left\{-\tfrac{1}{2}\int_{t_0}^{t_0+T}dt_1y(t_1)\int_{t_0}^{t_0+T}dt_2y(t_2)l(t_1,t_2)\right\}, \tag{8}$$

in which the function $l(t_1, t_2)$ is defined by the equation

$$\int_{t_0}^{t_0+T}dt\psi(t_1-t)l(t,t_2)=\delta(t_1-t_2),\quad 0<t_2-t_0<T. \tag{9}$$

The development of this expression is relegated to the Appendix.

Under the assumption that the signal is generated by a Gaussian process with autocorrelation function $\psi_S(\tau)$, and the noise by a statistically independent Gaussian process with autocorrelation function $\psi_N(\tau)$, and that the received signal $y(t)=n(t)+s(t)$, the joint probability density functional of a segment of the transmitted signal $s(t)$ and of the received signal $y(t)$, is proportional to

$$\exp\left\{-\tfrac{1}{2}\int_{t_0}^{t_0+T}dt_1[y(t_1)-s(t_1)]\times\int_{t_0}^{t_0+T}dt_2[y(t_2)-s(t_2)]l_N(t_1,t_2)-\tfrac{1}{2}\int_{t_0}^{t_0+T}dt_1s(t_1)\int_{t_0}^{t_0+T}dt_2s(t_2)l_S(t_1,t_2)\right\}. \tag{10}$$

Maximizing this with respect to $s(t)$ in the usual way leads to the following equation for the maximum likelihood estimate $S_{ML}(t)$,

$$\int_{t_0}^{t_0+T}dt_1y(t_1)l_N(t_2,t_1)=\int_{t_0}^{t_0+T}dt_1S_{ML}(t_1)\times[l_S(t_2,t_1)+l_N(t_2,t_1)], \tag{11}$$

where use has been made of the symmetry of l_S and l_N in their arguments.

Multiplying both sides by $\psi_S(t-t_2)$ and integrating with respect to t_2 gives

$$S_{ML}(t)=-\int_{t_0}^{t_0+T}dt_1y(t_1)K(t,t_1)+\int_{t_0}^{t_0+T}dt_1S_{ML}(t_1)K(t,t_1), \tag{12}$$

in which

$$K(t,t_1)=-\int_{t_0}^{t_0+T}dt_2\psi_S(t-t_2)l_N(t_2,t_1). \tag{13}$$

Equation (12) for $S_{ML}(t)$ can be solved in terms of the reciprocal function to K, which is designated by k and is given by the integral equation

$$\psi_S(t-t_1)=\int_{t_0}^{t_0+T}dt_2k(t_1,t_2)\times[\psi_S(t-t_2)+\psi_N(t-t_2)]. \tag{14}$$

This is a particular form of the Wiener-Hopf integral equation, which can be solved for $k(t_1, t_2)$, using the methods of reference 7.

Multiplying by $l_N(t, t_3)$ and integrating with respect to t gives

$$-K(t_1,t_3)=-\int_{t_0}^{t_0+T}dt_2k(t_1,t_2)K(t_2,t_3)+k(t_1,t_3), \tag{15}$$

which shows that k and K are, in fact, reciprocal functions.[5]

Multiplying Eq. (12) by $k(t_1, t)$ and integrating out t, and using Eq. (12) again to clear terms leaves

$$S_{ML}(t)=\int_{t_0}^{t_0+T}dt_1y(t_1)k(t,t_1), \tag{16}$$

which is the desired result.

The value of $S_{ML}(t=t')$ is a weighted average of $y(t)$ over the entire segment to $\leqslant t\leqslant t_0+T$ considered in the analysis, whereas a realizable filter performs a weighted integration over the past of the input time series. When Eqs. (14) and (16) are rewritten with the memory function of a realizable filter appearing in the place of

[5] W. V. Lovitt, *Linear Integral Equations* (McGraw-Hill Book Company, Inc., New York, 1924), p. 17.

the function k, they are seen to be identical with the result of Wiener[6] (as extended by Zadeh and Ragazzini[7]) for the optimum filter with lag $\sigma=t_0+T-t$. The transformation of the input $y(t)$ is thus a function of the argument of S_{ML} and is, therefore, not time invariant. This was brought about by the fact that a finite segment of the input $y(t)$ was treated.

In practice, input time series are usually very long and the maximum likelihood filter will, in principle, incorporate indefinitely long lag. This is due to the fact that the values of the received signal over some interval preceding and following any instant t_0 contain information relevant to the original signal at time t_0. In order to obtain absolutely optimum performance, it is only necessary that the lag be as great as the future part of the interval of relevance.

Since the maximum likelihood estimate in the above case is both sufficient and efficient, the filter of Wiener with infinite lag not only gives maximum fidelity (in the sense of minimum rms error), but it preserves all relevant information.

Although it is likely that only in the case of Gaussian processes considered here can exact explicit results be obtained, it should be possible to develop approximately optimum transformations for contaminated signals in the video (say), where the time series are no longer Gaussian.

The writer wishes to acknowledge the many helpful suggestions of Dr. Samuel G. Kneale and, in particular, his assistance in the development of the continuous "quadratic form" (Eq. A.13).

APPENDIX

Derivation of the Gaussian Probability Density Functional

The N-dimensional Gaussian probability density function is

$$\frac{|M|^{\frac{1}{2}}}{(2\pi)^{N/2}}\exp-\tfrac{1}{2}x^tMx, \tag{A.1}$$

where, in the present case, x is the column vector of the discrete random variates $y(T/jN+t_0)$, $j=1, 2, \cdots, N$, x^t its transpose, and M the inverse of the correlation matrix $\overline{\Phi}$.

The elements of $\overline{\Phi}$,

$$\phi_{ij}=\left\langle y\left(i\frac{T}{N}+t_0\right)y\left(j\frac{T}{N}+t_0\right)\right\rangle_{Av}$$

$$=\psi\left(i\frac{T}{N}-j\frac{T}{N}\right), \tag{A.2}$$

assuming stationarity.

Designating the elements of M by m_{ij}, the identity

$$\sum_k \phi_{ik}m_{kj}=\delta_{ij} \tag{A.3}$$

is satisfied.

Making the substitutions

$$l_{(j,k)}\left(\frac{T}{N}\right)^2=m_{j,k} \tag{A.4}$$

and using

$$\delta_{ij}=\frac{1}{T}\int_{-T/2}^{T/2}d\tau\exp\left[2\pi(-1)^{\frac{1}{2}}\frac{\dot{\tau}}{T}(i-j)\right]$$

$$=\lim_{L\to\infty}\frac{1}{T}\sum_{n=-L}^{n=L}\left(\frac{T}{2L}\right)\exp\left[2\pi(-1)^{\frac{1}{2}}\frac{n}{2L}(i-j)\right], \tag{A.5}$$

we get

$$\sum_{k=1}^{N}\phi_{ik}m_{kj}\left(\frac{N}{T}\right)=\sum_{k=1}^{N}\phi_{ik}l_{kj}\left(\frac{T}{N}\right) \tag{A.6}$$

$$=\lim_{L\to\infty}\frac{N}{T}\frac{1}{T}\sum_{n=-L}^{L}\left(\frac{T}{2L}\right)$$

$$\times\exp[2\pi(-1)^{\frac{1}{2}}]\frac{n}{T}\left(i\frac{T}{2L}-j\frac{T}{2L}\right). \tag{A.7}$$

Let $L=N$, then the right-hand side becomes

$$\int_0^T dt_2\psi(t_1-t_2)l(t_2, t_3), \tag{A.8}$$

while the left-hand side becomes

$$\lim_{L\to\infty}\frac{1}{2T}\sum_{n=-L}^{L}\exp[2\pi(-1)^{\frac{1}{2}}]\frac{n}{T}(t_1-t_3) \tag{A.9}$$

$$=\lim_{\beta\to\infty}\left\{\beta\frac{1}{2T}\int_{-T/2}^{T/2}dt\exp\left[2\pi(-1)^{\frac{1}{2}}\beta t\left(\frac{t_1-t_3}{T}\right)\right]\right\} \tag{A.10}$$

$$=\delta(t_1-t_3). \tag{A.11}$$

Writing the exponent of Eq. (A.1) as a double summation and using Eq. (A.4), one gets

$$-\tfrac{1}{2}\sum_i^n\sum_j^n x_ix_jl_{(i,j)}\left(\frac{T}{N}\right)^2, \tag{A.12}$$

which becomes in the limit

$$-\tfrac{1}{2}\int^T dt_1\int^T dt_2y(t_1)y(t_2)l(t_1, t_2). \tag{A.13}$$

[6] N. Wiener, *Extrapolation, Interpolation and Smoothing of Station-Time Series* (John Wiley and Sons, Inc., New York, 1949).

[7] Lofti A. Zadeh and John R. Ragazzini, J. Appl. Phys. **21**, 645 (1950).

JOURNAL OF APPLIED PHYSICS VOLUME 24, NUMBER 7 JULY, 1953

Transmission of Electromagnetic Waves through Pairs of Parallel Wire Grids*

WILLICE E. GROVES
University of California, Berkeley, California
(Received November 21, 1952)

The control and direction of electromagnetic waves is accomplished, in general, by the use of boundary materials and structures which produce desired effects on such waves when irradiated by them. An important class of boundary structure for this purpose is a surface having alternate areas of conducting and nonconducting material. Grids formed of a large number of parallel cylindrical conductors of circular cross section, uniformly spaced and lying in a common surface, are among the most generally useful of this class of boundary structure. Single layer parallel wire grids have received considerable study in the past. However, little information is available concerning the characteristics of multiple layers of such grids

An analytical solution is obtained for the power transmission coefficient of a double grid system. Power transmission coefficients for various combinations of system parameters are computed from the analytical solution and tested experimentally. The solution is found to yield excellent correlation with experiment until the interwire spacing approaches the wavelength.

I. NATURE OF THE PROBLEM

THE behavior of electromagnetic waves in free space and within physical matter is governed by natural laws and hence is beyond the control of man. Fortunately, however, this behavior varies with the kind of matter in which the waves are propagating. By making judicious use of these natural variations in behavior, one is able to exercise some measure of control and direction over electromagnetic waves. This is accomplished by the use of various materials and structures to form boundaries between various regions of space in a manner to produce desired effects upon the waves.

On some boundaries it may be desired to prevent the passage of all electromagnetic waves in order to keep them either within or without certain regions of space. On others it may be desired to permit the passage of waves in a given frequency band, or having a certain polarization, but to prevent all others from passing. Then again, it may be desired to prevent the passage of electromagnetic waves while simultaneously permitting the free passage of physical particles such as electrons or air molecules.

These and many other problems related to the control and direction of electromagnetic waves require the use of all sorts of boundary materials and structures. Consequently, the characteristics with respect to electromagnetic waves of every conceivable type of boundary material and structure have been receiving continuous and detailed research effort ever since the discovery of electromagnetic waves in 1887. Each investigation in this area adds to the general storehouse of knowledge which enables the marvelous capabilities of these waves to be controlled to better advantage.

An important class of boundary structure, which finds frequent use in high frequency electronic equipment, is a surface having alternate areas of conducting and nonconducting material forming a grating or grid. These are used in electron tubes to form boundaries having fixed or variable potentials through which electrons are caused to pass in controlled numbers or velocities. They are used to shield regions from spurious external electromagnetic waves or to prevent waves generated within the region from interfering with outside equipment. They are used as reflectors in antenna systems, effectively shaping beams of electromagnetic waves without causing excessive mechanical loading from weight or wind. Countless other ways have been and will be found for using this versatile class of boundary structure.

Grids formed of a large number of parallel cylindrical conductors of circular cross section, uniformly spaced and lying in a common plane or curved surface, are among the most generally useful of this class of boundary structure. Single grid boundary structures of this type have been quite thoroughly studied in past years. However, there appears to be a negligible amount of information available concerning the characteristics of two or more such grids used in combination with various spacings and relative orientation angles of their wires. Such combinations may possess some very interesting and useful characteristics.

The characteristics of a combination of grids of the type just described when used as a boundary structure affecting the transmission of electromagnetic waves will be discussed. At present, only combinations of two such parallel wire grids lying in adjacent parallel planes are considered. The spacing between the wires of the two grids will be arbitrary, except that it will be less than one wavelength of the incident radiation. The spacing between the planes of the two grids and the angle formed by the wires of the two grids will be considered arbitrary. The incident radiation will be considered to be uniform plane waves, incident normally to the planes of the grids. The additional detailed assumptions and the theoretical and experimental approximations used will be explained in subsequent sections. The relative

* This work was done at the University of California Antenna Laboratory and was supported in part by the U. S. Office of Naval Research under contract N7onr-29529.

transmission through the grids of the incident radiation will be examined both theoretically and experimentally with a view toward obtaining a mathematical formulation capable of predicting the characteristics of such a combination of grids.

II. THEORETICAL ANALYSIS

A uniform, linearly polarized plane wave is propagating in the positive z direction of a right-handed rectangular coordinate system. The electric vector E of this wave is directed parallel to the positive x axis. The corresponding H vector is in the direction of the positive y axis. Covering the entire xy plane which intersects the z axis at $z=0$ is a parallel wire grid formed of conductors having a circular cylindrical cross section of radius b. The wires of the grid are uniformly spaced with a center-to-center distance equal to d, and they form an angle ϕ_1 with the positive x axis.

A second grid of similar construction lies in the xy plane that intersects the z axis at $z=l$. The wires of this grid form an angle ϕ_2 with the positive x axis and an angle $\phi_2-\phi_1$ with the wires of the first grid.

A portion of the energy of the incident wave is reflected in the negative z direction, and a portion is transmitted through the grid system in the positive z direction. Considering the x and y components of the transmitted waves separately, the relative power transmitted through the grids may be written as the ratio of the time average square of the transmitted electric field to the time average square of the incident electric field, or

$$T_x=\langle E_{tx}^2\rangle_{Av}/\langle E_{inc}^2\rangle_{Av},$$
$$T_y=\langle E_{ty}^2\rangle_{Av}/\langle E_{inc}^2\rangle_{Av},$$

where E_{tx}, E_{ty}, and E_{inc} represent the complex electric vectors of the x and y components of the transmitted and incident waves. These ratios are the power transmission coefficients of the grid system.

The problem to be considered is the determination of the power transmission coefficients as a function of a, b, ϕ_1, ϕ_2, and l for double grid systems in which $d<\lambda$.

Let $\bar{E}_i$ be the incident electric field, $\bar{E}_r$ the reflected electric field, and $\bar{e}$ a unit vector in the direction of the grid wires.

For perfectly conducting grid wires,

$$\bar{E}_r=-\bar{e}(\bar{e}\cdot\bar{E}_i), \tag{1}$$

the minus sign accounting for the usual 180° phase reversal on reflection. For wires of finite conductivity, however, $\bar{E}_r$ will differ from this in both magnitude and phase. This may be indicated by writing

$$\bar{E}_r=-\bar{e}\kappa(\bar{e}\cdot\bar{E}_i), \tag{2}$$

where κ is a complex proportionality factor. Let

$$\kappa=\rho e^{i\delta}. \tag{3}$$

The transmitted electric vector, $\bar{E}_t$, must be so written that the parallel component of the *total* electric field at the plane of the grid will vanish in the limit of perfect reflection ($\kappa=1$). If $\bar{E}_t$ is written

$$\bar{E}_t=\bar{E}_i-\bar{e}\kappa(\bar{e}\cdot\bar{E}_i), \tag{4}$$

then the parallel component of the total electric field in the plane of the grid is

$$\bar{e}\cdot(\bar{E}_i+\bar{E}_r+\bar{E}_t)$$
$$=\bar{e}\cdot(\bar{E}_i-\bar{e}\kappa(\bar{e}\cdot\bar{E}_i)+\bar{E}_i-\bar{e}\kappa(\bar{e}\cdot\bar{E}_i)). \tag{5}$$

This evidently vanishes when $\kappa=1$. Thus, the transmitted wave may be considered to be a superposition of the original incident wave plus a scattered wave equal in magnitude and phase to the reflected wave. This would follow from the fact that the induced currents which produce the reflected wave in the $-z$ direction also produce a wave in the $+z$ direction of the same magnitude and phase, because of the symmetry about the $z=0$ plane. Consequently, at each incidence of a wave on a grid, the following will apply:

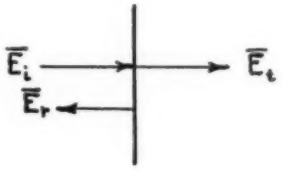

where

$$\bar{E}_r=-\bar{e}\kappa(\bar{e}\cdot\bar{E}_i), \tag{6}$$

$$\bar{E}_t=\bar{E}_i-\bar{e}\kappa(\bar{e}\cdot\bar{E}_i), \tag{7}$$

and $\bar{e}$ is either $\bar{a}$, a unit vector in the direction of the wires of grid a, or $\bar{b}$, a similar unit vector for grid b.

In the following, let

$\beta=e^{-jkl}$,
$\kappa=\rho e^{j\delta}$,
$\bar{a}$ = the unit vector in the direction of the wires of grid a,
$\bar{b}$ = the unit vector in the direction of the wires of grid b,
φ_1 = the acute angle formed by the wires of grid a and the positive x axis,
φ_2 = the acute angle formed by the wires of grid b and the positive x axis,
$h=\cos\varphi_1=\bar{a}\cdot\bar{a}_x$,
$m=\sin\varphi_1=\bar{a}\cdot\bar{a}_y$,
$n=\cos\varphi_2=\bar{b}\cdot\bar{a}_x$,
$p=\sin\varphi_2=\bar{b}\cdot\bar{a}_y$,
$r=\cos(\varphi_2-\varphi_1)=\bar{a}\cdot\bar{b}$.
$\bar{a}_x$ and $\bar{a}_y$ are unit vectors in the x and y directions.

In the case of a double grid system, the various multiple reflections and transmissions which occur after

the arrival of the initial wave at grid a may be scheduled as follows:

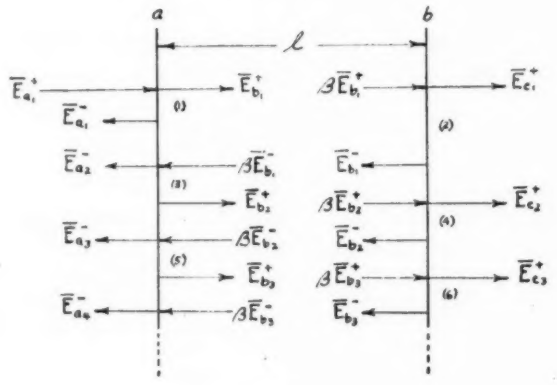

Using Eqs. (6) and (7) at each contact of waves and grids, and adding the transmitted components,

$$\bar{E}_t=\bar{E}_{c_1}{}^+ + \bar{E}_{c_2}{}^+ + \bar{E}_{c_3}{}^+ + \cdots \tag{8}$$

$$\begin{aligned}&=\bar{a}_x\beta-\bar{a}\kappa h\beta-\bar{b}\kappa\beta A+\bar{a}\kappa^2\beta^3 rA-\bar{b}\kappa^3\beta^3 r^2A\\&\quad+\bar{a}\kappa^4\beta^5 r^3A-\bar{b}\kappa^5\beta^5 r^4A+\bar{a}\kappa^6\beta^7 r^5A-\bar{b}\kappa^7\beta^7 r^6A \qquad (9)\\&\quad+\cdots\end{aligned}$$

where $A=n-r\kappa h$ or

$$\bar{E}_t=\bar{a}_x\beta-\bar{a}\Big[\kappa h\beta-\sum_{q=1}^{\infty}\kappa^{2q}\beta^{2q-1}r^{2q-1}A\Big]$$

$$-\bar{b}\sum_{q=1}^{\infty}\kappa^{2q-1}\beta^{2q-1}r^{2q-2}A. \tag{10}$$

This may be resolved into x and y components by taking the dot products $a_x\cdot E_t$ and $a_y\cdot E_t$:

$$\bar{E}_{tx}=\beta-\kappa h^2\beta+A\,(h\kappa^2\beta^2 r-n)\sum_{q=1}^{\infty}\kappa^{2q-1}\beta^{2q-1}r^{2q-2}, \tag{11}$$

$$\bar{E}_{ty}=-\kappa\beta hm+A\,(m\kappa\beta^2 r-p)\sum_{q=1}^{\infty}\kappa^{2q-1}\beta^{2q-1}r^{2q-2}. \tag{12}$$

Summing the geometric series by the usual method and restoring the time-dependent factor $\exp(j\omega t)$,

$$\bar{E}_{tx}=\beta\frac{(1-\kappa h^2)(1-\kappa^2\beta^2r^2)+\kappa(n-r\kappa h)(h\kappa\beta^2r-n)}{1-\kappa^2\beta^2r^2}e^{j\omega t}, \tag{13}$$

$$\bar{E}_{ty}=\beta\frac{-\kappa hm(1-\kappa^2\beta^2r^2)+\kappa(n-r\kappa h)(m\kappa\beta^2r-p)}{1-\kappa^2\beta^2r^2}e^{j\omega t}. \tag{14}$$

Taking $\frac{1}{2}ReEE^*$ yields the time average square of these field components, and dividing each by the time average square of the incident electric fields gives the desired power transmission coefficients, T_x and T_y. This is a lengthy but straightforward process, eventually leading to

$$T_x=\frac{\langle E_{tx}{}^2\rangle_{Av}}{\langle E_{inc}{}^2\rangle_{Av}}=\frac{A\cos 2kl+B\cos(2kl-\delta)+C\cos(2kl-2\delta)+D\cos(2kl-3\delta)+E}{1+\rho^4r^4-2\rho^2r^2\cos(2kl-2\delta)}, \tag{15}$$

$$T_y=\frac{\langle E_{ty}{}^2\rangle_{Av}}{\langle E_{inc}{}^2\rangle_{Av}}=\frac{G\cos(2kl-\delta)+H\cos(2kl-2\delta)+K}{1+\rho^4r^4-2\rho^2r^2\cos(2kl-2\delta)}, \tag{16}$$

where

$$A=-2nh\rho^4r^3,$$

$$B=2\rho^3rn(rn-h^3+h^3\rho^2r^2)$$
$$-2nh\rho^3r(n^2+h^2\rho^2r^2-2nh\rho r\cos\delta),$$

$$C=-2\rho^2r^2(1+h^4\rho^2-2h^2\rho\cos\delta)$$
$$+2\rho^2rl(n+h^3\rho^2r-hn^2\rho^2r),$$

$$D=-2\rho^3r^2h^2,$$

$$E=(1+\rho^4r^4)(1+h^4\rho^2-2h^2\rho\cos\delta)+2nh\rho^2r\cos2\delta$$
$$+2\rho\cos\delta(h^2\rho^4r^4-nh^3\rho^2r+nh^3\rho^4r^3-n^2)$$
$$+2\rho^2h(hn^2-n\rho^2r^3-h^3\rho^4r^4)$$
$$+\rho^2(n^2+h^2\rho^2r^2)(n^2+h^2\rho^2r^2-2nh\rho r\cos\delta),$$

$$G=-2pm\rho r(n^2+\rho^2r^2h^2-2nh\rho\cos\delta)$$
$$-2hm\rho r(mn-ph\rho^2r^2),$$

$$H=-2h^2m^2\rho^2r^2-2hm\rho^2r^2(pn-mh),$$

$$K=h^2m^2(1+\rho^4r^4)+(p^2+m^2\rho^2r^2)(n^2+\rho^2r^2h^2-2nh\rho r\cos\delta)$$
$$-2hm\rho^2(ph-mn\rho r^3)\cos\delta-2hm(mh\rho^4r^4-np).$$

The constants h, m, n, p, and r involved in the above equations are immediately determinable from tables as soon as the angles φ_1 and φ_2 are selected. The constants ρ and δ, however, must be computed or determined experimentally for each combination of wire radius and spacing. A method similar to that of Wessel[1] may be used for this purpose.

Referring to Fig. 1, when a uniform linearly polarized plane wave traveling in the positive z direction is incident normally on an infinite parallel wire grid, the component of the electric vector parallel to the wire induces currents in the wires of the grid. These, in turn, are the sources of scattered waves producing fields in the adjacent space. The vector potential produced at a point

[1] W. Wessel, Hochfrequenztech. u Elektroakust. **54**, 62–69 (1939).

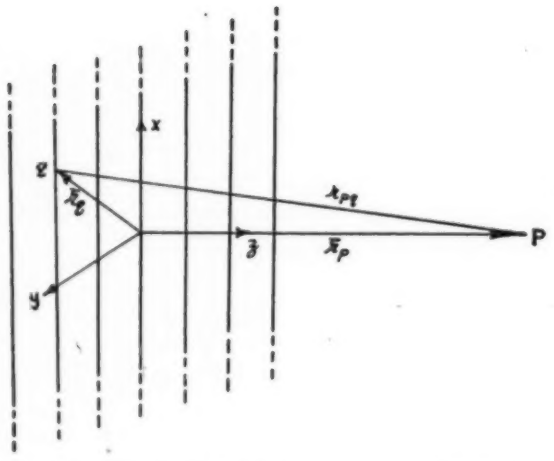

FIG. 1. Vector relationship between source and field points.

p resulting from these currents is

$$A_p=\frac{\mu_0}{4\pi}\int_v \bar{\imath}_q\frac{e^{-jkr_{pq}}}{r_{pq}}dv_q, \tag{17}$$

where $\bar{r}_q$ is the polar vector to the source point, and $\bar{r}_p$ is the polar vector to the field point,

$$r_{pq}=|\bar{r}_p-\bar{r}_q|.$$

Assuming the grid to be in the xy plane, with its wires parallel to the x axis, and that the field point is on the z axis,

$$\bar{r}_p=\bar{a}_z z, \quad r_q=\bar{a}_x x+\bar{a}_y y, \quad \bar{a}=\text{unit vector}.$$

If d is the spacing between the wires and there is a wire on the x axis,

$$y=nd, \quad (n=1, 2, 3\cdots)$$

Then $r_p=z$, and

$$r_q=(x^2+n^2d^2)^{\frac{1}{2}},$$
$$r_{pq}=(x^2+n^2d^2+z^2)^{\frac{1}{2}}.$$

So

$$A_{p_x}=\frac{\mu_0}{4\pi}\int \bar{\imath}_q\frac{\exp[-jk(x^2+n^2d^2+z^2)^{\frac{1}{2}}]}{(x^2+n^2d^2+z^2)^{\frac{1}{2}}}dv_q. \tag{18}$$

If the field point is assumed to be sufficiently far from the source point, the currents may be considered to be filamentary, and

$$\bar{\imath}_q dv_q=J_{q_x}dx_q \quad (J_q=\text{current density})$$

$$A_{p_x}=\frac{\mu_0}{4\pi}J_{q_x}\int\frac{\exp[-jk(x^2+n^2d^2+z^2)^{\frac{1}{2}}]}{(x^2+n^2d^2+z^2)^{\frac{1}{2}}}dx_q. \tag{19}$$

Summing the contributions of all grid wires, limited in number at first to $2N$,

$$A_{p_x}=\frac{\mu_0}{4\pi}J_{q_x}\sum_{-N}^{N}{}_n\int_{-\infty}^{\infty}\frac{\exp[-jk(x^2+n^2d^2+z^2)^{\frac{1}{2}}]}{(x^2+n^2d^2+z^2)^{\frac{1}{2}}}dx_q, \tag{20}$$

but

$$\int_{-\infty}^{\infty}=\frac{\pi}{j}H_0^{(2)}[k(z^2+n^2d^2)^{\frac{1}{2}}], \tag{21}$$

where $H_0^{(2)}$ represents the Hankel function of the second kind. Then

$$A_{p_x}=\frac{\mu_0}{4\pi}J_{q_x}\sum_{-N}^{N}{}_n\frac{\pi}{j}H_0^{(2)}[k(z^2+n^2d^2)^{\frac{1}{2}}]. \tag{22}$$

As $N\to\infty$, and for sufficiently large z, the summation of Hankel functions is given approximately by[2]

$$\sum_{-N}^{N}H_0^{(2)}[k(z^2+n^2d^2)]=\frac{2}{kd}e^{-jkz}. \tag{23}$$

Using this, Eq. (22) becomes

$$A_{p_x}=-j\frac{\mu_0}{4\pi}\frac{\lambda}{d}J_x e^{-jkz}. \tag{24}$$

Since

$$\bar{E}=\frac{1}{j\omega\mu_0\epsilon_0}\nabla(\nabla\cdot\bar{A})-j\omega\bar{A}, \tag{25}$$

and

$$\nabla\cdot\bar{A}=\frac{\partial}{\partial x}A_{p_x}=0, \tag{26}$$

the scattered electric field becomes

$$E_{p_x}=-j\omega A_{p_x}=-\frac{\omega\mu_0\lambda}{4\pi d}J_x e^{-jkz}. \tag{27}$$

However, the grid current, and hence the scattered field, is proportional to the incident field. Assuming the incident field to be

$$\bar{E}_{\text{inc}}=e^{-jkz}\bar{a}_x, \tag{28}$$

the scattered field in the direction of the z axis is

$$E_{p_x}=-\kappa E_{x_{\text{inc}}}=-\kappa e^{-jkz}. \tag{29}$$

Then

$$-\kappa e^{-jkz}=-\zeta\frac{J_x}{2d}e^{-jkz}, \quad \left[\zeta=\left(\frac{\mu_0}{\epsilon_0}\right)^{\frac{1}{2}}\right], \tag{30}$$

or

$$\kappa=\rho e^{j\delta}=\zeta\frac{J_x}{2d}. \tag{31}$$

This provides an expression for ρ and δ in terms of the grid current. To compute the current, $E=-j\omega\bar{A}$ is applied to the field and source points within the wires:

$$E_{p_x}=\frac{-j\omega\mu_0}{4\pi}\int_{v_q} i_{q_x}\frac{e^{-jkr_{pq}}}{r_{pq}}dv_q. \tag{32}$$

[2] R. Weyrich, *Die Zylinderfunctionen und ihre Anwendung* (Leipzig, 1937).

Let the field point be in the center wire, on the x axis. Then

$$E_{px}=\frac{-j\omega\mu_0}{2\pi}\sum_1^\infty{}_n\int_{vq} i_{qx}\frac{e^{-jkr_{pq}}}{r_{pq}}dv_q - \left[\frac{j\omega\mu_0}{4\pi}\int_v i_{qx}\frac{e^{-jkr_{pq}}}{r_{pq}}dv_q\right], \quad (33)$$

where the summation includes the contributions to the electric field in the center wire from all other wires, and the last term is the contribution from source points within the center wire.

Multiplying by i_{pq}^* and integrating over the center wire from $x=0$ to $x=l$,

$$\int_0^l E_{px}i_{pq}^*dx_p=\frac{-j\omega\mu_0}{2\pi}\sum_1^\infty{}_n\int_0^l\int_{vq} i_qi_p^*\frac{e^{-jkr_{pq}}}{r_{pq}}dv_q - \left[\frac{j\omega\mu_0}{4\pi}\int_{vp}\int_{vq} i_qi_p^*\frac{e^{-jkr_{pq}}}{r_{pq}}dv_q\right]_{n=0}. \quad (34)$$

In the summation, the sources all lie in the other wires. Hence, when $a\gg b$, the wires may be considered to be line sources. Then in the summation,

$$i_qi_p^*dv_qdv_p\rightarrow J_qJ_p^*dx_qdx_p, \quad (35)$$

$$\int_0^l E_{px}i_p^*dx_p =\frac{-j\omega\mu_0}{2\pi}\sum_1^\infty{}_n\int_0^l\int_{-\infty}^\infty J_p^*J_q\frac{e^{-jkr_{pq}}}{r_{pq}}dx_pdx_q - \left[\ \right]_{n=0}. \quad (36)$$

Also, in the summation,

$$r_{pq}=[(x_q-x_p)^2+n^2d^2]^{\frac{1}{2}}. \quad (37)$$

Let $\xi=x_q-x_p$, $dx_q=d\xi$, and carry out the x_p integration.

$$\int_0^l E_{px}i_p^*dx_p =\frac{-j\omega\mu_0}{2\pi}\sum_1^\infty{}_n J_p^*J_{ql}\int_{-\infty}^\infty\frac{\exp-j[k(\xi^2+n^2d^2)^{\frac{1}{2}}]}{(\xi^2+n^2d^2)}d\xi - \left[\ \right]_{n=0}, \quad (38)$$

which becomes

$$\int_0^l E_{px}i_p^*dx =\frac{-j\omega\mu_0}{2\pi}\sum_1^\infty{}_n J_p^*J_ql\frac{\pi}{j}H_0^{(2)}(knd)-\left[\ \right]_{n=0}. \quad (39)$$

Considering the last term,

$$\left[\ \right]_{n=0}=\frac{j\omega\mu_0}{4\pi}\int_{vp}\int_{vq} i_p^*i_q\frac{e^{-jkr_{pq}}}{r_{pq}}dv_pdv_q. \quad (40)$$

The current flows in a very thin surface layer on the perfectly conducting wires, and for $a\gg b$, is uniformly distributed on the circumference of the wires. Then

$$i_p^*i_qdv_pdv_q\rightarrow J_p^*J_q\frac{d\varphi_p}{2\pi}dx_p\frac{d\varphi_q}{2\pi}dx_q. \quad (41)$$

The coordinates of the source and field points on the surface of the wire are $(x_q, b\cos\varphi_q, b\sin\varphi_q)$ and $(x_p, b\cos\varphi_p, b\sin\varphi_p)$, so

$$r_{pq}=[(x_q-x_p)^2+b^2(\cos\varphi_q-\cos\varphi_p)^2 +b^2(\sin\varphi_q-\sin\varphi_p)^2]^{\frac{1}{2}} =\left[(x_q-x_p)^2+4b^2\sin^2\frac{\varphi_q-\varphi_p}{2}\right]^{\frac{1}{2}}. \quad (42)$$

Let

$$\xi=x_q-x_p, \qquad d\xi=dx_q,$$
$$\varphi_q-\varphi_p=\varphi, \quad d\varphi_q=d\varphi.$$

Then

$$\left[\ \right]_{n=0}=\frac{j\omega\mu_0}{4\pi}\int_0^l\int_0^{2\pi}\int_{-\infty}^\infty\int_0^{2\pi} J_p^*J_q \times\frac{\exp-j\left[k\left(4b^2\sin^2\frac{\varphi}{2}+\xi^2\right)^{\frac{1}{2}}\right]}{\left(4b^2\sin^2\frac{\varphi}{2}+\xi^2\right)^{\frac{1}{2}}}dx_p\frac{d\varphi_p}{2\pi}d\xi\frac{d\varphi_q}{2\pi}, \quad (43)$$

$$=\frac{j\omega\mu_0}{4\pi}\int_0^{2\pi} J_p^*J_ql\frac{\pi}{j}H_0^{(2)}\left(2kb\sin\frac{\varphi}{2}\right)\frac{d\varphi}{2\pi}. \quad (44)$$

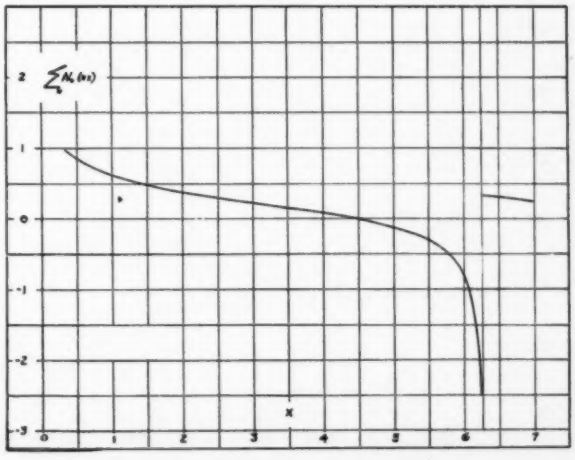

FIG. 2. Plot of function.

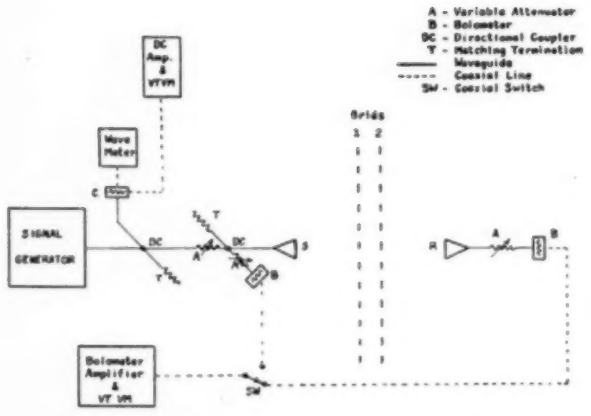

FIG. 3. Block diagram of experimental arrangement.

So

$$\int_0^l E_{pz} i_p^* dx = \frac{-\omega\mu_0}{2} \sum_{n=1}^{\infty} J_p^* J_q l H_0^{(2)}(knd) - \frac{\omega\mu_0}{4\pi} \int_0^{2\pi} J_p^* J_q l H_0^{(2)}\left(2kb \sin\frac{\varphi}{2}\right)\frac{d\varphi}{2}, \quad (45)$$

but

$$\int_0^l E_{pz} i_p^* dx_p = J_p^* E_{pz} l = -J_p^* l E_{x_{inc}}. \quad (46)$$

Hence, if

$$\psi = \frac{\varphi}{2},$$

$$E_{inc} = J_q \left[\frac{\omega\mu_0}{2} \sum_{n=1}^{\infty} H_0^{(2)}(knd) + \frac{\omega\mu_0}{4\pi} \int_0^{\pi} H_0^{(2)}(2kb \sin\psi) d\psi \right]. \quad (47)$$

Let

$$Z' = \frac{E_{x_{inc}}}{J_q} = R' + j\omega L', \quad (48)$$

$$Z' = \frac{\omega\mu_0}{4\pi} \left[2\pi \sum_{n=1}^{\infty} H_0^{(2)}(knd) + \int_0^{\pi} H_0^{(2)}(2kb \sin\psi) d\psi \right], \quad (49)$$

where R = radiation resistance/meter and L = self-inductance/meter.

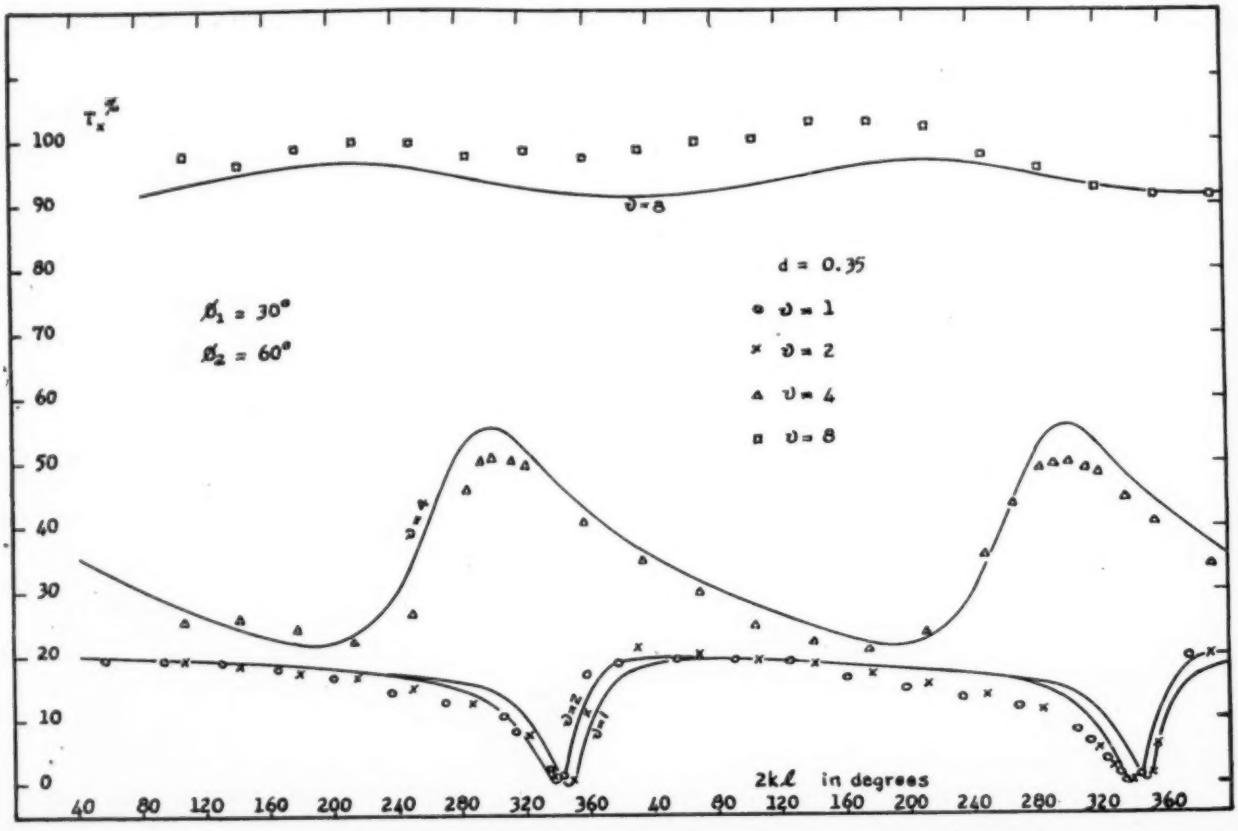

FIG. 4. Transmission coefficient T_x, as a function of intergrid spacing, for $\phi_1 = 30°$, $\phi_2 = 60°$.

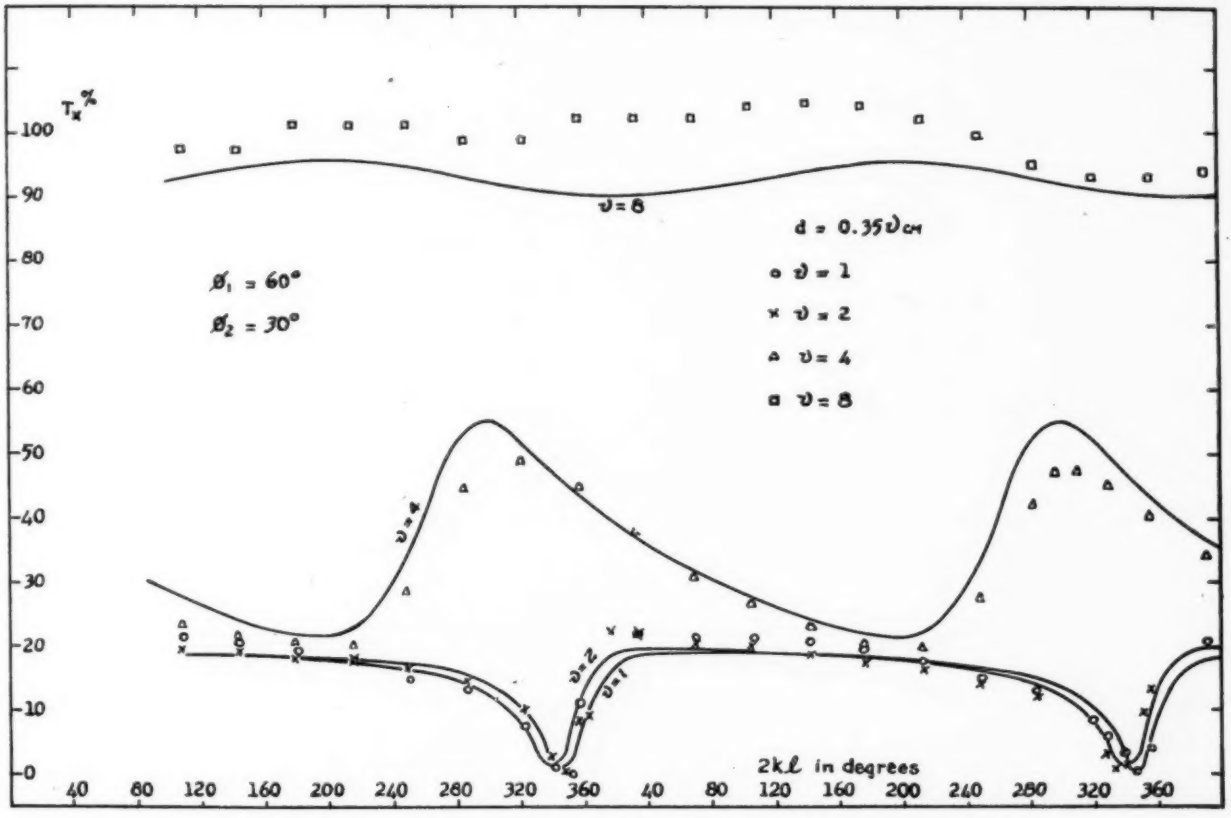

FIG. 5. Transmission coefficient T_x, as a function of intergrid spacing, for $\phi_1=60°$, $\phi_2=30°$.

If $2kb \ll 1$ $(\lambda \gg 4\pi b)$

$$H_0^{(2)}(2kb\sin\psi) \cong \frac{2}{j\pi}\ln j\gamma kb\sin\psi$$

$$= 1-\frac{2j}{\pi}\ln\gamma kb\sin\psi, \tag{50}$$

$$\gamma = 1.7811\cdots,$$

and

$$\int_0^{\pi}\left(1-\frac{2j}{\pi}\ln\gamma kb\sin\psi\right)d\psi = \pi - 2j\ln\frac{\gamma kb}{2}. \tag{51}$$

Then

$$Z' = \frac{\omega\mu_0}{4\pi}\left[2\pi\sum_{n=1}^{\infty}J_0(knd)\right.$$

$$\left.-j2\pi\sum_{n=1}^{\infty}N_0(knd)+\pi-2j\ln\frac{\gamma kb}{2}\right], \tag{52}$$

$$R' = \frac{\omega\mu_0}{2}\left[\sum_{n=1}^{\infty}J_0(nkd)+\tfrac{1}{2}\right], \tag{53}$$

$$L' = -\frac{\omega\mu_0}{2}\left[\sum_{n=1}^{\infty}N_0(nkd)+\frac{1}{\pi}\ln\frac{\gamma kb}{2}\right]. \tag{54}$$

From Ignatowsky,[3] when $\lambda > d$,

$$\sum_{n=1}^{\infty}J_0(nkd) = \frac{\lambda}{2\pi d}-\frac{1}{2}. \tag{55}$$

So

$$R' = \frac{\omega\mu_0}{2}\frac{\lambda}{2\pi d} = \frac{\zeta}{2d}, \tag{56}$$

where

$$\zeta = (\mu_0/\epsilon_0)^{\frac{1}{2}}, \tag{57}$$

$$\lambda > d,$$

$$R = \frac{R'}{R'} = 1, \tag{58}$$

$$L = \frac{L'}{R'} = -kd\left[\sum_{n=1}^{\infty}N_0(nkd)+\frac{1}{\pi}\ln\frac{\gamma kb}{2}\right], \tag{59}$$

$$Z = \frac{Z'}{R'} = 1+j\omega L, \tag{60}$$

but from Eq. (31)

$$\kappa = \frac{\zeta}{2d}J_x = J_xR' = \frac{E_{x_{\text{inc}}}}{Z'}R' = \frac{1}{Z}, \tag{61}$$

[3] W. von Ignatowsky, Ann. Physik 44, 369–436 (1914).

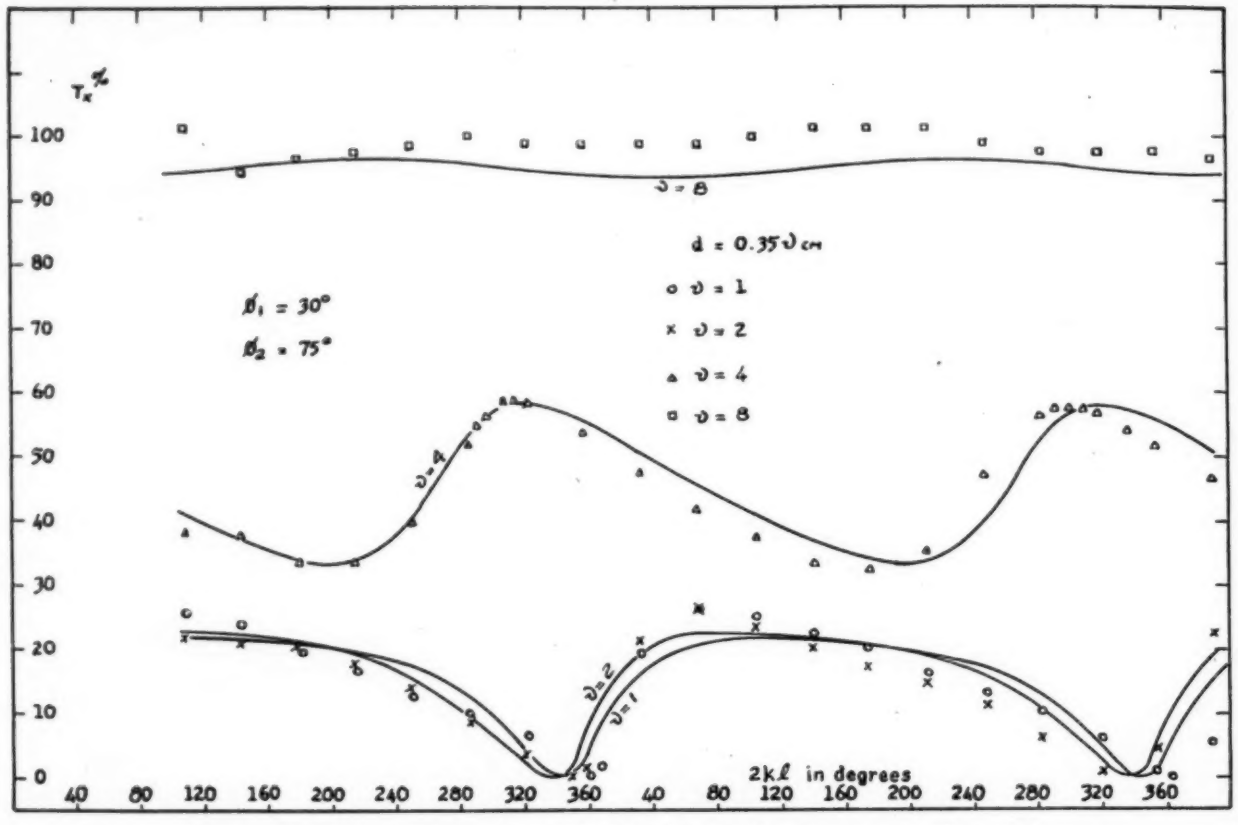

FIG. 6. Transmission coefficient T_x, as a function of intergrid spacing, for $\phi_1=30°$, $\phi_2=75°$.

or

$$\kappa=\frac{1}{1+j\omega L}=U+jV=\rho e^{j\delta}. \tag{62}$$

Then

$$U=\frac{1}{1+\omega^2L^2}, \tag{63}$$

$$V=\frac{-\omega L}{1+\omega^2L^2}, \tag{64}$$

$$\rho=(U^2+V^2)^{\frac{1}{2}}, \tag{65}$$

$$\delta=\tan^{-1}\frac{-V}{U}. \tag{66}$$

Wessel computed, by means of a formula from Ignatowsky, tables of the function

$$\sum_{n=1}^{\infty} N_0(nkd).$$

Figure 2 is a plot of the data contained in these tables.

III. EXPERIMENTAL INVESTIGATION

Two grids were constructed, having the following dimensions and properties:

Length of conductors:	91.5 cm (28.6λ)
Radius of conductors:	$b=0.0875$ cm
Material:	Brass
Conductivity:	1.57×10^7 mhos/meter
Minimum spacing of wires:	0.35 cm
Actual spacing of wires:	$d=0.35\nu$ ($\nu=1, 2, 3, \cdots$)
Width of grid:	91.5 cm (28.6λ)
Wavelength:	$\lambda=3.2$ cm.

Using Eqs. (59), (63), (64), (65), and (66), and the above constants of the grids, ρ and δ were calculated for four values of ν, yielding the following:

ν	ρ	δ
1	0.996	−5.2°
2	0.991	−7.7°
4	0.721	−43.9°
8	0.198	−78.4°.

(67)

Figure 3 is a diagram of the experimental arrangement used. The signal source was a type 2k39 reflex klystron, with a laboratory constructed power supply and modulator. The reflector voltage was square wave modulated at 1000 cycles per second. The power output was approximately 0.4 watts at a wavelength of 3.2 cm.

A wavelength of approximately 3 cm was chosen primarily to facilitate the construction of the grids. It allowed the grids to have over-all transverse dimensions at least an order of magnitude greater than the wavelength without becoming impractically large. An additional important reason for this choice was the availability of excellent equipment designed for this band.

At the output wave guide of the signal generator, a directional coupler extracted a sample of the signal and supplied it to a DeMornay-Bud type 382 cavity wave meter with associated crystal detector and indicating amplifier. This provided a means of monitoring the wavelength of the output signal.

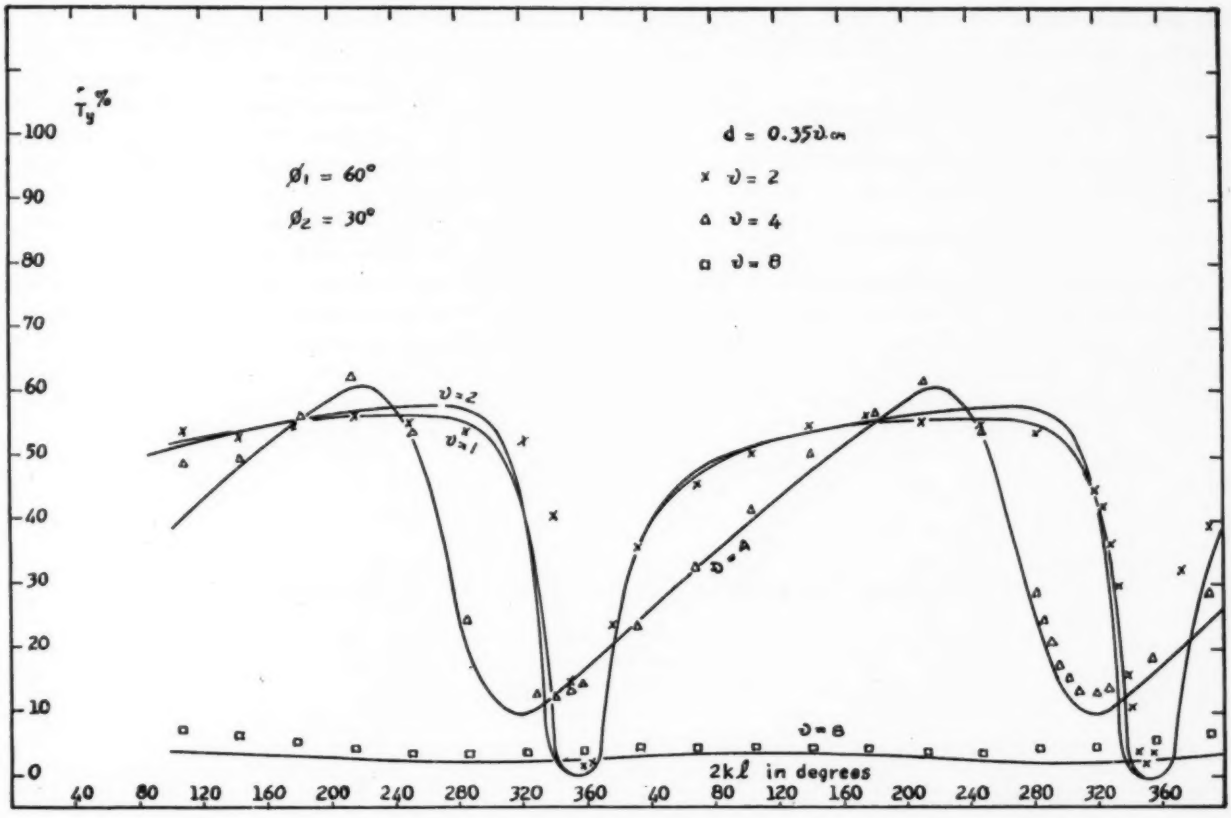

FIG. 7. Transmission coefficient T_y, as a function of intergrid spacing, for $\phi_1 = 60°$, $\phi_2 = 30°$.

The wave guide from the signal generator was terminated in a variable attenuator, a directional coupler, and a rectangular electromagnetic horn radiator. The variable attenuator was adjusted to serve as the primary load on the signal generator, sufficiently isolating it from the horn radiator that variations in the reaction of the grids on the horn caused negligible variations in the frequency and power output of the signal generator. The directional coupler extracted a signal proportional to the power traveling toward the sending horn near its throat. This signal passed through a variable attenuator to a bolometer detector. This arrangement served to monitor the power radiated by the horn.

The sending horn and the directional coupler were mounted on a tripod so that the axis of the beam radiated by the horn was horizontal. The tripod head was arranged to permit the polarization of the radiated beam to be rotated about the beam axis to any desired angle with respect to a vertical reference.

The receiving device was a similar horn, mounted on a second tripod at a distance of approximately $1\frac{1}{2}$ meters in front of the sending horn. The receiving horn was mounted horizontally so that its axis coincided with that of the sending horn, with its mouth directed toward the sending horn. The mounting of the receiving horn was also arranged so that its polarization could be rotated about the common axis between the horns to any desired angle.

Approximately halfway between the sending and receiving horns, a large plywood frame supported the two grids within a circular aperture at its center. The grids were so supported that their centers were on the common axis of the horns, and their planes were normal to this axis. The grid nearest the sending horn was bolted rigidly in the frame. The grid farthest from the sending horn was mounted on long threaded bolts so that it could be moved along the common axis by means of thumb screws, while remaining parallel to the fixed grid. Thus, the spacing between the two grids could be varied continuously from about two to forty millimeters. Holes were provided around the periphery of the circular aperture in the frame at 15° intervals, permitting the grids to be mounted with their wires at various angles with respect to the vertical.

The bolometer on the sending horn directional coupler and the one terminating the receiving horn were connected by coaxial cable to separate terminals of a coaxial switch. The center terminal of this switch was connected to the input of a Hewlett-Packard type 415A Standing Wave Meter. This instrument provided the necessary dc bias for the bolometers, and, by operating the coaxial switch, indicated the relative signal levels at the sending and receiving horns.

Transmission coefficients T_x and T_y were measured for pairs of grids having values of ν of 1, 2, 4, and 8, and for various values of φ_1 and φ_2. The spacing between

the grids was varied between approximately 40 and 720 electrical degrees. Theoretical values of T_x and T_y were computed from Eqs. (15) and (16) for the same values of ν, φ_1, φ_2, and l, using the results tabulated in Eq. (67).

Figures 4, 5, 6, and 7 are curves plotted from the computed and measured values of T_x and T_y for a few typical cases.

IV. CONCLUSIONS

The experimental values obtained for the transmission coefficients of a pair of grids agree quite closely with the values computed from the equations derived in Sec. II for all wire spacings except that for which $\nu=8$. For this case, in which the wire spacing is approaching the wavelength, the variation is due to the use of a curved wave front in the incident radiation, rather than the assumed plane wave, together with the use of a directional receiving device which discriminates against scattered radiation from wires some distance off the axis of measurement. In addition, the error resulting from the assumption that the field between the grids is composed only of the dominant plane waves becomes appreciable when the wire spacing approaches λ, and the intergrid spacing is less than 2.5λ. When the spacing between grid wires is appreciably less than λ, Eqs. (15) and (16) yield a good approximation of the transmission coefficients of double grid configurations which fulfill the basic assumptions.

JOURNAL OF APPLIED PHYSICS VOLUME 24, NUMBER 7 JULY, 1953

Starting Currents in the Backward-Wave Oscillator

L. R. WALKER
Bell Telephone Laboratories, Murray Hill, New Jersey
(Received January 23, 1953)

The starting current of a simple model of the backward-wave oscillator described by Kompfner and Williams has been calculated. The effect of space charge is included. The starting current I_0 may be written in the form

$$I_0=\frac{4V_0}{Z_0}\left[\frac{a_0(4QC)}{2\pi N}\right]^3,$$

where V_0 is the beam voltage, Z_0 is the impedance of the circuit, N is the length of the oscillator in wavelengths measured on the circuit and $a_0(4QC)$ is a dimensionless quantity which has been evaluated as a function of the space-charge parameter $4QC$.

A NOVEL form of microwave oscillator has been described recently by Kompfner and Williams.[1] In this generator an electron stream interacts with a particular spatial harmonic of one of the transmission modes of a periodic structure of the type used in certain traveling wave amplifiers.[2] It is characteristic of the device that while the driven harmonic has a phase velocity close to that of the electron stream and travels "forward", the power flow of the transmission mode is in the opposite direction or "backward." Thus power absorbed by the circuit from the beam at any point flows backward and produces modulation of the beam. There are in effect a multiplicity of feedback paths between the circuit and the beam, and the possibility exists that such a system, entered by an unmodulated beam, may be unstable for certain frequencies. It is intended here to find out under what conditions this may occur for a simple but representative system.

It will be supposed that the circuit has a pair of modes of propagation for which the phase and group velocities are oppositely directed; for a passive circuit this is to say that the phase velocity and power flow are in opposite directions. The two modes have equal and opposite phase velocities and, similarly, contrary but equal group velocities. The "phase velocity" of a transmission mode is not, for periodic structures, an unambiguous term, since each such mode may be resolved into an indefinite number of space harmonics, every one of which has its own distinct phase velocity. With equal propriety any one of these phase velocities may be used to label the mode. However, the group velocity is the same for all, and thus the power flow has a definite direction and magnitude characteristic of the mode. It follows that for any periodic structure every mode is of the type considered here, provided that the electrons interact with a forward-moving space harmonic.[3] In the following analysis it will be assumed that only a single mode is excited by the electrons, and that, if this mode has space harmonics, only one of these interacts with the electron stream. This assumption may not be met in practice by every structure, and it is always necessary to check it in specific cases. The mode having

[1] R. Kompfner and N. Williams, Institute of Radio Engineers Conference on Electron Devices, Ottawa, Ontario, June 1952.
[2] S. Millman, Proc. Inst. Radio Engrs. **39**, 1035 (1951).
[3] An example of a mode of this type in a nonperiodic structure is given by Pierce. J. R. Pierce, *Traveling-Wave Tubes* (D. Van Nostrand Company, Inc., New York, 1950), Chap. XI.

its phase and group velocity reversed from the interacting mode will interact weakly with the electrons. If it be supposed that the circuit is matched at the input end, then this mode cannot be excited by reflections, and hence it too may be ignored.

Since starting conditions are in question, small signal analysis will be used. The electron beam flowing in the positive x direction has a dc velocity, v_0, and a dc charge density, ρ_0, corresponding to a beam voltage, V_0, and a dc current, I_0; it is considered to be sufficiently thin and close to the circuit for the same electric field to act on all electrons at a position x and for the ac current injected into the circuit between x and $x+dx$ to be $(\partial i/\partial x)dx$, where i is the ac current in the beam. Transverse motions of the electrons are excluded. The ac voltage of the circuit wave (of the relevant space-harmonic in periodic structures) is V, and the undriven wave is of the form

$$V=V_1\exp j[\omega t-\beta x],$$

where ω is the angular frequency and $\beta=\beta(\omega)$ is the phase constant and is supposed real. The equation which describes the excitation of the circuit wave by the beam is taken to be

$$\frac{\partial V}{\partial x}+j\beta V=\frac{Z_0}{2}\frac{\partial i}{\partial x}, \tag{1}$$

where Z_0 is that impedance which when placed at the input end completely absorbs the circuit wave ($-Z_0$ is the characteristic impedance of the mode). To justify Eq. (1), one may write, if V^* and i^* are the complex conjugates of V and i,

$$\frac{\partial V^*}{\partial x}-j\beta V^*=\frac{Z_0}{2}\frac{\partial i^*}{\partial x},$$

then calculate the power extracted from the beam between x_1 and x_2. This is given by

$$\begin{aligned}P(x_1,x_2)&=\tfrac{1}{4}\,\mathrm{Re}\left[\int_{x_1}^{x_2}\left(\frac{\partial V}{\partial x}i^*+\frac{\partial V^*}{\partial x}i\right)dx\right]\\&=\tfrac{1}{4}\,\mathrm{Re}[Vi^*+V^*i]_{x_1}^{x_2}\\&\qquad-\tfrac{1}{4}\,\mathrm{Re}\left[\int_{x_1}^{x_2}\left(V\frac{\partial i^*}{\partial x}+V^*\frac{\partial i}{\partial x}\right)\right]\\&=\tfrac{1}{4}\,\mathrm{Re}[Vi^*+V^*i]_{x_1}^{x_2}-\frac{1}{2Z_0}[VV^*]_{x_1}^{x_2}.\end{aligned}$$

This implies that the power flow in the circuit at a point x is $-(VV^*/2Z_0)$, which indicates that the power flows against the electron stream.

The effect of the field upon the electrons is calculated in the usual way from the equation of motion and the equation of continuity. Letting the amplitudes of the ac charge density, velocity and current be ρ, v, and i, then

$$i=\rho_0 v+v_0\rho,$$

$$j\omega\rho+\frac{\partial}{\partial x}(\rho_0 v+v_0\rho)=0,$$

$$\left(j\omega+v_0\frac{\partial}{\partial x}\right)v=-\frac{e}{m}\frac{\partial V_T}{\partial x},$$

where $\partial V_T/\partial x$ represents the total field. It is made up of a part contributed by the circuit voltage and a part arising from space charge. Eliminating ρ and v gives

$$\left(j\omega+v_0\frac{\partial}{\partial x}\right)^2 i=-j\omega\frac{e\rho_0}{m}\frac{\partial V_T}{\partial x}. \tag{2}$$

It will be assumed that the part of V_T arising from space charge is given by[4]

$$V_T-V=\rho/C_1, \tag{3}$$

where C_1 is a constant of the circuit. Since

$$\frac{\partial\rho}{\partial t}=j\omega\rho=-\frac{\partial i}{\partial x},$$

V_T is given by

$$V_T=V+\frac{j}{\omega C_1}\frac{\partial i}{\partial x}. \tag{4}$$

Equations (1), (2), and (4) have now to be solved subject to boundary conditions of the following form. The beam enters at $x=0$ with no modulation, which implies $i(0)=0$ and $(\partial i/\partial x)(0)=0$. The circuit voltage at $x=0$ may be any arbitrary number, $V(0)$, since the boundary conditions are homogeneous. These three conditions will completely determine a solution of the equations. But at $x=x_0$, the far end of the circuit, $V(x_0)$ must be zero by the following consideration. If the circuit be matched at the far end, the mode of interest cannot be excited there by reflections of the small amount of the reversed mode which will always exist. Also since the power in the main mode flows backward, there can be no excitation by the electrons at $x=x_0$. The imposition of this extra condition on the solution already found leads to an equation involving the frequency and the various parameters of the problem. This equation will have complex coefficients and in general the solution for the frequency will be complex, or an initial disturbance will either decay or grow. For some values of the parameters the frequency will be real. Thus, if the equation of condition be solved for real frequencies, a relation is found between the parameters which will correspond to those conditions under which the tube is on the verge of oscillation.

[4] Reference 3, p. 111.

Equations (1), (2), and (4) may be solved by Laplace transforms since it is clear that the solutions will not grow faster than exponentially and such solutions will be valid in $0<x<\infty$. Laplace transforms will be represented by putting bars over the functions involved. Multiplying (1), (2), and (4) by e^{-px} and integrating from 0 to ∞, gives, when the boundary conditions at $x=0$ are used,

$$(p+j\lambda)\bar{V}-V(0)=\frac{Z_0}{2}p\bar{\imath},$$

$$(pv_0+j\omega)^2\bar{\imath}=-j\omega\frac{e\rho_0}{m}[p\bar{V}_T-V(0)], \qquad (5)$$

$$\bar{V}_T-\bar{V}=\frac{j}{\omega C_1}p\bar{\imath}.$$

Eliminating $\bar{\imath}$ and $\bar{V}_T$ gives

$$\left\{\left[(p+j\omega/v_0)^2-\frac{e\rho_0}{mC_1v_0^2}p^2\right][p+j\lambda]+j\frac{\omega e\rho_0Z_0}{2mv_0^2}p^2\right\}\bar{V}$$

$$=\left\{(p+j\omega/v_0)^2-\frac{e\rho_0}{mC_1v_0^2}p^2+\frac{j\omega e\rho_0Z_0}{2mv_0^2}p\right\}V(0). \qquad (6)$$

Substituting for p in (6) the expression

$$p=\omega/v_0[-j+Cz],$$

where

$$C^3=\frac{e\rho_0Z_0}{2mv_0}=\frac{I_0Z_0}{4V_0},$$

and writing

$$Q=\frac{e\rho_0}{4mv_0^2C_1C^3} \quad \text{and} \quad \delta=\frac{\lambda-\omega/v_0}{\frac{\omega C}{v_0}},$$

then (6) becomes

$$[z^2+4QC(1+jCz)^2+C(1+jCz)]V(0)$$

$$=\frac{\omega}{v_0}\{[z^2+4QC(1+jCz)^2][z+j\delta]-j(1+jCz)^2\}\bar{V}. \qquad (7)$$

It will now be assumed that C is much smaller than unity, although $4QC$ is not. Equation (7) now becomes

$$\bar{V}=\frac{v_0}{\omega}V(0)\frac{z^2+4QC}{(z^2+4QC)(z+j\delta)-j}. \qquad (8)$$

Inverting the Laplace transform

$$V(x)=\frac{v_0V(0)\exp-(j\omega x/v_0)}{2\pi j\omega}$$

$$\times\int_{z_0-j\infty}^{z_0+j\infty}\frac{z^2+4QC}{(z^2+4QC)(z+j\delta)-j}e^{az}dz, \qquad (9)$$

where

$a=\omega Cx/v_0$ and $\mathrm{Re}(z_0)$ is sufficiently positive.

The boundary condition, $V(x_0)=0$, then implies

$$0=\int_{z_0-j\infty}^{z_0+j\infty}\frac{z^2+4QC}{(z^2+4QC)(z+j\delta)-j}e^{a_0z}dz, \qquad (10)$$

with

$$a_0=\frac{\omega Cx_0}{v_0}.$$

If, identically,

$$(z^2+4QC)(z+j\delta)-j=(z-z_1)(z-z_2)(z-z_3), \qquad (11)$$

Eq. (10) may be reduced to

$$0=\Sigma(z_i-z_j)(z_k^2+4QC)e^{a_0z_k}, \qquad (12)$$

where i, j, k represent a cyclic permutation of 1, 2, 3.

Since general properties of (12) are in question rather than solutions for specific values of the parameters, it is convenient to represent the three quantities z_1, z_2, z_3 and the parameters δ and $4QC$ in terms of two rather nonphysical but useful parameters in such a way that (11) holds. Defining ν and σ, then, by means of the equations

$$\delta=\frac{\sigma}{\nu^2}-\nu^4, \qquad (13)$$

and

$$4QC=\frac{\sigma^2-1}{\nu^4}, \qquad (14)$$

it is found that

$$z_{1,2}=j\frac{\nu^4}{2}\pm\left[\frac{1}{\nu^4}-\left(\frac{\sigma}{\nu^2}-\frac{\nu^4}{2}\right)^2\right]^{\frac{1}{2}}, \qquad (15)$$

and

$$z_3=-j\sigma/\nu^2; \qquad (16)$$

σ is unity in the absence of space charge and otherwise greater than unity. ν may be considered to run from 0 to ∞ since this represents all values of δ from $-\infty$ to $+\infty$. The fact that there will be other values of ν, in general, complex, which correspond to a given δ is not troublesome. It is easily shown that choosing a different ν for a particular δ has only the effect of changing the labels on the z's and since Eq. (12) involves all the z's symmetrically the relabelling gives nothing new.

Substitution of (13), (14), (15), and (16) into (12) gives after some calculation

$$\nu^6\left[\sigma+\frac{j}{2R}\left(-\sigma\nu^4+\frac{2\sigma^2-1}{\nu^2}\right)\right]\exp\left[\left(j\frac{\nu^4}{2}-R\right)a_0\right]$$

$$+\nu^6\left[\sigma-\frac{j}{2R}\left(-\sigma\nu^4+\frac{2\sigma^2-1}{\nu^2}\right)\right]$$

$$\times\exp\left[\left(j\frac{\nu^4}{2}+R\right)a_0\right]+\exp\left(-j\frac{\sigma a_0}{\nu^2}\right)=0, \qquad (17)$$

where R is the positive square root of $1/\nu^4-(\sigma/\nu^2-\nu^4/2)^2$. Putting $\nu^3=\tau$ and $a_0/\nu^2=\mu$, (17) becomes

$$2\tau^2\left\{\sigma\cosh\mu[1-(\sigma-\tau^2/2)^2]^{\frac{1}{4}}-j\frac{2\sigma^2-1-\sigma\tau^2}{2[1-(\sigma-\tau^2/2)^2]^{\frac{1}{4}}}\sinh\mu[1-(\sigma-\tau^2/2)^2]\right\}+\cos(\sigma+\tau^2/2)\mu-j\sin(\sigma+\tau^2/2)\mu=0. \quad (18)$$

For a real frequency σ, τ, and μ are all real so that (18) separates into the pair of real equations

$$-2\tau^2\sigma\cosh\mu[1-(\sigma-\tau^2/2)^2]^{\frac{1}{4}}=\cos(\sigma+\tau^2/2)\mu, \quad (19a)$$

$$-\tau^2\frac{(2\sigma^2-1-\sigma\tau^2)}{[1-(\sigma-\tau^2/2)^2]^{\frac{1}{4}}}\sinh\mu[1-(\sigma-\tau^2/2)^2]^{\frac{1}{4}}=\sin(\sigma+\tau^2/2)\mu. \quad (19b)$$

This separation is valid regardless of the sign of $1-(\sigma-\tau^2/2)^2$ since $\sinh x/x$ is real for x purely real or purely imaginary. Squaring and adding (19a) and (19b),

$$\sinh^2\mu[1-(\sigma-\tau^2/2)^2]^{\frac{1}{4}}=\frac{(1-2\sigma\tau^2)}{\tau^4}[1-(\sigma-\tau^2/2)^2],\quad 1>(\sigma-\tau^2/2)^2, \quad (20a)$$

$$\sin^2\mu[(\sigma-\tau^2/2)^2-1]^{\frac{1}{4}}=\frac{(1-2\sigma\tau^2)}{\tau^4}[(\sigma-\tau^2/2)^2-1],\quad 1<(\sigma-\tau^2/2)^2, \quad (20b)$$

and using (19b)

$$\sin^2(\sigma+\tau^2/2)\mu=(1-2\sigma\tau^2)(2\sigma^2-1-\sigma\tau^2)^2. \quad (21)$$

Equations (20) and (21) may be solved graphically by obtaining μ from each as a function of σ (or τ) at fixed τ (or σ), but it is useful to have some qualitative information before doing this. Writing

$$f=\sigma+\tau^2/2,$$

and

$$g=\sigma-\tau^2/2,$$

(20) and (21) become

$$\sinh^2\mu(1-g^2)^{\frac{1}{4}}=\frac{1-f^2+g^2}{(f-g)^2}(1-g^2),\quad g<1, \quad (22a)$$

$$\sin^2\mu(g^2-1)^{\frac{1}{4}}=\frac{1-f^2+g^2}{(f-g)^2}(g^2-1),\quad g>1, \quad (22b)$$

and

$$\sin^2\mu f=(1-f^2+g^2)(fg+g^2-1)^2. \quad (23)$$

The right-hand sides are always positive and thus

$$1+g^2\geq f^2. \quad (24)$$

Similarly the right-hand sides of (22b) and (23) are less than unity, and if one is unity then so is the other, since from (19a) both cosines vanish together. Thus,

$$(1-f^2+g^2)(g^2-1)\lessgtr(f-g)^2,$$

or

$$(g^2-1)^{\frac{1}{4}}+1/g\lessgtr f,$$

so that f lies within the limits

$$(1+g^2)^{\frac{1}{4}}\geq f\geq(g^2-1+1/g)^{\frac{1}{4}},\quad \text{for}\quad g>1.$$

Figure 1 shows the region in the $f-g$ plane defined by these inequalities and the conditions

$$f+g\geq 2,$$

and

$$f-g>0,$$

which follow from $\sigma>1$ and $\tau^2>0$.

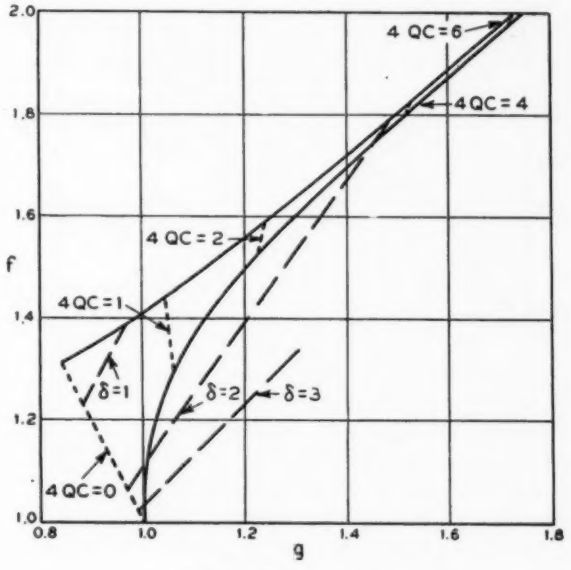

FIG. 1. The $f-g$ plane.

For $g<1$, where (22a) holds, which is the region in which some of the z's are complex and there exist growing waves as elementary solutions, it is clear from Eqs. (19a) and (19b) that both $\sin\mu f$ and $\cos\mu f$ are negative and, thus, μf satisfies

$$(2n+1)\pi<\mu f<(2n+3/2)\pi,\quad n=0, 1, 2, \cdots,$$

$\mu(1-g^2)^{\frac{1}{4}}$, on the other hand, is single valued. Proceeding as indicated before to solve for μ from (22a) and (23), it is found that each branch of μf corresponding to a different n leads to a solution. This number n will be called the mode number. Each such solution exists for $g=1$ and so may be expected to be prolonged to $g>1$. In this region the situation is more involved since $\mu(g^2-1)^{\frac{1}{4}}$ is now also multivalued. The branches of $\mu(g^2-1)^{\frac{1}{4}}$ join along the line $f=(g^2+1)^{\frac{1}{4}}$ where $\mu(g^2-1)^{\frac{1}{4}}$ is π, 2π, 3π, etc., and along $f=(g^2-1)^{\frac{1}{4}}+1/g$, where $\mu(g^2-1)^{\frac{1}{4}}$ is $\pi/2$, $3\pi/2$, $5\pi/2$, etc. Similarly μf branches along the same lines, but has the values 2π, 3π, 4π, etc., at $f=(g^2+1)^{\frac{1}{4}}$ and $3\pi/2$, $5\pi/2$, etc., at $f=(g^2-1)^{\frac{1}{4}}+1/g$.

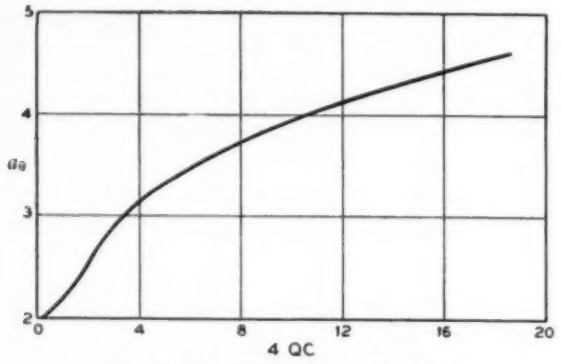

FIG. 2. a_0 *vs* $4QC$ for the $n=0$ mode.

Following a particular mode or n value into the region, $g>1$, $\mu(g^2-1)^{\frac{1}{2}}$ is 0 at $g=1$ and increases to $\pi/2$ as the lower boundary, $f=(g^2-1)^{\frac{1}{2}}+1/g$, is approached; μf meanwhile goes to $(2n+3/2)\pi$ at this boundary. Thus the first contact with the lower boundary satisfies

$$\begin{aligned}\mu(g^2-1)^{\frac{1}{2}}&=\pi/2,\\ \mu f&=(2n+3/2)\pi,\\ f&=1/g+(g^2-1)^{\frac{1}{2}},\end{aligned}\tag{25}$$

and is, thus, fully determined. Now, moving to the upper boundary, $f=(g^2+1)^{\frac{1}{2}}$, $\mu(g^2-1)^{\frac{1}{2}}$ goes to π and μf to $(2n+2)\pi$, so that the contact point satisfies

$$\begin{aligned}\mu(g^2-1)^{\frac{1}{2}}&=\pi,\\ \mu f&=(2n+2)\pi,\\ f&=(g^2+1)^{\frac{1}{2}}.\end{aligned}\tag{26}$$

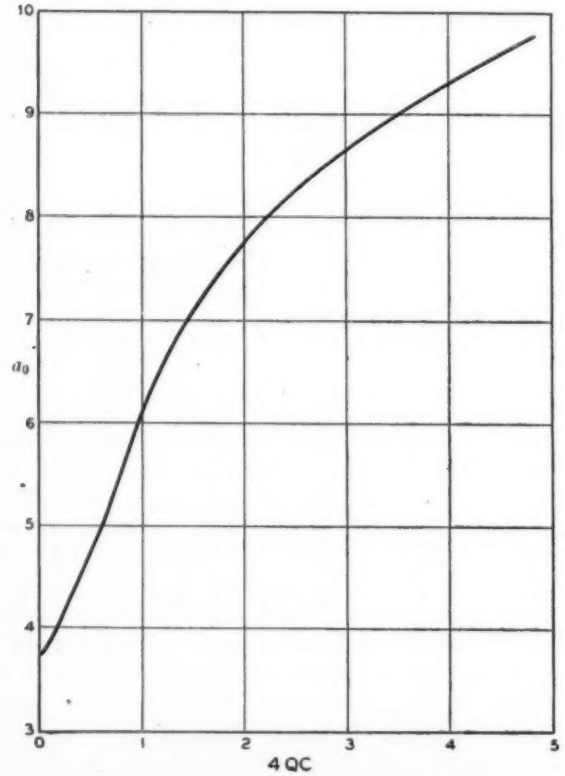

FIG. 3. a_0 *vs* $4QC$ for the $n=1$ mode.

The process continues and for the mth contact at the lower boundary

$$\begin{aligned}\mu(g^2-1)^{\frac{1}{2}}&=(2m-1)\pi/2,\\ \mu f&=(2n+3/2+m-1)\pi,\\ f&=1/g+(g^2-1)^{\frac{1}{2}},\end{aligned}\tag{27}$$

TABLE I.

First mode				Second mode			
m	m'	$4QC$	a_0	m	m'	$4QC$	a_0
0		1.251	2.220	0		.6373	4.943
	0	2.325	2.690		0	1.098	6.323
1		3.452	3.000	1		1.252	6.659
	1	4.793	3.273		1	1.650	7.298
2		6.189	3.494	2		1.914	7.637
	2	7.756	3.686		2	2.325	8.066
3		9.313	3.869	3		2.659	8.381
	3	11.04	4.040		3	3.097	8.714
4		12.71	4.191	4		3.471	9.001
	4	14.59	4.332		4	3.923	9.297
5		16.38	4.445	5		4.328	9.552
	5	18.38	4.590		5	4.795	9.806

Values of a_0 as a function of $4QC$ calculated from the contact points. m refers to the number of the contact with the lower boundary, m' to contacts with the upper boundary.

or

$$g^2=\frac{1}{2}\left\{1+\left[1+\left(\frac{2m-1}{2m+1}\right)^2\right]^{\frac{1}{2}}\right\},\tag{28}$$

$$\mu=\frac{(2m-1)\pi}{(g^2-1)^{\frac{1}{2}}};$$

and for the mth contact with the upper boundary

$$\begin{aligned}\mu(g^2-1)^{\frac{1}{2}}&=m\pi,\\ \mu f&=(2n+1+m)\pi,\\ f&=(g^2+1)^{\frac{1}{2}},\end{aligned}\tag{29}$$

TABLE II.

First mode				Second mode			
m	m'	$4QC$	δ	m	m'	$4QC$	δ
0		1.251	1.502	0		.6373	1.823
	0	2.325	1.602		0	1.098	1.179
1		3.452	1.961	1		1.252	1.502
	1	4.793	2.232		1	1.650	1.383
2		6.189	2.537	2		1.914	1.593
	2	7.756	2.816		2	2.325	1.602
3		9.313	3.085	3		2.659	1.768
	3	11.04	3.341		3	3.097	1.822
4		12.71	3.590	4		3.471	1.960
	4	14.59	3.834		4	3.923	2.031
5		16.38	4.143	5		4.328	2.154
	5	18.38	4.299		5	4.795	2.232

Values of δ as a function of $4QC$ calculated from the contact points. m refers to the number of contact with the lower boundary, m' to contacts with the upper boundary.

giving

$$g^2=\frac{(2n+1+m)^2+m^2}{(2n+1+m)^2-m^2},\tag{30}$$

$$\mu=[\tfrac{1}{2}(2n+1)(2n+1+2m)\pi]^{\frac{1}{2}}.$$

These equations thus give an indefinite number of points for each mode. It turns out for the $n=0$ and $n=1$ modes that when the two sets of points are used to calculate values of a_0 as a function of $4QC$ all the points lie very close to a single curve. Thus sufficient information may be found by solving graphically up to $g=1$ and using the contact points from there on. Values of δ calculated from the two branches are somewhat separated and the δ *vs* $4QC$ curve is correspondingly sinuous. In Tables I and II the values of a_0 and δ as a function of $4QC$ found from the contact points are shown. For $4QC=0$, $a_0=1.97$, $\delta=1.52$; for $n=0$ and $a_0=3.69$, $\delta=2.67$ for $n=1$.

Figures 2 and 3 show a_0 and δ as a function of $4QC$ for the first two modes. The frequency of oscillation should now be found by solving the equations

$$\lambda=\omega/v_0[1+C\delta(4QC)], \tag{31}$$

$$a_0=\frac{\omega C x_0}{v_0}=a_0(4QC). \tag{32}$$

This will be complicated since the frequency is involved in numerous ways. But if C is small, ω must nearly satisfy

$$\lambda(\omega)=\omega v_0, \tag{33}$$

so that the circuit wave and electrons are almost in step. If the phase characteristic of the circuit is known then ω will be known as a function of voltage. C must satisfy

$$C=\frac{a_0 v_0}{\omega x_0}=\frac{a_0}{\lambda x_0}=\frac{a_0}{2\pi N}=\frac{a_0(4QC)}{2\pi N}, \tag{34}$$

where N is the number of wavelengths along the length of the tube, or again

$$\left(\frac{I_0 Z_0}{4V_0}\right)^{\frac{1}{3}}=\frac{a_0(4QC)}{2\pi N},$$

$$I_0=\frac{4V_0}{Z_0}\left[\frac{a_0(4QC)}{2\pi N}\right]^3. \tag{35}$$

This value of I_0 may be identified with the starting current in the nth mode when the values of $a_0(4QC)$ for the nth mode are inserted. Strictly it has not been shown that greater values of I_0 correspond to oscillation and smaller ones to damping. This can be done fairly readily for the zero space-charge case, however. The operating voltage, V_0, will be given in terms of the synchronous voltage, V_{0s}, by the relation

$$V_0=V_{0s}[1+C\delta(4QC)]^2\sim V_{0s}[1+2C\delta(4QC)]. \tag{36}$$

Figures 4 and 5 show δ *vs* $4QC$ for the first two modes.

It may be remarked that the analysis shows quite clearly that backward-wave oscillation is an interference phenomenon and does not require operating conditions which admit growing wave solutions. The numbers n and m which have appeared in the analysis are clearly identifiable with integral numbers of half-wavelengths of the elementary waves out of which the solution is built.

This work was carried out in part under a contract with the U. S. Office of Naval Research whose support is acknowledged.

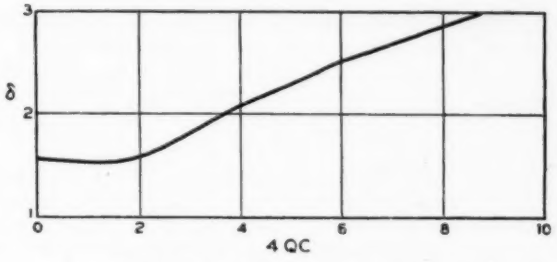

FIG. 4. δ *vs* $4QC$ for the $n=0$ mode.

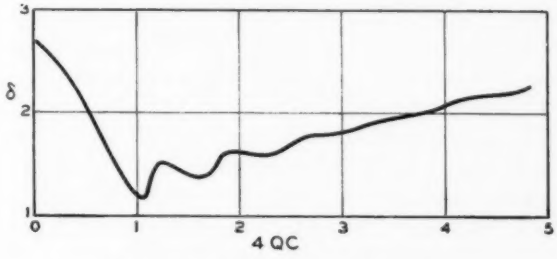

FIG. 5. δ *vs* $4QC$ for the $n=1$ mode.

New Developments in the Production and Measurement of Ultra High Vacuum

D. ALPERT
Westinghouse Research Laboratories, East Pittsburgh, Pennsylvania
(Received November 7, 1952)

A new vacuum technology is described which makes it possible to achieve working pressures as low as 10^{-10} mm Hg in a routine and straightforward fashion. This is accomplished without the use of chemical getters, special traps, or refrigerants of any kind. Essential to this technology are several new instruments which have been especially developed for the production or measurement of ultra high vacua. These new tools have permitted us to carry out a number of researches concerning the phenomena which occur at very low pressures. The ultra high vacuum technology has also made possible a new experimental approach in the fields of gaseous and physical electronics.

I. INTRODUCTION

FOR some years specialists who work with highly evacuated systems have agreed that pressures as low as 10^{-10} mm Hg are readily attainable. The average worker carrying out experiments requiring good vacuum conditions has viewed such claims with considerable skepticism, first of all because there have previously been no direct means for measuring such pressures, and secondly because the procedures for achieving such vacua have in the past been neither clearly understood nor adequately defined. The present paper describes several new instrumental developments carried out at these laboratories which have made it possible not only to achieve and measure such pressures, but also to carry out experiments which clarify and give new insight into the various physical mechanisms which take place in the pressure region below 10^{-8} mm Hg.[1] On the basis of these developments, together with the important work by others in this field, a new set of vacuum techniques has been evolved in our laboratories. The present paper describes some of the novel aspects of this technology which make it possible to achieve and measure pressures as low as 10^{-10} mm Hg[2] in a straightforward and relatively simple manner.

The interest in attaining extremely low pressures arises from the requirements met in a wide variety of experimental activities. The field of gaseous electronics is an example. It is well known that in a number of investigations involving the ionization of gases,[3] an impurity of one part in a million may significantly alter the physical characteristics of the gas in question. In these investigations the evacuation of the vacuum system is just a preliminary to the usual experiment in which the gas is then introduced into the system, the degree of evacuation setting an obvious limitation on the degree of gas purity which is possible. For obtaining very low contamination in gases in the millimeter range of pressures, it is necessary to attain extremely low residual pressures. By using the techniques developed in our laboratories, gas samples have been prepared with an impurity content of less than one part in a billion.[4]

In the field of physical electronics there are many instances in which ultra high vacua are required, for example in studies of the physical properties of solid surfaces. Nottingham[5,6] and Anderson[7] have shown that the work function of a metal is tremendously affected by the adsorption of small quantities of gas on the surface. At a pressure of 10^{-6} mm Hg an adsorbable gas forms a monolayer on a clean surface in about one second; hence at this pressure an experiment intended to study the properties of the clean surface itself would have to be carried out in a small fraction of a second. On the other hand, at 10^{-10} mm Hg the monolayer forms a in few hours and the surface remains clean for a sufficient time in which to make measurements. Experiments in this laboratory have shown indications of partial pressures of adsorbable gases of 10^{-13} mm Hg or less. In a general way, it may be said that the ability to attain and measure pressures several orders of magnitude lower than those usually considered satisfactory makes it possible to carry out a wide variety of experiments which would otherwise be infeasible.

The present paper was written with the intent (1) to describe those characteristics of recent instrumental developments which have not been discussed in previous publications,[8,9,10] (2) to discuss some of the physical mechanisms which are believed to occur at very low pressures, and (3) to describe in some detail the vacuum systems, procedures, and instrumentation which have been evolved in our laboratory. With this "ultra high vacuum technique," we achieve working vacuums between 10^{-9} mm Hg and 10^{-10} mm Hg in a manner which is in no case more difficult than the procedures conventionally used to attain the usual

[1] Much of this work was described in a paper presented at the Massachusetts Institute of Technology Conference on Physical Electronics, Cambridge, Massachusetts, in March, 1952.
[2] The pressures referred to in this article are equivalent nitrogen pressures unless otherwise specified.
[3] See, for example, review article by Druyvestyn and Penning, Revs. Modern Phys. **12**, 87 (1940).
[4] M. A. Biondi, Rev. Sci. Instr. **22**, 535 (1951).
[5] W. B. Nottingham, J. Appl. Phys. **8**, 762 (1937).
[6] W. B. Nottingham, Phys. Rev. **55**, 203 (1939).
[7] P. A. Anderson, Phys. Rev. **57**, 122 (1940).
[8] R. T. Bayard and D. Alpert, Rev. Sci. Instr. **21**, 571 (1950).
[9] Alpert, Matland, and McCoubrey, Rev. Sci. Instr. **22**, 370 (1951).
[10] D. Alpert, Rev. Sci. Instr. **22**, 536 (1951).

"good" vacuum of 10^{-7} mm Hg; this is accomplished without the use of special getters, charcoal traps, or refrigerants of any kind.

II. LIMITATIONS OF CONVENTIONAL IONIZATION GAUGES IN THE MEASUREMENT OF ULTRA HIGH VACUA

From the time of its initial development by Buckley[11] and Dushman[12] the ionization gauge has been the most widely used instrument for the measurement of low pressures. While it has certain limitations which will be discussed presently, the ionization gauge has been characterized by its simplicity of construction and operation, and its ability to read pressures lower than were possible with other means. The conventional ionization gauge[13] structurally resembles a triode vacuum tube. A filament serves as a source of electrons. However, the grid serves as the electron collector and is operated at a positive potential (100 to 200 v) with respect to the cathode, while the cylindrical plate is negative by 10 to 50 v. Electrons from the cathode, before being collected at the grid, are capable of ionizing gas molecules both inside the grid structure and between the grid and the negatively charged outer cylinder. Since the number of ions produced per electron is assumed proportional to the gas density, the current to the ion collector is used as an indication of the pressure. More precisely, it is the ratio of this ion current to the electron current arriving at the grid which constitutes a measure of the pressure. The sensitivity S of a given ion gauge is defined in terms of this ratio for a given pressure:

$$S=(i_c/i_g)/p,$$

where i_c is the ion collector current, i_g is the grid electron current, and p is the pressure in mm Hg.

A typical value for S is 10 $(\text{mm Hg})^{-1}$, while a normal operating electron current is 10 milliamperes; under these conditions the ion current at a pressure of 10^{-8} mm Hg is 10^{-9} ampere. Hence, if the ability to read the ion current were the only limitation on the ionization gauge pressure range, it would be possible to read pressures as low as 10^{-16} mm Hg, a value orders of magnitude lower than those which have thus far been obtained.

We now know that the standard ionization gauge as used prior to 1948 was not capable of indicating pressures below 10^{-8} mm Hg. There is good reason however to believe that pressures considerably below this value were attained as early as 1931.[14] In 1935 P. A. Anderson,[15] using the change in work function of a clean tungsten surface as an indication, attained pressures which very likely were below 10^{-9} mm Hg. He was able to achieve conditions in which changes in the work function because of adsorption of residual gas on a freshly cleaned surface did not take place for at least an hour. In 1937 Nottingham[5] used the rate of deactivation of a thoriated tungsten filament as a measurement of the magnitude of the residual gas pressure. He showed that "this deactivation time served as a better indication of the condition of the tube than any measurements" obtained with the ionization gauge. In particular it was clear that although the ionization gauge had reached its lowest ion current corresponding to 10^{-8} mm Hg, significant changes in the state of vacuum were still indicated by the variation in thermionic emission from a thoriated tungsten filament. These observations constituted the first indications that vacuums better than 10^{-8} mm were attainable, and at the same time served to heighten the mistrust of the ionization gauge as an instrument for the measurement of low pressures; it was not until considerably later that the low-pressure limit of the ionization gauge was clearly recognized as such in the literature.

It was Nottingham who recognized that a lower limit did exist on the range of the ionization guage and in 1947[16] put forth a hypothesis to account for it. He suggested that there exists a residual current to the ion collector which is completely independent of the pressure. This current is caused by soft x-rays created when the electrons from the filament strike the grid. The x-rays in turn release photoelectrons from the ion collector which are accelerated to the grid, the electron current from the ion collector giving a current of the same sigh as ions arriving at the collector. Thus the pressure in a conventional ionization gauge must exceed 10^{-8} mm Hg in order to produce an ion current appreciably in excess of the residual current.

In 1948, Apker[17] suggested a method for using an ionization gauge to indicate the state of vacuum in a system when the total pressure was less than 10^{-8} mm Hg. This technique, often called the "flash filament" method, has been further investigated by Nottingham and by Molnar.[18]

The procedure consists of incorporating an auxiliary tungsten filament within the ionization gauge. The filament is first cleaned by momentarily flashing to a temperature above 1500°K. After a time Δt during which it is kept at room temperature the filament is again flashed. The second flash suddenly releases the molecules adsorbed on the filament during the time Δt, and the resultant burst of gas registers as a momentary change in the reading of the ionization gauge giving a so-called peak pressure indication.[19] This peak pressure reading increases at first linearly with Δt, corresponding

[11] O. E. Buckley, Proc. Natl. Acad. of Sci. U. S. **2**, 683 (1916).
[12] S. Dushman and C. G. Found, Phys. Rev. **17**, 7 (1921).
[13] For a discussion of ion gauges, see for example, S. Dushman, *Scientific Foundations of Vacuum Techniques* (John Wiley and Sons, Inc., New York, 1949), chapter 6.
[14] E. K. Jaycox and H. W. Weinhart, Rev. Sci. Instr. **2**, 401 (1931).
[15] P. A. Anderson, Phys. Rev. **37**, 958 (1935).
[16] Private communication.
[17] L. Apker, Ind. Eng. Chem. **40**, 846 (1948).
[18] Private communications.
[19] Δt must be sufficiently large so that the adsorbed gas will give a peak pressure greater than 10^{-8} mm Hg.

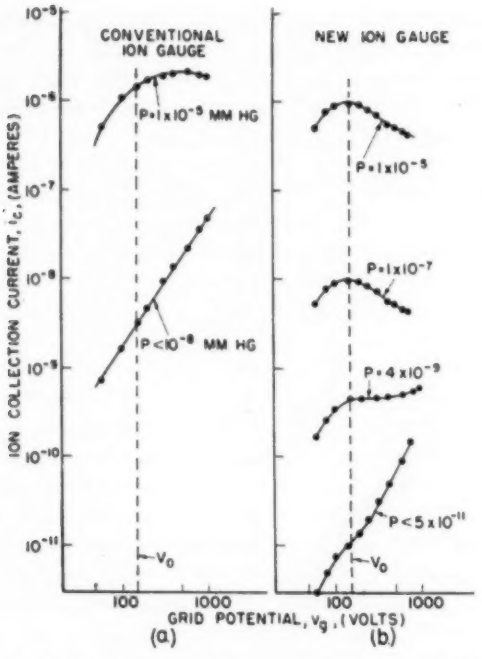

FIG. 1. (a) Typical data for conventional guage (RCA type 1949). (b) Typical data for Bayard-Alpert guage. V_0 is the normal operating voltage (150 v).

to the accumulation of adsorbed molecules on the flash filament; for sufficiently large Δt the peak pressure approaches a constant value and shows very small increases with further increase in Δt. This behavior is assumed to be due to the ready adsorption of molecules at early times when the filament is clean, the rate depending on the pressure of adsorbable molecules in the volume. The leveling-off point is taken to correspond to the time when the flash filament is covered with a monolayer of the molecules. One can calculate the rate at which molecules arrive at the filament surface at a given pressure (on the basis of kinetic theory) and estimate the number of molecules per cm² in a complete monolayer. The flash filament procedure gives $(\Delta t)_M$, the time required to cover the filament with a monolayer. From these numbers one can estimate the pressure in the vacuum system even though it lies below the measurable range of the ionization gauge. A rough check on these assumptions, and hence a calibration of the flash filament technique, is possible in a straightforward way by raising the pressure to a point where it can be read directly with the ion gauge and then comparing this value with the flash filament measurement.

The advantage of the flash filament method lies in its great simplicity. It was the first technique which became widely used in the measurement of pressures below 10^{-8} mm Hg. A great disadvantage of the method is that it discriminates severely between different types of gases; in particular it indicates only the partial pressures of certain adsorbable gases. Another difficulty is that it requires a considerable time interval for a single pressure determination. Nevertheless, the flash filament technique has been of great help in ultra high vacuum researches.

III. THE BAYARD-ALPERT IONIZATION GAUGE

Subsequent to 1947 a number of investigators were independently studying the causes for the low-pressure limitation on the ordinary ionization gauge. With the publication in 1950 of the paper[8] describing the Bayard-Alpert ionization gauge, the x-ray hypothesis was substantiated, and an ionization gauge was described with a low-pressure limit at least one thousand times smaller than heretofore available. Within a few months after the publication of this paper, two other independent investigations were reported[20,21] which demonstrated the x-ray effect and suggested methods for substantially reducing this limitation.

The original evidence for a residual current independent of the pressure had come from the observation that the conventional gauge never read values below 10^{-8} mm. Independent evidence for the existence of a residual current also can be obtained from other measured characteristics of the ionization gauge. If the ion collector current i_c is measured for varying grid potentials v_g, at a given pressure and electron current, the curve showing i_c *vs* v_g has a characteristic shape for pressures above 10^{-7} mm Hg. This curve, Fig. 1(a) upper curve, is similar to those for the gas ionization probability by electron impact[22] and is typical of data taken on RCA type 1949 gauges. Note that i_c rises rapidly with v_g up to 200 v and varies slowly with grid voltages above this value. When the pressure is lowered considerably (ion gauge reading 10^{-8} mm Hg), the curve of i_c *vs* v_g is radically different as shown by the lower curve in Fig. 1(a). This residual curve continues to rise rapidly with grid potential, the slope on a log-log plot falling between 1.5 and 2. In the intermediate range of pressures (10^{-7} to 10^{-8} mm Hg) the measured curve corresponds to a superposition of the "gas ionization" curve and the "residual" curve. These results, obtained independently in our laboratory, are in agreement with data published in 1931 by Jaycox and Weinhart[23] and with unpublished results of Nottingham.

The Bayard-Alpert ionization gauge was the direct product of an experiment which was proposed to examine the Nottingham hypothesis that the residual current was due to photoelectrons leaving the ion collector. A design for an ion gauge was sought which would operate in the usual manner but whose ion collector would intercept only a small fraction of the

[20] J. J. Lander, Rev. Sci. Instr. **21**, 672 (1950).
[21] G. H. Metson, Brit. J. Appl. Phys. **2**, 46 (1951).
[22] See, for example, K. T. Compton and C. C. Van Voorhis, Phys. Rev. **27**, 724 (1946).
[23] If the data of Jaycox and Weinhart (taken at what they considered to be 10^{-8} mm Hg) is plotted in the manner described, the resulting curve is not characteristic of "gas ionization" but is very similar to our "residual" curve. This constitutes evidence that Jaycox and Weinhart had attained pressures considerably below 10^{-8} mm Hg.

x-rays produced at the grid. The new gauge, Fig. 2, has the usual three elements, but is inverted from the conventional arrangement; the filament is outside the cylindrical grid while the ion collector, now a very fine wire, is suspended within the grid. The volume enclosed by the grid is made comparable to that between the grid and ion collector of an ordinary ionization gauge. The positive potential on the grid forms a potential well for the ions created within the grid-enclosed volume so that many of them are collected at the center wire; the ion collection efficiency is thus comparable to that of the conventional ionization gauge. On the other hand, the solid angle which the ion collector presents to x-rays from the grid is at least one thousand times smaller than that for the conventional cylindrical collector.

The i_c *vs* v_g characteristics of a Bayard-Alpert gauge are shown in Fig. 1(b). At higher pressures the curve for the new gauge is similar to the RCA gauge, but it is evident that the new gauge continues to have typical "gas ionization" characteristics at much lower pressures. At 4×10^{-9} mm Hg the collector current is still predominantly due to gas ionization. Even at the lowest pressures which were attained, less than 5×10^{-11} mm Hg, it is clear (lowest curve) that the gauge has still not reached the point where the x-ray effect is predominant at normal operating voltages. At higher grid voltages the "residual effect" is clearly the predominant one. The ratio of residual currents for the two types of ion gauges is found to be equal to the calculated ratio of the solid angles which they present to x-radiation. These results clearly substantiated the x-ray hypothesis and indicated that ionization gauges could be built to measure even lower pressures.

It should be noted that in order to extend the low pressure range of any ionization gauge, it is necessary to reduce the residual x-ray current without correspondingly reducing the gas sensitivity of the gauge. This was achieved in the Bayard-Alpert gauge by greatly reducing the x-ray effect. One can further improve an ionization gauge by increasing its sensitivity while keeping the x-ray effect constant. It was observed very early in the experimental program that the potential well produced by enclosing the negatively charged ion collector within the positive grid structure was essential to the efficient collection of ions and that the sensitivity of the gauge could be increased by more effectively surrounding the collector. Furthermore, it was observed that the glass walls of the ion gauge envelope may float at a negative potential at normal operating voltages. It therefore was clear that the step of enclosing the top and bottom of the grid structure would enhance the ion collection efficiency. Special models of the gauge employing smaller ion collectors and enclosed grid structure[24] have been constructed and found to have an inherent x-ray limitation corresponding to a pressure of 10^{-13} mm Hg. However, for general use, we have continued to use the gauge design originally reported in the literature because of its relative simplicity and adequacy for most ultra high vacuum work.

A unique feature of the Bayard-Alpert gauge is the distribution of potential in the ionizing region. Since the collector is coaxial with the cylindrical grid, one has a logarithmic potential distribution between grid and ion collector with the greatest change in potential immediately adjacent to the collector wire. It follows that the ionizing electrons retain most of their energy throughout their trajectory within the grid volume. For the particular geometry used at present, the equipotentials are such that an incoming electron with 150-ev energy falls below an efficient ionizing energy (50 ev) only when it penetrates to a distance of about 0.010 in. from the collector wire. This represents a fractional ion collection volume of only one percent in which the ionizing cross section is very small. In the conventional ionization gauge quite the opposite is true; the electrons are all decelerated so that they are inefficient for ionization over a major portion of their trajectory.

The design details of the gauge are shown in Fig. 2. Most of the dimensions can be inferred from the com-

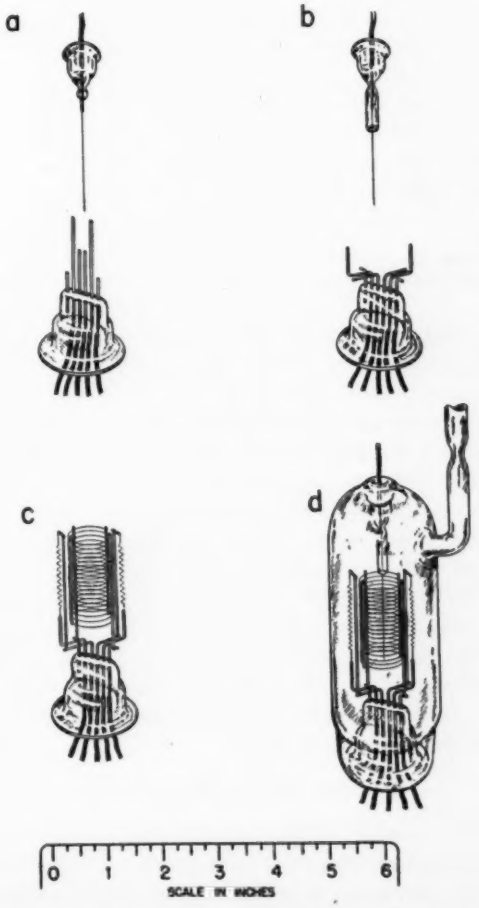

FIG. 2. Steps in ion guage construction.

[24] W. B. Nottingham has independently developed ion gauges with enclosed grids. (Private communication.)

parison scale. The assembly of the parts is indicated by steps *a-d* of the figure, and is quite straightforward. The second tungsten filament is electrically separated from the first and has at least two desirable uses aside from its value as a spare. It may be used in connection with the flash filament method; in addition, the electron emission characteristics of this filament may be used as a separate indication of vacuum conditions. The glass skirt around the ion collector lead-in serves several purposes: it prevents x-rays from striking the large diameter tungsten lead-in wire and this maintains a lower solid angle for their interception; it lengthens the surface leakage path and prevents current from the charged walls of the gauge from reaching the ion collector. If for any reason a metallic film is evaporated or otherwise deposited on the glass walls of the gauge, the glass skirt prevents the formation of a direct path to the ion collector. The ion collector (a 0.006-in. diameter tungsten wire) is gradually tapered by an electrolytic etching process so as to give the minimum x-ray solid angle and at the same time to retain enough stiffness to prevent large mechanical deformation or oscillations. The grid structure is helically wound 0.005-in. molybdenum wire spot welded to molybdenum supporting members. The filaments are made from 0.006-in. diameter tungsten wire.

TABLE I. Values of sensitivity ratios for various gases.

Gas	Dushman and Young[a]	Wagener and Johnson[b]
H_2	0.47	0.53
He	0.16	
Ne	0.24	
N_2	1	1
A	1.19	
CO		1.07
CO_2		1.37
H_2O		0.89
O_2		0.85
Kr	1.9	
Xe	2.7	
Hg	3.4	

[a] See reference 28.
[b] See reference 29.

The new gauge has a minimum of metallic surface so that it is easily outgassed by electron bombardment of grid and collector which raises the element temperature to ~1200°C with considerably less power than required for a conventional gauge. It may be operated on a standard power supply and its over-all simplicity indicates that it may well have advantages not only in the special field of ultra high vacuum, but also in the more general field of high vacuum.

IV. ION GAUGE SENSITIVITY

The x-ray effect in the conventional ionization gauge constitutes a restriction which serves to limit its usefulness and previously has thrown doubt upon its dependability. In addition, there are two other limitations of ion gauges in general which cast grave suspicion on any quoted pressure reading based on the ionization gauge alone. These two disadvantages are (1) the sensitivity varies for different gasses and vapors, and (2) the ion gauge serves as a pump to "clean-up" gases. After a study of this pumping action of an ionization gauge, H. Schwarz[25] made the statement: "Everyone who measures pressures under 10^{-4} with an ionization gauge must regard his measurements with more or less skepticism." This skepticism has so pervaded the literature on high-vacuum techniques that a brief discussion of the physical processes involved is in order. It is the intent of this discussion to evaluate the validity of these criticisms and to define if possible the limitations on the ionization gauge imposed by these mechanisms.

A considerable amount of work has been done, especially by Dushman and his colleagues,[26-28] on determining the sensitivity of ion gauges for various gases. More recently Wagener and Johnson[29] have also made measurements of ion gauge sensitivities for a variety of gases. From the many measurements which have been carried out, the following conclusions can be drawn: (a) while the sensitivities may vary appreciably from one gauge design to another, the ratio of sensitivities for the different gases seems to be essentially independent of the design of gauge used; (b) though there are certain variations in the methods used for measuring the sensitivities, the results of the various measurements are in good agreement. Table I gives the sensitivities of a given gauge for a number of common gases. The data are given in terms of a quantity R which is the ratio of the sensitivity for the gas in question to the sensitivity for nitrogen. This ratio is particularly convenient since the pressure usually is given an as equivalent nitrogen pressure.

While Table I demonstrates graphically the inherent limitation of the ionization gauge resulting from the variation of sensitivity, it should be observed that the sensitivity for many of the gases falls within a factor of two of the gauge sensitivity for nitrogen. The important exceptions are helium and neon, which have low sensitivities and whose pressure may therefore be underestimated, and mercury which has a high sensitivity and whose pressure may therefore be overestimated.

Huthsteiner and Dushman[30] have also made measurements on some of the vapors of organic liquids and solids such as iodine ($R=5.5$), cadmium ($R=2.4$), silicone oil ($R=2.7$), napthalene ($R=0.85$), and Octoil-S ($R=5$). Thus it is seen that even including some vapors of high molecular weight, the sensitivity ratio does not vary by an order of magnitude.

In the case of gases or vapors which can react chemically or electrochemically (as ions) with the

[25] H. Schwarz, Z. Physik **122**, 437 (1943).
[26] S. Dushman and C. G. Found, Phys. Rev. **23**, 734 (1924).
[27] N. B. Reynolds, Physica **1**, 192 (1931).
[28] S. Dushman and A. H. Young, Phys. Rev. **68**, 278 (1945).
[29] S. Wagener and C. B. Johnson, J. Sci. Instr. **28**, 278 (1951).
[30] S. Dushman, reference 13, p. 356.

filament or other metallic elements, the measurement of the sensitivity of the ion gauge becomes difficult. It is known that oil vapors used in diffusion pumps are decomposed by the cathode into various molecules of lower molecular weight, so that the gas density in the gauge is greater than that in the rest of the system. The ions of these molecules obviously contribute toward the observed positive ion current, and the magnitude of the additional current must depend on the rate at which the decomposition products are formed and removed. In most studies at low pressures, however, it is essential that the system be sealed off or otherwise isolated from major sources of contamination as a prerequisite for achieving pressures below 10^{-8} mm Hg. Any oil vapor remaining in the system will therefore be decomposed (ultimately to H_2, CO, CO_2 or various hydrocarbons) and removed quickly, the ion gauge reading itself being a reasonable measure of the removal rate. In other words, the accurate measurement of the pressures of chemically active gases is a problem in itself, but in general it is not often encountered in ultra high vacua.

From the foregoing considerations it may be seen that while the ionization gauge does suffer from a variation of sensitivity with the gas in question, reasonably accurate pressure determinations can be obtained if the composition of the gas mixture is known. In addition, since the sensitivity to many of the common gases is very close to that for nitrogen, pressure measurements on mixtures of unknown composition are sufficiently accurate in many experiments. In view of the extreme simplicity of the gauge and its associated electrical circuits, its wide usage is easily understood.

V. PUMPING ACTION OF THE IONIZATION GAUGE

The other disadvantage which has been ascribed to ionization gauges generally is that they act as pumps to remove gases from the enclosure. Since the gauge may indeed change the pressure in a system while it is measuring it, this action constitutes a difficulty which must be assessed carefully to appreciate the ultimate limitations which it imposes on the measurement of pressure.

In order to properly operate an ionization gauge and interpret its readings it is necessary to have a knowledge of the electrical and chemical pumping speeds for various gases. For a system in which pressure equilibrium has not been established, a knowledge of this pumping speed and the conductance of the leads makes possible a quantitative estimate of the over-all pressure distribution in the system. Although such considerations are of obvious importance in this field, relatively little experimental work has been carried out. The work of Schwarz[31] contains the most recent data in the literature; investigations now in progress at our laboratories have provided new data at lower pressures and with well outgassed surfaces.

When an ionization gauge is turned on, it may remove gases by either of two distinct types of clean-up, chemical and electrical. The former is due to chemical reactions which take place as a result of heating the cathode to normal operating temperatures (~2300°K). This action is quite independent of the second type of clean-up and occurs whether or not accelerating potentials are applied to the other electrodes. An example of this type of removal is found in the case of molecular hydrogen, which dissociates upon striking a tungsten filament running at a temperature above 1500°C. The resulting atomic hydrogen is extremely active chemically and is immediately removed from the enclosure upon striking the walls of the ionization gauge. Other active gases such as oxygen, chlorine, and certain hydrocarbon vapors may be removed in a similar manner.

Electrical clean-up of gases refers to the type of gas removal which takes place only when the accelerating potentials are applied to the electrodes of the ionization gauge. It has been shown by Schwarz[31] and others that the predominant removal mechanism is due to the entrapment of the collected ions. That is, the positive ions formed by electron impact are driven into the negatively charged surfaces of the gauge where they are neutralized and are trapped within the solid surface. That such a mechanism may be used for other purposes is indicated by the work of J. Koch,[32] who separated and stored isotopes of neon by using a mass spectrometer to drive the neon ions of different mass into separate metallic disks.

In the case of the ionization gauge, the ions formed may be collected not only at the ion collector but also at any other negatively charged surface. In particular, we have demonstrated that at normal operating voltages the glass walls of the ionization gauge assume a potential very close to that of the hot cathode, and it is thus possible to capture the ions at the glass envelope of the gauge. Schwarz has indicated[33] that glass acts even more efficiently than metals for this type of pumping.

The rate of pressure reduction by either electrical or chemical means should be proportional to the pressure in the enclosure itself. Hence, by analogy with the equation for the pumping speed of a conventional pump,[34] we may write for the rate of change of pressure p resulting from electrical clean-up

$$\frac{dp}{dt}=-\frac{S_E}{V}(p-U_E), \tag{1}$$

where

S_E is the electrical pumping speed of the ion gauge attributable to the ion pumping action (usually given in l/sec),

V is the volume of enclosure, and

U_E is the ultimate pressure attainable by electrical pumping.

[31] H. Schwarz, Z. Physik **122**, 437 (1944).

[32] J. Koch, Nature **161**, 566 (1948).

[33] H. Schwarz, Z. Physik **117**, 23 (1940).

[34] S. Dushman, reference 13, p. 128.

The solution of (1) is

$$p = U_E + (p_0 - U_E)\exp\left(-\frac{S_E}{V}t\right), \tag{2}$$

where p_0 is the initial pressure at $t=0$. We may write (2) in the form

$$p - U_E = (p_0 - U_E)\exp(-t/\tau_E), \tag{3}$$

where

$$\tau_E = V/S_E.$$

It is seen that τ_E is the pumping time required to reduce the pressure $(p-U_E)$ by a factor of $1/e$. The quantity τ_E is thus an important parameter in assessing the effect of the pumping action of the ionization gauge. It is clear that if the ion gauge is run for a time comparable to τ_E, the effect of the pumping action will be appreciable.

For the pumping due to chemical action, one may write expressions similar to (1) and (2) in which S_E, τ_E, and U_E are replaced by S_C, the effective pumping speed, τ_C, the characteristic pumping time, and U_C, the ultimate pressure due to chemical removal processes. Hence the total rate of pressure reduction is given by

$$\frac{dp}{dt} = -\frac{S_E}{V}(p - U_E) - \frac{S_C}{V}(p - U_C). \tag{4}$$

Few data are available for the case in which the pressure is comparable to the values U_E and U_C, and a discussion will not be presented here. For the case in which $p \gg U_E$ or U_C, Eq. (4) reduces to

$$\frac{dp}{dt} = -\frac{S}{V}p, \tag{5}$$

where S, the total pumping speed, is then equal to the sums of the individual speeds and the expression for the over-all characteristic time constant is

$$\frac{1}{\tau} = \frac{1}{\tau_E} + \frac{1}{\tau_C}. \tag{6}$$

A reasonable evaluation of the τ's is required in order to assess the importance of the pumping action of the ionization gauge.

For chemically inert gases we have $S_C = 0$ and proceed to evaluate S_E or τ_E on the assumption that the only removal process is that due to "ion pumping." We make the simplifying assumption that every ion collected is permanently removed from the volume. The electrical pumping speed obviously depends on the sensitivity of the gauge, i.e., the number of ions collected per electron emitted from the filament, and on the total current from filament to grid. Using a typical value of gauge sensitivity and an emission current of 10 milliamperes, one has an ion current of $10^{-(n+1)}$ ampere for a pressure of 10^{-n} mm Hg of nitrogen. This corresponds to a rate of removal of $6\times10^{18}\times10^{-(n+1)}$ molecules per second when the density is $3.2\times10^{19}\times10^{-n}$ molecule per liter.

If in Eq. (1) we assume $U_E \ll p$ and rewrite in terms of the molecular density we get

$$S_E = -\left(V\frac{dn}{dt}\right)\Big/ n = -\left(\frac{dN}{dt}\right)\Big/ n \tag{7}$$

where N, the total number of molecules in the enclosure, is equal to nV. The pumping speed, S_E, is thus given by the ratio of the total rate of removal to the molecular density. Substituting the quantities given above into Eq. (7) gives a value for S_E of 0.02 l/sec, or approximately one l/min. The corresponding τ_E for a volume of one liter is then about one minute. Note that the pumping speed is proportional to the electron emission current If the emission current is reduced to 10 microamperes the pumping speed is reduced to 2×10^{-5} l/sec, while τ_E is increased to 16 hours.

In the case of chemically active gases which are removed upon striking the hot cathode, one can also make an order of magnitude estimate for the pumping speed of the ion gauge. Again we make a simplifying assumption, this time that each molecule which strikes the hot cathode surface is immediately removed. The rate of removal is then obtained from the simple kinetic theory expression for the number of molecules ν striking unit area per unit time; $\nu = n\bar{v}/4$, where n is the molecular density and $\bar{v}$, the mean molecular velocity. The chemical pumping speed is given by

$$S_C = -\left(\frac{dN}{dt}\right)\Big/ n = \frac{n\bar{v}A}{4}\cdot\frac{1}{n} = \frac{\bar{v}A}{4} \tag{8}$$

where A is the cathode surface area. The mean velocity is, of course, a function of the gas in question and the temperature of the enclosure. For oxygen at room temperature $\bar{v} \cong 4\times10^4$ cm/sec. The surface area of the filament in the gauges is approximately 0.2 cm^2. Substituting into Eq. (8) we get for S_C a value of the order of a l/sec. The corresponding τ_C for a one liter volume is then approximately one second.

In order to compare the above estimates with experiments, it is first necessary to reduce the experimental data in such a way as to correspond to the electron current and volume which were somewhat arbitrarily chosen for the above calculations. If Schwarz's data is then replotted in the manner suggested by Eq. (3), it is possible to obtain from his results values for the characteristic pumping time τ. In the case of hydrogen, Schwarz demonstrated that clean-up was initiated as soon as the cathode was heated to operating temperatures and proceeded at a very rapid rate whether or not accelerating voltages were applied to the electrodes. While τ_C is somewhat difficult to estimate from his data, his measured value lay between one and two seconds, in good agreement with the above hypotheses.

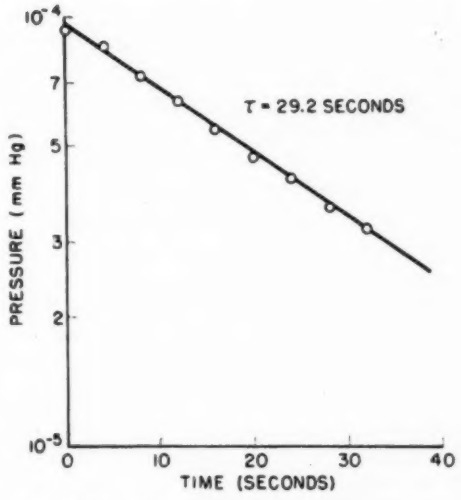

FIG. 3. Reduction in pressure caused by ionization gauge in nitrogen (after Schwarz).

For the case of nitrogen, which was removed only when accelerating voltages were applied, we show data taken by Schwarz in Fig. 3. The data has been normalized for a volume of one liter and an electron emission current of 10 ma. It is seen that the measured electrical pumping time is in order of magnitude agreement with our calculations. Preliminary data taken in this laboratory give a value of τ somewhat less than but comparable to that of Schwarz. The difference may be attributable to a number of sources, since τ is dependent on the geometrical design of the gauge, the degree of outgassing, and the sensitivity of the gauge. In most gauges, and in particular the Bayard-Alpert gauge, the ion collector receives only a fraction of the total number of ions created, the remainder being collected at other surfaces such as the glass walls of the gauge. Thus it is to be noted that in both experiments the pumping times correspond to a rate of removal in excess of one molecule removed per ion received at the collector. In view of the differences in the experimental arrangements and the degree of outgassing which was possible, it is not surprising that our results should differ somewhat from those of Schwarz. On the other hand, we may say that in both cases the results are consistent with the ion-pumping hypothesis for the removal of chemically inert gases.

These results clearly demonstrate that ion gauges may be used as very effective means for evacuating a system. The pumping speeds which have been measured, approximately a few liters per minute for inert gases and considerably greater values for active gases, make it possible to evaucate a well outgassed system in a short period of time.

The question arises, however, as to how much gas can be removed by these processes before saturation of the ion gauge surfaces takes place. We know that the magnitude of the pumping speed as well as the value of the ultimate residual pressure vary considerably with the ion gauge design and its previous history. Meyeren[35] showed that the total amount which could be taken up by ion pumping was of the order of a few monolayers of gas on the surface. For a conventional gauge operating at 10^{-4} mm Hg one would collect a monolayer (approximately 10^{15} molecules per cm^2) on the surface of a gauge in about one hour. Hence one might expect the pumping action to stop after about one hour at 10^{-4} mm Hg. This has been roughly verified in our laboratory, i.e., if the pressure is maintained at 10^{-4} mm Hg by the continuous introduction of additional gas, the gauge pumps for about an hour before showing strong saturation effects. At a pressure of 10^{-9} mm Hg, however, it would be expected that a gauge with a similar history would pump for about 10^8 seconds or three years. In our laboratory a vacuum system has been continuously maintained at such a pressure for 75 days by the pumping action of an ion gauge without any indication of saturation.

From the foregoing considerations of the pumping action of ion gauges, we may draw the following conclusions: (1) The ionization gauge may be used not only to measure pressures accurately but also to evacuate a system. (2) The characteristic pumping times (or pumping speeds) for common gases are known or can be easily measured. (3) If the gauge is to be used to read pressures without significantly altering them, one must either reduce the gauge pumping speed or operate the gauge for sufficiently short time intervals; in either case the time during which a reading is taken should be made small compared to the characteristic pumping time. (4) While much research remains to be done, a start has been made toward obtaining an understanding of the basic removal mechanisms which take place in an ionization gauge.

Careful measurements should be made with a wide variety of gases to learn the relative importance of the electrical and chemical processes for each gas. It would furthermore be desirable to investigate other possible mechanisms for gas removal which may take place. Finally it would be of great value to have better information concerning the rate at which the gauge is saturated by a given pumping mechanism.

VI. VACUUM VALVE

In addition to the need for new ways of measuring ultra high vacua, there has been the need for certain basic improvements in the techniques for producing high vacua. As has been stated, vacuums below 10^{-8} mm Hg had previously been attained. However, in most cases they were achieved in systems which were ultimately sealed off from the diffusion pumps.[36] In those few cases in which the tubes were not sealed off, very special treatment of the diffusion pumps was required; then careful precautions were required to isolate the system

[35] W. Meyeren, Z. Physik **84**, 531 (1933).
[36] S. Dushman, reference 13, p. 730, Sec. on "Production of Extremely Low Pressures in Sealed-off Devices."

from the pumps by refrigerated traps. A need has long been felt for a method of sealing the vacuum system from the diffusion pumps without the contamination and inconvenience involved in the usual seal-off of a glass constriction.

A similar need has been felt in the handling of very pure gases; for instance, in studying breakdown characteristics of noble gases. In such researches one requires not only the original evacuation of the system to ultra high vacuum conditions, but also the ability to transfer gases from one portion of the system to another without introducing large impurities. The use of ordinary greased stopcocks or mercury cutoffs for this purpose is out of the question; they may introduce impurities into a system which are orders of magnitude greater than the ultimate residual pressure attainable. Not only is the vapor pressure of the stopcock grease in many cases objectionable, but the amount of occluded noncondensible gas evolved with each rotation of a stopcock may be hundreds of times greater than the amount of residual gas in the system.

The vacuum valve[10] which has been developed in these laboratories permits the evacuation of manipulative vacuum systems to pressures as low as those previously attainable only in sealed-off enclosures. It is capable of high-temperature bakeout and has proved to be of great value in ultra high vacuum work.

As shown in the schematic diagram of Fig. 4a, the valve is designed in two sections. It consists of a separate valve assembly which becomes part of the vacuum system, and a driver mechanism which opens and closes the valve. Aside from the vacuum leads, the valve assembly contains only three machined parts: the copper cup, $1\frac{3}{4}$-in. diameter with $\frac{1}{4}$-in. diameter holes for the vacuum orifices, the flexible Kovar diaphragm which allows a movement (up and down) of about 0.1 in., and the Kovar nose which has a highly polished 45° conical[37] surface and seats in the copper cup. All of the joints in this assembly are brazed (eutectic silver-copper solder) simultaneously in a hydrogen furnace without the use of flux. When the valve assembly emerges from the furnace it is free from surface oxides and ready without any cleansing procedure to be incorporated into the vacuum system.

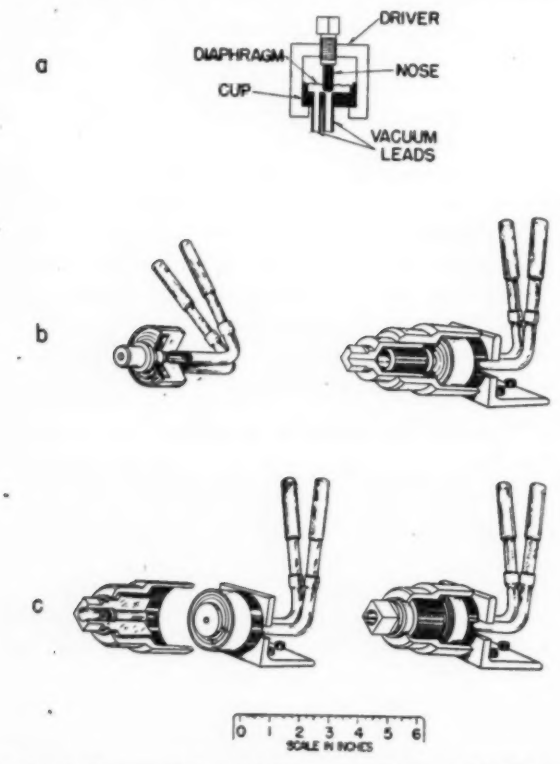

FIG. 4. Vacuum Valve. (a) Schematic diagram. (b) Valve with differential screw driving mechanism. (c) Valve with driver using simple screw.

In our design the driver mechanism and the valve assembly are separate. This makes it possible to bake the valve at high temperatures without also baking the driver threads and lubricant. Furthermore, in case of valve failure it is not necessary to discard the entire mechanism. In principle, almost any design of thrust mechanism would suffice, as suggested by the simple straddle clamp and screw in the schematic diagram of Fig. 4a. The important design considerations for most applications are: (1) a total thrust of one to two tons is required to close the valve to the desired conductance values, (2) the valve must be sufficiently well anchored to the base of the vacuum system so that the closing torque applied to the valve will not strain the glass of the system excessively, and (3) the valve should open and close gradually, especially for gas-handling systems.

Two designs for the driver mechanisms have been developed and successfully used in our vacuum work, one using a differential screw mechanism as shown in Fig. 4b, the other a simple screw thrust mechanism, Fig. 4c. The differential screw mechanism, though more costly, has a larger mechanical advantage and provides an excellent needle valve action. The differential driver mechanism consists of an outside screw and housing (stainless steel), a differential screw (silicon bronze) with a thread pitch of 20 per in. outside and 26 per in. inside, and a drive screw (stainless steel) which is bolted to the valve nose before the rest of the driver is installed. A backing plate (stainless steel) is provided to withstand the large forces exerted upon the copper body and to anchor the driving mechanism in place. It is threaded (26 threads per in.) so as to accommodate and rigidly fasten the outside housing to the valve assembly. The differential screw is machined with a $\frac{1}{2}$-inch square head to fit a socket or torque wrench, the latter being useful to measure the closing torque.

The vacuum valve for the simple screw mechanism (Fig. 4c) is identical to the one shown in Fig. 4b except for one detail: the external portion of the nose is

[37] This angle has proved to be more satisfactory than the 60° nose reported originally.

machined to form a flat disk one inch in diameter. The simple screw (32 threads per in.) exerts its thrust against this flat disk which forms the thrust bearing; it is well lubricated upon each installation with a mixture of bearing grease and molybdenum disulfide. A countersunk hole is bored through the main screw and fitted with a sleeve bearing which serves not only to align the screw with the valve nose, but also to retract the nose to open the valve. To disengage the driver from the valve, it is simply necessary to remove the (10-32) Allen-head screw from the sleeve bearing and then to unscrew the entire driver mechanism from the backing plate. The simple screw driver mechanism is smaller, less expensive, and easier to install and remove than the differential driver; yet its thrust for a given torque is comparable and it has relatively good needle valve action.

During bake-out periods, the driver mechanism for either type of valve is removed completely. It is then necessary to fasten a small "bake-out clamp" to hold the valve in its open position while the system is at high temperature. A bake-out clamp consists of a U-shaped stainless steel strap which is fastened to the nose with a single 10-32 screw and maintains it at a fixed position with respect to the copper cup.

The seat for the valve nose is formed not by machining but by forcing the highly polished Kovar nose into the $\frac{1}{4}$-in. orifice in the copper. That is, the seat is formed the first time the valve is closed. The conductance of the valve when open is comparable to that of a large greased stopcock with $\frac{1}{4}$-in. diameter tubulation. When closed, the conductance on some valves has been found to be as small as 10^{-11} l/sec or less. This leakage conductance, of course, is a function of the closing torque exerted on the valve driver; the torque generally chosen is about 20 to 30 lb-ft. The leakage conductance of a valve is easily determined by measuring the rate of pressure rise in a container of known volume on one side of the valve when a given higher gas pressure is introduced on the other. Consistent and reproducible results have been achieved with different valves closed to the same torque or with the same valve on successive closings. A comparison of two valves which had been in continuous use on a given system for over a year showed that with a closing torque of 20 lb-ft the conductances were 5×10^{-9} l/sec and 5.5×10^{-9} l/sec. While such excellent agreement may be fortuitous, it indicates that the valves are surprisingly similar in characteristics even after many months of service.

As the valves are used, the condition of the nose and valve seat deteriorates slightly and the leakage conductance becomes larger. The deterioration is due to a variety of causes such as the oxidation or scoring of the smooth metallic surfaces, work-hardening of the copper seat, or the collection of foreign particles at the valve seat. In view of these possibilities, the surprising thing is that the valves last as long as they do. After a year's time, the two valves mentioned above (which had begun with a conductance when closed of 10^{-11} l/sec) had conductance values of about 10^{-10} l/sec when closed with a torque of 20 lb-ft. This conductance is more than adequate for most experiments. For example, if a one-liter volume filled with gas were isolated from the evaucating pumps by a valve with a conductance of 10^{-10} l/sec, it would take several years for the pressure in the container to drop by one percent due to leakage through the valve.

The amount of gas given off upon each opening or closing is very small compared with the corresponding amount for a grease stopcock. The quantity of gas "squeezed" out upon closing a valve to 30 lb-ft is approximately 5×10^{-10} mm-l or less.

At the time of this writing, some 75 to 100 valves have been made and used with excellent results on twelve to fifteen vacuum systems. The pumping speed through the valves has proved quite adequate for system volumes of the order of a liter. If higher pumping speeds are desired it is a straightforward engineering problem to design a scaled-up version of the valve. The valves can be repeatedly baked out at temperatures above 400°C, and finally, they act as excellent needle valves for the controlled transfer of gas from one portion of a system to another.

VII. ABSOLUTE MANOMETER

In addition to the low pressure gauge and adequate vacuum (or gas-handling) valves, the conventional "all-purpose" vacuum system generally includes an absolute manometer which is used either for calibration or for the measurement of gas pressures higher than those which can be measured by an ionization gauge. The conventional instrument used for this purpose is the McLeod gauge or the liquid manometer containing mercury, low vapor-pressure oil, or both. While the liquid manometer has the advantage of being an absolute instrument of great simplicity, it presents at least two serious difficulties when used in experiments requiring very high gas purity: (1) it cannot be outgassed at high temperatures, and even when isolated by special traps it may act as a source of contamination; (2) if such isolating traps are used, it cannot measure the pressure of condensible vapors. Other manometers have been reported[38] in which the deflection of a calibrated metallic diaphragm is used as an indication of pressure. Such instruments are limited by their relatively small pressure range and by the fact that a high temperature bakeout (400°C–500°C) may destroy their calibration if not the instruments themselves.

The absolute manometer developed in these laboratories by Alpert, Matland, and McCoubrey[9] is a null-reading device which spans the pressure range above 10^{-1} mm Hg and does not suffer from the above difficulties.

This new manometer has been described in detail in

[38] V. H. Dibeler and F. Cordero, J. Research Natl. Bur. Standards **46**, 1 (1951).

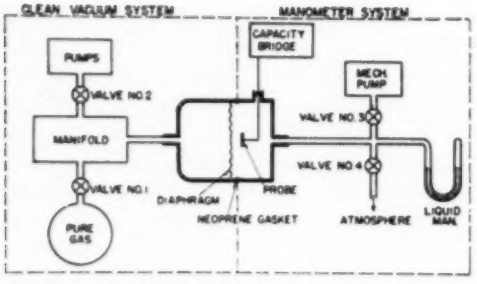

FIG. 5. Null-reading absolute manometer.

the above article, and we shall mention here only its principle of operation. It makes use of a liquid manometer for its absolute calibration but uses a metallic diaphragm as the pressure-sensitive element in contact with the pure gas system. The diaphragm (drawn from 0.005-in. Kovar sheet) separates the "ultra high vacuum" system from a system which includes an ordinary manometer as shown in Fig. 5. With the pressure on both sides of the diaphragm identical, e.g., with both systems evacuated, the diaphragm assumes an equilibrium position as indicated by its capacity to an electrical probe. When a sample of pure gas is introduced into the clean system, a comparable amount of air is let into the manometer system until the diaphragm reassumes its null position. The liquid manometer then directly reads the pure gas pressure.

The sensitivity of the manometer is limited by the null-reading device in two ways: (1) the deflection sensitivity and mechanical stability of the diaphragm itself, and (2) the ability of the electrical probe to detect the departures of the diaphragm from the null position. These two limiting considerations combine to give a maximum error in the reading of about 10^{-2} mm Hg; this is, of course, independent of the pressure and is comparable to the probable error in the reading of an oil manometer. The upper pressure limit of the gauge is determined by the type of direct-reading manometer used.

An interesting and very useful combination of instruments results from the use of the manometer together with a vacuum valve. If the manometer is attached to a system of volume V which is connected through a vacuum valve to a small valume v, the arrangement may be used to introduce measured quantities of gas at pressures far smaller than those which can be measured by the manometer alone. This is accomplished in the following manner: (1) With the valve open introduce into $V+v$ a gas pressure measurable on the manometer, say p_m. (2) Close the vacuum valve and exhaust volume V. (3) Expand the gas from v into $V+v$. The pressure in the system is now $[v/(V+v)]p_m$. If the volumes v and V are chosen judiciously, it is possible to introduce gas at any desired pressure below those which can be read on the manometer. In our systems we have adjusted v/V to be approximately 1/30. If the initial gas pressure were 1 mm Hg, a single expansion as described above would give a resulting pressure of approximately 0.03 mm Hg; if the expansion procedure were repeated the resulting pressure would be roughly 10^{-3} mm Hg; four such expansions would give 10^{-6} mm Hg. In this way very small measured quantities of gas or vapor may be introduced into a system without contamination. We thus have a method for making an absolute calibration of an ionization gauge for any gas or vapor at low pressures; it would be particularly useful for those active gases for which the calibration is very difficult[29] because they rapidly attack the hot cathode of the ionization gauge. This expansion method has proved to be of great value for the introduction of small quantities of known impurities into pure gas samples.

Only a few null-reading manometers of this type have thus far been built and used in this laboratory. Considerable improvements in the design are possible. A more sensitive diaphragm would allow more accurate readings. If the entire manometer including the capacitative probe could be made as a single unit the operation of the device would be simplified. These improvements are contemplated in a forthcoming design. On the other hand, the manometer in its present form has been successfully utilized in a number of experimental programs. To our knowledge, it is the only manometer in its range which can be outgassed at high temperatures; it requires no traps or refrigerants to separate it from the vacuum system manifold. The manometer effectively reads pressures extending above the range of the ionization gauge and the two types of gauges, when used together, cover the entire pressure range above 10^{-10} mm Hg.

VIII. PUMPS FOR ULTRA HIGH VACUA

Having described in some detail the special instruments which have been developed in our laboratory, we come to a question which is asked perhaps more often than any other by visitors to our laboratory: "By what pumping means do you attain such low pressures?" The answer is that while we use oil diffusion pumps almost exclusively, we do not rely on the diffusion pumps to evacuate below 10^{-8} mm Hg. The oil diffusion pumps are used during the bake-out period and continuously run thereafter, but it is not possible to lower the pressure further without auxiliary means. In our systems, the pumping action of the ionization gauge is used to reach pressures in the ultra-high vacuum range.

We have shown that at some pressure between 10^{-7} and 10^{-8} mm Hg the oil diffusion pump ceases to be a sink and becomes a source for contamination of a clean vacuum system. The experiment was carried out as follows: a simple vacuum system containing two ionization gauges and a vacuum valve was set up and connected as shown schematically in Fig. 6. One gauge was connected to the sealed-off system while the other was in direct contact with the diffusion pump. After careful bakeout of the entire system at 420°C the ion gauges were outgassed; then the valve was closed and both

gauges run continuously at normal operating conditions. Figure 6 shows the pressures as a function of time for the isolated part of the system (dashed line *A*) and for the portion in contact with the pump (solid curve *B*). Initially both systems came down to pressures in the ultra high vacuum range. After several hours however, the pressure adjacent to the diffusion pump began to rise and returned to the initial value of approximately 10^{-7} while the pressure in the isolated system remained at its lowest value for the duration of the experiment.

On the basis of the previous discussion of the ionization gauge pumping action, the above results can be readily interpreted as follows. At the outset of the experiment both ion gauges pumped so as to reduce the pressure in their respective volumes to a value in the ultra high vacuum range. This was achieved even in the case of the gauge in contact with the diffusion pump. After several hours, however, this gauge began to reach saturation since it had removed a considerable amount of oil vapor and associated pump products. During the next few days the pumping action steadily deteriorated until the system reached an equilibrium pressure of 10^{-7} mm Hg, characteristic of the diffusion pump. The ion gauge in the sealed-off portion of the system continued to pump during the 900 hours of the experiment.

From this experiment it is clear that the ionization gauge is capable of evacuating a system to values far below the equilibrium pressure which the diffusion pumps alone can reach. Furthermore if the system is completely isolated from the diffusion pumps, it is possible to maintain ultra high vacua indefinitely without the use of refrigerants or traps of any kind. It has thus become our practice to incorporate a vacuum valve in many of the sytems to isolate at will the vacuum manifold from the diffusion pump so as to remove any direct contact between them.

The diffusion pumps in these systems have thus been relegated to the tasks of "preliminary" pumping during the bakeout of the system and the routine checking for large leaks, though they are run continuously during an experiment. Hence it is not easy to differentiate between the effectiveness of various diffusion pump designs. Those most commonly used in our laboratory are two-stage glass oil diffusion pumps manufactured by Distillation Products, Incorporated. The oil most commonly used is Octoil-S. Little difference in the ultimate achievable vacuum has been observed either with three-stage glass or with various steel diffusion pumps. By relying on electrical pumping, it has been possible to reach pressures between 10^{-9} mm Hg and 10^{-10} mm Hg with any of the above diffusion pumps.

The procedure used by earlier specialists[36] to achieve very low pressures involved the use of mercury diffusion pumps which required a number of liquid air traps to prevent complete contamination by mercury vapor. The vacuum system, or that portion of it which could be heated, was prepared by prolonged bakeout at high temperatures. Then the manifold or evacuated section was completely sealed off from the pumps. In most cases the above workers used "getters" of various types to evacuate the manifold or tube after it was sealed off from the system.

The use of the various components which have been described in the present paper makes it possible to achieve ultra high vacuum in a manipulative system. We have eliminated the need for refrigerated traps at any stage in the evacuation procedure. Finally, we have not resorted to chemical "getters" to achieve pressures as low as 10^{-10} mm Hg. We have used standard Bayard-Alpert ionization gauges both as the means for measuring and as the pump for producing ultra high vacua.

IX. DESIGN AND OPERATION OF VACUUM SYSTEMS

We now proceed to the description of the actual vacuum systems in which we have incorporated the various components and procedures discussed in this paper. During the past several years a large number of systems have been built in our laboratories, and at the present time there are no less than eleven vacuum systems in operation, any one of which can attain vacuums in the range between 10^{-9} and 10^{-10} mm Hg. The engineering design principles have evolved over a substantial period of time and are the result of the combined efforts of a number of scientific workers. They are presented here in some detail because they have provided great flexibility, durability, and ease of construction and maintenance; they constitute a new approach to the design of vacuum systems in general, a field which has long been treated as an art rather than a science.

A fundamental requirement for achieving ultra high vacua is that the entire system be outgassed at high temperatures. This is generally done by designing the furnace (or furnaces) around the vacuum components.

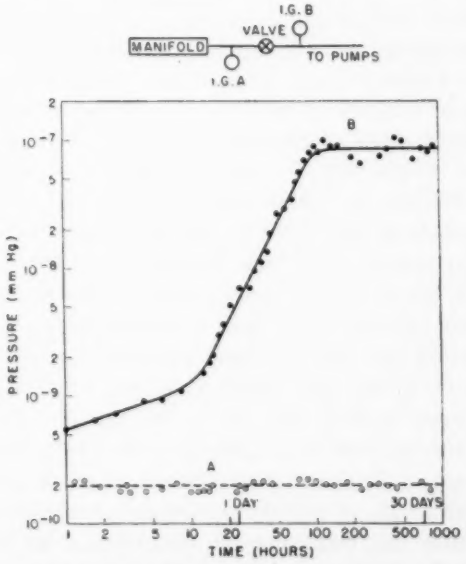

FIG. 6. A. Pressure *vs* time in sealed-off portion of system. B. Pressure *vs* time in ion guage in contact with diffusion pump.

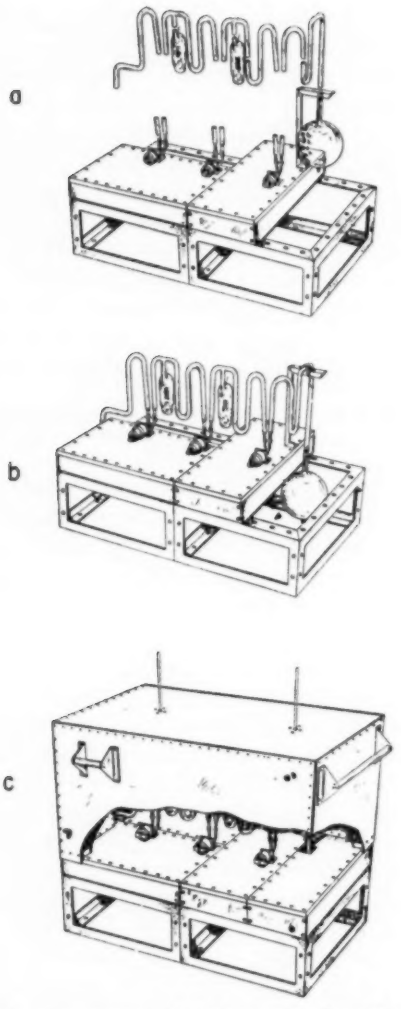

FIG. 7. Vacuum system. (a) Before assembly. (b) Assembly completed. (c) During bakeout.

We have adopted a new approach to this problem and have integrated the over-all design in such a manner that standard furnaces may be used for systems which vary widely in complexity and size. The systems are assembled on a series of module units, each sixteen inches square, which not only constitute the structure to which the vacuum components are fastened, but also act as the base of the enclosing bake-out oven (see Fig. 7). In most systems each base is made up of two sections or pads, one of which is bolted rigidly to the frame while the other remains movable so as to have added access to portions of the system. These base pads are aluminum boxes two inches deep, filled with glass wool insulation and covered with an asbestos board top ($\frac{1}{2}$-in. thick) to which the various components may be rigidly fastened. The furnaces for the vacuum systems are made in standard sizes which cover either one or two module units. It is possible (by removing the end from a furnace) to enclose three or more units simply by placing the furnaces end to end. Figures 7a, b, and c show a typical layout for a relatively complex system before assembly, and during bakeout with the furnace in place.

As exhibited in Fig. 8, a furnace is made up of two sheet-aluminum ($\frac{1}{16}$ in. thick) shells, one within the other, and spaced at the edges by two-inch wide strips of asbestos board. The intervening volume is filled with glass wool insulation. For a single module furnace, eight heaters[39] are used. To distribute the temperature uniformly, the heaters are clamped, four on either side, to stainless steel plates $\frac{1}{8}$ in. thick and a foot square. A double module furnace contains two such heater arrangements. The power required to outgas a system at 450°C is approximately one kilowatt per module. The furnaces are sufficiently light in weight to afford ease in handling. As a result, a given furnace may be moved about readily for use on different systems. The temperature is regulated by a Partlow Model MP-10 KL thermostatic control, installed on the vacuum system, which maintains the temperature to within a few degrees of the desired value.

Figure 7 shows the actual assembly of the vacuum manifold. Note that the metallic components such as the vacuum valves, manometer, etc., are first rigidly fastened to the base pads. The manifold itself is supported primarily by the vacuum leads from the valves or manometer; where necessary a small angle-iron clamping support is inserted. There are, of course, no grease joints in the entire system and the glass-to-metal joints are Kovar-to-glass seals with appropriate transition seals to the Pyrex manifold. It will be observed that loops or large bends are frequently introduced into the glass manifold; they act as expansion members to reduce the strain on the various joints and transition seals. The system is carefully laid out in advance so that the various manifold sections and bends can be prefabricated in the glass shop. For the final assembly in the laboratory almost every joint (see Fig. 7a) is a vertical seal in Pyrex glass. This work is usually completed by the glass-blower in less than a day.

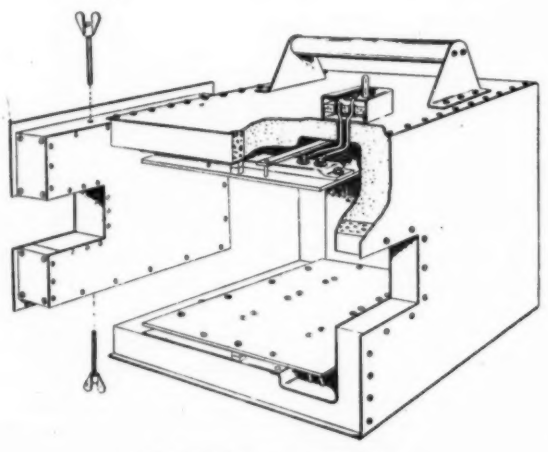

FIG. 8. Furnace construction.

[39] Chromalox strip heater elements No. SE 1225.

A typical vacuum system is shown in Fig. 9. This versatile system is used for general gas-filling purposes and is shown schematically in Fig. 10. With this system it is possible to achieve pressures of 10^{-9} mm Hg or better and to introduce known quantities of pure gas or vapors ranging in pressure from atmospheric down to 10^{-4} mm Hg. Most of the components which have been described in this paper are incorporated into the system; the associated controls are typical of those in use in our laboratory. A number of features are included which will not be dealt with in detail. For example, the furnace power supply contains an automatic timer so that the system may be baked out for a predetermined interval. In practice, the systems are usually baked over night; the power is automatically turned off at about 5 A.M. and the furnace slowly cools and is ready for removal by 8 A.M. A special interlocking control circuit, which includes a thermocouple gauge, is provided for turning off the diffusion pumps and other equipment in case a leak develops in the system. The diffusion and mechanical pumps are mounted beneath the vacuum bench, the latter being enclosed in an acoustically treated housing.

It can be seen that the system design is very flexible. If it is desired to enlarge or expand a system, it is only necessary to bolt down an additional module frame and make a single joint connecting the new portion into the existing system. Since the isolation valve is a feature common to many of the systems, it is possible to break a single connection and dismantle the system or repair it without losing vacuum in the pumps. Perhaps the most graphic demonstration of the relative ease with which ultra high vacua may be achieved with these methods is the rapidity with which a system can be brought into operation. In a number of instances a system has been installed by the glass-blower during the course of a morning, checked for large leaks during the afternoon, and baked out overnight; by the following noon, the system had attained a pressure in the 10^{-10} mm range.

After the assembly of the vacuum system is completed, the procedure for obtaining ultra high vacua is

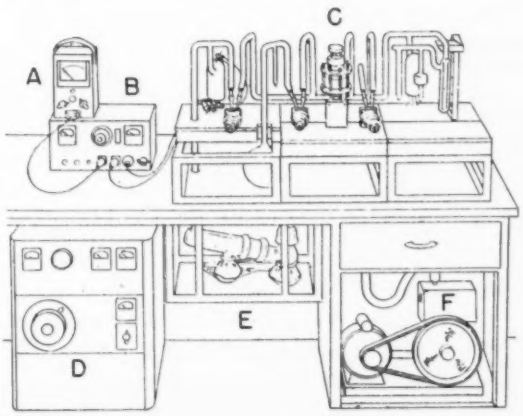

FIG. 9. Gas-handling system. This is a line tracing of a photograph of the system.

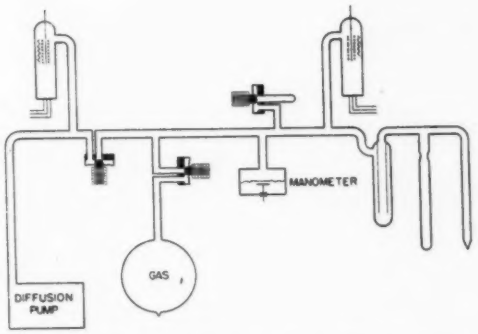

FIG. 10. Schematic diagram of gas-filling system.

quite straightforward. It may be summarized in the following steps: (1) Start mechanical and diffusion pumps and check for large leaks with thermocouple and ionization gauge. (2) Set up furnace and outgas system at a temperature between 400°C and 500°C for several hours. (3) Remove furnace; outgas elements of ionization gauge at elevated temperatures (above 1200°C). (4) Close isolating valve. (5) Check for small leaks. (6) Operate ionization gauge continuously to evaucate down to 10^{-10} mm Hg.

In step one, the only leaks which are checked carefully are those giving an initial equilibrium pressure greater than 10^{-5} mm Hg. For a system which has not been baked out, it is significant that the equilibrium pressure due to adsorbed gases is of the above magnitude even in the absence of leaks. Hence, we do not make an effort to detect the smaller leaks at this time. After having reached a pressure of the order of 10^{-5} mm Hg, the furnaces are turned on. We have not accurately specified the bake-out time for the reason that it depends strongly on the previous history of the system. Under some conditions, vacuums below 10^{-9} mm Hg have been attained after a bakeout of only two hours. As a general rule, however, we have adopted the practice of keeping the system at high temperature for six to eight hours.

When the bakeout has been completed and the furnaces removed, the valve drivers are set in place, the manometer probe cup is installed, and the ionization gauge is adjusted for outgassing. To outgas the gauge, the ion collector and grid are tied together and heated by electron bombardment from the cathode. This may be done by applying about 750 v ac or dc between filament and grid and adjusting the bombarding current by controlling the temperature of the filament. About 70 w is required to raise the grid and ion collector to a temperature of 1200°C. The bombardment current varies with the condition of the surfaces and the state of vacuum; it is necessary to limit the total outgassing power to prevent the formation of an active discharge or the overheating of the electrodes. An hour or more is required to outgas the ionization gauge completely, the interval depending again on the initial condition of the gauge.

Upon completing this process, the isolating valve is

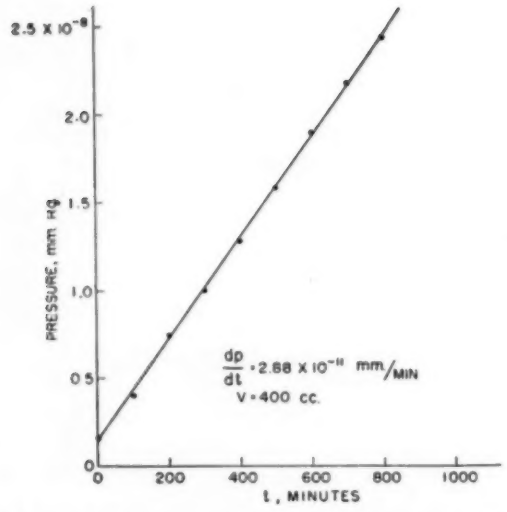

FIG. 11. Rate of pressure rise in a typical vacuum system.

closed[40] and the ionization gauge is adjusted to run at normal operating conditions. For normal operation the grid is 100 to 150 v positive, the ion collector 30 v negative, with respect to the cathode. In the absence of leaks, the system reaches a pressure of 10^{-9} mm Hg to 10^{-10} mm Hg in less than an hour.

X. DETECTION OF LEAKS

It might seem that the problems of eliminating the leaks in a system which is to attain a vacuum 10^2 to 10^3 times better than the conventional 10^{-7} mm Hg might be thousands of times more difficult. However, with the ability to achieve and to measure the lower pressures comes also the ability to detect leaks which are proportionately smaller. Just as a leak resulting in an equilibrium pressure of 10^{-4} mm Hg is easy to find on a system whose "standard" vacuum is 10^{-7} mm Hg, so a leak resulting in an equilibrium pressure of 10^{-7} mm Hg is simple to find on a system for which the "standard" vacuum is 10^{-10} mm Hg. In contrast, the location of leaks in the 10^{-7} to 10^{-8} mm Hg range in a *conventional* system runs into difficulties aside from the low pressure limitation of the conventional ionization gauge. The leaks in such systems are camouflaged because the equilibrium vapor pressure of the hydrocarbons[41] from the diffusion pumps are of this order.

In the ultra high vacuum range, we have relied mostly on standard methods of leak-detection. However, the new and extremely sensitive instruments for measuring pressure increase the effectiveness of these methods remarkably. For example, the application of acetone, ether, or carbon tetrachloride to the leak in a system operating at an equilibrium pressure of 5×10^{-9} mm Hg may either send the current reading flying off-scale to an equivalent pressure above 10^{-8} mm Hg, or it may temporarily clog the leak and reduce the pressure to 10^{-9} mm or less. A leak of this size would be undetectable on a conventional system. As a matter of fact, we have readily located leaks of this magnitude which could not be detected by a helium leak-detector even after the location of the leak had been determined by ion gauge indication.

Another standard technique for ascertaining the presence of leaks is a "shut-off" test. In this procedure, the vacuum system is isolated from the diffusion pumps and the rate of pressure rise on a continuously run ion gauge is a measure of the tightness of the system. At ultra high vacuum, our previous discussion revealed that the pressure as read on a continuously run ion gauge decreases when the system is sealed from the pumps, otherwise an appreciable leak is present. Obviously, to get a meaningful rate of rise, it is necessary not only to isolate the diffusion pumps from the system but to shut off the ion gauge pumping as well;[42] when this is done, the rate of rise in the vacuum system is a very sensitive and quickly measured criterion for the state of vacuum in the system. A rate of rise is measured by taking intermittent readings on the ionization gauge; that is, readings are taken at intervals of minutes, while the duration of a given reading is a few seconds. A typical rate of rise curve for a "tight" system is shown in Fig. 11.

Measurement of the rate of rise in pressure is particularly useful in distinguishing a system with a true external leak from a so-called virtual leak, i.e., a high pressure reading caused by adsorbed gases within the system. In the latter case, the ultimate equilibrium pressure is determined primarily by the equivalent vapor pressure of the volatile constituents adsorbed, and a rate of rise measurement usually indicates a constant high pressure value. When a true leak is present, the *rate of rise* is constant over a long period of time and depends on the size of the hole. In principle, it is possible with this method to detect the presence of a hole in our systems with a conductance of 10^{-16} l/sec, a value thousands of times smaller than is detectable by a helium leak detector when used in the conventional way.

It is of interest to ask: What is the smallest rate of rise which has been observed with a "tight" vacuum system? It has been found for a number of systems that after all observable leaks have been eliminated and the systems outgassed repeatedly, there remains a "residual" rate of rise of pressure. While this residual rate of rise varies somewhat with the size and geometry of the system, its value has been determined for an average system to be of the order of 3×10^{-11} mm Hg per minute.

[40] In systems which do not contain isolating valves, it is still possible to achieve ultra high vacua as indicated by the experiment shown in Fig. 7; however, this experiment also demonstrates the eventual return to higher pressures.

[41] Appreciable hydrocarbon vapor pressures have been found even on systems using mercury diffusion pumps. See J. Blears, J. Sci. Instr., Supplement 1 (1951).

[42] See Sec. V.

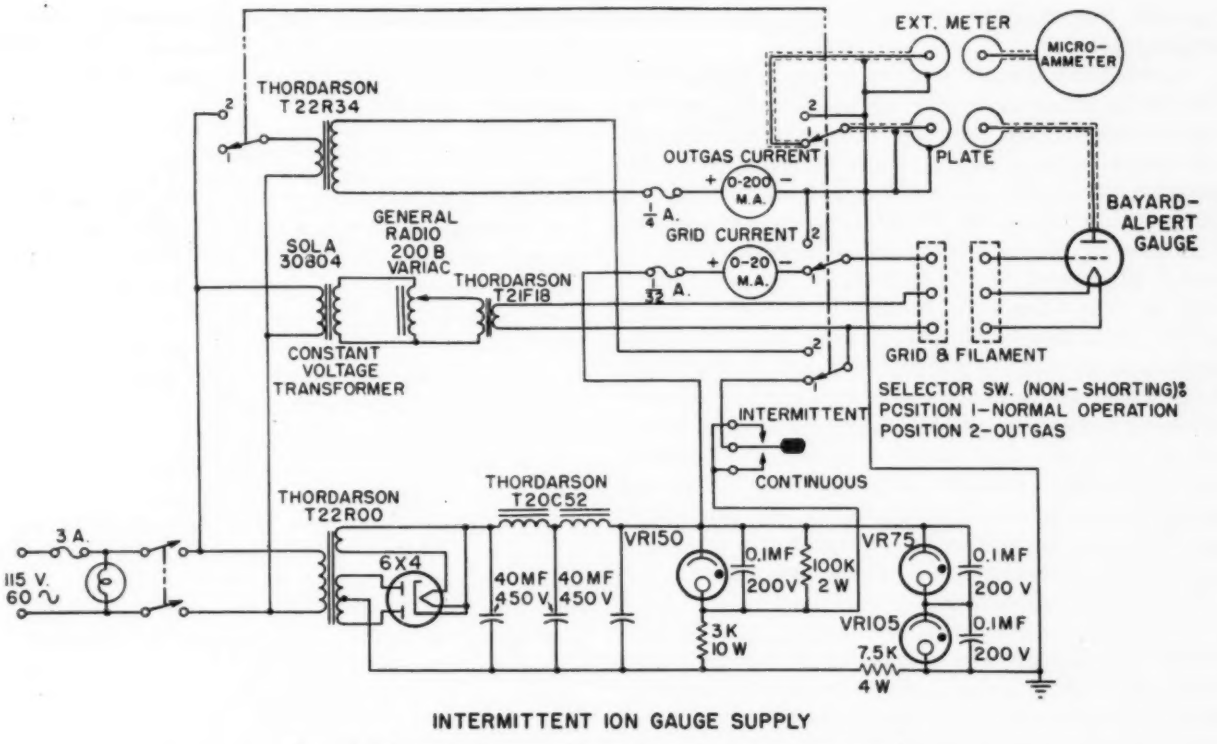

FIG. 12. Schematic diagram of intermittent ion guage power supply.

This corresponds to a rate of rise of a micron per century.[43]

The leak-hunting methods described have proved to be very effective in ultra high vacuum technique. The criteria for leak-free operation have been more rigidly established, and the means for localizing and detecting leaks are considerably more sensitive than have ever been possible on conventional systems. By adhering rigorously to the procedures outlined above, we have found it simpler to set an ultra high vacuum system into operation than was previously possible for conventional systems and to attain pressures orders of magnitude lower.

XI. ION GAUGE POWER SUPPLY

The Bayard-Alpert gauge[44] may be operated with standard ion gauge power supplies since the sensitivity and operating voltages are comparable to those for conventional ion gauges. However, many modern control circuits are so designed as to automatically control the electron emission from the filament at a specified value. It is not convenient, therefore, to use them in such a way as to limit the pumping action of the ion gauge to a very small value. For proper use of an ion gauge, intermittent operation should be provided for the electron accelerating potential or the filament heater voltage or both. It should also be possible to vary the electron emission current over a wide range of values. Finally, the supply should provide adequate power to outgas all the electrodes to high temperatures. A control circuit which meets all of these requirements as well as the automatic regulation of the electron emission is rather complex; a new design has recently been developed by P. R. Malmberg and A. O. McCoubrey, of this laboratory, and will be described in a forthcoming publication. A simple electronic circuit, which meets all of the above requirements except the electronic regulation of the emission current, has been widely used in our laboratory for several years. It is particularly suited for use with the Bayard-Alpert ion gauge.

As shown in the schematic diagram, Fig. 12, it consists of a regulated source of ion gauge electrode potentials and filament power as well as a source of outgassing power. Regulation of the electrode potentials is obtained through the use of voltage regulator tubes. In our laboratory, the filament power is regulated by the use of an external source of regulated 110 v ac. It is suggested that in the absence of such a source, it is possible to use a constant-voltage transformer as shown in the diagram. In normal operation, the ion collector is held at ground potential, the grid at 180 v positive, and the filament at 30 v positive with respect to the collector or ground. The filament temperature and the corresponding electron emission are adjusted by means of a

[43] This rate of rise has since been shown in our laboratory to be due to the diffusion of atmospheric helium (present in the atmosphere to a few parts in a million) through the glass walls of the vacuum system. A description of this work will appear in a forthcoming publication.

[44] These ionization gauges are now available commercially as Westinghouse tube type WL-5966.

variable autotransformer which feeds the filament transformer.

Intermittent operation of the gauge is obtained by keying the potential (+30 v) of the filament. The intermittent-continuous switch is a three-position center-off switch with a spring return in the intermittent position. Thus the ion gauge operates normally in either of the outer two switch positions, in one case continuously, in the other for short intervals while the switch is manually held in place. In the center or off position, the filament is floating with respect to the other electrodes and quickly assumes a potential slightly more positive than the grid. It is important to key the filament potential rather than that of the grid; by doing so large transients in collector current caused by rapid change in the potential of a nearby electrode are avoided. This provides the intermittent application of the electron accelerating potential, while maintaining the filament at its operating temperature. It is also easy to turn the filament on or off intermittently by controlling the filament power accordingly.

To outgas the ion gauge, the grid and collector are raised to appropriate temperatures by electron bombardment, 750 v ac being applied between the electrodes and the filament. In the "outgas" position, the normal-outgas switch energizes the outgas transformer primary connects the filament to the "hot" side of secondary and connects the grid and collector to ground. Separate meters are provided to read the grid currents for the normal and outgassing operations. An average rectified current of 100 milliamperes at 750 v heats the grid and collector to approximately 1200°C.

The control circuit does not include an internal means for reading the ion current to the collector. We have used a number of different external meters including a vibrating-reed electrometer for the measurement of very small currents. A very convenient and commercially available meter is the RCA Ultrasensitive Microammeter WV-84A, which provides full-scale currents down to 10^{-8} ampere with a corresponding smallest division reading of 2×10^{-10} ampere. This meter can easily be adapted to read currents down to 2×10^{-11} ampere (10^{-9} ampere full scale); this is accomplished by adding a 500-megohm input resistor on an extra switch position. A coaxial connector should be substituted for the input terminals to provide the additional shielding required for this range. With these changes, it is possible to use the instrument to read ion gauge pressures as low as 2×10^{-10} mm Hg.

XII. CONCLUSIONS

A new technology is now available for the production and measurement of pressures in the ultra high vacuum range. The new techniques have important applications in the fields of gaseous electronics and physical electronics, and a number of new experiments in these fields have already been carried out. It is also possible to make improved quantitative measurements of the diffusion of gases through solids and in the fields of surface chemistry and physics.

This paper has described the means for and the problems encountered in the production and measurement of ultra high vacuum. There are many questions still to be answered concerning the physical processes which are involved and the limitations of the instruments which have been used. The lowest total (equivalent nitrogen) pressure which we have thus far obtained is approximately 3×10^{-11} mm Hg; the partial pressure of the adsorbable gases in such a system has been estimated to be less than 10^{-13} mm Hg. The determination of the limiting factors which prevent the attainment of even lower pressures is an objective of current research programs at these laboratories. The new vacuum techinques are extremely valuable for further researches in this field. For example, studies of the diffusion of helium through glass have been carried out using these techniques, and the results are being readied for publication.

ACKNOWLEDGMENTS

It is a pleasure to acknowledge the help of many colleagues at the Westinghouse Research Laboratories for their consultation, advice, and suggestions in the course of this work. Almost all the members of the Physics Department have made contributions to the development of the techniques presented here. The author is particularly indebted to R. S. Buritz and C. G. Matland for their help in carrying out the researches described and in the preparation of the manuscript.

Convection Currents in Porous Media. V. Variational Form of the Theory*

F. T. ROGERS, JR.
U. S. Naval Ordnance Test Station, Inyokern, California †
(Received January 5, 1953)

A theory for the mean thermal gradient at the onset of convective flow of a fluid in a porous medium and heated from below, is given in variational form. Thermal equilibrium is not assumed, nor is viscosity assumed to be constant. An approximate solution is given for the theory, and is shown to agree quite well with published data. No attempt is made to maintain complete mathematical rigor in the derivations.

INTRODUCTION

THE problem of determining the conditions under which convection begins in a liquid in a porous medium heated from below was first posed in connection with the migration of NaCl through underground strata[1] and with other related geophysical problems.[2] More recently it has been encountered in connection with the operation of chemical catalytic reactors, as a phenomenon to be considered in heat transfer and in mechanical transport of liquids. It is now known to be valuable in the study of fluid dynamics in porous media *per se*[3] and of liquid boundary layers, especially those in which viscosity is strongly temperature-dependent.[4]

Only a relatively small body of experimental data has been published, largely by H. L. Morrison and colleagues.[5–9] These data represent negative mean thermal vertical gradients ($\beta_e>0$) at the onset of convective flow in various liquids entrapped in various unconsolidated porous media, and were taken with nonequilibrium temperature distributions representable by the empirical equation,[7]

$$T\cong-\beta_e D(1-e^{-z/\tau})/(1-e^{-D/\tau}), \tag{1}$$

where z is vertical Cartesian coordinate, D is depth (or thickness of layer) of liquid in porous medium, and τ is a characteristic distance associable with the nonequilibrium thermal state. They make reference to the temperature dependence of viscosity through the quantity

$$\nu=-(1/T)\ln(\mu/\mu_0), \tag{2}$$

supposed constant for a given liquid; here μ_0 is viscosity at $z=0$ where $T=0$. A further bit of pertinent data has been published,[10] concerning observed patterns of flow.

Efforts to calculate β_e from theory have not been uniformly successful. The case of $\nu=0$ and $\varphi=D/\tau=0$, i.e., for constant viscosity and for a thermal environment linear in z, has been satisfactorily solved[1,2] after the method of Rayleigh.[11] But the more general case, which is also the one encountered in many applications, for which $\nu\neq0$ and $\varphi\neq0$, has not been so done. A first attempt[6] at its solution merely succeeded in showing that a theory for β_e could be worked out and could be given quantitative significance. A second attempt led to the calculation[9] of a formula for β_e at ν, $\varphi\neq0$, which agrees rather well with the above-mentioned data, but not so well as could be desired. In none of these instances has consideration been given to the recent flow-pattern observations.[10]

In this paper we discuss a reformulation of the theoretical problem, which takes into account the observed patterns of "quasi-columnar" flow. Then we seek a method of solution (though not in ultimate detail) based upon the calculus of variations, in order to eliminate one (as yet) unjustified mathematical assumption in the previous[9] solution. Finally, we compare an approximate solution with the totality of published experimental data, which are founded upon visual techniques for determining β_e.

REFORMULATION

The formulation of basic differential equations is outlined in reference 10 and does not need to be repeated here.[12] For quasi-columnar flow, the equations of motion and of continuity yield (to the first order of small terms)

$$\frac{d}{dz}\left(\mu\frac{dw}{dz}\right)-E^2\mu w+E^2kg\rho_0\alpha\theta=0. \tag{3}$$

Here w is the z component of (small) fluid velocity (v), k is flow-permeability[13] of porous medium, g is acceler-

* Preliminary accounts of this work have been presented before the 310th and 316th meetings of the American Physical Society; see Bull. Am. Phys. Soc. **26**, No. 8, 23 (1951) and **27**, No. 8 (1952) (to be published).

† Post Office address: Michelson Laboratory, China Lake, California.

[1] C. W. Horton and F. T. Rogers, Jr., J. Appl. Phys. **16**, 376 (1945).

[2] E. R. Lapwood, Proc. Cambridge Phil. Soc. **44**, 508 (1948).

[3] See Wilson, Sibbitt, and Jakob, J. Appl. Phys. **22**, 1027 (1951), on gas flow in porous media.

[4] See M. Summerfield, J. Am. Rocket Soc. **20**, 85 (1950).

[5] Morrison, Rogers, and Horton, J. Appl. Phys. **20**, 1027 (1949).

[6] F. T. Rogers and H. L. Morrison, J. Appl. Phys. **21**, 1177 (1950).

[7] F. T. Rogers and L. E. Schilberg, J. Appl. Phys. **22**, 233 (1951).

[8] F. T. Rogers and L. E. Schilberg, Nucleonics **9**, 47 (1951).

[9] Rogers, Schilberg, and Morrison, J. Appl. Phys. **22**, 1476 (1951).

[10] H. L. Morrison and F. T. Rogers, Jr., J. Appl. Phys. **23**, 1058 (1952).

[11] Lord Rayleigh, Phil. Mag. **32**, 529 (1916).

[12] The method of reference 10 is essentially that of reference 1. Reference 2 shows how the Navier-Stokes equations for viscous flow, can be made to yield the same results.

[13] Attention is called to the different usages respecting flow-permeability, as between references 1 and 2. See also P. Ya. Polubarinova-Kochina and S. B. Falkovich in *Advances in Applied*

ation of gravity, ρ_0 is density of fluid at $z=0$, α is coefficient of cubical expansion of fluid relative to porous medium, and θ is the (small) amount by which temperature is altered by virtue of v. Reference 10 suggests

$$E\sim 2\pi/a_0 W, \tag{4}$$

where a_0 is the first zero of J_0 and W is an "effective diameter" of quasi-columnar flow "cells." On the other hand, the equation for heat conduction yields (to the first order),

$$\frac{d^2\theta}{dz^2}-E^2\theta-\frac{dT}{dz}\frac{w}{h^2}=0, \tag{5}$$

where h^2 is thermal diffusivity of fluid and porous medium *in situ*.

These same Eqs. (3) and (5), with E^2 replaced by A, are obtained for "cellular" flow patterns, according to reference 9. There $A\sim\pi^2/D^2$.

Equations (3) and (5) can be put into a more convenient form by the changes of dependent variables,

$$\left.\begin{aligned}\psi_1&=(\mu_0/kg\rho_0\alpha E^2)^{\frac{1}{2}}w\\ \psi_2&=[h^2(1-e^{-\varphi})/\beta_e\varphi]^{\frac{1}{2}}\theta/[f_s(z)]^{\frac{1}{2}},\end{aligned}\right\} \tag{6}$$

where $f_s(z)$ is a multiple-step function approximating $e^{-z/2\tau}$; these changes are particularly and specifically tailored to Eq. (1). Except, then, at a finite number of isolated points associated with the multiple steps of f_s, the following equations hold:

$$\left.\begin{aligned}\frac{d}{dz}\left[F(z)\frac{d\psi_1}{dz}\right]-E^2F(z)\psi_1+qf_s(z)\psi_2=0\\ \frac{d^2\psi_2}{dz}-E^2\psi_2+qf_s(z)\psi_1=0\end{aligned}\right\}. \tag{7}$$

Here $F(z)=\exp[-\nu T(z)]$ from Eq. (2); a factor $e^{-z/2\tau}\div f_s(z)$ in the latter equation is replaced by $f_s(z)$; and

$$q=[kg\rho_0\alpha E^2\beta_e\varphi/\mu_0 h^2(1-e^{-\varphi})]^{\frac{1}{2}}.$$

In terms of the useful quantity $B=2\pi^2h^2\mu_0/kg\rho_0\alpha D^2$,

$$q^2=(2\pi^2E^2/D^2)[\varphi/(1-e^{-\varphi})](\beta_e/B). \tag{8}$$

Equations (7) are thus approximations to Eqs. (3) and (5), involving Eq. (1), of such a type that continuous solutions of them are approximate to corresponding solutions of Eqs. (3) and (5); the use of $f_s(z)$ obviously introduces errors of approximation into the theory, but it is difficult to see that they are worse than the very minor ones which would be introduced by use of f_s in the potential-energy function,

$$\Omega=p+g\rho_0 z-g\rho_0\alpha\int T\partial z.$$

Mechanics, II, edited by R. von Mises and T. von Karman (Academic Press, New York, 1951), pp. 154–217.

Following the practice of reference 1, we use the boundary conditions,

$$\left.\begin{aligned}\psi_1(0)=\psi_2(0)=0\\ \psi_1(D)=\psi_2(D)=0\end{aligned}\right\}\psi_1,\psi_2\not\equiv 0 \text{ in } (0, D). \tag{9}$$

Inasmuch as present experimental practices are directed toward measurement of β_e and not of $w(z)$ or $\theta(z)$, we propose to solve Eqs. (7) and (9) as directly as possible for β_e or for some measure of it. Considering that Eqs. (7) are in self-adjoint form and that imposition of Eqs. (9) identifies a characteristic-value problem, we seek primarily for the least eigenvalue of β_e and maintain only such secondary interest in eigenfunctions for ψ_1 and ψ_2 as may be necessary. Consider the quantity

$$\int_0^D k dz=\int_0^D\left\{F(z)\left(\frac{d\psi_1}{dz}\right)^2+\left(\frac{d\psi_2}{dz}\right)^2 +E^2[F(z)\psi_1^2+\psi_2^2]-2qf_s(z)\psi_1\psi_2\right\}dz, \tag{10}$$

from the domain of integration of which are excluded the isolated values of z corresponding to the steps in $f_s(z)$. By direct differentiation it can readily be shown that $d[(\partial k/\partial\psi_1')]/dz-\partial k/\partial\psi_1=0$ and $d[(\partial k/\partial\psi_2')]/dz-\partial k/\partial\psi_2=0$ for all values of z except those excluded above. Consequently, solutions of Eqs. (7) and (9) confer upon $\int_0^D k dz$ a stationary value with respect to "weak" variations, by the Euler-LaGrange principle.

The stationary value of $\int_0^D k dz$ for eigenfunctions ψ_1 and ψ_2 can be evaluated directly by standard means. Integration by parts and the application of Eqs. (9) yields

$$\left.\begin{aligned}\int_0^D F(z)\left(\frac{d\psi_1}{dz}\right)^2dz=-\int_0^D\psi_1\frac{d}{dz}\left[F(z)\frac{d\psi_1}{dz}\right]dz,\\ \int_0^D\left(\frac{d\psi_2}{dz}\right)^2dz=-\int_0^D\psi_2\frac{d^2\psi_2}{dz^2}dz,\end{aligned}\right\}$$

and since

$$\left.\begin{aligned}\frac{d}{dz}\left[F(z)\frac{d\psi_1}{dz}\right]=E^2F(z)\psi_1-qf_s(z)\psi_2\\ \frac{d^2\psi_2}{dz^2}=E^2\psi_2-qf_s(z)\psi_1\end{aligned}\right\}$$

from Eqs. (7), direct substitution yields

$$\int_0^D k dz=\int_0^D\{-E^2F(z)\psi_1^2+qf_s(z)\psi_1\psi_2 -E^2\psi_2^2+qf_s(z)\psi_1\psi_2+E^2[F(z)\psi_1^2+\psi_2^2] -2qf_s(z)\psi_1\psi_2\}dz=0.$$

Inasmuch as only a finite munber of isolated values of z are discarded from the domain $[0, D]$ of integration, we may consider that the integral over-all values of z,

$$\int_0^D \left\{ F(z)\left(\frac{d\psi_1}{dz}\right)^2+\left(\frac{d\psi_2}{dz}\right)^2 + E^2[F(z)\psi_1^2+\psi_2^2]-2qf_s(z)\psi_1\psi_2 \right\} dz=0, \quad (11)$$

determine β_c, provided that for this purpose $f_s(z)$ in Eq. (11) is replaced by $e^{-\frac{1}{2}z/\tau}$.

The present reformulation of the problem is embodied in Eq. (11). In what follows we devote as little attention as possible to ψ_1 and ψ_2, *per se*, partly for the reason given above and partly because the precision of published data is not considered adequate to warrant detailed calculations of ψ_1 and ψ_2.

SOLUTIONS

For the case $\nu=0$ and $\varphi=0$, $F=1$ and $f_s=1$; hence eigenfunctions of Eqs. (7) and (9) are $\psi_1=c_1 \sin sz$ and $\psi_2=c_2 \sin sz$, where s is an integral multiple of π/D. Put into Eq. (11), they yield

$$(s^2+E^2)(c_1^2+c_2^2)-2qc_1c_2=0.$$

From the former of Eqs. (7), $c_1=[q/(s^2+E^2)]c_2$, so that $q=s^2+E^2$; using $s=0$, and reducing by Eqs. (4) and (8), we find

$$\beta_c=\frac{4\pi^2\mu_0 h^2}{kg\rho_0\alpha D^2}\cdot\frac{D^2}{a_0W^2}, \quad (12)$$

which result has already been reported.[10] The same result is had if c_1 and c_2 are related through the latter of Eqs. (7) rather than through the former. It may also be had from Eqs. (7) and (9) alone, quite independently of Eq. (11), through the consistency relations for the requirement that c_1 and c_2 not vanish; this is the basis of the methods used heretofore[1,2,7,10] for calculations of β_c.

The insensitivity of Eq. (11) to precise details of ψ_1 and ψ_2, when used to calculate β_c, and in comparison with the precision of published data, is illustrated by the following example for $\nu=0$ and $\varphi=0$. If ψ_1 and ψ_2, not satisfying Eqs. (9), are used in Eq. (11), as $\psi_1=c_3$ and $\psi_2=c_4$, where $c_3=(q/E^2)c_4$ by the former of Eqs. (7), then Eq. (12) results again. This is, to be sure, an example of extreme insensitivity; others for ν or $\varphi\neq 0$ suggest that the use of constants for ψ_1 and ψ_2 generally does not alter β_c by anything like as much as an order of magnitude. This same general insensitivity of β_c to boundary conditions has long been known[14] for the analogous phenomenon of convection where no porous medium is present; Jeffreys, using quite different boundary conditions than did Rayleigh,[11] obtained[15–17] relations which were within a factor of 3 the same as Rayleigh's.

For the more general case in which $\nu\neq 0$ and $\varphi\neq 0$; we shall in consequence use $\psi_1=c_5$ and $\psi_2=c_6$ in computing β_c. From the former of Eqs. (7), we take

$$E^2F_{Nu}c_5=qf_{Nu}c_6. \quad (13)$$

From Eq. (11) we extract

$$E^2c_5^2F_{Nu}+E^2c_6^2-2qc_5c_6f_{Nu}=0. \quad (14)$$

On combining Eqs. (13)–(14), we find

$$q^2=E^4F_{Nu}/(f_{Nu})^2;$$

by means of Eqs. (4) and (8) this may be written as,

$$B=\tfrac{1}{2}a_0^2\left(\frac{W}{D}\right)^2\frac{\varphi}{1-e^{-\varphi}}\frac{f_{Nu}^2}{F_{Nu}}\beta_c. \quad (15)$$

f_{Nu} may be computed directly as $[\int_0^D \exp(-z/2\tau)dz]/D = 2[1-\exp(-\frac{1}{2}\phi)]/\phi$. F_{Nu} on the other hand cannot, but it can be estimated as follows. For not too excessive values of $\nu\beta_cD$

$$e^{+\nu T}=e^{-\nu\beta_cD}+(1-e^{-\nu\beta_cD})e^{-bz},$$

where b is a constant determined by fitting (as by least squares) the right member to the left; hence by direct integration and since $T=0$ at $z=0$ and $T=-\beta_cD$ at $z=D$,

$$F_{Nu}=(1-\nu\beta_c/b)e^{\nu\beta_cD}. \quad (16)$$

Assembling these average values together with Eq. (15),

$$B=2a_0^2(1-e^{-\frac{1}{2}\phi})^2\beta_cW^2/D^2(1-e^{-\phi})(1-\nu\beta_c/b)\phi e^{\nu\beta_cD}. \quad (17)$$

Clearly the combined factors in ϕ are just $(2/\phi)\sinh^2\frac{1}{4}\phi \times \operatorname{csch}\frac{1}{2}\phi$. Equally clearly, the reciprocal of F_{Nu} as computed by Eq. (16) cannot be correct for large $\nu\beta_cD$; F_{Nu} must always be positive, and so must its reciprocal. Hence $(1-\nu\beta_c/b)^{-1}$ cannot hold at large $\nu\beta_cD$; rather we replace it in Eq. (18) by $1+U(\nu\beta_cD, \phi, \cdots)$, where $U>0$ and U increases strongly with $\nu\beta_cD$. Hence the formula

$$B=4a_0^2(W/D)^2[(\sinh^2\tfrac{1}{4}\phi \operatorname{csch}\tfrac{1}{2}\phi)/\phi]\beta_c \times e^{-\nu\beta_cD}[1+U(\nu\beta_cD, \phi, \cdots)], \quad (18)$$

which may be considered as the end result of our present theoretical calculations.

DISCUSSION

It does not appear feasible to calculate U with any degree of precision unless more precise calculations of ψ_1 and ψ_2 eigenfunctions are available. U arises from F_{Nu}, and F_{Nu} in turn arises from our use of $\psi_1=c_5$ and $\psi_2=c_6$ which are very poor approximations to physical

[14] See the discussion of the use of approximate eigenfunctions to calculate approximate eigenvalues by the variational method, as given by H. Margenau and G. M. Murphy in *The Mathematics of Physics and Chemistry* (D. Van Nostrand Company, Inc., New York, 1943), p. 364.

[15] H. Jeffreys, Phil. Mag. **2**, 833 (1926).
[16] H. Jeffreys, Proc. Roy. Soc. (London) **118A**, 195 (1928).
[17] H. Jeffreys, Proc. Cambridge Phil. Soc. **26**, 170 (1930).

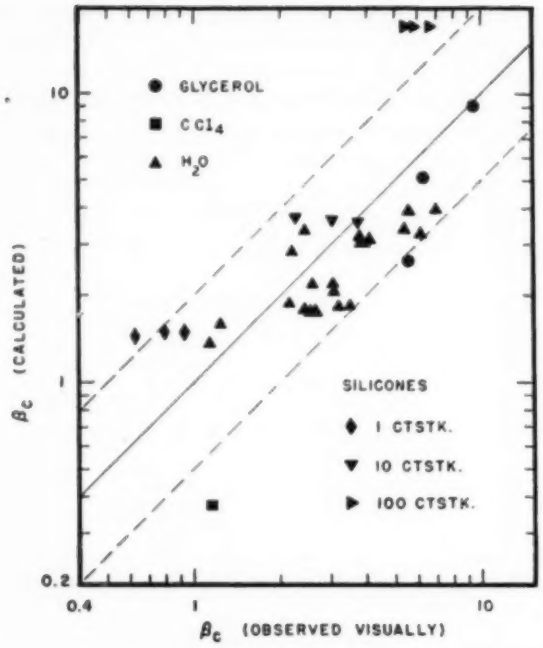

FIG. 1. Comparison of observed mean thermal gradients at the beginning of convective flow of various liquids in unconsolidated media, with those values predicted by Eqs. (18)–(19). Points on the solid line indicate agreement of theory with experiment. Points on the two dashed lines indicate disagreement of theory and experiment by a factor of two. Details of reduction of data are given in the text.

reality. Consequently for practical usage, U had best be determined from the experimental data by Eq. (18). We have, using all published data,[4,5,8] in this way computed that

$$U \cong 14(\nu\beta_c D)^{\frac{1}{2}}, \tag{19}$$

a purely empirical expression.

The method of computation is pertinent here. β_c-values were taken directly from the published papers, as were ν and D. In the case of test number 3 with CCl_4, a re-examination of original data had disclosed a minor error, so that 1.15°C/cm was adopted rather than 0.8. Moreover, where alternative values of β_c are reported[9] for various techniques, we have adopted those based on visual observations. Likewise φ-values were used as reported,[9] except that for the test number 3 with CCl_4 we used $\varphi=0.8$ rather than the published value of zero. The earlier data did not include φ as such, but as summarized[9] they reported (as θ_m) approximately the quantity $[1-\exp(-\frac{1}{2}\varphi)]/[1-\exp(-\varphi)]-\frac{1}{2}$ from which φ-values were obtained. Inasmuch as no direct observations were made on W, we used $W=D$ in determining Eq. (19); it is our belief that W may in general have been a little less than D, by perhaps several percent. a_0 was taken as 2.405. By these means, the product of all factors except $[1+U]$ in the right member of Eq. (18) was computed.

The left member, B, of Eq. (18), which is $2\pi^2h^2\mu_0/kg\rho_0\alpha D^2$, was computed from the published data as corrected according to the footnote 14 in reference 9. Hence for each of the 36 tests reported, excepting the unsuccessful test number 13 with H_2O, we computed a value of $[1+U]_{exp}$ from Eq. (18). A graph of $[1+U]_{exp}$ *vs* $\nu\beta_c D$ then led directly to Eq. (19). We should mention that other expressions could have been achieved as readily, and that Eq. (19) was used as being apparently the simplest.

The quantity [L.M. Eq. (18)]÷[R.M. Eq. (18)], based upon the experimental above data and upon Eq. (19), shows no trend when plotted against $\nu\beta_c D$. Furthermore it appears to have the value unity. Hence Eq. (18) seems to be excellent for practical usage. More importantly, since U is not largely significant for $\nu\beta_c D<$about 0.3, it appears that Eq. (18) is in accord with experimental experience (based upon visual observations for β_c) to within a *random* amount which presumably represents experimental uncertainty. Whether this same fortunate state of affairs will hold for a comparable number of data based upon the radiactive-trace method of observation,[7,8] which generally produces smaller values of β_c than the visual method, cannot be ascertained at present because of the paucity of such data.

This situation suggests that Eqs. (18)–(19) should well represent the experimental data as to β_c from visual measurements. Figure 1 illustrates the extent to which this is so. In applying Eqs. (18)–(19) to the several cases reported, two problems are encountered: double-valuedness in prediction of $\nu\beta_c D$, and nonexistence for sufficiently large νBD. In general, the lesser $\nu\beta_c D$ value must be taken; but in the cases of tests numbers 2 and 5 with glycerol, the larger correlates with experiment while the smaller does not, and so is used. The reason behind this is not clear. For large νBD values encountered in tests number 6 with glycerol and in all tests with the 100-DC-200 silicone fluid, we use the nearest point on curves of $\nu\beta_c D$ *vs* νBD. In practically all cases, provided only that these interpretive practices are used, Eqs. (18)–(19) lead to β_c values which are within a factor of 2 equal to those observed by these means. From a practical point of view, then, Eqs. (18)–(19) are definitely better than the equations reported previously[6,9] when used to predict visual β_c-values. From the point of view of fundamental hydrodynamics, it seems that the variational type of theory as here advanced may be a very powerful tool in future studies of the theory of phenomena like the one here discussed; it is remarkable that such crude eigenfunctions as used above, can lead to such agreement with experiment as Fig. 1 exhibits.

JOURNAL OF APPLIED PHYSICS VOLUME 24, NUMBER 7 JULY, 1953

Probe Studies of Energy Distributions and Radial Potential Variations in a Low Pressure Mercury Arc*

R. M. Howe†
Research Laboratory of Electronics, Massachusetts Institute of Technology, Cambridge, Massachusetts
(Received January 29, 1953)

Probe measurements were made in the plasma of a low pressure mercury arc. The electron-energy distributions showed depletions from a Maxwellian distribution in the high energy range. Coupling effects between adjacent probes were investigated and were found to be quite small but in the proper direction to agree with the Langmuir-Tonks theory. Drift-current distortion of the random electron-energy distributions was measured with a bidirectional probe and compared with theory. A multisection probe extending from tube axis to tube wall allowed a determination of radial potential and density variations. Results over a pressure range from 3.4 microns to 35 microns showed good agreement with the ambipolar diffusion theory based on cumulative ionization. A direct calculation of ionization rate in the plasma was made from the ionization probability for a one-step ionizing process; comparison of this calculation with the observed ionization rate at 1.7 microns indicated that at that pressure the ionization is half direct, half cumulative. For higher arc pressures cumulative ionization evidently predominates.

I. INTRODUCTION

THE study of the positive column of a low pressure mercury arc by means of probes has been the subject of many researches in the past twenty-five years. The wide interest in this field undoubtedly stemmed from the initial work in 1924 of Langmuir and Mott-Smith,[1] who pointed out the incorrectness of the previous practice of obtaining plasma potentials by finding the voltage at which a probe inserted in the plasma drew no net current. They showed that a complete voltage-current characteristic for the probe must be considered, from which one can obtain the true plasma potential as well as much additional information concerning the physical processes taking place in the plasma of the arc.

The original Langmuir-probe type of analysis, successful as it was, left several things unexplained. The Langmuir-Tonks[2] theory of 1929 was a logical attempt to account for at least one of these difficulties but it too seemed to present additional discrepancies with experiment.

The purpose of the research described here was to restudy the positive column (plasma) of the low pressure mercury arc by employing both improved vacuum and measuring techniques now available. In particular, an attempt was made to study the electron-energy distributions in the plasma with considerable exactness by means of probes and to obtain improvements over Killian's original determinations[3] of radial variations of plasma potential and density in a cylindrical discharge.

* This work has been supported in part by the Army Signal Corps, the Air Materiel Command and the U. S. Office of Naval Research.

† Now at the University of Michigan, Ann Arbor, Michigan.

[1] I. Langmuir and H. Mott-Smith, Gen. Elec. Rev. **26**, 731 (1923); **27**, 449, 538, 616, 810 (1924); J. Franklin Inst. **196**, 751 (1923).

[2] I. Langmuir and L. Tonks, Phys. Rev. **34**, 876 (1929).

[3] T. Killian, Phys. Rev. **35**, 1238 (1930).

II. PROBE THEORY

The positive column of a mercury-arc discharge consists of a luminous plasma having very nearly equal densities of positive ions and electrons. The electrons are known to possess something approximating a Maxwellian distribution of energies, whereas the energy distribution of the positive ions is not known. If a plane probe is inserted in the positive column, the electric current to the probe will be a function of probe voltage. When the probe is very negative with respect to the plasma, only positive ions will be collected; when the probe is positive with respect to the plasma, electrons directed at the probe will be collected. When the probe is somewhat negative with respect to the plasma, only those electrons which are energetic enough to overcome the retarding potential will be collected along with the positive ions. By subtracting the positive ion current from the total probe current, we obtain the electron current i_-. A plot of $\log i_-$ *vs* V, the probe potential with respect to the anode, is commonly known as the probe characteristic curve (for example, see Fig. 8).

For a Maxwellian distribution of electrons the electron current to a collector of area A is given by

$$i_- = A n_- e \left(\frac{kT_-}{2\pi m}\right)^{\frac{1}{2}} \exp\left(\frac{-e(V_p - V)}{kT_-}\right) \text{ for } V \leqslant V_p, \quad (1)$$

where n_-, e, m, and T_- are electron density, charge, mass, and temperature, respectively; k is Boltzmann's constant; and V_p is the plasma potential with respect to the anode. A plot of $\log i_-$ *vs* V will yield a straight line having a slope $0.434e/kT_-$ from which the electron temperature T_- can be calculated. Probe curves from low pressure mercury arcs are nearly always roughly linear and hence represent approximate Maxwellian distributions. Knowing T_- and the total random electron current I_- (as measured for the probe slightly positive with respect to the plasma), we can calculate the electron density n_-.

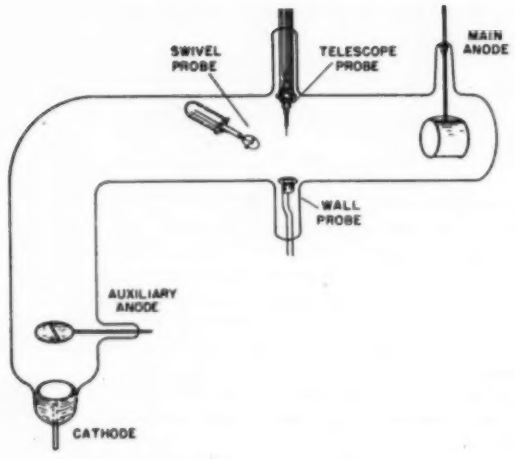

FIG. 1. Mercury-arc tube.

This probe theory assumes that the presence of the probe in the plasma does not disturb the plasma potential. Langmuir originally assumed[1] that this is possible because a space-charge sheath of small thickness forms around the probe when the potential of the probe is different from that of the plasma. For negative probe voltages this sheath consists of positive ions; for positive probe voltages the sheath consists of electrons. In either case, the voltage drop between probe and plasma takes place over the relatively narrow region of the sheath. By applying the Langmuir-Childs equation for space-charge-limited current one can show that for plane probes of reasonable size (a few millimeters across) the sheath thickness is small compared with the probe diameter. For a cylindrical probe whose diameter is small compared with sheath thickness it can be shown[4] from the space-charge equation that the positive ion current is proportional to $(V_p-V)^{\frac{1}{2}}$. This relationship is observed experimentally for a thin wire collector.[5]

If the sheath picture is correct, we should be able to make an estimate of the expected ratio of the total random electron current I_- to the total random positive ion current I_+, based on the assumption that the positive ions as well as the electrons have a Maxwellian distribution. For the electric-field gradients observed in the plasma, it is easy to show that the electron density n_- is many orders of magnitude greater than the net charge density n_+-n_- (where n_+ is the positive ion density). Therefore $n_+\approx n_-$, and from Eq. (1) and its equivalent expression for positive ions we can solve for I_-/I_+ by setting $V_p=V$. Thus

$$\frac{I_-}{I_+}=\left(\frac{T_-}{T_+}\right)^{\frac{1}{2}}\left(\frac{M}{m}\right)^{\frac{1}{2}}, \qquad (1a)$$

where T_+ is the positive ion temperature and M is the mass of the positive ions. It is reasonable that the positive ions will have a temperature associated with random motion which is not greater than the electron temperature T_- and more likely much less than T_-. Hence $T_-/T_+\geqslant 1$, and from Eq. (1a) $I_-/I_+\geqslant 605$ for mercury. But actual probe measurements of I_-/I_+ invariably yield ratios between 200 and 400. On the basis of a Maxwellian distribution in positive ion energies, therefore, it would appear that we are collecting far too much positive ion current.

Several possible explanations for this perplexity are apparent when one realizes that the arrival of a positive ion at the probe surface cannot be distinguished from the departure of an electron. Electrons might be leaving for the following reasons:

1. The arrival of positive ions can cause electrons to be ejected,[6] probably because of the energy released upon recombination at the surface.
2. The absorption of ultraviolet light at the probe surface will eject photoelectrons.[7]
3. Metastable mercury atoms may cause the emission of electrons when they strike the probe surface and lose their energy of excitation.[8]

If the current obtained when the probe is very negative does not consist entirely of the arrival of positive ions, the energy delivered to the probe should be less than that calculated on the basis of positive ion current alone. Several attempts to verify this have been made utilizing electrically heated probes. Oliphant[9] finds evidence of electron emission from probes in rare-gas discharges, while Molthan[10] concludes that there is no appreciable electron emission.

It appears doubtful if any of the above effects are capable of explaining the very considerable lack of agreement between the random current theory and the experimentally observed positive ion currents to the probe. Rather, the answer to the dilemma would seem to lie in the original assumption that the presence of the negative probe has not altered the plasma potential immediately outside the sheath. Under this assumption positive ions which strike the sheath are accelerated toward the probe and collected. Thus, at the boundary of the sheath all positive ions are moving toward the probe surface. But to say that the plasma potential just beyond this boundary is unchanged despite the presence of the adjacent sheath is to claim that the positive ions have random motions in all directions. This transition from completely random motions to directed motions obviously cannot take place in an infinitely short distance but requires a distance of the order of mean free paths of the positive ions. As we move from the region of complete random motion through the transition region to the edge of the sheath, the plasma potential will be slowly decreasing. The

[4] I. Langmuir, H. Mott-Smith, Gen. Elec. Rev. **27**, 449 (1924).
[5] I. Langmuir and H. Mott-Smith, Gen. Elec. Rev. **27**, 616 (1924); and reference 2.
[6] M. L. E. Oliphant, Proc. Roy. Soc. (London) **127**, 373 (1930).
[7] C. Kenty, Phys. Rev. **44**, 891 (1933).
[8] C. Kenty, Phys. Rev. **38**, 377 (1931); **43**, 181, 776 (1933).
[9] M. L. E. Oliphant, Proc. Roy. Soc. (London) **132**, 631 (1931).
[10] W. Molthan, Z. Physik **98**, 227 (1935).

result is a shallow potential well for positive ions extending many sheath thicknesses beyond the sheath itself. It is possible for this shallow potential well to account for the observed positive ion current, which is too large to be due to purely random current collected by the surface of the space-charge sheath. This idea is treated quantitatively in the Langmuir-Tonks theory[2] and will be discussed in the light of some experimental results later in this article.

III. APPARATUS

A. Description of the Mercury-Arc Tube

Although probe measurements were made in three different tubes, most of the data were obtained from the tube shown in Fig. 1. The envelope of this tube is made of Pyrex glass and is circular in cross section so that the geometry of the main body is cylindrical. A pool of mercury at the bottom of the vertical section serves as the cathode. There are two anodes: a cylindrical main anode and a disk-shaped auxiliary anode (for the purpose of stabilizing the arc). All press leads are tungsten, while the anode and probe structures are made of tantalum.

The three probe assemblies used in the tube of Fig. 1 are shown in greater detail in Fig. 2. The swivel probe consists of a plane disk-shaped collector which is hinged so that its axis can be swung either parallel or perpendicular to the axis of the tube. This probe is used to study the effect of drift current on the probe characteristics. The supporting stem of the swivel probe is shielded from the plasma by a cylindrical guard extending from probe to wall. The telescope probe is an array consisting of five coaxial cylinders extending from tube axis to tube wall. The exposed portion of each cylinder serves as a collector as well as a shield for the cylinders inside. This probe assembly is used to study radial variation in plasma properties. Diametrically opposite the telescope probe is the wall probe, which is a plane disk-shaped collector mounted flush with the tube wall and surrounded by a shield.

All probe and shield surfaces are constructed of 3-mil tantalum sheet. Probes and shields are insulated from each other simply by mechanical clearance resulting from careful alignment.

The above description applies to the tube shown in Fig. 1. Two other tubes were used. The first was almost identical in geometry with the tube described except for a shorter vertical section in its envelope; the second tube had a straight envelope with no bend and was mounted vertically. Only plane probes were used in these latter two tubes, and results were similar to those obtained with the tube in Fig. 1.

B. Processing of the Tube

Before the probes and shields were mounted on the press leads, the tube was baked for a number of hours at 500°C while under high vacuum. Main and auxiliary anodes were outgassed by heating to about 1500°C with rf induction. This procedure allowed a preliminary check for leaks in the many presses. The side tubes supporting the presses were then cracked off about $\frac{3}{4}$ inch from the press ends to permit easy access with the spot welder to the tungsten leads.

All probe assembly components were pre-outgassed at a temperature of about 1900°C by mounting them in dummy tubes and bombarding them with 2000-volt electrons. The parts were then welded to the press leads, which finally were sealed back onto the main envelope. The completed tube was sealed onto the vacuum system along with two mercury stills. The inner still and the mercury-arc tube were baked at 500°C under high vacuum, after which clean mercury in the outer still was distilled into the inner still. The outer still was then sealed off of the system, and mercury from the inner still was distilled into the tube proper. After the electrodes had been outgassed by rf induction, the arc was lit by touching a high-voltage spark generator to the outside of the mercury bulb. Tube current was increased until both anodes were red, and this condition was maintained for several hours. During the latter portion of this run the vacuum, as measured by the centimeters stick of a McLeod gauge, was as good as that observed when the arc was off. In addition, all probes were flashed white-hot by driving them to anode potential or higher. For wall probes it was necessary to cause the arc to transfer partially to the probe in order to get adequate heating.

After replenishing the supply of mercury in the bulb of the discharge tube, the inner still was sealed off of the system and the pumping lead to the tube itself preheated. Again the tube was run under extreme overload for about 30 minutes, after which the final seal-off was made. All probe measurements were made with the tube sealed off of the vacuum system.

C. Bath Arrangement

Early experimenters with mercury arcs controlled the pressure of the mercury in the discharge by varying

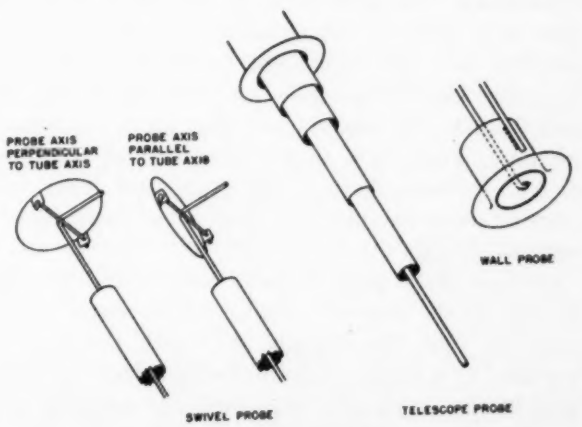

FIG. 2. Probe assemblies.

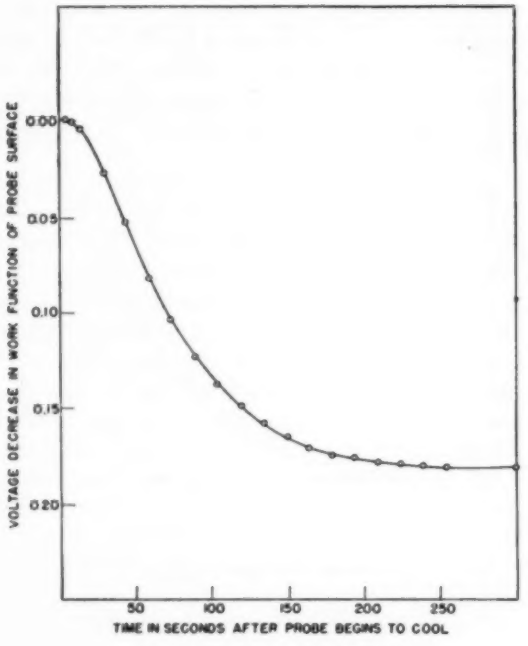

FIG. 3. Contact-potential shift.

the temperature of a water bath surrounding the mercury-bulb portion of the tube. Care was usually taken to maintain other sections of the tube at temperatures above the bath temperature in order to discourage the condensation of mercury on these other sections. The pressure of the mercury gas in the tube was then taken as the vapor pressure of mercury at bath temperature.

Klarfeld[11] has pointed out that this procedure is apt to lead to considerable error in the calculation of mercury pressure and that the best procedure is to submerge the entire tube in a water bath of constant temperature. With this arrangement mercury droplets condense over all portions of the tube; since all these regions are at the same temperature, a constant pressure equal to the vapor pressure of mercury at water bath (and hence tube wall) temperature is assured.

This technique has been used in the research described here. The entire tube was submerged in a tank filled with water. Good circulation of the water was provided by a stirring paddle turned by a small induction motor. The resulting turbulence maintained the bath temperature constant to within 0.1°C throughout the tank. There is a small correction (of the order of 1°C) between bath temperature and inner wall temperature of the tube as a result of the conduction of heat out through the tube walls.

The first probe measurements were taken with only the bulb of the mercury tube cooled by water. Later, when the tube was entirely immersed, the pressure decreased by a factor of about twenty, which is graphic proof of the importance of completely submerging a mercury-arc tube in water if accurate knowledge of the pressure is desired.

[11] B. Klarfeld, J. Tech. Phys. U.S.S.R. 5, 913 (1938).

IV. MEASUREMENT TECHNIQUES

A. Contact Potential Shifts

It was observed that the contact potential of the probe surface changes with time after the probe is flashed red-hot by electron bombardment. This shift in contact potential is found by observing the probe current as a function of time after flash for a probe voltage close to the floating potential. In this region of probe voltage the positive ion and electron currents nearly balance, and as a result the net probe current is very sensitive to a small change in contact potential (since electron current varies exponentially with probe voltage). A typical plot of contact-potential shift *vs* time after flash is shown in Fig. 3. It is apparent from the curve that some 10 sec elapse before the contact potential begins to change.

The following observations indicate that this change in contact potential of the probe surface is an effect due to mercury settling on the probe surface and is not due to contaminating gas.

1. The change in contact potential was of the same magnitude and had the same time constant for all three of the experimental tubes used, even when the tubes were being pumped on the vacuum system.

2. Probe assemblies which allowed faster conduction of heat away from the probe surface exhibited a shorter time constant and a slightly greater contact-potential shift. This is consistent with the hypothesis that the change in contact potential is a temperature effect; the cooler the probe, the more mercury can be present in equilibrium on the surface.

3. For a given arc current the change in contact potential was greater for lower mercury pressures. Again this is in agreement with the temperature hypothesis, since at lower pressures the random currents are lower. This means that heating effects caused by positive ion and electron bombardment at the floating potential will be less. Thus the final equilibrium probe temperature will be lower.

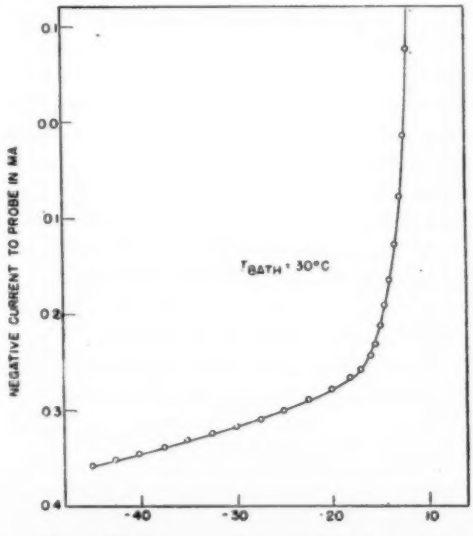

FIG. 4. Voltage-current curve for wire probe.

4. The change in contact potential observed corresponds to a lowering of the work function, which is what is expected for a surface layer of electropositive atoms such as mercury. On the other hand, oxygen and nitrogen are known to raise the work function of a surface when they adsorb on it.

This shift in contact potential makes it imperative to flash the probe red-hot before each current reading. Otherwise, a gradual shift in probe-contact potential takes place as the probe voltage is varied from very negative values up to plasma potential. To get sufficient heating for probes located near or at the tube wall it is necessary to run the probe to a voltage high enough to cause the arc to transfer to the probe. A resistor in series with the probe serves to limit the current to the desired value after the arc has transferred.

It is interesting to note that no change in positive current for very negative probe voltages was observed after a flash. This would indicate that no important photoelectric or metastable effects are taking place at the probe surface, since such effects would probably be quite dependent on the surface state of the probe.

B. Extrapolation of Positive-Ion Current

A determination of the positive ion current is extremely important in a study of electron-energy distributions from probe curves, since it is the positive ion current which must be subtracted from the total probe current in order to obtain the electron current. This need for an accurate knowledge of the positive ion current i_+ is particularly important in the voltage range where i_+ and the total probe current i_p are nearly equal and where the electron current i_- is therefore a small difference.

The only method of obtaining i_+ for various probe voltages is to use an extrapolation from the negative-voltage saturation region of the probe curve, since in this region we believe we are collecting no electrons. For a plane collector, the positive ion saturation curve is usually fairly linear, particularly at higher mercury pressures; but for small cylindrical collectors, the plot may have considerable curvature, as can be seen in Fig. 4. Where a definite curvature exists, one empirical approach makes use of a plot of $\log i_p$ *vs* $\log(V_p - V)$, where $(V_p - V)$ is the retarding potential of the probe relative to plasma potential. When this method is used (as in Fig. 5) one obtains a fairly linear saturation curve. The departure from linearity which is due to the start of electron collection is much more clearly marked, and the value of i_+ is taken from the linear extrapolation on this log-log plot.

All this method attempts to do is maintain an i_p *vs* V trend established in the negative-voltage region of saturation, so that one can make reasonable guesses for i_+ and hence i_-. Obviously one cannot take too seriously values of i_- which are very much less than i_p (i.e., obtained from the small difference between i_+ and i_p). It is also apparent that for values of i_- of the same order as or greater than i_p, any subtle differences in i_+ extrapolation techniques cannot affect appreciably the value of i_-.

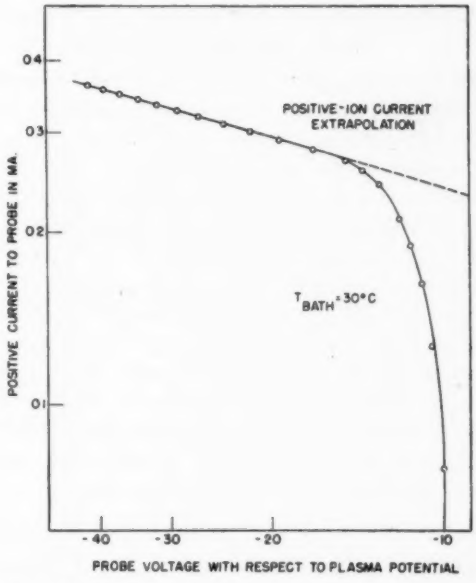

FIG. 5. Log voltage—log current curve for wire probe.

C. Oscillations

A DuMont 224A oscilloscope was used to monitor cathode-to-anode potential and probe-to-anode potential. Oscillations up to 5 Mc/sec could have been detected, but nothing other than random noise or "grass" was ever observed on the oscilloscope. Later attempts to detect oscillations at frequencies up to 1000 Mc/sec yielded negative results.

D. Tube Current

All probe measurements were taken with a cathode-to-main-anode current of 4 amp and a cathode-to-keeping-anode current of 2 amp. Increasing the currents much above these figures resulted in overheating of the anodes, while decreasing the main-anode current below approximately 2 amp usually caused the arc to go out within a few minutes. An additional keeping anode located at the top of the vertical section of the tube would probably have stabilized the arc sufficiently to permit the use of much lower currents to the main anode.

E. Inconsistent Results for Bath Temperatures in the 50°C Region

At bath temperatures in the 50°C region the probe curves seemed to be nonreproducible at times, particularly for probe voltages a little below plasma potential. The reason for these fluctuations was never determined. No changes in arc voltage were observed either with the dc meter or the oscilloscope. Perhaps this pressure range lies in a transition region between two stable conditions of the arc.

F. Current-Density Discrepancy between Wire Probe and Swivel Probe

Both the swivel probe and wire probe are located at the tube axis. Hence the ratio of electron currents collected by the two probes should be the same as the ratio of their areas, i.e., 0.60 cm²/0.13 cm²=4.6. The observed ratio of electron currents is 3.2 for 22°C, 30°C, and 40°C baths. The discrepancy may lie in the uncertainty in determining the area of the swivel probe. This probe is a complicated structure, and it is difficult to estimate what fraction of the area is effective in collecting electrons. The 0.60 cm² area used above represents the total of all the area, including both front and back sides of the disk and tabs as well as the exposed portion of the supporting stem (see Fig. 2). The effective swivel-probe area for collecting electrons may be considerably less than this total area.

V. COUPLING EFFECTS BETWEEN PROBES

Simple probe theory assumes that the presence of the probe in the plasma does not appreciably alter the plasma potential. The validity of this assumption can be tested experimentally by observing whether the potential of one probe affects the current collected at an adjacent probe. For example, the characteristic curve of the wire probe can be observed for different potentials of the first surrounding shield. Several important facts are apparent from these measurements.

First of all, as the shield voltage is varied from −12 to +1 volt with respect to the plasma, the wire-probe curves shift to the right by approximately 0.2 volt. This indicates that the presence of the shield at a potential negative with respect to the plasma has shifted the plasma potential itself to a slightly more negative value. This lowering of the plasma potential as a result of the presence of a surface at negative potential in the plasma is consistent with the Langmuir-Tonks theory discussed earlier, in which it is argued that, as a result of the flow of positive ions into the wall (or probe) surface where recombination takes place, a rather shallow potential well for the positive ions is set up around this surface. In our case the 0.2-volt shift is rather smaller than one might expect, but we are, of course, dealing here with a much smaller surface than the tube wall. We must also remember that the 0.2-volt shift is only the average effect the shield exerts on the entire plasma surrounding the wire probe. The shift in plasma potential may, in fact, be much larger right next to the shield.

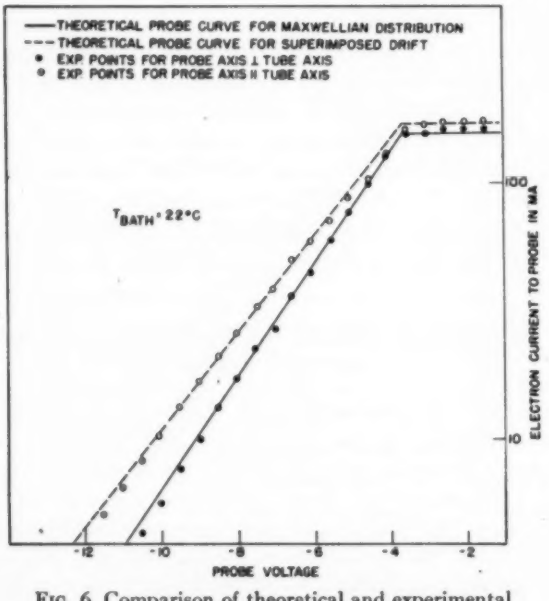

FIG. 6. Comparison of theoretical and experimental drift-current effects.

Secondly, we find that as the shield is made positive, the positive ion current to the wire probe decreases by 2 percent; yet at the same time the total electron current increases by approximately 1.5 percent. Both of these effects are in a direction suggesting that, as the shield potential is changed from negative to positive, the potential of the plasma surrounding the wire probe is raised slightly. In other words, at negative voltages the shield causes a lowering of the plasma potential over a fairly broad region.

These coupling tests seem to indicate that by far the greater part of the potential drop between a negative probe and the plasma takes place over a very narrow sheath region. However, there is evidence that there exists an additional small voltage drop extending over a considerable region of the plasma, as postulated by Langmuir and Tonks. Because of the smallness of the coupling effect observed, all probe measurements with the exception of coupling tests themselves were taken with the shields floating.

VI. EVALUATION OF DRIFT-CURRENT EFFECT

By means of the swivel probe it is possible to investigate distortion of the probe-characteristic curve resulting from the effect of drift current. When the probe is oriented so that its axis is perpendicular to the tube axis, it receives only random current. When the probe is oriented such that its axis is parallel to the tube axis, it is subjected to drift current as well as random current. Note that in the latter position the two sides of the probe are facing the cathode and anode, respectively. This means that any departures from the random-current probe characteristic will be a result only of second-order changes in the distribution function caused by effects of the drift current.

Let us assume that when drift current is present the spherically symmetrical distribution in electron momentum is displaced linearly in momentum space by an amount equal to the drift momentum. Starting with a Maxwellian distribution, we write for our new distribution

$$f(p_x, p_y, p_z) = n_-(2\pi mkT)^{-\frac{3}{2}} \times \exp\left[-\frac{(p_x-p_0)^2+p_y^2+p_z^2}{2mkT}\right], \quad (2)$$

where $p_{x,y,z}$ = the momentum in x, y, and z directions, respectively, and p_0 = the momentum associated with the drift velocity. The current density i_d to a probe at potential V relative to plasma potential V_p is given by

$$i_d(V)=e\int_{p_x=[2me(V_p-V)]^{\frac{1}{2}}}^{p_x=\infty}\int_{p_y=-\infty}^{p_y=\infty}\times\int_{p_z=-\infty}^{p_z=\infty}\frac{p_x}{m}f(p_x,p_y,p_z)dp_xdp_ydp_z, \quad (3)$$

where the probe surface is normal to the x direction. After the integration has been performed we have

$$i_d(V)=n_-e(2\pi mkT)^{-\frac{1}{2}}\times\left[\exp\left(-\left\{\left[\frac{e(V_p-V)}{kT}\right]^{\frac{1}{2}}-\frac{\alpha}{2(\pi)^{\frac{1}{2}}}\right\}^2\right)+\frac{\alpha}{2}\left(1-\operatorname{erf}\left\{\left[\frac{e(V_p-V)}{kT}\right]^{\frac{1}{2}}-\frac{\alpha}{2(\pi)^{\frac{1}{2}}}\right\}\right)\right], \quad (4)$$

where α is the magnitude of the ratio of drift current to random current. For the side of the probe facing the cathode, the drift current and random current are in the same direction and therefore α is positive; for the side facing the anode, their directions are opposite and α is negative.

It seems reasonable to assume that the drift current at any point across the tube is proportional to the electron density n_- at that point. From the telescope probe measurements we know n_- across the tube; from the total tube current we can then calculate the drift-current density at the tube axis. When this is done at a bath temperature of 22°C and a tube current of 4 amp, α turns out to be 1.05. From Eq. (4) we can find the current to both sides of the plane probe. This calculated current is compared with the observed currents in Fig. 6. The agreement seems good over the range in which the distribution is Maxwellian, indicating that our original assumption that the symmetrical distribution was displaced linearly in velocity space was not unreasonable.

It is apparent from Fig. 6 that there is no appreciable difference between total electron current or plasma potential as measured with the two orientations; nor, it turns out, is there any appreciable difference in positive ion currents. The greatest distortion of random-current curves by drift current occurs at the lowest pressures; distortion almost disappears for a bath temperature of 61.5°C.

The various members of the telescope array are subject, on the average, to the collection of both pure random current (corresponding to the perpendicular orientation of the swivel probe) and to random plus drift current (corresponding to the parallel orientation of the swivel probe). Hence, the average probe current for the two swivel-probe orientations should yield a

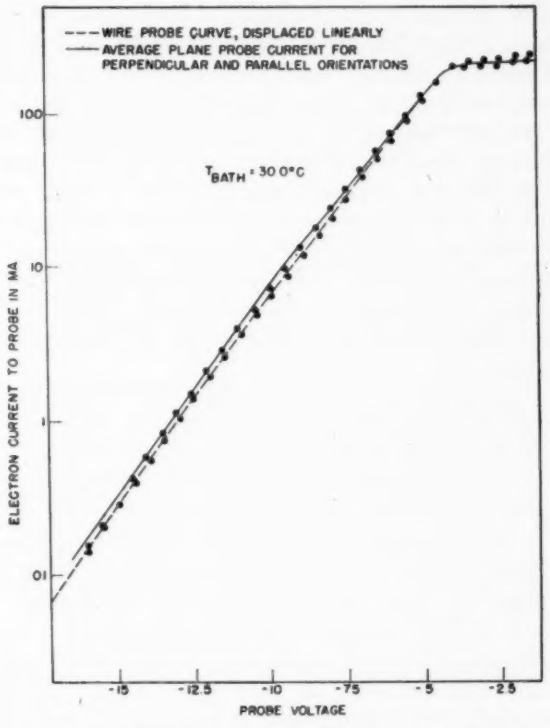

FIG. 7. Comparison of average drift-random effect with wire-probe curve.

probe characteristic curve similar to that obtained for the wire probe, which is the central member of the telescope array. Figure 7 shows that this is true.

As a result of these considerations we can say that the members of the telescope-probe array will give us good plasma potentials and total electron currents, but that the shape of the actual probe curves cannot be taken as an exact measure of the electron-energy distribution except at the highest pressures used. At these highest pressures the wire probe will, in fact, probably give a better indication than the plane probe of true electron-energy distribution because of the much smaller collecting area of the wire probe.

VII. ELECTRON-ENERGY DISTRIBUTIONS IN THE PLASMA

Probe measurements in the plasma of arc discharges nearly always show deviations from Maxwellian distributions in the high-energy electron region. These deviations show up as departures from linearity in the retarding-potential region of the probe characteristic curve. In Figs. 8–10 are shown probe curves at the tube axis for bath temperatures of 22°C, 40°C, and 61.5°C. Wall-probe curves are similar. All the curves exhibit a bilinear character in which the upper, straight-line portion of the curves represents from 95 percent to 99 percent of the electron current. The lower region of the curves would seem to indicate a deficiency of electrons from a Maxwellian distribution.

It is not possible to tell conclusively from the probe

curve whether a given departure from linearity represents a depletion or a surplus of electrons from a Maxwellian distribution. This was first pointed out by Druyvesteyn,[12] who showed that one could obtain the actual electron-energy distribution by a method which involves taking the second derivative d^2i_-/dV^2, where i_- is the electron current to the probe and V is the probe voltage. To do this from the probe curve itself results in considerable inaccuracy, but the second derivative can be obtained directly from probe measurements by observing the increase in probe current when a small sinusoidal voltage is superimposed on the dc probe voltage.[13]

Despite the questionable correlation between probe curves and actual energy distributions, it seems evident that the curves of Figs. 8–10 do represent a depletion from a Maxwellian distribution in the high-energy region, since there are several reasons why we should expect such a depletion. First, electrons are continually making collisions with mercury atoms, and there is a probability that these collisions will be inelastic for electrons with energies above approximately 5 volts; such collisions result either in excitation or ionization of the unexcited mercury atoms.[14] Also the concentration of excited atoms, particularly metastables, may be an appreciable fraction of the concentration of all mercury atoms, and inelastic collisions with these excited atoms may produce additional excitation or ionization. We know that ions are being produced in the plasma at a considerable rate. Whether the ionization is the result of a single collision or of multiple collisions with electrons, it is clear that for every ion which is created there must have been at least one inelastic collision by an electron, a collision which results in a very large loss of energy for that electron. Therefore, the very existence of an ionization process demands a net transfer of electrons in velocity space through the distribution from low energies to high energies, where they suffer inelastic collisions and drop back again to low energies. In order to maintain this unbalance from thermal equilibrium there must be a depletion in the high energy range from a Maxwellian distribution.

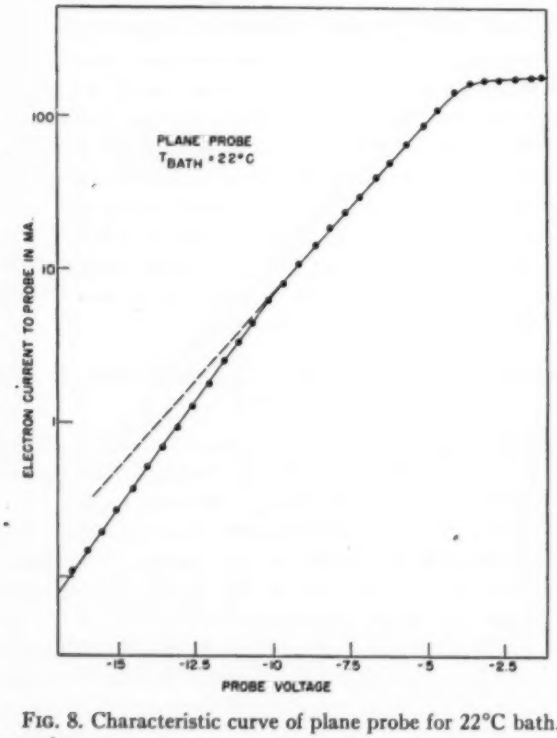

FIG. 8. Characteristic curve of plane probe for 22°C bath.

There is another reason for expecting this depletion. From measurements with the wall probe we can find its floating potential, i.e., the potential for which the net flow of current to the probe is zero. If we assume that the adsorption fractions for mercury ions and electrons are the same for both glass and tantalum, respectively,[15] then the floating potential of the probe is equal to the potential of the glass walls of the tube, since these glass walls can receive no net current. Furthermore, if the adsorption fractions are not exactly the same, the wall potential still will not be very different from the floating potential of the probe, since the electron current varies so markedly with small voltage changes.

The potential of the tube walls will thus be fairly negative with respect to the plasma near the walls (−4.5 volts for a 61.5°C bath, −10 volts at 22°C). This voltage drop takes place over the positive ion sheath at the walls. Most of the low energy electrons which are directed toward the walls will be reflected back into the plasma. Only those which have an energy associated with motion normal to the walls that is large enough to overcome the retarding potential of the sheath can stick to the glass walls. The current of these high energy electrons flowing into the walls is just enough to balance the positive ion current flowing to the wall; recombination then takes place at the wall.

In order to maintain this selective flow of high energy electrons into the wall the distribution must again exhibit a depletion of high energy electrons from a Maxwellian distribution. In the plasma region near the walls this depletion should be quite noticeable. As we go a number of mean free paths away from the wall, the depletion caused by wall currents will gradually disappear as the motions again become random. The mean free path, as calculated from Brode,[16] is about equal to the tube radius at 22°C bath temperature, so that depletion caused by wall current should be present in the distribution at the tube axis. At 40°C, however, the mean free path is only about one-sixth of the tube radius, so that depletion effects of the wall should be smoothed out in the distribution at the axis. However, depletions caused by exciting or ionizing collisions will

[12] M. J. Druyvesteyn, Z. Physik **64**, 790 (1930).
[13] R. H. Sloane and E. I. R. MacGregor, Phil. Mag. **18**, 193 (1934).
[14] W. B. Nottingham, Phys. Rev. **55**, 203 (1939).
[15] B. Klarfeld, J. Tech. Phys. U.S.S.R. **5**, 924 (1938).
[16] R. B. Brode, Phys. Rev. **35**, 504 (1930).

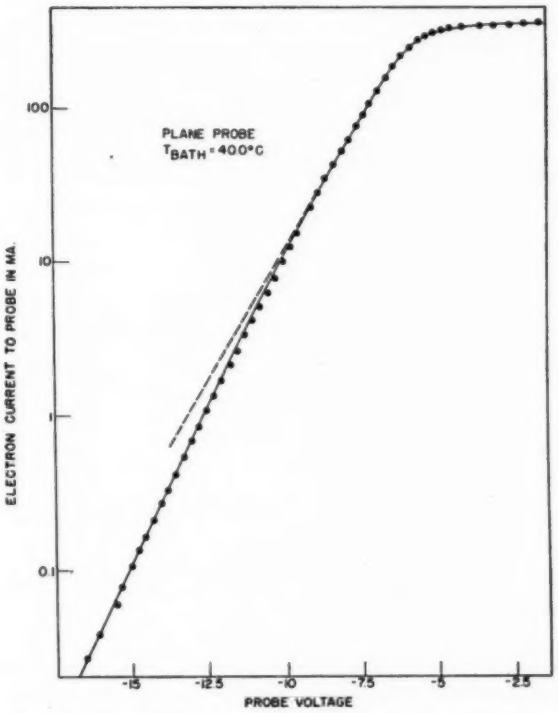

FIG. 9. Characteristic curve of plane probe for 40°C bath.

be present in the distribution at both the tube wall and axis.

Professor W. P. Allis has calculated the distribution function necessary to cause a net transfer of electrons in velocity space through the distribution from low energies to high energies. In this derivation he has assumed that the electron-electron interaction cross section varies inversely as the energy squared. The resulting distribution can be represented approximately by

$$\begin{aligned} f(u)du &= Au^{\frac{1}{2}}[e^{(u_0-u)/\theta}-1]du \quad u<u_0 \\ &= 0 \qquad\qquad\qquad\qquad u>u_0 \end{aligned}, \tag{5}$$

where u=energy of the electron, $\theta=(2/3)\bar{u}$ ($\bar{u}$=the average energy), A=a constant depending on the electron density, and u_0=a constant depending on the net rate of flow through velocity space. The approximation is good for $u_0/\theta>5$.

This distribution evidently goes to zero at $u=u_0$. This is because the distribution has been calculated such that there is a constant flow of electrons through velocity space toward higher energies; at $u=u_0$ the distribution has merely died out in the act of trying to furnish this flow of electrons. In an actual case where such a distribution applies, the inelastic collisions which cause the flow through velocity space will begin to set in at an energy u_1 which is considerably less than u_0. If the probability for inelastic collisions as a function of energy u is known, then a second theoretical distribution can be calculated for $u>u_1$ and patched onto the $f(u)$ distribution at $u=u_1$.

From the distribution $f(u)$ the following formula for the random current collected on the surface of a plane probe is obtained:

$$\begin{aligned} I_p(V) &= C\left\{e^{(u_0-eV)/\theta}-\left[1+\frac{(u_0-eV)}{2\theta^2}\right]\right\} \quad 0<eV<u_0, \\ &= 0 \qquad\qquad\qquad\qquad\qquad\qquad eV>u_0 \end{aligned} \tag{6}$$

where $-V$=the probe voltage relative to the plasma and C=a constant depending on the electron density. In Fig. 11 the probe curve calculated from Eq. (6) is compared with the experimental currents for the plane probe at 30°C bath temperature. θ was obtained from the slope of the upper straight-line portion of the experimental probe curve, and the theoretical curve was translated linearly until a good fit with the experimental points was obtained. Note that the agreement between the experiment and theory is good to approximately -14 volts (actually -10 volts with respect to plasma potential). The point of departure from the theory lies in the very region where inelastic collisions with the wall, as well as ionizing collisions, begin and where the calculated distribution can therefore no longer be correct.

A similar agreement between the calculated distribution and experiment is shown in Fig. 12, where the wire-probe data are compared with theory at a bath temperature of 61.5°C. The plane-probe data at this high pressure do not show such good agreement, but the wire probe is believed to yield more reliable results because of its smaller area and because drift current is negligible at 61.5°C. Good agreement between experi-

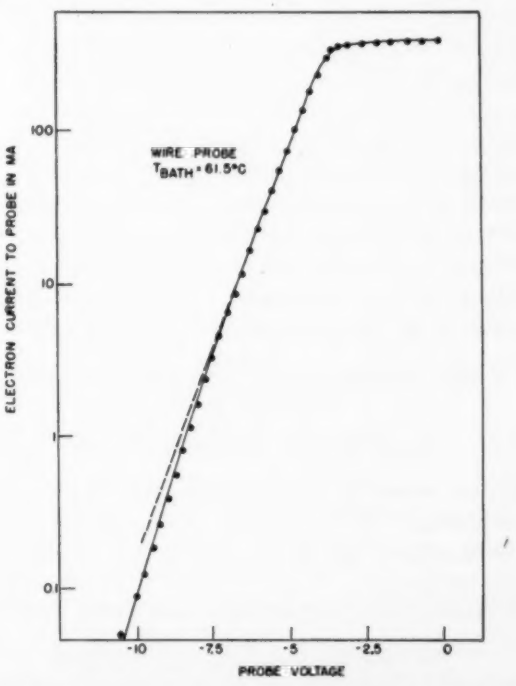

FIG. 10. Characteristic curve of wire probe for 61.5°C bath.

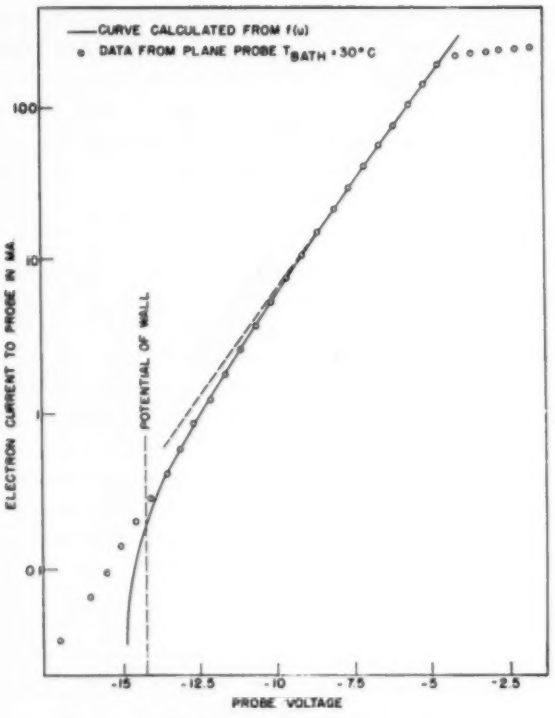

FIG. 11. Comparison of theoretical probe curve with experiment for 30°C bath.

mental and theoretical probe curves is also obtained at 40°C and 50°C bath temperatures. Agreement between theory and experiment is not as good at a bath temperature at 22°C. This may be because mean free paths are of the order of tube radius at this pressure; one would therefore expect the theory to break down.

Because inelastic collisions causing excitation and ionization are occurring in the same energy region as inelastic collisions with the wall, it seems difficult at the present time to determine the rate of electron transfer through velocity space giving rise to the depleted distribution, and hence to calculate the electron-electron interaction cross section. When quantitative values for metastable concentrations as well as excitation and metastable ionization probabilities become available, then a reasonable calculation of electron-electron interaction cross section will be possible.

VIII. RADIAL POTENTIAL AND DENSITY DISTRIBUTIONS

A. Ambipolar Diffusion Theory

Let us review briefly the ambipolar diffusion theory of Schottky.[17] Both electrons and positive ions are diffusing out of the plasma to the tube walls. In the steady state this diffusion current $\bar{\Gamma}$ is the same for both positive ions and electrons, and hence we write

$$\bar{\Gamma}=-D_-\nabla n_- -\mu_- \bar{E} n_- \quad \text{for electrons} \qquad (7)$$

and

$$\bar{\Gamma}=-D_+\nabla n_+ +\mu_+ \bar{E} n_+ \quad \text{for positive ions,} \qquad (8)$$

where $D_\pm$ = diffusion constant for electrons or positive ions, $n_\pm$ = density of electrons or positive ions, $\mu_\pm$ = mobility of electrons or positive ions, and $\bar{E}$ = electric field (radial for a cylindrical discharge).

In the plasma of the arc n_- and n_+ are very nearly equal, so we assume

$$n_-=n_+=n. \qquad (9)$$

With this simplification we can eliminate $\bar{\Gamma}$ from Eqs. (7) and (8) and obtain

$$\bar{E}=\frac{D_- - D_+}{\mu_- + \mu_+}\left(-\frac{\nabla n}{n}\right). \qquad (10)$$

Since $D_- \gg D_+$ and $\mu_- \gg \mu_+$, we have as a further approximation

$$\bar{E}\approx\frac{D_-}{\mu_-}\left(-\frac{\nabla n}{n}\right). \qquad (11)$$

In cylindrical coordinates $\nabla n = dn/dr$ since n is a function of r only. Equation (11) thus becomes

$$-E dr=\frac{D_-}{\mu_-}\frac{dn}{n}$$

from which

$$V_p=-\int E dr=\frac{D_-}{\mu_-}\ln\left(\frac{n}{n_0}\right), \qquad (12)$$

where we have set the plasma potential $V_p=0$ at $n=n_0$.

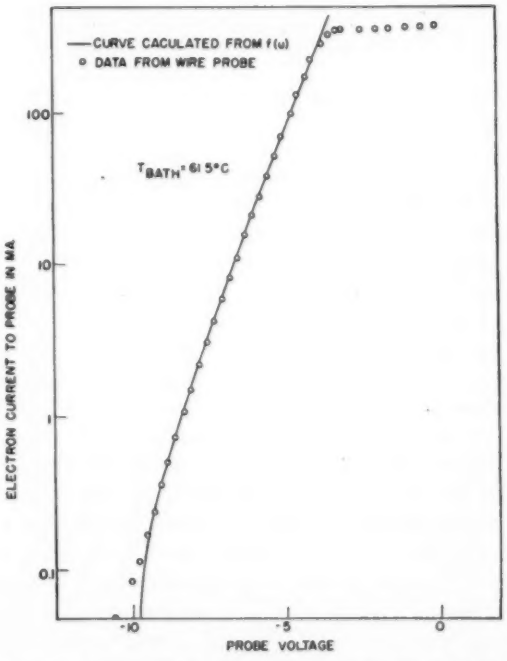

FIG. 12. Comparison of theoretical probe curve with experiment for 61.5°C bath.

[17] W. Schottky, Physik. Z. 25, 342, 635 (1924).

For a Maxwellian distribution $D_-/\mu_- = kT_-/e$, and Eq. (12) reduces to

$$n = n_0 \exp(eV_p/kT_-) \tag{13}$$

which is the familiar Boltzmann density formula.

If we eliminate $\bar{E}$ from Eqs. (7) and (8) (again letting $n_- = n_+ = n$), we can solve for the diffusion current $\bar{\Gamma}$ and obtain

$$\bar{\Gamma} = -D_a \nabla n, \tag{14}$$

where D_a is the ambipolar diffusion constant and is given by

$$D_a = \frac{D_-\mu_+ + D_+\mu_-}{\mu_+ + \mu_-}. \tag{15}$$

Ionization in the plasma of the arc discharge can take place in two ways: by direct or by cumulative ionization. When electrons ionize gas atoms by single collisions, it is known as direct ionization. When electrons raise gas atoms to an excited state as a result of a first collision and later ionize the excited atoms with a second collision, the process is known as cumulative ionization. Clearly the rate of ionization in the direct process will be proportional to the electron density n_-, while the rate of ionization in the cumulative, two-step process will be proportional to n_-^2. Each ionization results in the creation of a new free electron.

The rate of creation of new electrons in a unit volume must be equal to the rate at which they diffuse out, i.e., be equal to the divergence of the diffusion current $\bar{\Gamma}$. Thus, for direct ionization

$$\nabla \cdot \bar{\Gamma} = \nu_i n_-, \tag{16}$$

where ν_i is the average number of ionizing collisions made per second by one electron. The magnitude of ν_i will depend on: (a) the ionization probability as a function of electron energy and (b) the actual electron-energy distribution. Since probe measurements in this research and in Killian's work[3] have shown the energy distribution to be practically independent of distance from the tube axis, ν_i can be assumed to be independent of spacial coordinates. From Eq. (14) the above equation becomes

$$\nabla^2 n + \frac{\nu_i}{D_a} n = 0, \tag{17}$$

where $n_- = n$. For our case we have cylindrical geometry. We impose the boundary condition that $n = 0$ at $r = R'$, where r is the radial distance from the tube axis and R' is the effective radius of the tube for diffusion theory, i.e., the radial distance at which n would go to zero were it not for the presence of a sheath at the tube wall.

Assuming that n is a function of r only, we find that for cylindrical coordinates and the above boundary condition the solution of Eq. (17) is given by a Bessel function of order zero. That is

$$n(r) = n_0 J_0\left(\frac{2.405r}{R'}\right), \tag{18}$$

where n_0 = plasma density at the axis ($r = 0$).

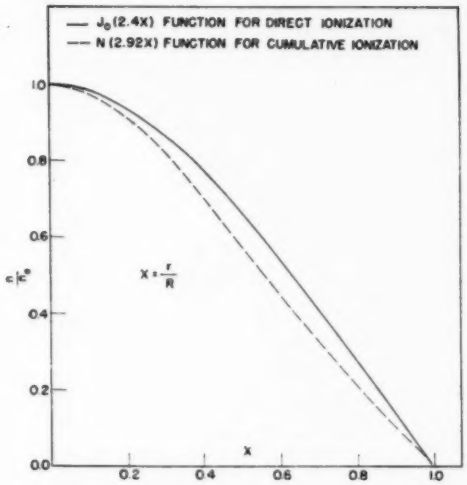

FIG. 13. Radial density distributions from diffusion theory.

It can be shown that R' should exceed the actual tube radius R by $3/4\lambda$, where λ is the mean free path of the electrons. However, this is true when the diffusion takes place for electrons of all energies, whereas only the high energy electrons in the plasma penetrate the sheath and reach the wall.

In the derivation of Eq. (17) it was assumed that the ionization was a direct, one-step process. In the case of cumulative ionization the rate of creation of free electrons will be proportional not to n_- but to n_-^2. This makes Eq. (17) nonlinear. Spenke[18] has recently solved this nonlinear equation, and the resulting function $\mathfrak{N}(2.92r/R')$ is shown in Fig. 13 along with $J_0(2.4r/R')$ for comparison. As would be expected, the $\mathfrak{N}$ curve resulting from cumulative ionization dips down more sharply from the tube axis than the J_0 curve arising from direct ionization.

From Eq. (12) we see that for direct ionization the plasma potential is given by

$$V_p = \frac{D_-}{\mu_-} \ln\left[J_0\left(\frac{2.405r}{R'}\right)\right], \tag{19}$$

whereas for cumulative ionization

$$V_p = \frac{D_-}{\mu_-} \ln\left[\mathfrak{N}\left(\frac{2.92r}{R'}\right)\right], \tag{20}$$

where $D_-/\mu_- = kT_-/e$ for a Maxwellian distribution.

B. Comparison of Diffusion Theory with Experiment

The various members of the telescope assembly serve as probe collectors positioned from tube axis to tube

[18] E. Spenke, Z. Physik **127**, 221 (1950).

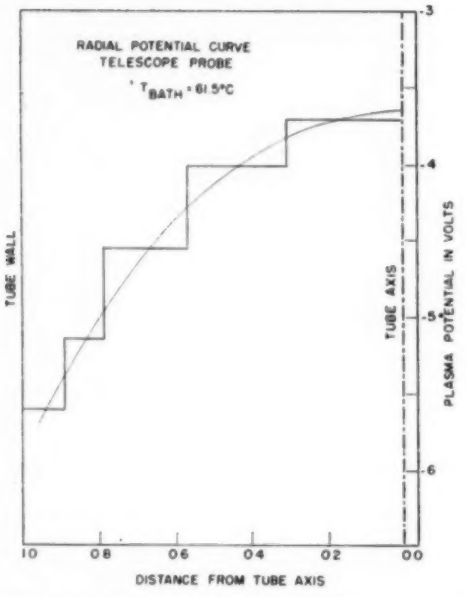

FIG. 14. Radial variation in plasma potential as a step function

wall. The plasma potential or density, as obtained from each of these probes, represents the average taken over the length of the probe. Hence it would seem appropriate to plot radial potential or density data in the form of a step function, as shown in Fig. 14, where the width of each step represents the finite length of each probe. A smooth curve can be drawn through the steps, and it is reasonable to assume that this curve is a fair representation of the continuous plasma variation in potential from tube axis to tube wall. The smooth curve suggests, in turn, that we arbitrarily assign the mid-

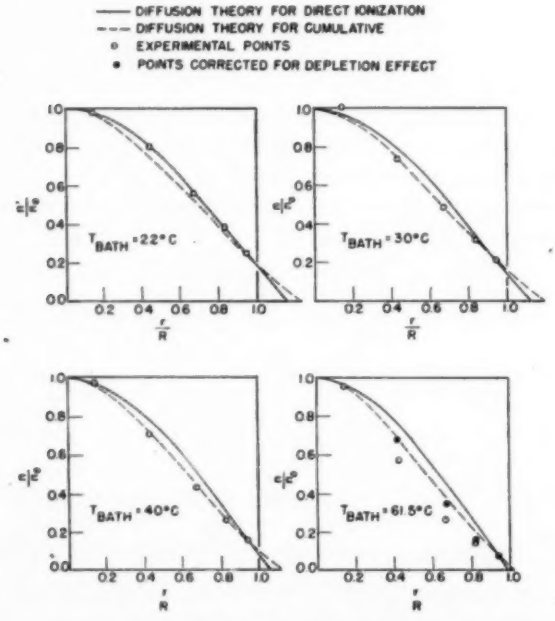

FIG. 15. Comparison of experimental radial density distributions with diffusion theory.

point of each probe segment as the representative point for the radial distance of that probe from the tube axis.

In this way the experimental points have been plotted in Fig. 15, where the observed radial density distribution is compared with the J_0 and $\mathfrak{N}$ curves for direct and cumulative ionization, respectively. The value of R' has been selected in each case to make a good fit between theory and experiment near the wall. At 30°C and 40°C bath temperature the cumulative ionization theory seems to be a better fit. At 22°C the direct ionization theory is a little better. However, at this low pressure the mean free path of the electrons is the order of the tube radius. Therefore the applicability of diffusion theory is somewhat doubtful.

At 61.5°C bath temperature the observed density distribution dips below the cumulative ionization curve. This is believed to be the result of plasma density depletion which is due to the larger area of those probes located away from the tube axis. This theory is borne out by comparing the probe currents obtained from the swivel probe and wire probe at the same bath temperatures. Both of these collectors are located at the tube axis, but the swivel probe has approximately four times the area of the wire probe (0.60 cm² compared with

TABLE I.

T_{bath}	Pressure	λ (for kT_-)	$\frac{3/4\lambda}{R}$	$\frac{R'-R}{R}$
22°C	0.00175 mm	2.3 cm	0.64	0.24
30°C	0.0034	1.0	0.28	0.20
40°C	0.0076	0.4	0.11	0.12
61.5°C	0.035	0.07	0.02	0.027

0.13 cm²). At 22°C, 30°C, and 40°C the ratio of electron current at the swivel probe to electron current at the wire probe remains fixed, indicating that no depletion effect is taking place, whereas at 61.5°C the ratio is down by 30 percent. One can also observe a definite darkening of the plasma in the region surrounding the swivel probe when it is maintained at or above plasma potential. All of these facts indicate that at 61.5°C bath temperature (0.035-mm Hg), the finite area of the probe can cause an appreciable decrease in plasma density about the probe. If one makes a linear correction with the probe area of the experimental densities (based on the difference in densities as measured with plane and wire probes at the axis), points are obtained which lie more nearly on the cumulative ionization curve at 61.5°C.

We have already pointed out that $R'-R$ should equal $3/4\lambda$ when diffusion to the wall takes place for electrons of all energies. It was also observed that in our case only the high energy electrons penetrate the sheath, and that therefore one would expect $R'-R$ to be greater than $3/4\lambda$ (in general, λ increases with the electron-energy increase). Nevertheless, we find that $R'-R \approx 3/4\lambda$ when one calculates the mean free path λ

from Brode's curves[16] for electrons of energy kT_-. This is illustrated in Table I.

The actual mean free paths of electrons are probably smaller than those obtained for collisions with mercury atoms as a result of electron-electron interactions. Thus the above agreement may be pure chance; that is, the mean free path of the fast electrons which diffuse to the wall may be just enough smaller than the values taken from Brode's curve to give approximate agreement with those same values calculated for an energy kT_-.

The theoretical plasma potential variations with radius are compared with experiment in Fig. 16. At 22°C the plasma potential has been calculated from

$$\frac{kT_-}{e}\ln\left[J_0\left(\frac{2.4r}{R'}\right)\right].$$

For the higher bath temperatures

$$\frac{kT_-}{e}\ln\left[\mathfrak{R}\left(\frac{2.92r}{R'}\right)\right]$$

has been used. T_- was obtained from the upper slope of the plane- (swivel-) probe curve in each case. The agreement seems to be well within the experimental error, even though it is not quite correct to substitute kT_-/e for D_-/μ_- when the distribution is not perfectly Maxwellian. Indeed, to say that T_- as obtained from the upper slope of the plane-probe curve is an electron temperature loses its meaning in the face of a non-Maxwellian distribution.

A direct determination of D_-/μ_- can be obtained by plotting $\log n_-$ (obtained from Eq. (1) when $V=V_p$) *vs* plasma potential V_p for the telescope probes at each bath temperature. This has been done in Fig. 17. Reference to Eq. (12) shows that the resulting linear plots should have a slope of $0.434\mu_-/D_-$. When these slopes are converted to temperature units, the resulting temperatures are lower than those obtained from the upper slope of the probe curves themselves. At 20°C, 30°C, 40°C, and 61.5°C the temperatures are 18.5 percent, 10 percent, 7 percent, and 10 percent low, respectively. This is exactly what we should expect, since D_-/μ_- must be less than kT_-/e for a distribution depleted from a Maxwellian in the high energy region, where kT_-/e represents the slope of the probe curve at low energies.

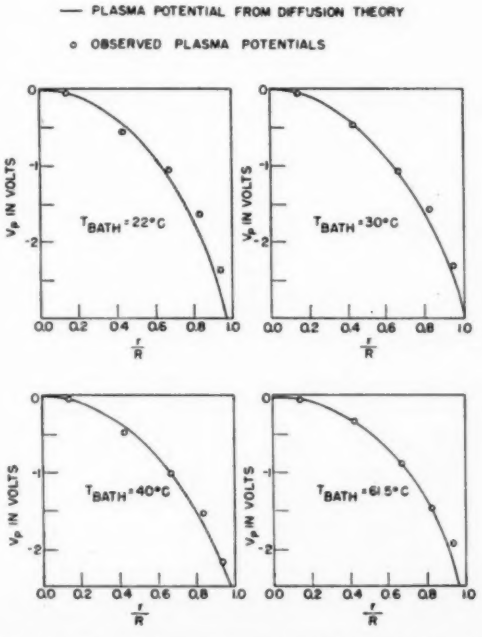

FIG. 16. Comparison of experimental radial potential distributions with diffusion theory.

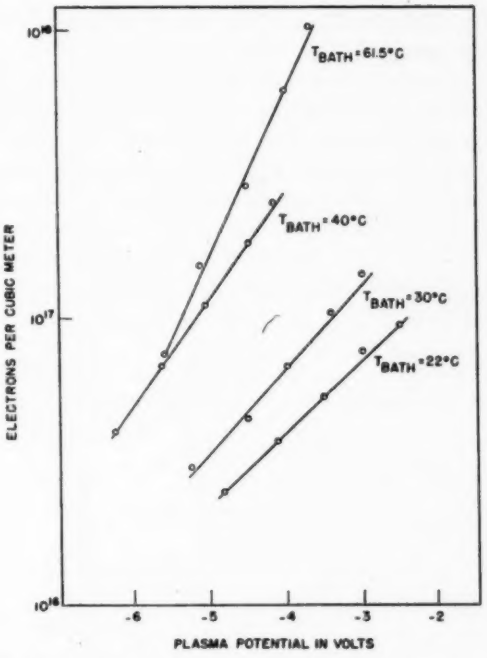

FIG. 17. Log density *vs* plasma potential from tube axis to wall.

IX. CONCLUSIONS REGARDING THE IONIZATION PROCESS IN THE ARC

In the previous section we saw that the radial potential and density distributions in the arc seemed to show better agreement with diffusion theory when cumulative ionization was assumed. From these facts alone, however, it is hardly safe to infer the type of ionizing process, since the difference between the theoretical radial density distributions for direct and cumulative ionization processes is not large. A more straightforward approach is to calculate the rate of direct ionization in the plasma from the known ionization probability and electron-energy distribution. If this calculated rate of ionization falls short of the observed rate (as obtained from the positive ion current to the wall), the difference must be due to cumulative ionization. The theoretical distribution function given in Eq. (5) and illustrated in Figs. 11 and 12 has been used for this calculation at 22°C bath temperature, since it

exhibits a reasonably good fit with experiment over the required energy range. The distribution must be displaced in velocity space to take care of the drift effects (at 22°C this increases the direct ionization by a factor of two). The positive ion wall current resulting from ionization calculated in this way is 2.10 amp/m² compared with the observed wall current of 4.58 amp/m². This would indicate that even at 22°C bath temperature (0.00175-mm Hg) a direct process accounts for only half of the ionization; the remainder is presumably cumulative.

For bath temperatures of 30°C and above the density of high energy electrons capable of direct ionization is even less than at 22°C, indicating that cumulative ionization predominates. These results are substantially in agreement with the work of Klarfeld,[15] who concluded that for mercury-arc pressures above 0.001-mm Hg cumulative ionization is taking place.

The author is indebted to Professor W. B. Nottingham for his many valuable suggestions and constant interest in this research and to Professor W. P. Allis for his considerable help with the theory.

APPENDIX. SUMMARY OF DATA

T = 22°C	i_+ (ma)	i_- (ma)	T_- (°K)	V_{plasma} (volts)	Area (cm²)	i_+ dens. (amp/m²)	i_- dens. (amp/m²)	electrons per $m_{-1}{}^3 \times 10$
Plane probe	0.505	157	23 800	−3.7	0.60	8.42	2620	
Wall probe	0.0423	13.0	23 500	−4.35	0.923	4.58	1410	
Wire probe	0.157	48.5		−2.5	0.133	11.8	3650	9.52
Cyl No. 1	0.377	117		−3.0	0.396	9.52	2950	7.70
Cyl No. 2	0.335	109		−3.5	0.537	6.25	2070	5.40
Cyl No. 3	0.139	47.3		−4.1	0.331	4.20	1430	3.73
Cyl No. 4	0.112	42.1		−4.8	0.441	2.54	955	2.50
T = 30°C								
Plane probe	0.624	210	18 800	−4.25		10.4	3500	
Wall probe	0.0444	13.9	18 600	−4.8		4.8	1510	
Wire probe	0.219	64		−3.0		16.5	4810	14.2
Cyl No. 1	0.448	141		−3.4		11.3	3560	10.5
Cyl No. 2	0.365	125		−4.0		6.80	2330	6.85
Cyl No. 3	0.152	51		−4.5		4.60	1540	4.53
Cyl No. 4	0.121	46		−5.25		2.75	1040	3.06
T = 40°C								
Plane probe	0.897	317	14 340	−5.6		15.0	5290	
Wall probe	0.050	16.5	14 300	−6.1		5.42	1790	
Wire probe	0.331	100		−4.15		24.9	7520	25.3
Cyl No. 1	0.652	218		−4.5		16.5	5500	18.5
Cyl No. 2	0.48	177		−5.05		8.94	3300	11.1
Cyl No. 3	0.189	68		−5.63		5.72	2060	6.92
Cyl No. 4	0.140	53.5		−6.25		3.18	1210	4.06
T = 61.5°C								
Plane probe	2.28	820	10 400	−4.85		38.0	13 650	
Wall probe	0.063	28	10 200	−5.25		6.83	3030	
Wire probe	1.00	352	9530	−3.70		75.2	26 500	105
Cyl No. 1	1.57	615		−4.0		39.6	15 500	62.5
Cyl No. 2	0.982	396		−4.55		18.3	7380	29.3
Cyl No. 3	0.294	127		−5.13		8.88	3840	15.2
Cyl No. 4	0.189	84		−5.6		4.28	1900	12.0

JOURNAL OF APPLIED PHYSICS VOLUME 24, NUMBER 7 JULY, 1953

A Certain Problem in Heat Conduction

HENRY ZATZKIS
Department of Mathematics, University of Connecticut, Storrs, Connecticut
(Received February 6, 1953)

A homogeneous sphere is surrounded by an infinite homogeneous medium. Heat is generated inside the sphere at a prescribed rate. The temperature distribution inside and outside the sphere is computed.

I. INTRODUCTION

IN connection with a certain problem in biophysics Schaefer and Schwan[1] posed the following problem: A homogeneous sphere of radius R is imbedded in an infinite homogeneous medium. Initially the temperature is zero everywhere. From the time $t=0$ on, heat is generated continuously in the interior of the sphere, at the rate of $Q(t)$ per unit volume per unit time.

The question is, what is the temperature distribution inside and outside the sphere at any later time? Schaefer and Schwan attacked the problem experimentally by setting up a large-scale model. Then, using dimensional analysis, they computed from their data the values for the actual physical conditions. They admitted the possibility that the temperature at the boundary of the two media may show a jump, but they postulated that the heat current density shall change continuously. We shall, however, assume that the temperature changes continuously, whereas the heat current may change discontinuously due to the presence of the heat generation inside the sphere. Naturally, both quantities change continuously in the steady-state case. Whereas the results obtained by the above-named investigators are not general and apply only to the particular type of heat generation employed in their experiments, we shall give here a general solution valid for any arbitrary mode of heat production.

We shall use spherical coordinates and choose the center of the sphere as origin. The following notation will be used:

r = radial distance,
t = time,
ρ = density of sphere,
c = specific heat of sphere,
k = thermal conductivity of sphere,
$a^2=k/c\rho$ = thermal diffusivity of sphere,
R = radius of sphere,
$Q(t)$ = rate of heat produced in the sphere per unit time per unit volume,
k' = thermal conductivity of surrounding medium,
C = thermal diffusivity of surrounding medium,
$U=U(r,t)$ = temperature inside sphere,
$U'=U'(r,t)$ = temperature outside sphere,

$$\operatorname{erf}(x)=\frac{2}{\sqrt{2\pi}}\int_0^x e^{-w^2}dw.$$

[1] H. Schaefer and H. Schwan, Ann. Physik 43, 99 (1943).

The Laplace transform $L\{F(t)\}$ of a function $F(t)$ will be denoted by the corresponding lower case letter $f(s)$, i.e.,

$$f(s)=L\{F(t)\}=\int_0^\infty e^{-st}F(t)dt.$$

The problem to be solved can now be formulated:

$$\partial U/\partial t=a^2\nabla^2U+Q/\rho c, \quad (0\leqq r<R,\ 0\leqq t) \tag{1}$$

$$\partial U'/\partial t=C^2\nabla^2U', \quad (R<r,\ 0\leqq t) \tag{2}$$

$$Q=Q(t), \text{ continuous}, \quad (0\leqq t) \tag{3}$$

$$Q(0)=0, \tag{4}$$

$$U(r,0)=0, \tag{5}$$

$$U'(r,0)=0, \tag{6}$$

$$\lim_{r\to\infty}U'(r,t)=0 \text{ for all } t, \tag{7}$$

$$U(R,t)=U'(R,t)\equiv F(t) \text{ for all } t. \tag{8}$$

II. THE INTERIOR PROBLEM

It is well known[2] that the solution of the equation

$$\partial U/\partial t=a^2\nabla^2U$$

in the presence of a continuous distribution of heat sources with density $Q(x,y,z,t)$ is given by

$$U(x,y,z,t)=\frac{1}{8\pi^{\frac{3}{2}}c\rho a^3}\int_{x'=-\infty}^{x'=\infty}\int_{y'=-\infty}^{y'=\infty}\int_{z'=-\infty}^{z'=\infty}\int_{w=0}^{w=t}\frac{Q(x',y',z',w)}{(t-w)^{\frac{3}{2}}}$$
$$\times\exp\left[-\frac{(x-x')^2+(y-y')^2+(z-z')^2}{4a^2(t-w)}\right]dx'dy'dz'dw.$$

The solution of Eq. (1) is therefore

$$U(x,y,z,t)=\frac{1}{\rho c}\int_0^t Q(w)dw$$
$$+\frac{1}{8\pi^{\frac{3}{2}}c\rho a^3}\int\int\int_{\text{sphere}}\int_{w=0}^{w=t}\frac{Q(w)}{(t-w)^{\frac{3}{2}}}$$
$$\times\exp\left[-\frac{(x-x')^2+(y-y')^2+(z-z')^2}{4a^2(t-w)}\right]dx'dy'dz'dw. \tag{9}$$

[2] B. Baule, *Die Mathematik des Naturforschers und Ingenieurs* (S. Hirzel, Zürich, 1947), Vol. VI, third edition, p. 64.

By using polar coordinates, the volume integral can be evaluated and we obtain

$$U(r,t)=\frac{1}{\rho c}\int_0^t Q(w)dw$$
$$+\frac{a}{\sqrt{2\pi}rc\rho}\int_0^t Q(w)\left\{\exp\left[-\frac{(R-r)^2}{4a^2(t-w)}\right]\right.$$
$$\left.-\exp\left[-\frac{(R+r)^2}{4a^2(t-w)}\right]\right\}(t-w)^{\frac{1}{2}}dw$$
$$+\frac{1}{2\rho c}\int_0^t Q(w)\left[\operatorname{erf}\left(\frac{r-R}{2a(t-w)^{\frac{1}{2}}}\right)\right. \quad (10)$$
$$\left.-\operatorname{erf}\left(\frac{r+R}{2a(t-w)^{\frac{1}{2}}}\right)\right]dw.$$

At the surface of the sphere the temperature is

$$F(t)\equiv U(R,t)=\frac{a}{\sqrt{\pi}rc\rho}\int_0^t Q(w)$$
$$\times\left\{1-\exp\left[-\frac{R^2}{a^2(t-w)}\right]\right\}(t-w)^{\frac{1}{2}}. \quad (11)$$

III. THE EXTERIOR PROBLEM

This problem is best handled by the method of the Laplace transform. The transform of Eq. (2) is in polar coordinates

$$\frac{d^2(ru')}{dr^2}=\frac{s}{C^2}(ru'). \quad (12)$$

Therefore

$$u'=\frac{1}{r}\left[A\exp\left(\frac{s^{\frac{1}{2}}}{C}r\right)+B\exp\left(-\frac{s^{\frac{1}{2}}}{C}r\right)\right]. \quad (13)$$

Condition (7) shows that $A=0$, i.e.,

$$u'=B\exp\left(-\frac{s^{\frac{1}{2}}}{C}r\right). \quad (14)$$

Equation (8) determines B, *viz.*

$$u'(R,s)=\frac{B}{R}\exp\left(-\frac{s^{\frac{1}{2}}}{C}R\right)=f(s), \quad (15)$$

hence

$$B=Rf(s)\exp\left(\frac{s^{\frac{1}{2}}}{C}R\right), \quad (16)$$

and therefore

$$u'(r,s)=\frac{R}{r}f(s)\exp\left[-\frac{(r-R)}{C}s^{\frac{1}{2}}\right]. \quad (17)$$

The inverse Laplace transform of Eq. (17) finally gives the result

$$U'(r,t)=\frac{R(r-R)}{2\sqrt{\pi}rC}$$
$$\times\int_0^t\frac{F(w)}{(t-w)^{\frac{3}{2}}}\exp\left[-\frac{(r-R)^2}{4C^2(t-w)}\right]dw. \quad (18)$$

That this solution satisfies the correct boundary condition can easily be verified by using a new variable of integration z, where

$$t-w=\frac{(r-R)^2}{4C^2z^2}. \quad (19)$$

We then obtain

$$U'(r,t)=\frac{2R}{r\sqrt{\pi}}\int_0^\infty F\left(t-\frac{(r-R)^2}{4C^2z^2}\right)\exp(-z^2)dz. \quad (20)$$

Equation (20) shows that

$$U'(R,t)=\frac{2}{\sqrt{\pi}}F(t)\int_0^\infty e^{-z^2}dz=F(t). \quad (21)$$

If the expression for $F(t)$, given by Eq. (11), is substituted into Eq. (18), we finally obtain for the exterior temperature the result

$$U'(r,t)=\frac{aR(r-R)}{2\pi Cc\rho r^2}\int_{x=0}^{x=t}\int_{y=0}^{y=x}\frac{Q(y)}{(x-y)^{\frac{1}{2}}}$$
$$\times\left\{\exp\left[\frac{(r-R)^2}{a^2(t-y)}\right]-1\right\}(t-y)^{\frac{1}{2}}dydx. \quad (22)$$

Potential Analog Network Synthesis for Arbitrary Loss Functions*

ERNEST SHIU-JEN KUH
Bell Telephone Laboratories, Murray Hill, New Jersey
(Received March 9, 1953)

A general method is developed for designing networks with arbitrary loss functions based on the potential analogy. An appropriate potential problem is formed on the basis of the given loss function by introducing continuous charge distribution on the complex frequency plane. After the potential problem is solved, the technique of quantization of charge is used to find the natural modes of the network function.

I. INTRODUCTION

NETWORK synthesis, in general, has two main parts: first, the approximation problem, or the determination of the location of the poles and zeros of the network function to give a desired response; second, the realization problem, or the determination of the configuration of the network and the circuit elements to yield these poles and zeros. In this work, only the first part is investigated; but the second part can be handled by already known methods.[2,3] A general method is presented here for solving the approximation problem for arbitrary loss functions in the steady-state theory of lumped constant linear passive networks.

This paper presumes a knowledge of the potential analogy applied in network synthesis.[4–6] The terms used throughout are defined in the following way. Letting

$$W(p)=V+j\Psi=\frac{1}{2\pi}\ln\frac{(p-p_1)(p-p_2)(p-p_3)\cdots\dagger}{(p-p_a)(p-p_b)(p-p_c)\cdots} \tag{1}$$
$$=\frac{1}{2\pi}\ln G(p)$$

hence

$$V=\frac{1}{2\pi}\ln|G| \quad \text{and} \quad \Psi=\frac{1}{2\pi}\measuredangle(G), \tag{2}$$

where W is the complex potential function of a system of filamentary charges piercing the complex frequency p plane, V is the real potential and Ψ is the stream or flux function. $G(p)$ is the complex power ratio function of a 4-terminal network, defined as input over output. On the real frequency axis of the complex frequency plane, $p=j\omega$,

$$G(j\omega)=e^{2\alpha}, \quad \text{or} \quad V=\alpha/\pi, \tag{3}$$

where α is the loss function in nepers. Positive filamentary charges (p_a, p_b, p_c) correspond to poles of $G(p)$ or points of infinite loss, and negative charges (p_1, p_2, p_3) to zeros of $G(p)$ or the natural modes.

The use of the potential analogy method in solving the band-pass filter problem was developed recently.[6–9] This technique is now extended and modified for the problem of the arbitrary loss function. Therefore a review of the band-pass filter problem is necessary.

On the complex frequency plane a conducting plate which gives a constant potential is laid along the prescribed pass band. Positive filamentary charges are located symmetrically anywhere on the plane, as desired. The whole potential problem is solved with the prescribed boundary conditions as shown in Fig. 1. A

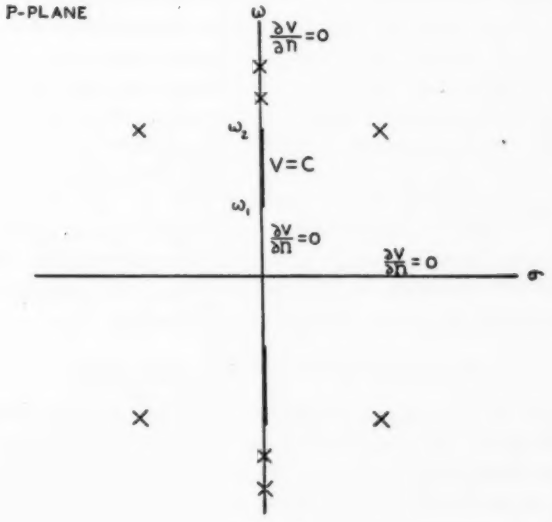

FIG. 1.

* This paper is one portion of a Ph.D. dissertation "A study of the network synthesis approximation problem for arbitrary loss functions" written for the Electrical Engineering Department of Stanford University, February, 1952. Also see reference 1.

† Units are defined arbitrarily.

[1] E. S. Kuh, "A study of the network synthesis approximation problem for arbitrary loss functions," Tech. Report No. 44, Electronics Research Laboratory, Stanford University (February, 1952).
[2] S. Darlington, J. Math. Phys. **18**, 257–353 (1939).
[3] E. A. Guillemin, "A summary of modern methods of network synthesis" in *Advances in Electronics* (Academic Press, Inc., New York, 1951), Vol. 3.
[4] W. W. Hansen and O. C. Lundstrom, Proc. Inst. Radio Engrs. **33**, 528–538 (1945).
[5] S. Darlington, Bell System Tech. J. **30**, 315–365 (1951).
[6] J. F. Klinkhamer, Philips Research Reports **3**, 60–80, 378–400 (1948).
[7] R. M. Fano, J. Franklin Inst. **249**, 189–205 (1950).
[8] D. L. Trantman, Jr., "Amplifier synthesis through conformal representation," Tech. Report No. 41, Electronics Research Laboratory, Stanford University (December, 1951).
[9] G. L. Matthaei, "A general method for synthesis of filter transfer functions as applied to L-C and R-C filter examples," Tech. Report No. 39, Electronics Research Laboratory, Stanford University (August, 1951).

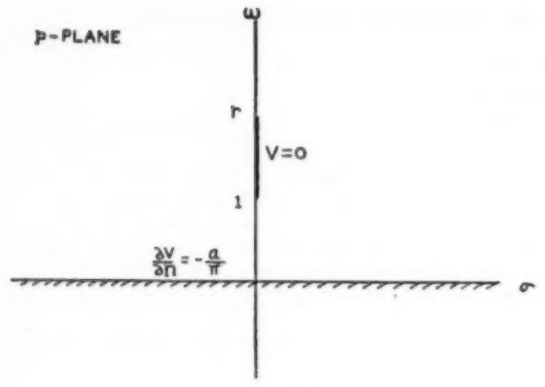

FIG. 2.

complete picture of potential variation and flux can now be calculated.

A plate of continuous charge corresponds to a branch cut of the network function, which is not physically realizable. Therefore what is left to be done is to approximate the plate's effect by suitably placing filamentary negative charges. The method is stated briefly as follows: The total charge m in the band from

$$\omega_1 \text{ to } \omega_2 \text{ is } \int_{\omega_1}^{\omega_2} -2\pi(\partial V)/(\partial n)d\omega,$$

where $\partial V/\partial n$, the normal derivative of the potential off the plate, is proportional to the negative of the charge density. The continuous charge must now be replaced by m unit filamentary charges such that the proper density is approximated in some fashion. The obvious way is to quantize the continuous charge at the centroids of the charge density curve for each unity subarea. With the negative filamentary charges so obtained, the potential along the band is constant in equal ripple manner and has its minimum at negative infinity. The next step is to move the negative charges off the $j\omega$ axis along the flux lines and onto an *equipotential surface*. All the ripples will remain equal as the negative charges move outwards but their magnitude will gradually decrease. Thus, by specifying the amount of the ripple, negative charges can be located.

II. STATEMENT OF THE PROBLEM

Let an arbitrary loss function $\alpha_0=f(\omega)$ (not a constant as above, and not directly realizable) be given in a prescribed frequency band. The poles and zeros of $G(p)$ are wanted such that the loss function α gives a close approximation to α_0 in the given band. In terms of the potential problem, filamentary charges are needed so that V in the given band gives an approximation to α_0/π, as seen in Eq. (3). Moreover symmetry of the charges and physical realizability must be considered.

This problem differs from the usual filter problem in that the real potential along the band of interest is not a constant. Although the potential problem can still be solved by specifying the desired real potential along the given band, yet the quantization procedure is not applicable. The theory given in the next section will illustrate how the filamentary charges can be found by modifying the potential problem and introducing continuous charge distribution. This method is different from Darlington's[5] in that there is no need to choose a contour.

Before developing the complete theory, a special example of a linearly increasing loss function $\alpha_0=f(\omega)=a\omega$, for a frequency band $1\leq\omega\leq r$ is taken. Suppose

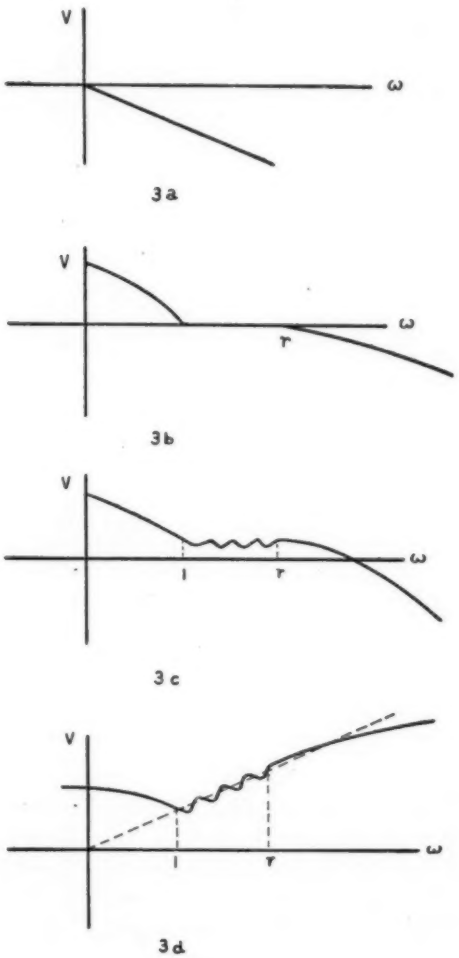

FIG. 3.

that an immobile‡ uniform continuous charge with $-\partial V/\partial n=a/\pi$, is laid on the σ axis on the p plane as shown in Fig. 2. From the electrostatic theory, the real potential along the imaginary axis is linearly decreasing as shown in Fig. 3a. An uncharged conducting plate is then put down on the imaginary axis from $\omega=1$ to $\omega=r$. The potential is therefore required to be a constant along the band as shown in Fig. 3b. Now the potential

‡ The word "immobile" is used to differentiate the fixed continuous charge distribution from that of a conducting plate. The charges on a conducting plate can be moved by outside field.

problem in Fig. 2 with boundary conditions, $V=0$ for $\sigma=0$, $1\leq\omega\leq r$ and $\partial V/\partial n=-a/\pi$ for $\omega=0$ is solved. Since the real potential along the band of interest is constant, the same quantization procedure as in the filter problem can be performed. The real potential along the band would be expected to have a filter characteristic of the equal ripple type in the presence of both the quantized charges and the undisturbed continuous charge on the σ axis, as shown in Fig. 3c. Finally, if the continuous charge along the σ axis is removed, the potential along the given band, due to the filamentary charges alone, will be expected to have an equal ripple approximation to the linearly increasing function, as shown in Fig. 3d.

To solve the aforementioned potential problem, the following transformation is required to take account of the infinite amount of charge on the σ axis. Letting

$$V_1=V+a/\pi\omega \tag{4}$$

the new boundary conditions become

$$\partial V_1/\partial\omega=-a/\pi+a/\pi=0 \quad \text{for} \quad \omega=0, \tag{5}$$

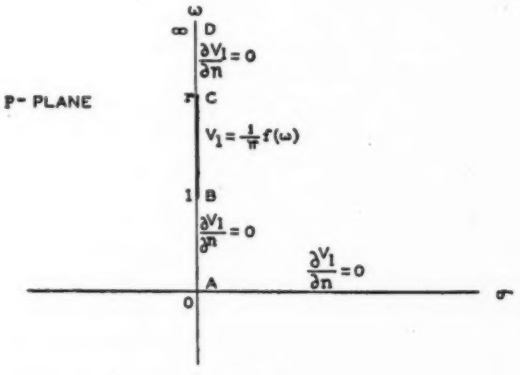

FIG. 4.

and

$$V_1=a/\pi\omega \quad \text{for} \quad \sigma=0 \quad \text{and} \quad 1\leq\omega\leq r. \tag{6}$$

With these boundary conditions, V_1 can be found by using an elliptic tangent transformation as discussed in the next section. Hence the problem of the linearly increasing loss function can be solved.

III. THEORY

The general theory is developed from the preceding particular example. The complete potential problem can be separated into three parts. First, a complex potential W_1, is obtained with a boundary condition $V_1=\alpha_0/\pi$ in the given band. This corresponds to V_1 in the preceding example as seen from Eq. (6). Second, a continuous charge distribution on the p plane is introduced such that in the given band, $V_2=-\alpha_0/\pi$. This corresponds to the $-a/\pi\omega$ term in Fig. 3a of the preceding example. It is seen that the sum of V_1 and V_2 is a constant along the band of interest. Third, a complex potential W_3 is formed by specifying the total number and position of the positive filamentary charges. This is exactly the same as the complex potential in the filter problem with a conducting plate at the prescribed band. It is clear that the superposition of the three still gives a constant potential along the prescribed frequency band. If now quantization of negative charge is performed and the continuous charge due to W_2 thrown away, a good approximation of the required potential along the given band is obtained. Actually, the continuous charge distribution along the σ axis is only used in the calculation for quantization purpose. Next, the three complex potential functions are discussed separately.

The first part involves only the solution of a straightforward potential problem. In order to specify it, the loss function $\alpha_0=f(\omega)$ is prescribed for a frequency band $1\leq\omega\leq r$ without losing any generality. Then the potential problem is given in terms of the following boundary conditions on the complex frequency plane.

$$V_1=1/\pi f(\omega), \quad \text{for} \quad \sigma=0, \quad 1\leq\omega\leq r \tag{7}$$

and from the symmetry of the right and left, upper and lower half-planes,

$$\frac{\partial V_1}{\partial n}=0 \quad \text{for} \quad \begin{cases} \sigma=0, & \begin{cases} 0\leq\omega\leq 1 \\ r\leq\omega\leq\infty \end{cases} \\ \text{and} & \omega=0, \quad 0\leq\sigma\leq\infty. \end{cases} \tag{8}$$

Thus on the p plane, charge exists only in the band $1\leq\omega\leq r$ on the $j\omega$ axis, and the total charge is zero because there is to be no charge elsewhere. Since V is an even function with respect to both σ and ω, a solution covering one-quarter of the p plane is sufficient. The elliptic-tangent transformation may be used to transform the semi-infinite plane into a rectangular cell as shown in Figs. 4 and 5. The corresponding critical points are indicated and the boundary conditions specified. Mathematically,

$$p=sn(z, k), \tag{9}$$

where

$$k=(1-k'^2)^{\frac{1}{2}} \quad \text{and} \quad k'=1/r. \tag{10}$$

k and k' are called the modulus and complementary

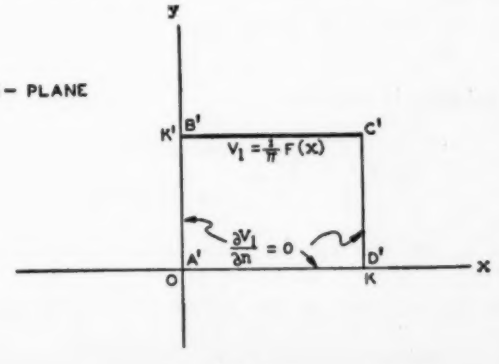

FIG. 5.

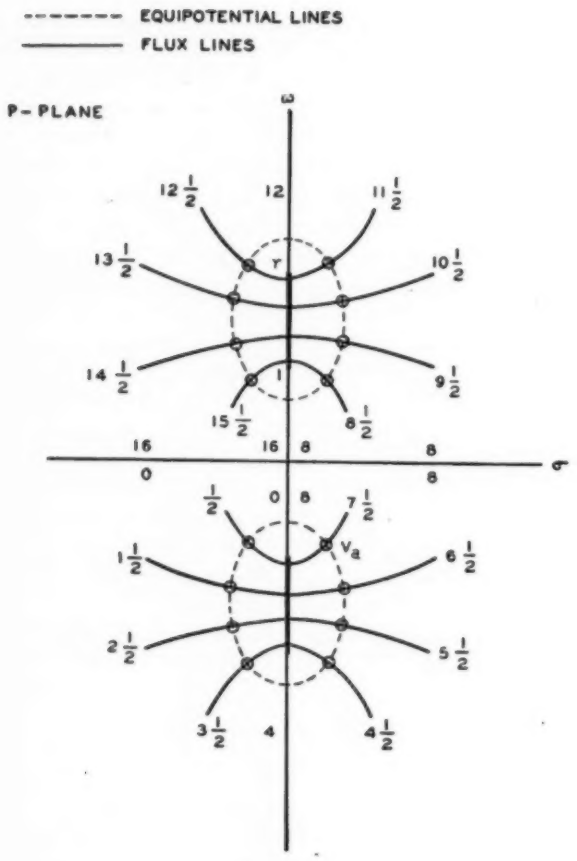

FIG. 6.

modulus. The notation used here follows that in most mathematical textbooks on the Jacobian elliptic functions.[10] Thus K and K' in Fig. 5 are the usual symbols related to the periods of the functions.

Solving the potential problem inside a rectangular cell is straightforward. The boundary conditions are transformed as

$$V_1=1/\pi f(\omega)=1/\pi f\left[\frac{1}{dn(x,k)}\right]$$

$$=1/\pi F(x), \quad \text{for} \quad z=x+jK' \tag{11}$$

and

$$\frac{\partial V_1}{\partial n}=0, \quad \text{for} \quad z=x, \quad \text{and} \quad z=\begin{cases} jy \\ K+jy. \end{cases} \tag{12}$$

The solution is therefore,

$$W_1=\frac{a_0}{2}+\sum_{n=1}^{\infty} a_n\frac{\cos(n\pi z/K)}{\cosh(n\pi K'/K)}, \tag{13}$$

where a_n are the Fourier coefficients of the function $1/\pi F(x)$.

The second part of the method is to introduce a symmetrical charge distribution on the complex frequency plane such that $V_2=-1/\pi f(\omega)$ along the prescribed band, $1\leq\omega\leq r$. This is an independent problem, and V_2 is due to this charge alone. The solution is given by

$$W_2=-1/\pi f(-jp). \tag{14}$$

Note that this equation is good only for $\omega\geqq 0$. At real frequencies, $\sigma=0$,

$$W_2=V_2+j\Psi_2=-1/\pi f(\omega). \tag{15}$$

This is nothing more than the application of the theory of analytic continuation. From the given value of the real potential along a band on the imaginary axis, the potential and the flux function for the rest of the $j\omega$ axis are constructed. Hence the complex potential throughout the p plane is also obtained. Charge distribution is introduced (by implication) somewhere on the p plane along with W_2. In the preceding example this continuous charge distribution is most easily seen on the σ axis with a uniform charge density, $-2\pi\partial V/\partial n=2a$.

The third complex potential function, W_3, is formed from positive filamentary charges and the negatively charged conducting plate on the prescribed band. The number of positive charges must be a multiple of four, because of the symmetries of the upper and lower, right and left half-planes:—moreover, it must be equal to the desired number of negative charges on the plate and its image below the real axis. Depending upon how good an approximation is required and how many elements can be afforded in the final network, the total number of positive charges is determined. The positions of the filaments of charge are somewhat arbitrary, yet the charges should be placed in the most efficient way, from the point of view of the final result of the approximation, the calculation procedure, and the desired network configuration. Usually they are put on the $j\omega$ axis either at the point of infinity or at zero frequency, depending on the shape of the required curve. To show how this potential problem is solved, for simplicity, all the positive charges (m units) are put at infinity. On the z plane, correspondingly, m positive charges are placed at the point $(K,0)$. Using the method of images, it is found

$$W_3=m/2\pi \ln \operatorname{sn}(S, k_1)+C, \tag{16}$$

where sn is the Jacobian-sine function and C is a real negative constant to fulfill the condition $V_3=0$ along the given band. Because of the difference of the periods of this and the elliptic function used in the transformation, a change of variable and modulus has to be made. The results are

$$S=A[z-(K+j2K')]. \tag{17}$$

and

$$k_1=\frac{1-k'}{1+k'}, \quad A=\frac{1}{1+k'}. \tag{18}$$

The reason that W_3 must be added to the first two complex potential functions is to insure that there is

[10] E. T. Whittaker and G. N. Watson, *A Course of Modern Analysis* (Cambridge University Press, Cambridge, 1950).

only negative charge along the prescribed band. It is found that the sum of W_1 and W_2 has a saddle point inside the prescribed band (i.e. two different kind of charges exists above and below the saddle point). W_3 is therefore added to move the saddle point outside such that quantization of charge is possible.

After the discussion of the three complex potential functions, the final stage, the quantization of charges, is reached. Letting

$$W_t = W_1 + W_2 + W_3, \tag{19}$$

the following transcendental equation,

$$W_t = V_t + j\Psi_t = V_a + j\begin{cases}\Psi_1\\ \Psi_2\\ \Psi_3\\ .\\ .\\ .\end{cases} \tag{20}$$

is to be solved. The roots represent the natural modes of the network function. V_a is the real potential of an equipotential line on which the negative filamentary charges are quantized. Ψ_1, Ψ_2, Ψ_3, etc. represent the flux lines passing through the centroids of each unity charge on the band. Thus if $m=16$, four unit charges are found in each quadrant. Ψ_1, Ψ_2, Ψ_3, etc. are then $\frac{1}{2}$, $1\frac{1}{2}$, $2\frac{1}{2}$, etc. as shown in Fig. 6. The procedure of solving Eq. (20) is rather involved. However, this can be done graphically to a good approximation.

IV. EXAMPLE

Again the linearly increasing loss function $\alpha_0 = f(\omega) = a\omega$ is taken. But instead of going through the logic, the theory developed in the last section is used. From Eq. (11),

$$\frac{1}{\pi}F(x) = \frac{1}{\pi}\frac{a}{dn(x, k)}. \tag{21}$$

The Fourier expansion of this function is tabulated in many books.[10] Hence

$$a_n = (\Psi)^n \frac{2aq^n}{Kk'(1+q^{2n})}, \tag{22}$$

where q is another parameter used in elliptic function theory,

$$q = \exp[-(\pi K'/K)]. \tag{23}$$

Therefore

$$W_1 = \frac{a}{2Kk'} + \frac{2a}{Kk'}\sum_{n=1}^{\infty}(-)n\frac{q^n}{1+q^{2n}}\frac{\cos(n\pi z/K)}{\cosh(n\pi K'/K)}. \tag{24}$$

This series converges very rapidly; only three or four terms are needed to get practical results.

From Eq. (14),

$$W_2 = -1/\pi(-jap) = jap/\pi, \tag{25}$$

where

$$V_2 = -\frac{1}{\pi}a\omega, \quad \Psi_2 = -\frac{1}{\pi}a\sigma. \tag{26}$$

For the third complex potential, taking $m=16$, from Eq. (16),

$$W_3 = 16/2\pi \ln \mathrm{sn}(S, k_1) + C. \tag{27}$$

Numerical values are found from elliptic function tables.[11]

The superposition of the three gives the total compelx potential function W_t. Choosing $a=\pi$ and $V_a=0.4$, the natural modes of the final network are found to be $(-0.0436, \pm 1.012)$, $(-0.1194, \pm 1.216)$, $(-0.1002, \pm 1.971)$, $(-0.1603, \pm 1.586)$. The result is plotted in Fig. 7. It is seen that the curve α is an approximation to the given curve α_0 in a Tchebycheff sense.

V. CONCLUSION

In the preceding sections the basic idea and method of obtaining a good approximation to an arbitrary loss

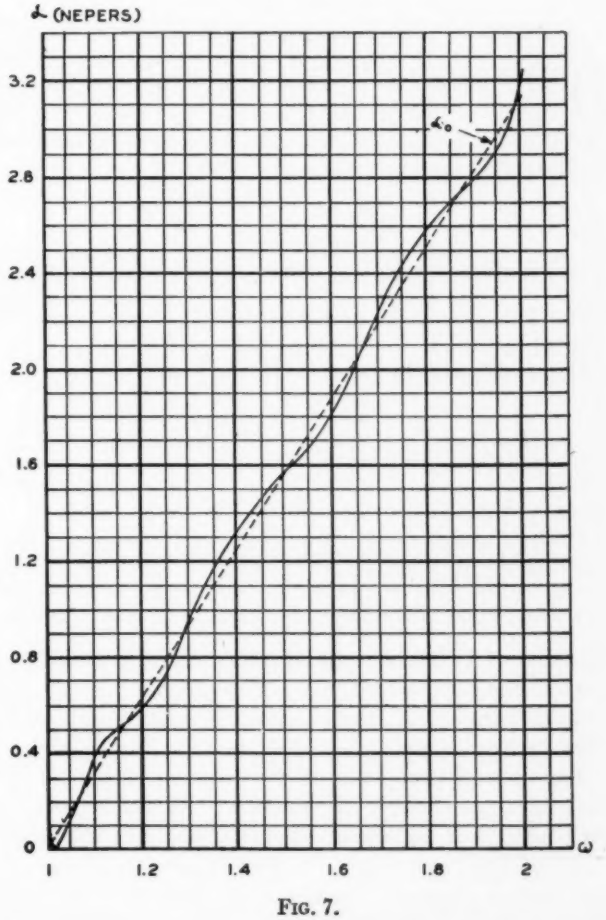

FIG. 7.

[11] G. W. Spenceley and R. M. Spenceley, "Smithsonian Elliptic Functions Tables," Smithsonian Institution, Washington, D. C., (1947).

function are described. Equal ripple results have been found for some simple examples. Since the Tchebycheff polynomial does not appear explicitly in the method,[12] no formal proof has been found as to whether this method yields an exactly equal ripple approximation or not. However, some physical reasoning based on the conformal mapping theory can be given to show why equal ripple results might be expected. Since this is of relatively little practical interest, the reader is referred to reference 1.

The author is indebted to Professor D. F. Tuttle for his many valuable suggestions. Acknowledgment is also due Mr. V. H. Grinich for reading the manuscript. This research was sponsored by the U. S. Office of Naval Research under Contract N6onr-251.

[12] S. Darlington, Bell System Tech. J. 31, 613–665 (1952).

JOURNAL OF APPLIED PHYSICS VOLUME 24, NUMBER 7 JULY, 1953

Matrix Solution of Equations of the Mathieu-Hill Type

LOUIS A. PIPES
University of California and U. S. Naval Ordnance Test Station, Inyokern, China Lake, California
(Received March 2, 1953)

This paper presents a method for the solution of a class of linear, second-order differential equations with periodic coefficients of the Mathieu-Hill type. The method is based on a procedure involving powers of matrices and is adequate for the study of a large class of physical problems. The stability of the solution is considered and the general method is illustrated by its application to typical special cases.

I. INTRODUCTION

THE mathematical analysis of a considerable variety of physical problems leads to a formulation involving a differential equation that may be reduced to the following general form:

$$\frac{d^2x}{dt^2}+F(t)x=0, \tag{1.1}$$

where $F(t)$ is a single-valued *periodic* function of fundamental period, T, that may be represented by a general Fourier series of the form

$$F(t)=A_0+\sum_1^\infty A_n\cos(nwt)+\sum_1^\infty B_n\sin(nwt), \tag{1.2}$$

where $w=2\pi/T$.

If the Fourier series expansion for $F(t)$ degenerates into the simple form

$$F(t)=A_0+A_1\cos(wt), \tag{1.3}$$

then Eq. (1.1) is known as *Mathieu's* differential equation. If the function $F(t)$ is a periodic function of the general form, (1.2), the equation is known as *Hill's* differential equation.

The general properties of the solution of Eq. (1.1) have been extensively discussed in the mathematical literature.[1–3] A survey of the nature of the analyses arising from practical applications indicates that they may be divided into two main categories. In the first category are problems in which an equation of the type (1.1) arises as a consequence of the separation of variables of a boundary-value problem. In this case the appropriate solution is required to be a periodic function. In the second category are found problems that may be regarded as initial-value problems in which an equation of the type (1.1) is involved. In this case the solutions are *not* restricted to periodic ones. The following physical problems are of the second type:

1. The production of electric currents by periodically varying the parameters of electric circuits. This phenomenon is commonly called "parametric excitation" in the current literature.[4–7]
2. The vibrations of the side rods of locomotives.[8]
3. The propagation of waves in stratified media.[9,10]
4. The propagation of electric currents in filter circuits and other periodic electric structures.[10,11]
5. The theory of modulation in wireless.[12]
6. The theory of super-regeneration.[13]

[1] N. W. McLachlan, *Theory and Application of Mathieu Functions* (Oxford University Press, London, 1946). Contains 226 references to the international literature.
[2] E. T. Whittaker and G. N. Watson, *Modern Analysis* (Cambridge University Press, Cambridge, 1927), pp. 404–428.
[3] L. Brillouin, Quart. Appl. Math. 6, 167–178 (1948); 7, 363–380 (1950).
[4] M. Brillouin, Eclairage Electrique XI, 49–59 (1897).
[5] A. Erdelyi, Ann. Physik 19, 585 (1934).
[6] Barrow, Smith, and Baumann, J. Franklin Inst. 221, No. 3, 403 (1936).
[7] N. Minorsky, J. Franklin Inst. 240, No. 1, 25–46 (1945).
[8] S. Timoshenko, *Vibration Problems in Engineering* (D. Van Nostrand Company, Inc., New York, 1937), pp. 167–181.
[9] Lord Rayleigh, Phil. Mag. 24, 145–159 (1887).
[10] L. Brillouin, *Wave Propagation in Periodic Structures* (McGraw-Hill Book Company, Inc., New York, 1946).
[11] G. A. Campbell, Bell System Tech. J. 1, 1–32 (1922).
[12] J. R. Carson, Proc. Inst. Radio Engrs. 10, 62 (1922).
[13] A. Erdelyi, Ann. Physik 23, 21 (1935).

7. The theory of the stability of an inverted pendulum by periodic movements of its point of support.[14]

8. The theory of astronomic perturbations.[15,16]

9. The quantum theory of metals.[17]

10. The theory of the stability of the solutions of certain nonlinear differential equations.[18]

This is by no means an exhaustive list of the types of physical problems whose mathematical analyses involve equations of the type (1.1) directly, but it serves to indicate the importance of this equation in mathematical physics. The determination of the *periodic* solutions of equations of the type (1.1) has been the subject of considerable investigation.[1,2] The purpose of this discussion is to present a method for the solution of equations of the type (1.1) subject to prescribed initial conditions when the solutions are *not* required to be periodic. This method is based on an application of Sylvester's theorem of matrix algebra,[19] to the solution of the problem. The method presented reduces the solution of Eq. (1.1) subject to given initial conditions to that of computing powers of matrices and is applicable to the solutions of the physical problems enumerated above.

II. THE USE OF MATRIX ALGEBRA IN SOLVING HILL'S EQUATION

A general method for the determination of the solution of (1.1) in terms of given initial values of $x(t)$ and $\dot{x}(t)=v(t)$ by means of the theory of matrices will now be presented. It has been found that in solving problems of the initial-value type, the matrix method has certain advantages over methods that make use of the conventional Floquet theory of Hill's equation.[1,2,20]

Let $u_1(t)$ and $u_2(t)$ be two linearly independent solutions of the equation

$$\frac{d^2x}{dt^2}+F(t)x=0, \tag{2.1}$$

in the fundamental interval $0\leqslant t\leqslant T$. The value of $x(t)$ and its first derivative, $\dot{x}(t)=v(t)$, may be expressed in the following form:

$$\begin{aligned} x(t)&=A_1u_1(t)+A_2u_2(t),\\ v(t)&=A_1\dot{u}_1(t)+A_2\dot{u}_2(t), \end{aligned} \quad \text{for } 0\leqslant t\leqslant T. \tag{2.2}$$

It is convenient to write (2.2) in the matrix form

$$\begin{bmatrix} x(t)\\ v(t)\end{bmatrix}=\begin{bmatrix} x\\ v\end{bmatrix}_t=\begin{bmatrix} u_{11}(t) & u_{12}(t)\\ u_{21}(t) & u_{22}(t)\end{bmatrix}\cdot\begin{bmatrix} A_1\\ A_2\end{bmatrix}. \tag{2.3}$$

A_1 and A_2 are *arbitrary* constants, and

$$\begin{bmatrix} u_{11}(t) & u_{12}(t)\\ u_{21}(t) & u_{22}(t)\end{bmatrix}=\begin{bmatrix} u_1(t) & u_2(t)\\ \dot{u}_1(t) & \dot{u}_2(t)\end{bmatrix}. \tag{2.4}$$

The Wronskian[21,22] of the two solutions, $u_1(t)$ and $u_2(t)$ is a *constant* in the fundamental interval, $0\leqslant t\leqslant T$, and is given by the determinant

$$W_0=\begin{vmatrix} u_{11}(t) & u_{12}(t)\\ u_{21}(t) & u_{22}(t)\end{vmatrix}=u_1(t)\dot{u}_2(t)-\dot{u}_1(t)u_2(t). \tag{2.5}$$

Since the two solutions $u_1(t)$ and $u_2(t)$ are linearly independent, $W_0\neq 0$, and the matrix (2.4) is nonsingular and has the following inverse,

$$\begin{bmatrix} u_{11}(t) & u_{12}(t)\\ u_{21}(t) & u_{22}(t)\end{bmatrix}^{-1}=\frac{1}{W_0}\begin{bmatrix} u_{22}(t) & -u_{12}(t)\\ -u_{21}(t) & u_{11}(t)\end{bmatrix}. \tag{2.6}$$

Let x_0 and v_0 be the *given* initial values of $x(t)$ and $v(t)$ at $t=0$, and introduce the following notation:

$$\begin{bmatrix} x\\ v\end{bmatrix}_0=\begin{bmatrix} x_0\\ v_0\end{bmatrix}. \tag{2.7}$$

Hence as a consequence of (2.3) we have

$$\begin{bmatrix} x_0\\ v_0\end{bmatrix}=\begin{bmatrix} u_{11}(0) & u_{12}(0)\\ u_{21}(0) & u_{22}(0)\end{bmatrix}\cdot\begin{bmatrix} A_1\\ A_2\end{bmatrix}, \tag{2.8}$$

or

$$\begin{aligned}\begin{bmatrix} A_1\\ A_2\end{bmatrix}&=\begin{bmatrix} u_{11}(0) & u_{12}(0)\\ u_{21}(0) & u_{22}(0)\end{bmatrix}^{-1}\cdot\begin{bmatrix} x_0\\ v_0\end{bmatrix}\\ &=\frac{1}{W_0}\begin{bmatrix} u_{22}(0) & -u_{12}(0)\\ -u_{21}(0) & u_{11}(0)\end{bmatrix}\cdot\begin{bmatrix} x_0\\ v_0\end{bmatrix}. \end{aligned} \tag{2.9}$$

This determines the column of arbitrary constants in terms of the given initial conditions. If (2.9) is substituted into (2.3), the result may be written in the form

$$\begin{aligned}\begin{bmatrix} x\\ v\end{bmatrix}_t&=\frac{1}{W_0}\begin{bmatrix} u_{11}(t) & u_{12}(t)\\ u_{21}(t) & u_{22}(t)\end{bmatrix}\\ &\quad\cdot\begin{bmatrix} u_{22}(0) & -u_{12}(0)\\ -u_{21}(0) & u_{11}(0)\end{bmatrix}\cdot\begin{bmatrix} x_0\\ v_0\end{bmatrix}. \end{aligned} \tag{2.10}$$

Cascading the Solution by the Use of Matrices

The extension of the solution beyond the fundamental period $0\leqslant t\leqslant T$ may be effectively carried out by matrix

[14] A. Stephenson, Proc. Manchester Phil. Soc. **52**, No. 8 (1908).
[15] G. W. Hill, Acta Math. **8**, 1 (1886).
[16] J. H. Poincaré, *Les Methodes Nouvelles de la Mécanique Céleste* (Paris, 1893), vol. II.
[17] F. Seitz, *Modern Theory of Solids* (McGraw-Hill Book Company, New York, 1940), Chap. VIII.
[18] N. W. McLachlan, *Ordinary Nonlinear Differential Equations in Engineering and Physical Science* (Oxford University Press, London, 1950), pp. 188–190.
[19] Frazer, Duncan, and Collar, *Elementary Matrices* (Cambridge University Press, Cambridge, 1938), pp. 64–85.
[20] G. Floquet, Ann. L'École Normale Supérieure **12**, 47–88 (1883).
[21] L. A. Pipes, Phil. Mag. **30**, 370–395 (1940).
[22] E. Meissner, Schweiz. Bauz. **72**, 95 (1918).

multiplication. If a change of variable of the form

$$\tau=t-nT, \quad \text{where} \quad 0\leqq\tau\leqq T \qquad n=0, 1, 2, 3, \ldots \tag{2.11}$$

is introduced in the Hill equation (2.1), the equation is transformed to

$$\frac{d^2x}{d\tau^2}+F(\tau)x=0, \tag{2.12}$$

as a consequence of the periodicity of $F(t)$ since

$$F(\tau+nT)=F(\tau). \tag{2.13}$$

Hence Hill's equation is *invariant* to the change in variable (2.11). It is thus apparent that a solution of the form (2.10) may be obtained in each interval $0\leqq\tau\leqq T$. The *final* values of x and v at the end of one interval of the variation of $F(t)$ are the *initial* values of x and v in the following interval.

At the end of the fundamental period $t=T$, (2.10) becomes

$$\begin{bmatrix}x\\v\end{bmatrix}_T=\frac{1}{W_0}\begin{bmatrix}u_{11}(T) & u_{12}(T)\\ u_{21}(T) & u_{22}(T)\end{bmatrix}\cdot\begin{bmatrix}u_{22}(0) & -u_{12}(0)\\ -u_{21}(0) & u_{11}(0)\end{bmatrix}\cdot\begin{bmatrix}x_0\\v_0\end{bmatrix}. \tag{2.14}$$

Let

$$[M]=\begin{bmatrix}A & B\\ C & D\end{bmatrix}=\frac{1}{W_0}\begin{bmatrix}u_{11}(T) & u_{12}(T)\\ u_{21}(T) & u_{22}(T)\end{bmatrix}\cdot\begin{bmatrix}u_{22}(0) & -u_{12}(0)\\ -u_{21}(0) & u_{11}(0)\end{bmatrix}$$

$$=\begin{bmatrix}[u_{11}(T)u_{22}(0)-u_{12}(T)u_{21}(0)] & \times[u_{12}(T)u_{11}(0)-u_{11}(T)u_{12}(0)]\\ [u_{21}(T)u_{22}(0)-u_{22}(T)u_{21}(0)] & \times[u_{22}(T)u_{11}(0)-u_{21}(T)u_{12}(0)]\end{bmatrix}. \tag{2.15}$$

Then by the use of this notation, (2.14) may be written in the following form:

$$\begin{bmatrix}x\\v\end{bmatrix}_T=[M]\begin{bmatrix}x_0\\v_0\end{bmatrix}=\begin{bmatrix}A & B\\ C & D\end{bmatrix}\cdot\begin{bmatrix}x\\v\end{bmatrix}_0. \tag{2.16}$$

Since the Wronskian W_0 of the two solutions, $u_1(t)$ and $u_2(t)$, is a constant, it may be seen that the determinant of the matrix $[M]$ has the following value:

$$|M|=\begin{vmatrix}A & B\\ C & D\end{vmatrix}=(AD-BC)=1. \tag{2.17}$$

At the end of the second period of the variation of $F(t)$ we have

$$\begin{bmatrix}x\\v\end{bmatrix}_{2T}=\begin{bmatrix}A & B\\ C & D\end{bmatrix}\begin{bmatrix}x\\v\end{bmatrix}_T=\begin{bmatrix}A & B\\ C & D\end{bmatrix}^2\begin{bmatrix}x_0\\v_0\end{bmatrix}=[M]^2\begin{bmatrix}x\\v\end{bmatrix}_0. \tag{2.18}$$

Similarly, it may be seen that at the end of n periods, we have

$$\begin{bmatrix}x\\v\end{bmatrix}_{nT}=\begin{bmatrix}A & B\\ C & D\end{bmatrix}^n\cdot\begin{bmatrix}x_0\\v_0\end{bmatrix}=[M]^n\begin{bmatrix}x\\v\end{bmatrix}_0. \tag{2.19}$$

The solution within the $(n+1)$th interval is given by

$$\begin{bmatrix}x\\v\end{bmatrix}_{nT+\tau}=\begin{bmatrix}u_{11}(\tau) & u_{12}(\tau)\\ u_{21}(\tau) & u_{22}(\tau)\end{bmatrix}\times\begin{bmatrix}u_{22}(0) & -u_{12}(0)\\ -u_{21}(0) & u_{11}(0)\end{bmatrix}\cdot\begin{bmatrix}x\\v\end{bmatrix}_{nT}, \tag{2.20}$$

where $0\leqq\tau\leqq T$.

Equation (2.20) is the solution of Hill's equation at any time $t>0$ in terms of the *initial* conditions and two linearly independent solutions of Hill's equation in the fundamental interval $0\leqq t\leqq T$.

Computation of Integral Powers of $[M]$

The integral powers of the matrix $[M]$ required in Eq. (2.19) may be most simply obtained by the use of *Sylvester's theorem*.[19] This important theorem states that if the characteristic or latent roots r_1 and r_2 of the matrix $[M]$ are *distinct* and $P([M])$ is any *polynomial* of $[M]$, then

$$P([M])=P(r_i)[H_0(r_1)]+P(r_2)[H_0(r_2)], \tag{2.21}$$

where

$$[H_0(r_i)]=\frac{[F(r_i)]}{\left(\frac{d\Delta}{dr}\right)_{r=r_i}}. \tag{2.22}$$

$[F(r)]$ is the *adjoint* of the characteristic matrix of the matrix $[M]$ given by No. 9 of Table I. $\Delta(r)$ is the characteristic function of the matrix $[M]$ as given by No. 5 of Table I; it has the form

$$\Delta(r)=r^2-r(A+D)+1. \tag{2.23}$$

Hence

$$\frac{d\Delta(r)}{dr}=2r-(A+D). \tag{2.24}$$

In order to apply Sylvester's theorem to the computation of $[M]^n$, let the polynomial of (2.21) be given by $P([M])=[M]^n$. If $A+D\neq\pm2$, the two latent roots of $[M]$ are distinct, and entry No. 10 of Table I readily

TABLE I. Fundamental relations involving the matrix $[M]$.

(1)	The matrix $[M]$	$[M]=\begin{bmatrix} A & B \\ C & D \end{bmatrix}$
(2)	The determinant of $[M]$	$\lvert M\rvert = AD-BC=1$
(3)	The inverse of $[M]$	$[M]^{-1}=\begin{bmatrix} D & -B \\ -C & A \end{bmatrix}$
(4)	The characteristic matrix of $[M]$	$[f(r)]=\begin{bmatrix} (r-A) & -B \\ -C & (r-D) \end{bmatrix}$
(5)	The characteristic function of $[M]$	$\Delta(r)=$ determinant of $[f(r)]$ $=r^2-r(A+D)+1$
(6)	The characteristic equation of $[M]$	$\Delta(r)=r^2-r(A+D)+1=0$
(7)	The characteristic or latent roots of $[M]$ (three cases)	Roots of $\Delta(r)=0$ If $(A+D)\neq 2$, $r_1=e^a$, $r_2=e^{-a}$ where $\cosh(a)=\frac{(A+D)}{2}$ If $(A+D)=+2$, $r_1=r_2=+1$ If $(A+D)=-2$, $r_1=r_2=-1$
(8)	The inverse of the characteristic matrix of $[M]$	$[f(r)]^{-1}=\frac{1}{\Delta(r)}\begin{bmatrix} (r-D) & B \\ C & (r-A) \end{bmatrix}$
(9)	The adjoint of the characteristic matrix of $[M]$	$[F(r)]=(r)[f(r)]^{-1}$ $=\begin{bmatrix} (r-D) & B \\ C & (r-A) \end{bmatrix}$
(10)	Integral powers of $[M]$ (distinct latent roots) $A+D\neq\pm 2$ $n=0, 1, 2, 3, \cdots$ $\cosh(a)=\frac{(A+D)}{2}$	$[M]^n=\frac{1}{S_1}\begin{bmatrix} S_{n+1}-DS_n & BS_n \\ CS_n & S_{n+1}-AS_n \end{bmatrix}$, where $S_n=\sinh(an)$
(11)	Integral powers of $[M]$ symmetric case, $A=D$ (distinct latent roots) $A=D\neq\pm 1$ $\cosh(a)=A$	$[M]^n=\begin{bmatrix} \cosh(an) & Z_0\sinh(an) \\ \frac{\sinh(an)}{Z_0} & \cosh(an) \end{bmatrix}$ $Z_0=(B/C)^{\frac{1}{2}}$ $n=0, 1, 2, 3, \cdots$
(12)	Integral powers of $[M]$ (equal latent roots) $(A+D)=+2$ $r_1=r_2=+1$	$[M]^n=\begin{bmatrix} n(A-1)+1 & nB \\ nC & n(D-1)+1 \end{bmatrix}$ $n=0, 1, 2, 3, \cdots$
(13)	Integral powers of $[M]$ (equal latent roots) $(A+D)=-2$ $r_1=r_2=-1$ $n=0, 1, 2, 3, \cdots$	$[M]^n=nE_{n-1}\begin{bmatrix} (A+1) & B \\ C & (D+1) \end{bmatrix}+E_nI$ $E_n=\exp(jn\pi)$ $I=\begin{bmatrix} 1 & 0 \\ 0 & 1 \end{bmatrix}=$ unit matrix

follows from Sylvester's theorem. In case that $A+D=2$, both latent roots become equal to unity and No. 12 Table I gives the powers of $[M]$ as a consequence of a confluent form of Sylvester's theorem (see reference 19, p. 85). If $A+D=-2$, both latent roots of $[M]$ become equal to -1. In this case entry No. 13 gives the proper form for the powers of $[M]$. In the important case of distinct latent roots and symmetry of $[M]$ so that $A=D$, the proper form for the powers of $[M]$ is given by No. 11 of Table I. Entries No. 10–No. 13 of Table I cover all possible special cases that can arise in practice. These forms are useful in the theory of four-terminal networks.[21] The general theory will now be applied to the solution of some representative special cases.

III. THE SOLUTION OF THE HILL-MEISSNER EQUATION

The Hill equation (1.1) in the special case for which the function $F(t)$ has the form of the rectangular ripple of Fig. 1, was used by Meissner[22] in his analysis of the vibrations of the driving rods of locomotives. The stability of the solution of this equation has been studied by van der Pol and Strutt.[23]

[23] B. van der Pol and M. J. O. Strutt, Phil. Mag. 5, 18 (1928).

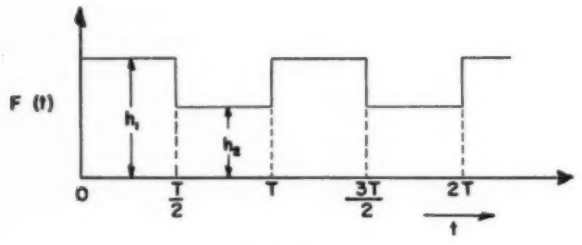

FIG. 1.

Let T be the fundamental period of the rectangular ripple, and let the ripple vary in height from h_1 to h_2. Hill's equation now reduces to

$$\frac{d^2x}{dt^2}+h_1x=0, \quad 0\leqslant t\leqslant T/2,$$
$$\frac{d^2x}{dt^2}+h_2x=0, \quad T/2\leqslant t\leqslant T. \tag{3.1}$$

If we let

$$w_1=\sqrt{h_1}, \quad \text{and} \quad w_2=\sqrt{h_2}, \tag{3.2}$$

it can be seen that the solution of (3.1) in the range $0\leqslant t\leqslant T/2$ may be written in the matrix form

$$\begin{bmatrix} x \\ v \end{bmatrix}_t = \begin{bmatrix} \cos(w_1t) & \sin(w_1t)/w_1 \\ -w_1\sin(w_1t) & \cos(w_1t) \end{bmatrix} \cdot \begin{bmatrix} x_0 \\ v_0 \end{bmatrix}$$
$$0\leqslant t\leqslant T/2, \tag{3.3}$$

where x_0 and v_0 are the initial values of x and $\dot{x}$ at $t=0$, and the column on the left gives the values of x and $\dot{x}$ at t. The values of x and v at $t=T/2$ are given by

$$\begin{bmatrix} x \\ v \end{bmatrix}_{T/2} = \begin{bmatrix} \cos(\theta_1) & \sin(\theta_1)/w_1 \\ -w_1\sin(\theta_1) & \cos(\theta_1) \end{bmatrix} \cdot \begin{bmatrix} x_0 \\ v_0 \end{bmatrix}, \tag{3.4}$$

where

$$\theta_1=w_1\frac{T}{2}=\frac{T}{2}\sqrt{h_1}. \tag{3.5}$$

Since the values of x and v at $t=T/2$ are the *initial* values of x and v in the next interval, $T/2\leqslant t\leqslant T$, we have

$$\begin{bmatrix} x \\ v \end{bmatrix}_T = \begin{bmatrix} \cos(\theta_2) & \sin(\theta_2)/w_2 \\ -w_2\sin(\theta_2) & \cos(\theta_2) \end{bmatrix}$$
$$\cdot \begin{bmatrix} \cos(\theta_1) & \sin(\theta_1)/w_1 \\ -w_1\sin(\theta_1) & \cos(\theta_1) \end{bmatrix} \cdot \begin{bmatrix} x_0 \\ v_0 \end{bmatrix}, \tag{3.6}$$

where

$$\theta_2=w_2\frac{T}{2}=\frac{T}{2}\sqrt{h_2}. \tag{3.7}$$

If the indicated multiplication in (3.6) is performed, the result may be written in the form

$$\begin{bmatrix} x \\ v \end{bmatrix}_T = \begin{bmatrix} A & B \\ C & D \end{bmatrix} \cdot \begin{bmatrix} x_0 \\ v_0 \end{bmatrix} = [M] \cdot \begin{bmatrix} x_0 \\ v_0 \end{bmatrix}. \tag{3.8}$$

In this case the matrix $[M]$ has the form

$$[M]=\begin{vmatrix} A & B \\ C & D \end{vmatrix}$$
$$= \begin{bmatrix} \left(M_1M_2-N_1N_2\frac{w_1}{w_2}\right) & \left(M_2\frac{N_1}{w_1}+M_1\frac{N_2}{w_2}\right) \\ -(M_1N_2w_2+M_2N_1w_1) & \left(M_1M_2-N_1N_2\frac{w_2}{w_1}\right) \end{bmatrix}, \tag{3.9}$$

where the notation

$$M_i=\cos(\theta_i), \quad \text{and} \quad N_i=\sin(\theta_i), \tag{3.10}$$

has been introduced.

The values of x and v at the end of n complete periods of the rectangular tipple of Fig. 1 are given by

$$\begin{bmatrix} x \\ v \end{bmatrix}_{nT} = \begin{bmatrix} A & B \\ C & D \end{bmatrix} \cdot \begin{bmatrix} x_0 \\ v_0 \end{bmatrix} = [M]^n \cdot \begin{bmatrix} x_0 \\ v_0 \end{bmatrix}. \tag{3.11}$$

If numerical values are given the matrix $[M]^n$ may be computed by No. 10 of Table I or its alternative forms.

The Stability of the Solution

The nature of the solution depends on the form taken by the powers of the matrix $[M]$. If

$$(A+D)\neq\pm 2, \tag{3.12}$$

the matrix $[M]$ has two *distinct* latent roots and $[M]^n$ is given by No. 10 of Table I. Now

$$\cosh(a)=\frac{(A+D)}{2}=\cos(\theta_1)\cos(\theta_2)$$
$$-\frac{\sin(\theta_1)}{2}\sin(\theta_2)\frac{[\theta_1^2+\theta_2^2]}{\theta_1\theta_2}, \tag{3.13}$$

as can be seen directly from (3.9). There are two separate cases to be considered. If

$$\left|\frac{(A+D)}{2}\right|>1, \tag{3.14}$$

then $\cosh(a)>1$, and a must have a positive real part. In this case (3.11) may be written with the aid of No. 10

of Table I in the following form,

$$\begin{bmatrix} x \\ v \end{bmatrix}_{nT} = \frac{1}{\sinh(a)} \times \begin{bmatrix} \left\{ \begin{matrix} \sinh[a(n+1)] \\ -D\sinh(an) \end{matrix} \right\} & B\sinh(an) \\ C\sinh(an) & \left\{ \begin{matrix} \sinh[a(n+1)] \\ -A\sinh(an) \end{matrix} \right\} \end{bmatrix} \cdot \begin{bmatrix} x_0 \\ v_0 \end{bmatrix}. \quad (3.15)$$

Since the real part of the number a is positive, it can be seen that x and v will *increase* with t. In physical applications this leads to *unstable* solutions. If

$$\left| \frac{(A+D)}{2} \right| < 1, \quad (3.15)$$

then

$$a = jb, \quad (3.16)$$

where

$$\cos(b) = \frac{(A+D)}{2}. \quad (3.17)$$

If the value $a=jb$ is substituted into (3.15), the result is

$$\begin{bmatrix} x \\ v \end{bmatrix}_{nT} = \frac{1}{\sin(b)} \times \begin{bmatrix} \left\{ \begin{matrix} \sin[b(n+1)] \\ -D\sin(bn) \end{matrix} \right\} & B\sin(bn) \\ C\sin(bn) & \left\{ \begin{matrix} \sin[b(n+1)] \\ -A\sin(bn) \end{matrix} \right\} \end{bmatrix} \cdot \begin{bmatrix} x_0 \\ v_0 \end{bmatrix}. \quad (3.18)$$

It can be seen that in this case the values of x and v *oscillate* with increasing t. This case leads to *stable* solutions in physical applications. The dividing line between stable and unstable solutions leads to the case for which

$$\left| \frac{(A+D)}{2} \right| = 1. \quad (3.19)$$

In this unique case the matrix $[M]$ has equal latent roots. If $(A+D)=2$, the latent roots are $r_1=r_2=1$ and the proper form for $[M]^n$ is given by No. 12 of Table I. If on the other hand, $(A+D)=-2$, the latent roots of $[M]$ are $r_1=r_2=-1$, and the proper form for $[M]^n$ is given by No. 13 of Table I. In general, the condition (3.19) leads to instability in the physical applications.

The question of the stability of the solution may be summarized by the following expressions:

$$\left| \frac{(A+D)}{2} \right| > 1 \quad \textit{unstable},$$

$$\left| \frac{(A+D)}{2} \right| < 1 \quad \textit{stable}, \quad (3.20)$$

$$\left| \frac{(A+D)}{2} \right| = 1 \quad \textit{unstable}.$$

These are the conclusions reached by van der Pol and Strutt[23] in a different manner by the use of the Floquet theory of Hill's equation. The present analysis indicates the intimate connection between the criterion for stability and the nature of the latent roots of $[M]$.

IV. SOLUTION OF HILL'S EQUATION IF $F(t)$ IS A SUM OF STEP FUNCTIONS

The matrix method of solution is particularly effective in solving Hill's equation in cases when the function $F(t)$ may be represented as a sum of step function in the interval $0 \leq t \leq T$ as shown in Fig. 2.

Let the function $F(t)$ be composed of m step functions each of length T_0 and heights $h_1, h_2, \cdots h_m$, where

$$mT_0 = T. \quad (4.1)$$

Let the following notation be introduced:

$$w_k = \sqrt{h_k}, \quad \theta_k = T_0\sqrt{h_k}, \quad (4.2)$$

$$[M]_k = \begin{bmatrix} P_k & Q_k \\ R_k & P_k \end{bmatrix} = \begin{bmatrix} \cos(\theta_k) & \sin(\theta_k)/w_k \\ -w_k\sin(\theta_k) & \cos(\theta_k) \end{bmatrix}. \quad (4.3)$$

If we let

$$\begin{bmatrix} A & B \\ C & D \end{bmatrix} = [M]_m \cdot [M]_{m-1} \cdots [M]_2 \cdot [M]_1 = [M], \quad (4.4)$$

it can be seen, by reasoning similar to that used in Sec. III, that at the end of the fundamental interval $T=mT_0$ the solution is given by

$$\begin{bmatrix} x \\ v \end{bmatrix}_T = \begin{bmatrix} A & B \\ C & D \end{bmatrix} \cdot \begin{bmatrix} x_0 \\ v_0 \end{bmatrix}. \quad (4.5)$$

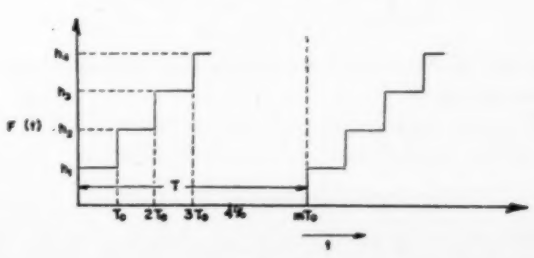

FIG. 2.

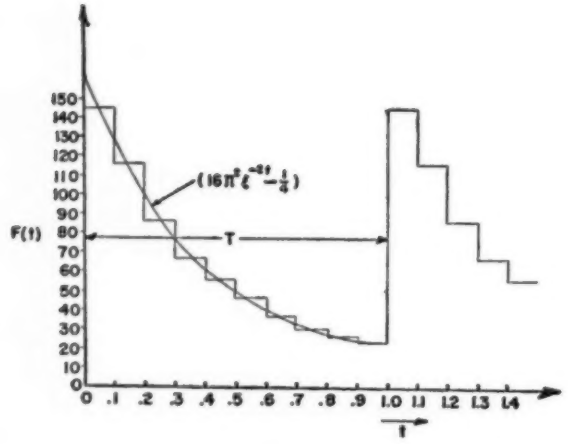

FIG. 3.

The solution at the end of n intervals when $t=nT$ is given by

$$\begin{bmatrix} x \\ v \end{bmatrix}_{nT} = \begin{bmatrix} A & B \\ C & D \end{bmatrix}^n \begin{bmatrix} x_0 \\ v_0 \end{bmatrix}. \tag{4.6}$$

The stability of the solution is then determined by (3.20).

This method can be used to study the stability and to obtain the approximate solution of equations of the Hill type by representing the given function $F(t)$ throughout the fundamental interval by a sum of step functions as in the method of mean coefficients.[19] To illustrate the general procedure consider a Hill's equation of the form

$$\frac{d^2x}{dt^2} + F(t)x = 0, \tag{4.7}$$

where the function $F(t)$ has the form

$$F(t) = (16\pi^2 e^{-2t} - \tfrac{1}{4}), \quad 0 \leqslant t \leqslant 1, \tag{4.8}$$

in the fundamental interval $0 \leqslant t \leqslant 1$ and is a *periodic* function of fundamental period $T=1$.

In order to represent the function $F(t)$ by step functions, divide the fundamental interval $T=1$ into ten equal subintervals of length $T_0 = \frac{1}{10}$. The average value of $F(t)$ in each sub interval will be taken to be equal to the height of the steps. Thus in the kth interval the representative step function will have the height

$$h_k = \frac{1}{T_0} \int_{(k-1)T_0}^{kT_0} F(t)dt, \quad k=1, 2, 3, \cdots. \tag{4.9}$$

A graph of $F(t)$ and its step-function representation is given in Fig. 3.

The *exact* solution of (4.7) in the range $0 \leqslant t \leqslant 1$, with the initial conditions $x_0=1$, $v_0=\frac{1}{2}$, is given by

$$x(t) = \exp(t/2)\cos(4\pi e^{-t}), \quad 0 \leqslant t \leqslant 1. \tag{4.10}$$

The values of h_k, w_k, and the elements of the matrices $[M]_k$ are tabulated in Table II. The matrices $[M]_k$ and the values of x_k and v_k of the solution at the end of the kth sub interval as a result of the initial conditions $x_0=1$ and $v_0=\frac{1}{2}$ are given in Table III. The matrix $[M]$ is obtained by the multiplication of the chain of matrices in the form

$$[M] = [M]_{10} \cdot [M]_9 \cdot [M]_8 \cdots [M]_1$$

$$= \begin{bmatrix} A & B \\ C & D \end{bmatrix} = \begin{bmatrix} 0.6504 & -1.8412 \\ 0.1956 & -3.9488 \end{bmatrix}. \tag{4.11}$$

TABLE II.

Step	h_k	w_k	P_k	Q_k	R_k
1	142.88	11.953	0.36673	0.07783	−11.1202
2	116.93	10.813	0.47015	0.08162	−9.5438
3	95.69	9.782	0.55851	0.08480	−8.1142
4	78.30	8.849	0.63339	0.08745	−6.8473
5	64.06	8.004	0.69644	0.08966	−5.7437
6	52.41	7.239	0.74922	0.09149	−4.7945
7	42.86	6.547	0.79326	0.09301	−3.9862
8	35.04	5.920	0.82983	0.09426	−3.3032
9	28.64	5.352	0.86016	0.09529	−2.7298
10	23.40	4.838	0.88523	0.09614	−2.2506

As a consequence of (4.11), we have

$$\frac{(A+D)}{2} = -1.6492 = \cosh(a). \tag{4.12}$$

The stability criterion (3.20) indicates that the solution is *unstable*. A table of hyperbolic functions gives the following value for a:

$$a = 1.085 + j\pi. \tag{4.13}$$

The solution at the end of n periods of the function $F(t)$ is given by (3.15) with the value given by (4.13) for a.

V. A CLASS OF HILL'S EQUATIONS WITH EXPONENTIAL VARIATION

If Hill's equation has the form

$$\frac{d^2x}{dt^2} + (k^2e^{-2t} - n^2)x = 0, \quad 0 \leqslant t \leqslant T \tag{5.1}$$

throughout the fundamental interval $0 \leqslant t \leqslant T$, it may be solved in this interval by means of Bessel functions[24] in the form

$$x(t) = A_1 J_n(ke^{-t}) + A_2 Y_n(ke^{-t}), \quad 0 \leqslant t \leqslant T, \tag{5.2}$$

where J_n and Y_n are Bessel functions of the first and second kinds of order n,[25] and the A's are arbitrary constants. If we let

$$z = ke^{-t}, \tag{5.3}$$

[24] E. Kamke, *Differentialgleichungen Lösungsmethoden und Lösungen* (Chelsea Publishing Company, New York, 1948), p. 442.

[25] N. W. McLachlan, *Bessel Functions for Engineers* (Oxford University Press, London, 1941).

and compute the derivative

$$\frac{d}{dt}J_n(z)=\frac{d}{dz}J_n(z)\frac{dz}{dt}=-zJ_n'(z), \tag{5.4}$$

it is evident that we may write $x(t)$ and $\dot{x}(t)=v$ in the convenient matrix form

$$\begin{bmatrix}x\\v\end{bmatrix}_t=\begin{bmatrix}J_n(z) & Y_n(z)\\-zJ_n'(z) & -zY_n'(z)\end{bmatrix}\cdot\begin{bmatrix}A_1\\A_2\end{bmatrix}. \tag{5.5}$$

The Wronskian, Eq. (2.5), now takes the form

$$W_0=-z[J_n(z)Y_n'(z)-J_n'(z)Y_n(z)]. \tag{5.6}$$

From the theory of Bessel functions[25] we have the following result:

$$J_n(z)Y_n'(z)-J_n'(z)Y_n(z)=2/\pi z. \tag{5.7}$$

If this is substituted into (5.6), we obtain

$$W_0=-2/\pi. \tag{5.8}$$

TABLE III.

Step k	$\begin{bmatrix}A & B\\C & D\end{bmatrix}=[M]_k$		$\begin{bmatrix}x\\v\end{bmatrix}$
1	0.36673	0.07783	$1.0=x_0$
	−11.1202	0.36673	$0.5=v_0$
2	0.47015	0.08162	0.4056
	−9.5438	0.47015	−10.9368
3	0.55851	0.08480	−0.7019
	−8.1142	0.55851	−9.0134
4	0.63339	0.08745	−1.1564
	−6.8473	0.63339	0.6617
5	0.69644	0.08966	−0.6746
	−5.7437	0.69644	8.3373
6	0.74922	0.09149	0.2777
	−4.7945	0.74922	9.6811
7	0.79326	0.09301	1.0938
	−3.9862	0.79326	5.9218
8	0.82983	0.09426	1.4184
	−3.3032	0.82983	0.3374
9	0.86016	0.09529	1.2088
	−2.7298	0.86016	−4.4053
10	0.88523	0.09614	0.6200
	−2.2506	0.88523	−7.0890

The matrix $[M]$ of (2.15) now becomes

$$[M]=\begin{bmatrix}A & B\\C & D\end{bmatrix}$$

$$=-\frac{\pi}{2}\begin{bmatrix}J_n(ke^{-T}) & Y_n(ke^{-T})\\-ke^{-T}J_n'(ke^{-T}) & -ke^{-T}Y_n'(ke^{-T})\end{bmatrix}$$

$$\cdot\begin{bmatrix}-kY_n'(k) & -Y_n(k)\\+kJ_n'(k) & +J_n(k)\end{bmatrix}. \tag{5.9}$$

The conditions for stability are given by (3.20) and the solution after n periods is given by

$$\begin{bmatrix}x\\v\end{bmatrix}_{nT}=\begin{bmatrix}A & B\\C & D\end{bmatrix}^n\cdot\begin{bmatrix}x_0\\v_0\end{bmatrix}. \tag{5.10}$$

If $k=4\pi$ and $n=\frac{1}{2}$, Eq. (5.1) reduces to the one discussed in Sec. IV by another method.

VI. HILL'S EQUATION WITH A SAWTOOTH VARIATION

As a final example of the general method, consider the solution of Hill's equation (1.1) when the function $F(t)$ has the form of a sawtooth wave as shown in Fig. 4.

The function $F(t)$ has the form

$$F(t)=at+b, \quad 0\leq t\leq T, \tag{6.1}$$

in the fundamental interval and repeats the variation at intervals of T. Hill's equation now takes the form

$$\frac{d^2x}{dt^2}+(at+b)x=0, \quad 0\leq t\leq T, \tag{6.2}$$

in the fundamental interval. Let

$$z=at+b. \tag{6.3}$$

This change of variable transforms (6.2) into the form

$$\frac{d^2x}{dz^2}+\frac{z}{a^2}x=0. \tag{6.4}$$

Equation (6.4) is a form of Stokes' equation. The linearly independent solutions of this equation have been tabulated.[26] The solution of (6.4) may also be expressed in terms of Bessel functions of order one-third[24] in the following form:

$$x=(z)^{\frac{1}{2}}[A_1J_{\frac{1}{3}}(kz^{\frac{3}{2}})+A_2Y_{\frac{1}{3}}(kz^{\frac{3}{2}})], \tag{6.5}$$

where the A's are arbitrary constants, and

$$k=2/3a. \tag{6.6}$$

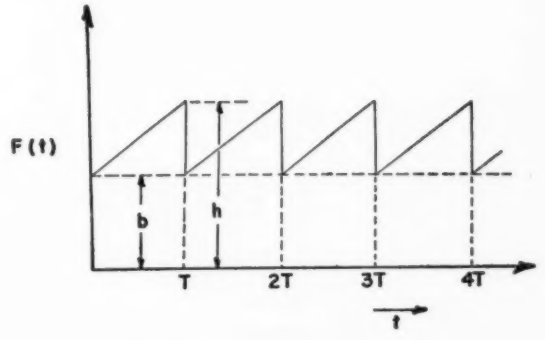

FIG. 4.

[26] *Tables of the Modified Hankel Functions of Order One-Third, and of Their Derivatives* (Harvard University Press, Cambridge Massachusetts, 1945).

In the notation of Sec. II we have

$$u_1(t)=(z)^{\frac{1}{2}}J_{\frac{1}{3}}(kz^{\frac{1}{2}}),\quad u_2(t)=(z)^{\frac{1}{2}}Y_{\frac{1}{3}}(kz^{\frac{1}{2}}). \tag{6.7}$$

By the use of the following recurrence relation of the theory of Bessel functions,[25]

$$\frac{d}{dy}J_n(y)=-\frac{n}{y}J_n(y)+J_{n-1}(y), \tag{6.8}$$

the following derivatives may be calculated:

$$\frac{du_1}{dt}=zJ_{-2/3}(kz^{\frac{1}{2}}),\quad \frac{du_2}{dt}=zY_{-2/3}(kz^{\frac{1}{2}}). \tag{6.9}$$

Hence the solution of (6.2) in the fundamental interval $0\leqslant t\leqslant T$ may be expressed in the following form:

$$\begin{bmatrix}x\\ v\end{bmatrix}_t=\begin{bmatrix}(z)^{\frac{1}{2}}J_{\frac{1}{3}}(kz^{\frac{1}{2}}) & (z)^{\frac{1}{2}}Y_{\frac{1}{3}}(kz^{\frac{1}{2}})\\ zJ_{-2/3}(kz^{\frac{1}{2}}) & zY_{-2/3}(kz^{\frac{1}{2}})\end{bmatrix}\cdot\begin{bmatrix}A_1\\ A_2\end{bmatrix}. \tag{6.10}$$

Let the following notation be introduced:

$$\theta=kb^{\frac{1}{2}}=\frac{2b^{\frac{1}{2}}}{3a}, \tag{6.11}$$

$$\phi=kh^{\frac{1}{2}}=\frac{2h^{\frac{1}{2}}}{3a}. \tag{6.12}$$

The Wronskian W_0 of (2.5) in this case is given by

$$W_0=\begin{vmatrix}(b)^{\frac{1}{2}}J_{\frac{1}{3}}(\theta) & (b)^{\frac{1}{2}}Y_{\frac{1}{3}}(\theta)\\ bJ_{-2/3}(\theta) & bY_{-2/3}(\theta)\end{vmatrix}$$

$$=b^{\frac{1}{2}}[J_{\frac{1}{3}}(\theta)Y_{-2/3}(\theta)-J_{-2/3}(\theta)Y_{\frac{1}{3}}(\theta)]. \tag{6.13}$$

The matrix $[M]$ of (2.15) is now

$$[M]=\frac{1}{W_0}\begin{bmatrix}(h)^{\frac{1}{2}}J_{\frac{1}{3}}(\phi) & (h)^{\frac{1}{2}}Y_{\frac{1}{3}}(\phi)\\ hJ_{-2/3}(\phi) & hY_{-2/3}(\phi)\end{bmatrix}$$

$$\cdot\begin{bmatrix}bY_{-2/3}(\theta) & (b)^{\frac{1}{2}}Y_{\frac{1}{3}}(\theta)\\ -bJ_{-2/3}(\theta) & (b)^{\frac{1}{2}}J_{\frac{1}{3}}(\theta)\end{bmatrix}=\begin{bmatrix}A & B\\ C & D\end{bmatrix}. \tag{6.14}$$

Hence

$$\begin{aligned}A&=\frac{b(h)^{\frac{1}{2}}}{W_0}[J_{\frac{1}{3}}(\phi)Y_{-2/3}(\theta)-J_{-2/3}(\theta)Y_{\frac{1}{3}}(\phi)],\\ D&=\frac{h(b)^{\frac{1}{2}}}{W_0}[J_{\frac{1}{3}}(\theta)Y_{-2/3}(\phi)-J_{-2/3}(\phi)Y_{\frac{1}{3}}(\theta)],\\ B&=\frac{(hb)^{\frac{1}{2}}}{W_0}[J_{\frac{1}{3}}(\theta)Y_{\frac{1}{3}}(\phi)-J_{\frac{1}{3}}(\phi)Y_{\frac{1}{3}}(\theta)],\\ C&=\frac{hb}{W_0}[J_{-2/3}(\phi)Y_{-2/3}(\theta)-J_{-2/3}(\theta)Y_{-2/3}(\phi)].\end{aligned} \tag{6.15}$$

The stability conditions for the solution are given by (3.20) and the magnitude of the solution after n periods is given by (2.19) in terms of the initial conditions.

Asymptotic Approximations

If b is large so that

$$(b^3)^{\frac{1}{2}}\gg\frac{3a}{2}, \tag{6.16}$$

then terms of the order of $1/\theta^{\frac{1}{2}}$ and $1/\phi^{\frac{1}{2}}$ can be neglected, and the various Bessel functions involved may be represented by the *dominant term* of their asymptotic expansions (see reference 25, pp. 158–161). If this is done, we have

$$\begin{aligned}J_{\frac{1}{3}}(w)&=\left(\frac{2}{\pi w}\right)^{\frac{1}{2}}\cos(w-\pi/4-\pi/6),\\ Y_{\frac{1}{3}}(w)&=\left(\frac{2}{\pi w}\right)^{\frac{1}{2}}\sin(w-\pi/4-\pi/6),\\ J_{-2/3}(w)&=\left(\frac{2}{\pi w}\right)^{\frac{1}{2}}\cos(w-\pi/4+\pi/3),\\ Y_{-2/3}(w)&=\left(\frac{2}{\pi w}\right)^{\frac{1}{2}}\sin(w-\pi/4+\pi/3).\end{aligned} \tag{6.17}$$

If the Bessel functions in (6.13) and (6.14) are represented by their dominant terms, (6.17), the following expressions are obtained for W_0 and $[M]$:

$$W_0=3a/\pi, \tag{6.18}$$

and

$$[M]=\frac{2}{3a}\left(\frac{bh}{\theta\phi}\right)^{\frac{1}{2}}\times\begin{bmatrix}(b)^{\frac{1}{2}}\cos(\theta-\phi) & \sin(\phi-\theta)\\ (bh)^{\frac{1}{2}}\sin(\theta-\phi) & (h)^{\frac{1}{2}}\cos(\theta-\phi)\end{bmatrix}. \tag{6.19}$$

In this case we have

$$\frac{(A+D)}{2}=\frac{\cos(\theta-\phi)}{3a}[b(h)^{\frac{1}{2}}+h(b)^{\frac{1}{2}}], \tag{6.20}$$

and the stability criterion (3.20) may be easily applied.

VII. CONCLUSION

The natural manner by which equations of the Mathieu-Hill type may be solved in terms of given initial conditions by the use of matrix algebra has been demonstrated. The powerful matrix notation, and the use of Sylvester's theorem to raise the matrices involved to the required powers, greatly facilitates the solution of equations of this type.

The Relaxation Distribution Function of Polyisobutylene in the Transition from Rubber-Like to Glass-Like Behavior

JOHN D. FERRY, LESTER D. GRANDINE, JR.,* AND EDWIN R. FITZGERALD†
Department of Chemistry, University of Wisconsin, Madison, Wisconsin

(Received March 7, 1953)

The steady flow viscosity of a sample of polyisobutylene of viscosity-average molecular weight 1.35 million, distributed by the National Bureau of Standards, has been measured from 15° to 100°C. Its logarithm is a linear function of $1/T^2$. Application of the method of reduced variables to dynamic mechanical data from −45° to 100°, previously reported for this polyisobutylene, yields composite curves reduced to 25°C for the real and imaginary parts of the complex compliance and complex shear modulus; the real part of the complex dynamic viscosity; and the mechanical loss tangent. The latter exhibits a broad and peculiarly asymmetric maximum. The reduced time scale extends from 1 to 10^{-9} sec. The reduction factors a_T obtained in this way are slightly higher than those derived either from the viscosity or from stress relaxation measurements of Tobolsky and associates. The distribution functions of relaxation and retardation times have been calculated by second approximation methods and their detailed shapes are defined in the transition region between rubber-like and glass-like behavior. The relaxation distribution function is compared with the idealized distribution of Tobolsky.

INTRODUCTION

THE dynamic mechanical properties of a sample of polyisobutylene distributed by the National Bureau of Standards, covering ranges of frequency and temperature within which the properties change from those characteristic of a soft rubber to those characteristic of a hard glass, have been given in a previous paper.[1] The frequency and temperature dependence of the real and imaginary parts of the complex compliance are now analyzed by the method of reduced variables[2,3] to provide two separate functions, one of time alone and one of temperature alone. The steady flow viscosity of this sample of polyisobutylene has also been measured, to compare its temperature dependence with that of the relaxation processes which determine the viscoelastic properties in the audio-frequency range, as well as with that of the slower relaxation processes reflected in measurements of stress relaxation.[4]

TABLE I. Viscosity data. (Temperatures in chronological order.)

Temp. °C	Load g	$\log\eta$ (in poises)
97.2	112.9	8.74
82.5	112.9	9.12
71.5	112.9	9.35
61.4	112.9	9.63
51.8	112.9	9.90
51.8	215.6	9.89
43.0	215.6	10.14
36.1	215.6	10.35
25.6	215.6	10.78
14.8	215.6	11.19

VISCOSITY MEASUREMENTS

The measurements of viscosity and dynamic properties[1] were made on the same sample, distributed by Dr. R. S. Marvin of the National Bureau of Standards.[5] Its viscosity-average molecular weight was 1.35 million. Data obtained on this sample for stress relaxation,[4] creep,[6] viscosities of concentrated solutions,[7] and dy-

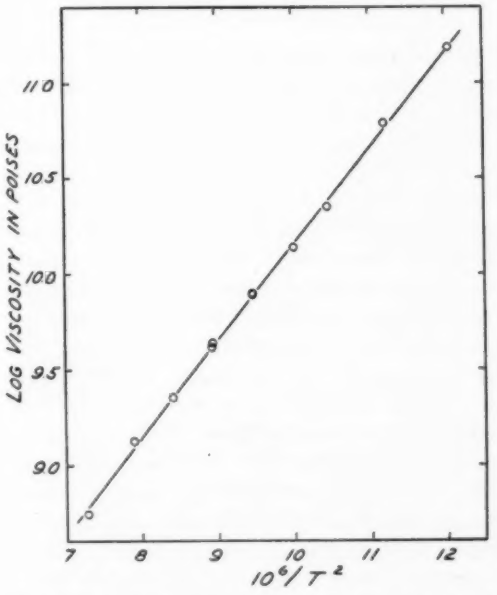

FIG. 1. Logarithm of viscosity in poises plotted against $1/T^2$.

* Union Carbide and Carbon Fellow in Physical Chemistry, 1950–1952. Present address: E. I. du Pont de Nemours and Company, Wilmington, Delaware.

† Present address: Department of Physics, The Pennsylvania State College, State College, Pennsylvania.

[1] Fitzgerald, Grandine, and Ferry, J. Appl. Phys. **24**, 650 (1953).

[2] J. D. Ferry, J. Am. Chem. Soc. **72**, 3746 (1950).

[3] Ferry, Fitzgerald, Johnson, and Grandine, J. Appl. Phys. **22**, 717 (1951).

[4] A. V. Tobolsky, J. Am. Chem. Soc. **74**, 3786 (1952).

[5] R. S. Marvin, Interim Report on the Cooperative Program on Dynamic Testing, National Bureau of Standards, 1951.

[6] C. A. Dahlquist and M. R. Hatfield, J. Colloid Sci. **7**, 253 (1952).

[7] Johnson, Evans, Jordan, and Ferry, J. Colloid Sci. **7**, 498 (1952).

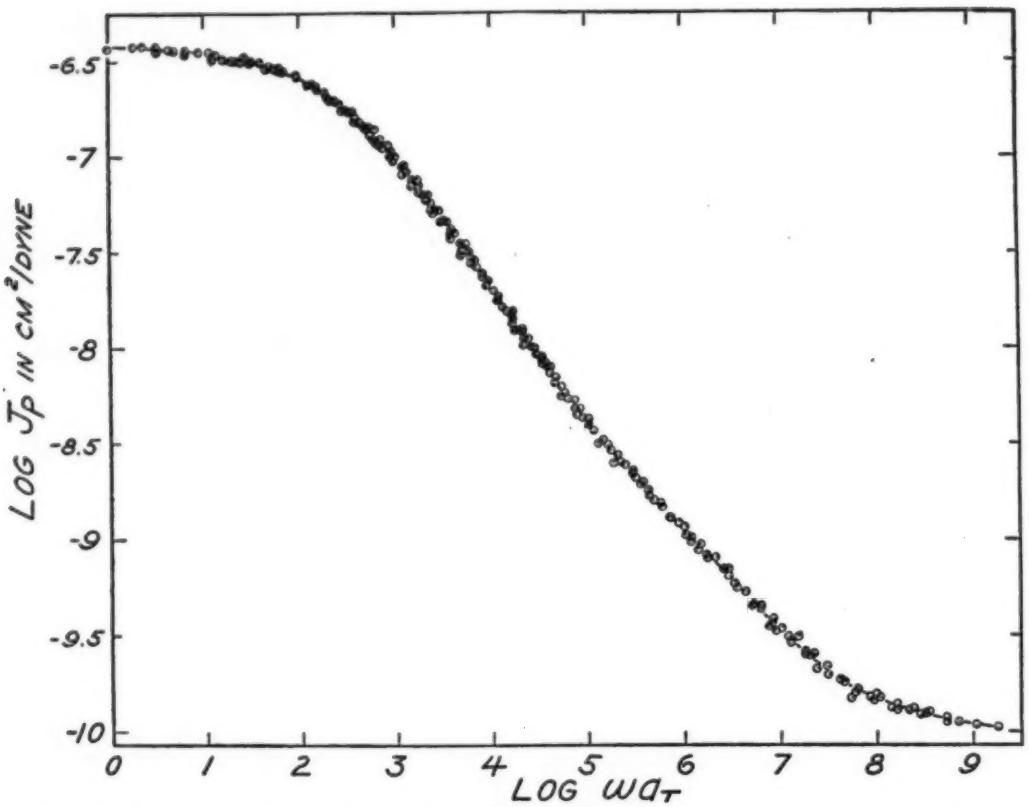

FIG. 2. Real part of complex compliance reduced to 25°C, plotted logarithmically against reduced frequency. Key to temperatures: downward pip, −44.6° (at highest reduced frequency); successive 45° rotations counterclockwise, −40.4°; −34.7° and −33.4°; −29.8° and −28.5°; −25.0° and −23.0°; −19.9°; thereafter approximately 5° increments corresponding to temperatures listed in Table II.

namic mechanical properties at extremely low frequencies[8] have been reported from various laboratories.

Steady flow viscosities were measured in an apparatus of the Pochettino type[9] which was originally constructed by Fox and Flory[10] and later modified in our Laboratory.[11,12] The polymer was molded in the apparatus for 4 hr at 80°C. Steady-state flow under constant load was established at about 100°C, and then the temperature was lowered in successive steps, with measurements at each temperature; the rate of fall of the inner cylinder was followed with a cathetometer telescope. The load was never removed, so the steady-state elastic compliance was not allowed to recover, and the long and uncertain delay for re-establishment of steady-state flow was avoided. At about 52°, however, the load was doubled, and time was allowed for re-establishment of steady-state flow; the same viscosity was obtained for both loads, lending confidence to the conclusion[10] that non-Newtonian effects are negligible under the conditions of these measurements.

The viscosity data are given in Table I. These values are probably among the highest ever to have been reported for a polymer. A plot of the logarithm of viscosity against the reciprocal of the absolute temperature is curved, as found in earlier studies on polyisobutylenes of somewhat lower molecular weights;[10,13,14] a plot against $1/T^2$ (Fig. 1) is quite linear, however, as observed by others,[10,14] and its slope is 5.1×10^5, in agreement with the value found by Leaderman[14] for

TABLE II. Values of $\log a_T$ from superposition of reduced dynamic data.

t, °C	$\log a_T$	t, °C	$\log a_T$
−44.6	4.75	4.9	0.98
−40.4	4.23	9.8	0.72
−34.7	3.69	14.8	0.51
−33.4	3.44	19.9	0.27
−29.8	3.22	25.0	0.
−28.5	3.06	30.2	−0.21
−25.0	2.84	34.9	−0.42
−23.0	2.68	40.0	−0.62
−19.9	2.45	50.0	−0.99
−14.8	2.08	59.8	−1.31
−9.9	1.78	80.0	−1.90
−5.0	1.51	99.9	−2.29
−0.1	1.22		

[8] W. Philippoff, J. Appl. Phys. **24**, 685 (1953).
[9] A. Pochettino, Nuovo cimento **8**, 77 (1914).
[10] T. G. Fox, Jr., and P. J. Flory, J. Am. Chem. Soc. **70**, 2384 (1948).
[11] Ferry, Grandine, and Udy (to be published).
[12] We are indebted for the use of this apparatus to Professor J. W. Williams, to whom it was transferred under a U. S. Office of Naval Research contract.
[13] J. D. Ferry and G. S. Parks, Physics **6**, 356 (1935).
[14] Leaderman, Smith, and Jones, unpublished experiments.

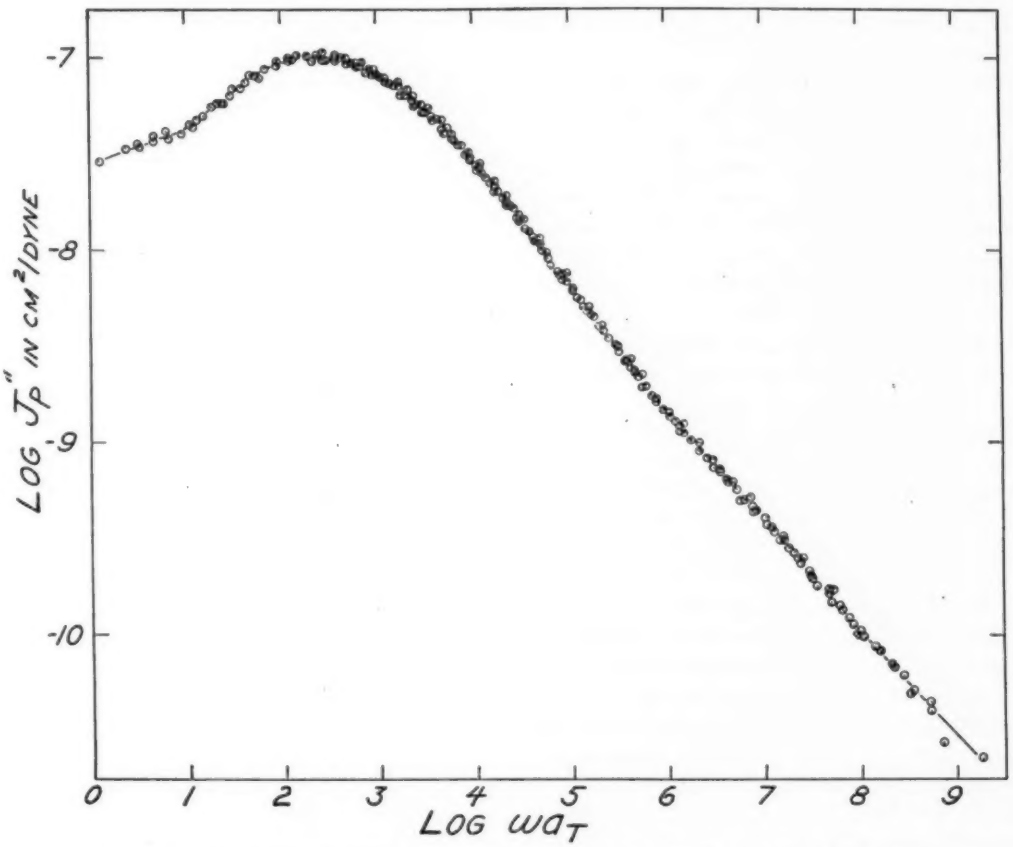

FIG. 3. Imaginary part of complex compliance reduced to 25°C, plotted logarithmically against reduced frequency. Key to temperatures same as in Fig. 2.

polyisobutylenes of quite low molecular weight. The logarithm of the viscosity in poises at 25.0° is found by interpolation to be 10.79.

REDUCED DYNAMIC DATA

The real and imaginary parts of the complex compliance J' and J'', given in the previous paper,[1] were reduced to 25°C by the following equations:[15]

$$J_p' = J'[T\rho/T_0\rho_0 + (J_\infty/J')(1 - T\rho/T_0\rho_0)], \quad (1)$$

$$J_p'' = J''(T\rho/T_0\rho_0). \quad (2)$$

Here ρ and ρ_0 are the densities at absolute temperatures T and T_0 (298°K), respectively. The ratios ρ/ρ_0 were calculated from the value of 0.58×10^{-3} deg^{-1} for the thermal expansion coefficient.[5] The glassy compliance J_∞ was estimated to be 1.1×10^{-10} cm²/dyne from the measured values of J' at the lowest temperatures and highest frequencies.

If all contributions to compliance except J_∞ are inversely proportional to temperature and density and are associated with retardation times all of which depend identically on temperature, then values of either J_p' or J_p'' at all frequencies and temperatures should form a single curve [2,15] when plotted against ωa_T, where ω is the circular frequency and a_T is the factor by which all retardation times change when the temperature is changed from T_0 to T. This superposition is closely fulfilled by both J_p' and J_p'', as shown in Figs. 2 and 3. The logarithms of the values of a_T which are chosen to make both real and imaginary components give these

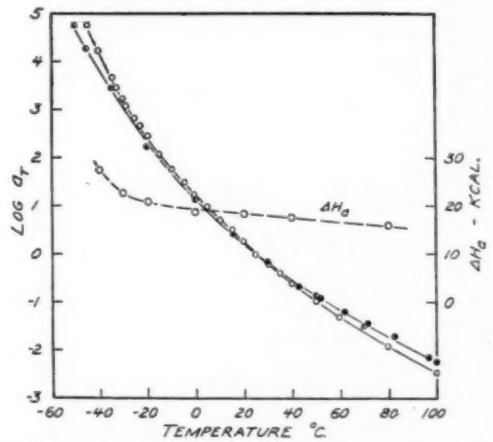

FIG. 4. Logarithm of reduction factor a_T plotted against temperature. Open circles, from superposition of dynamic data; half black, from superposition of stress relaxation data; full black, from viscosity. Dashed curve, apparent activation energy for relaxation (from dynamic data).

[15] J. D. Ferry and E. R. Fitzgerald, J. Colloid Sci. 8, 224 (1953).

single composite curves are listed in Table II and plotted against the temperature in Fig. 4.

These values of a_T are considerably more reliable than those given in an earlier publication for a different sample of polyisobutylene of slightly lower molecular weight,[3] because the matching of reduced dynamic data extends over a wider frequency range and the measurements themselves are more accurate. The new values do agree with the previous values of $\log a_T$ within about 8 percent, however; they are numerically somewhat smaller below 5°C and larger above.

According to the postulates of the method of reduced variables, the factor a_T should also be calculable[3] from the temperature dependence of the steady flow viscosity: $a_T=\eta T_0\rho_0/\eta_0 T\rho$. Values calculated in this manner from the data of Table I are also plotted in Fig. 4, as well as values derived by Tobolsky and McLoughlin[16,17] from superposition of reduced stress relaxation data. The results from stress relaxation agree with those from our viscosity measurements, but both are slightly smaller numerically than the results from our dynamic measurements. All three sets of values give fairly good straight lines when plotted logarithmically against $1/T^2$, the slopes being about 5.4, 5.4, and 5.8×10^5 for a_T from viscosity, stress relaxation, and dynamic data, respectively.

The reduced experimental data in Figs. 2 and 3 represent predictions of J' and J'' at 25°C over a frequency range of nine decades. With increasing frequency, the real component falls from $10^{-6.4}$ cm²/dyne, characteristic of a soft rubbery material, to 10^{-10} cm²/dyne, characteristic of a hard glass. The imaginary component attains a maximum of 10^{-7} cm²/dyne and falls below $10^{-10.5}$ cm²/dyne at the highest frequency attained.

These data may be also presented in the somewhat more familiar form of the real and imaginary components of the complex rigidity, G_p' and G_p''. These quantities (reduced to 25°C) are plotted in Fig. 5, together with the real part of the complex dynamic viscosity, $\eta_p'(=G_p''/\omega_p)$. The latter is about 10^5 poises at a circular frequency of unity—still more than 10^5 times smaller than the steady flow viscosity; at a circular frequency of 10^9 it has fallen to 2.5 poises.

The loss tangent, $J_p''/J_p'(=G_p''/G_p')$, which is also shown in Fig. 5, is of particular interest because of its unusual shape, with a broad maximum at $\omega_p=10^{4.8}$ and a plateau or shoulder extending from 10^6 to 10^7. These features are also apparent in the original data,[1] where at low temperatures the plateau appears as a small secondary maximum; the reduction to 25° changes the shape slightly because of the difference between the factors of Eqs. (1) and (2).

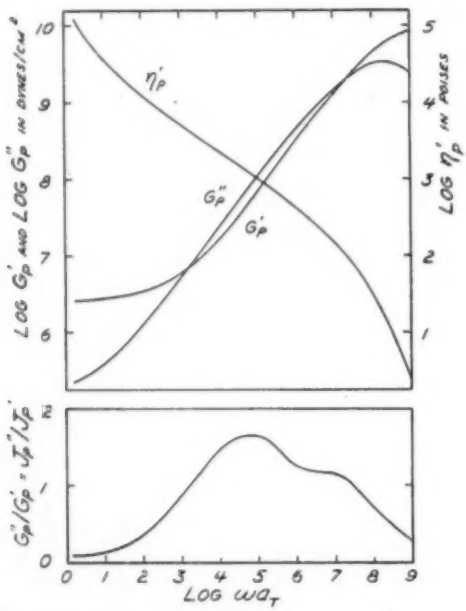

FIG. 5. Real and imaginary parts of complex shear modulus G_p' and G_p'', and real part of complex viscosity η_p', all reduced to 25°C, plotted logarithmically against reduced frequency; reduced loss tangent plotted against log reduced frequency.

TABLE III. Distribution functions of relaxation and retardation times, reduced to 25°C.

$\log\tau_p$	$\log\Phi$ from G'	$\log\Phi$ from G''	$\log L$ from J'	$\log L$ from J''
−9.0	8.97	9.18		
−8.5	9.27	9.36	−10.87	−10.63
−8.0	9.25	9.36	−10.59	−10.37
−7.0	8.84	8.84	−9.89	−9.79
−6.0	8.25	8.30	−9.26	−9.27
−5.0	7.63	7.60	−8.69	−8.70
−4.0	6.89	6.91	−7.83	−7.92
−3.0	6.28	6.32	−7.31	−7.32
−2.0	5.71	5.74	−7.22	−7.20
−1.0	5.30	5.28	−7.68	−7.53
−0.5	5.28	5.16	−7.98	−7.58

DISTRIBUTION FUNCTIONS

The distribution function of relaxation times Φ can be calculated from G' and G'' (Fig. 5), and the distribution function of retardation times L can be calculated from J' and J'' (Figs. 2 and 3), by the following formulas,[15,18,19] in which for convenience the subscript p is omitted:

$$\Phi_{\tau=1/\omega}=AG'(d\log G'/d\log\omega) \quad (3)$$

$$=BG''(1-|d\log G''/d\log\omega|), \quad (4)$$

$$L_{\tau=1/\omega}=-AJ'(d\log J'/d\log\omega) \quad (5)$$

$$=BJ''(1-|d\log J''/d\log\omega|). \quad (6)$$

The function $\Phi d\ln\tau$ is the differential contribution to the instantaneous rigidity associated with relaxation

[16] A. V. Tobolsky and J. R. McLoughlin, J. Polymer Sci. 8, 543 (1952).
[17] Tobolsky and McLoughlin denote this factor by κ when derived from superposition of time-dependent mechanical data.
[18] J. D. Ferry and M. L. Williams, J. Colloid Sci. 7, 347 (1952).
[19] M. L. Williams and J. D. Ferry, J. Polymer Sci. (to be published).

times whose logarithms lie between $\ln\tau$ and $\ln\tau+d\ln\tau$; $Ld\ln\tau$ is the differential contribution to the steady-state compliance associated with retardation times whose logarithms lie between $\ln\tau$ and $\ln\tau+d\ln\tau$. The factors A and B have been evaluated numerically as functions of m, the negative slope of a logarithmic plot of Φ against τ or the positive slope of L against τ, determined from a first approximation calculation.

The functions Φ and L, both reduced to 25°C, are given in Table III and plotted logarithmically against τ in Fig. 6. The agreement between values calculated from the real and imaginary components of the experimental data is in most cases excellent, providing a gratifying confirmation of the validity of the measurements. The detailed shapes of these functions are thus known throughout the region of time scale in which the consistency changes from that of a soft rubber to that of a hard glass. The function Φ goes through a maximum at $\tau_p=10^{-8.4}$ sec; L goes through a maximum at $10^{-2.3}$ sec.

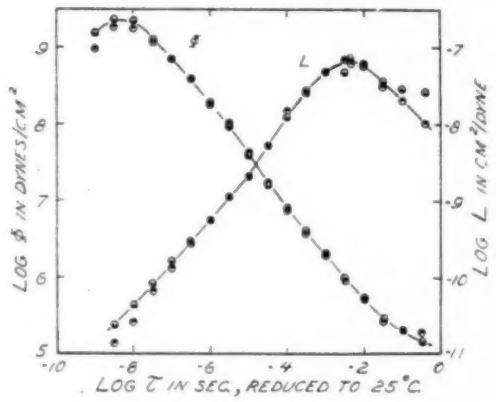

FIG. 6. Distribution functions of relaxation times (Φ) and retardation times (L), plotted logarithmically, reduced to 25°C. Key to points: top black, calculated from G_p' or J_p'; bottom black, from G_p'' or J_p''.

DISCUSSION

The above treatment separates the variables of temperature and time to provide a_T, a function of temperature alone, and Φ (or L), a function of time alone. Actually, Fig. 4 shows that a_T is not quite independent of the time scale. The steady flow viscosity is largely determined by elastic mechanisms with very long relaxation times, such as are measured in stress relaxation, and it is not surprising that these two types of data yield identical values of a_T. The slightly larger values obtained from the dynamic data suggest that mechanisms with short relaxation times are associated with slightly higher apparent activation energies for the unit relaxation process. If this is the case, the shapes of the functions Φ and L cannot be exactly independent of temperature either; they should be slightly sharper at low temperatures and slightly broader at high temperatures. It is not worth while to take these small differences into account at present, however.

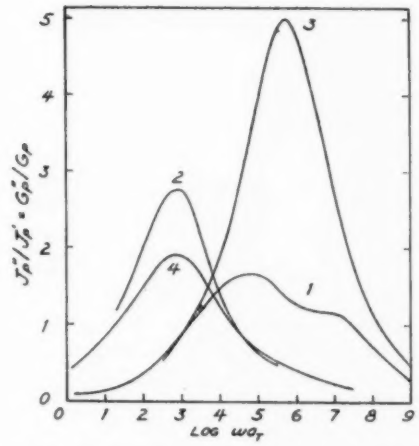

FIG. 7. Reduced loss tangents for (1) polyisobutylene, (2) polystyrene, (3) polyvinyl chloride-dimethyl thianthrene composition with 10 percent polymer, (4) polyvinyl chloride-dimethyl thianthrene composition with 40 percent polymer. Reference temperature for 1, 3, and 4, 25°C; for 2, 125°C.

To describe the temperature dependence of relaxation and retardation processes without the use of an arbitrary reference temperature, the factor a_T may be differentiated to give the apparent activation energy $\Delta H_a=Rd\ln a_T/d(1/T)$. This quantity, which ranges from 16.0 kcal at 80°C to 27.6 kcal at −40°, is also plotted in Fig. 4. It is considerably smaller and less temperature dependent than for other polymers in a comparable range of mechanical properties.[20] For example, at a frequency of 600 cycles/sec, polyisobutylene at −30° has the same value of J' (0.5×10^{-9} cm²/dyne) as polystyrene at 118.2°. But for polyisobutylene at −30°, ΔH_a is 23 kcal, and it is changing only moderately with temperature; for polystyrene at 118°, ΔH_a is 89 kcal and is changing much more rapidly. It is to be expected that the effects of chemical composition on mechanical properties will be largely apparent in the function ΔH_a, and to a much lesser extent in the shape of Φ and L.

That the time-dependent functions are affected by chemical composition to some degree, however, is shown in Fig. 7 by comparison of the loss tangents J''/J' for several different polymers as a function of frequency. The maximum of this ratio is much sharper in polystyrene[21] and two compositions[22] of polyvinyl chloride and dimethyl thianthrene, previously studied by the same experimental method, than in polyisobutylene. The plateau on the high frequency side of the maximum is seen only in polyisobutylene. These characteristics of the latter polymer may be in some way associated with the well-known steric hindrance of its methyl groups.

Combination of Fig. 6 with values of Φ at longer times derived from stress relaxation data of Andrews and

[20] J. D. Ferry and E. R. Fitzgerald, Proceedings of the Second International Congress on Rheology (to be published).
[21] L. D. Grandine, Jr., and J. D. Ferry, J. Appl. Phys. **24**, 679 (1953).
[22] E. R. Fitzgerald and J. D. Ferry, J. Colloid Sci. **8**, 1 (1953).

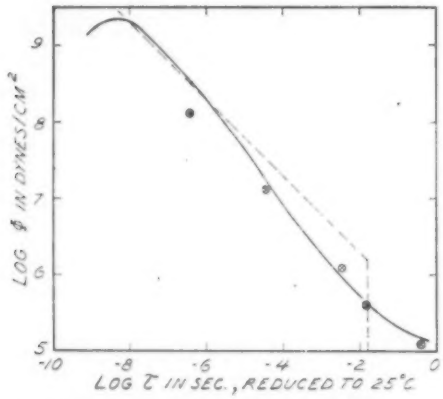

FIG. 8. Distribution function of relaxation times Φ, plotted logarithmically. Solid curve, reproduced from Fig. 6; points, from stress relaxation measurements of Tobolsky and associates; dashed lines, idealized distribution of Tobolsky.

Tobolsky[4,23] shows clearly that Φ goes through a minimum near $\tau=1$ sec and a broad maximum near 10^3 sec (reduced to 25°C). This is the region where Φ has previously been approximated by a constant.[24]

Measurements of stress relaxation reported by Tobolsky and McLoughlin[16] at very low temperatures, when reduced to 25°C, extend down to $\tau=10^{-6.5}$. Values of Φ derived from these measurements by a second approximation calculation[18] analogous to those of Eqs. (3) and (4) are compared in Fig. 8 with the curve for Φ from our dynamic measurements reproduced from Fig. 6. The values from the two sources agree well although they are reduced from measurements at quite different temperatures; at $\tau=10^{-4}$ sec, for example, the stress relaxation data are derived from experiments at $-70°$ to $-55°$, while the dynamic data are derived from measurements at $-10°$ to 35°C. This agreement bears out the validity of the method of reduced variables for predicting time-dependent mechanical properties over a wide range of frequency and shows that the slight differences in a_T associated with long and short relaxation times, apparent in Fig. 4, produce no serious distortion of the time-dependent functions obtained in this manner.

The distribution function Φ for polyisobutylene in the transition region from rubber-like to glass-like behavior has been approximated by Tobolsky[4,25] by an idealized wedge-shaped log-log plot with a slope of -0.5, to permit analytical calculations of time-dependent mechanical properties. This plot is included in Fig. 8; it lies near the experimentally determined curve, but it does not of course reproduce the maximum at $\tau=10^{-8.4}$, and it deviates considerably from the curved region above $\tau=10^{-4}$ sec. The latter deviation causes values of G' (or E', the real part of the complex dynamic Young's modulus) calculated from Tobolsky's idealized function to be in error by a factor of 2 to 2.5 in the frequency range from 10^3 to 10^5 cycles/sec (reduced to 25°C).

A recent theory of Rouse[26] for the viscoelastic properties of isolated polymer molecules predicts that in the region of short times the distribution function Φ should be proportional to $\tau^{-\frac{1}{2}}$, in accordance with the slope of Tobolsky's idealized plot. The same slope is predicted by the viscous coupling theory of Blizard,[27] which does not, however, relate the mechanical properties to molecular parameters. The experimental curve for polyisobutylene does not lie far from a line with this slope, as seen in Fig. 8. Other polymers, however, give somewhat steeper Φ curves.[20] Neither theory accounts for the minimum and secondary maximum in the Φ function of polyisobutylene which[23] lie at larger values of reduced time beyond the range of the present study.

ACKNOWLEDGMENTS

This work was part of a program of research on the physical structure and properties of cellulose derivatives and other polymers supported by the Allegany Ballistics Laboratory, Cumberland, Maryland, an establishment owned by the United States Navy and operated by the Hercules Powder Company under Contract NOrd 10431. It was also supported in part by a grant from Research Corporation and by the Research Committee of the Graduate School of the University of Wisconsin from funds supplied by the Wisconsin Alumni Research Foundation. We are grateful to Union Carbide and Carbon Corporation for assistance through its Fellowship in Physical Chemistry.

[22] R. D. Andrews and A. V. Tobolsky, personal communication.
[24] Andrews, Hofman-Bang, and Tobolsky, J. Polymer Sci. **3**, 669 (1948).
[25] The function D' used by Tobolsky is equal to 6.91Φ.
[26] P. E. Rouse, Jr. (to be published).
[27] R. B. Blizard, J. Appl. Phys. **22**, 730 (1951).

Helix Impedance Measurements Using an Electron Beam

D. A. WATKINS* AND A. E. SIEGMAN
Hughes Research and Development Laboratories, Culver City, California

(Received March 12, 1953)

Impedance measurements made on a tape helix with an electron beam are described. Curves showing the measured impedances of the fundamental and first backward space-harmonic components of the mode commonly used in traveling-wave tubes are presented for values of *ka* (circumference to free-space wavelength ratio) ranging from 0.15 to 0.6. The impedance of the fundamental is found to be less than that calculated from the sheath model by a factor ranging from 0.8 to 0.3. Phase velocities of other modes and components were observed for *ka* from 0.1 to 1.1; these agree with an analysis by Sensiper which predicts that certain values of the phase constant are not allowed for a single wire helix. A relationship for the impedance of one space-harmonic component in terms of the impedance of its fundamental is presented in approximate agreement with the experimental data. In addition to providing impedance data over a wide frequency range, the helix tester performed as a continuously voltage tunable backward-wave oscillator from 1500 to 4300 mc at a beam current of 1 ma.

THE helix is the circuit most frequently used for traveling-wave tubes because of several desirable properties. It is easy to construct, has a mode of propagation whose phase velocity is constant over a wide frequency range, and has high impedance. In the design of traveling-wave tubes it is important that the designer know what the circuit impedance is so that he may predict with reasonable accuracy the gain and power output to be expected.

Pierce[1] has calculated the velocity of propagation and the impedance of the helix by means of the sheath model, in which the actual helix is replaced by a cylindrical surface that is conducting only in the helical direction. The sheath model and the tape model helices are shown in Fig. 1. Experience shows that impedances calculated from the sheath model are higher than those actually obtained with wire helices by a factor ranging from one to about four, depending upon the diameter of the helix and the amount of dielectric material present. In addition, the sheath model fails to yield any information about the space-harmonic wave components[2] which must exist with an actual helix owing to its periodicity in the axial direction.

Cutler[3] has reported probe measurements of field strength for a helix, but they were made at only one frequency. Besides, probe measurements are difficult to make because the probe alters the field that it measures and fails to separate the various space-harmonic components. Such measurements are likely to be time-consuming and difficult or impossible to interpret.

Kompfner[4] has suggested a method of measuring circuit impedance in a traveling-wave tube based upon the careful adjustment of beam voltage and beam current to produce a cancellation of the rf signal applied to its input. Kompfner calculated the circuit impedance for which this cancellation occurs in terms of beam voltage, beam current, and the length of the circuit in wavelengths. The method is difficult to apply to ordinary tubes because the conditions for cancellation are influenced by the degree of space-charge, the distribution of circuit loss, and the radial distribution of beam current over the cross section of the circuit. Also, ordinary tubes are not likely to be operable over a wide frequency range (such as ten to one) because of poor input and output matching. Because of their importance in design, it was decided to measure the impedance and velocities of the field components on a helix utilizing a thin hollow electron beam in a specially constructed traveling-wave tube. In designing it, special care was taken to minimize sources of error and to yield the greatest amount of useful information. The experimental results obtained with this helix tester verify to a considerable extent the theoretical work of

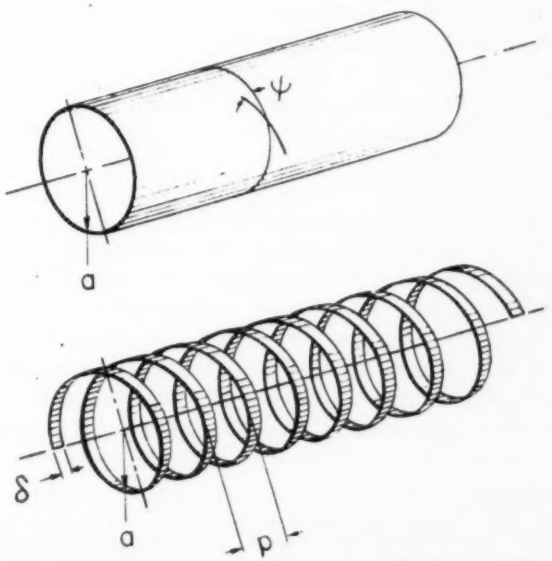

FIG. 1. The sheath model and tape model helices. The sheath model is conducting only in the helical direction making an angle ψ with a plane normal to the axis.

* Now at Stanford University, Stanford, California.

[1] J. R. Pierce, *Traveling-Wave Tubes* (D. Van Nostrand Company, Inc., New York, 1950), Appendix II.

[2] J. C. Slater, *Microwave Electronics* (D. Van Nostrand Company, Inc., New York, 1950), Chap. VIII.

[3] C. C. Cutler, Proc. Inst. Radio Engrs. **36**, 230 (1948).

[4] R. Kompfner, J. Brit. Inst. Radio Engrs. **10**, 283 (1950).

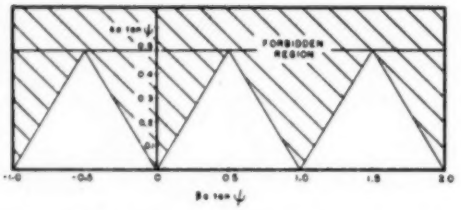

FIG. 2. Chart of the forbidden values of β for the tape helix shown in Fig. 1. Tan $\psi = p/2\pi a$. (From Sensiper, reference 5.)

Sensiper[5] on the tape helix and show qualitative agreement with the impedance calculations made by Tien[6] and based on Sensiper's field solutions. In addition, the results show that other wave components and modes have properties that make them useful for special applications.

THEORY

Sensiper's analysis of the tape helix reveals a number of possible modes of propagation, all with space-harmonic components. He shows that, because of the periodicity of the tape helix in free space, there are certain values of phase constant that are not allowed. These "forbidden regions" are shown in Fig. 2. The argument employed can be stated as follows.

Because of the periodic character of the structure, the field variation in the z direction can be described by a sum of Fourier components of the form $\exp -\Gamma_m z$ with appropriate coefficients. If Γ_m is an imaginary number, the wave is unattenuated with distance and corresponds to a "free mode" of propagation. If Γ_m is complex or real, the wave is attenuated. If Γ_m is imaginary, it may be written $\Gamma_m = j\beta_m$. Then, because of the periodicity of the structure,

$$\beta_m = \beta_0 + (2\pi m/p), \tag{1}$$

where β_0 is the phase constant of the fundamental space-harmonic component of the mode under consideration, p is the pitch of the helix, and m is a positive or negative integer. The radial dependence of the fields is written in terms of the radial propagation constant

$$j\gamma_m = j(\beta_m^2 - k^2)^{\frac{1}{2}} \tag{2}$$

where $k = \omega/c$, ω being the radian frequency and c the velocity of light in the medium surrounding the helix. Mks units are used throughout. For all the field components of a given mode of propagation to decay to zero at large radius, it is required that all the γ's be purely real; otherwise the field at infinite radius would have a finite value corresponding to radiation in the radial direction. For γ_m to be real, β_m must be greater than k. It is this condition that determines the boundaries of the forbidden regions. Thus β_0 is restricted to those values for which all of the associated β_m's for the particular mode are greater than k. It is noted that

$$\tan\psi = p/2\pi a, \tag{3}$$

where ψ is the pitch angle of the helix and a is its radius.

In the traveling-wave tube, the axial or z component of the electric field intensity is of the greatest interest since it is the only one that has appreciable coupling with an electron beam. The impedance used in traveling-wave tube theory is defined in terms of the electric field of the mth component and the total power as follows:

$$K_m = E_{zm}^2/2\beta_m^2 P, \tag{4}$$

where E_{zm} is the z component of the peak field strength of the mth space-harmonic component, and P is the total average power carried by all of the space-harmonic components of the mode being considered. From Sensiper one obtains the following expression for E_{zm} inside the helix in terms of the current in the tape:

$$E_{zm} \simeq j \frac{|I|\, e^{-j(\beta_m z - m\theta)}}{p\omega\epsilon_0 a} (\gamma_0 a)(\gamma_m a) \times \tan\psi I_m(\gamma_m r) K_m(\gamma_m a) \frac{\sin\frac{\gamma_m \delta}{2}}{\frac{\gamma_m \delta}{2}}, \tag{5}$$

where $|I|$ is the magnitude of the current in the tape, $I_m(\gamma_m r)$ and $K_m(\gamma_m a)$ are the modified Bessel functions, and δ is the width of the tape. The approximations made in obtaining Eq. (5) are (1) that $\beta_m \simeq \gamma_m$, a good approximation for waves traveling slowly enough to interact with electron streams; (2) that the rf current is of constant magnitude across the tape; (3) that there is no rf current in a direction perpendicular to the tape; (4) that the current does not vary in phase in a direction perpendicular to the tape and that the pitch angle ψ is small. We do not know how good the last three approximations are for wide tapes. Sensiper shows that they are very good for narrow tapes, and the writers believe that they are good for wide tapes also.

Using Eq. (5) one obtains the following relationship

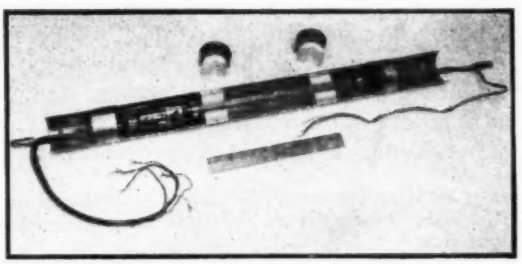

FIG. 3. Experimental helix tester shown in its container with input and output connections.

[5] S. Sensiper, "Electromagnetic Wave Propagation on Helical Conductors," Ph. D. dissertation, in abbreviated form as Research Laboratory of Electronics Report No. 194, Massachusetts Institute of Technology, Cambridge, Massachusetts, (1951).

[6] P. K. Tien, "Helix Impedance of Traveling-Wave Tubes," Technical Report No. 50, Electronics Research Laboratory, Stanford University, Stanford, California (1952).

between the impedances of two space-harmonic components of the same mode at $r=a$:

$$K_m = K_0 \frac{I_m^2(\gamma_m a) K_m^2(\gamma_m a) M_m^2}{I_0^2(\gamma_0 a) K_0^2(\gamma_0 a) M_0^2}, \tag{6}$$

where

$$M_m = \frac{\sin \frac{\gamma_m \delta}{2}}{\frac{\gamma_m \delta}{2}}. \tag{7}$$

For $\gamma_m a > 2$, $I_m(\gamma_m a) K_m(\gamma_m a) \simeq \frac{1}{2\gamma_m a}$, and Eq. (6) becomes

$$K_m \simeq K_0 \frac{(\gamma_0 a)^2 M_m^2}{(\gamma_m a)^2 M_0^2}. \tag{8}$$

Equation (8) is interesting because it shows that the impedance of a space-harmonic can be as high as that of its fundamental, depending upon the ratio of their phase velocities. The ratio M_m^2/M_0^2 is of the order of 0.5 for typical cases.

The mode commonly used in traveling-wave tubes is Sensiper's mode h_{10}. For this mode, the zeroth and all of the space-harmonic components with positive values of m are *forward* waves. By a forward wave is meant a wave whose phase velocity ω/β_m and group velocity $d\omega/d\beta_m$ are in the same direction. All of the components of this mode with negative m are *backward* waves; that is, their phase and group velocities are in opposite directions. The interaction of an electron stream with a forward wave is as described in Pierce's[1] theory of the traveling-wave tube. Interaction with a backward wave is much different, being of a regenerative character. This kind of interaction was described by Kompfner[7] and is the basis of his backward-wave oscillator.

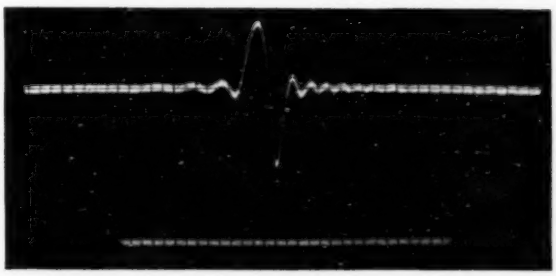

(a)

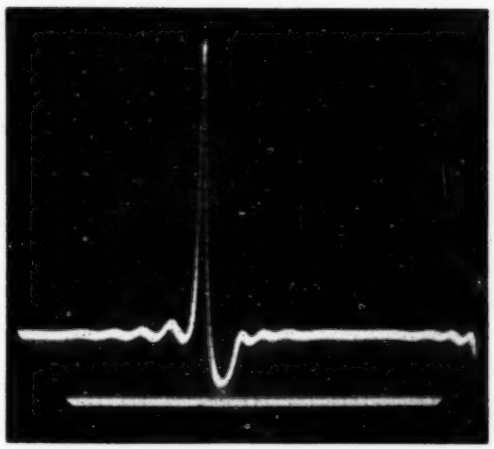

(b)

FIG. 4. Power out *vs* beam voltage for interaction with (a) a forward wave and (b) with a backward wave.

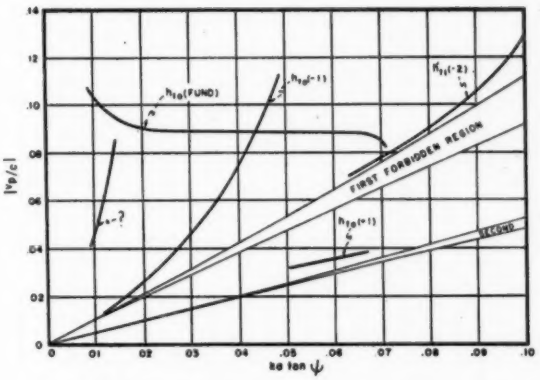

FIG. 5. Phase velocities of observed wave components *vs* $ka \tan \psi$, a parameter proportional to frequency. Tan $\psi = 0.0944$.

EXPERIMENTAL RESULTS

The traveling-wave tube used for our measurements consisted of a tape helix and a hollow-beam electron gun enclosed in a glass envelope. The helix was suspended as nearly as possible in free space by use of the glass configuration shown in cross section in Fig. 7. Its dimensions were: mean diameter, 0.486 in.; length, 15.0 in.; $\tan\psi$, 0.0944; $\delta/p = 0.444$; tape width, 0.064 in.; tape thickness, 0.020 in. The envelope was constructed by shrinking 7070 glass tubing onto a rod in which three longitudinal groves has been milled. An annular-ring cathode, followed by grid and anode with similar annular openings, furnished a hollow cylindrical beam at an r/a of 0.825 with respect to the helix. The beam thickness was 0.005 in. Beam focusing was accomplished by immersing the entire structure in an axial magnetic field of approximately 1000 gauss. That the beam retained its original diameter was verified by use of a three-element collector consisting of an inner plug, a coaxial outer ring, and a main collector behind the opening between the plug and ring. With normal beam focusing, more than 85 percent of the total beam current passed through the 0.010-in. wide annular slit, which had the same mean diameter as the cathode ring. Roughly equal amounts of the remaining current were intercepted by the plug and ring elements. Less than

[7] R. Kompfner, "Backward Waves," presented at the Tenth Annual Conference on Electron Tube Research, Ottawa, Canada, June 16, 1952.

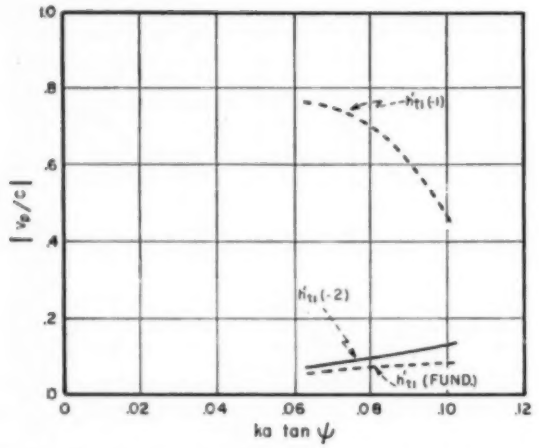

FIG. 6. Phase velocities of components of the h_{t1}' mode *vs* ka tanψ. Tan $\psi = 0.0944$. The solid line was observed and the broken lines calculated therefrom, using Eq. (1).

0.2 percent of the cathode current was intercepted by the helix.

The ends of the tape helix were brought out as leads through the glass envelope; matching to the helix was accomplished by connecting the leads directly to the center conductors of coaxial lines. The VSWR of the connections was better than 3.5 to 1 over most of the frequency range. In operation the tube was supported in a piece of brass tubing of diameter 3 in. by two bushings of polystyrene foam (Fig. 3), and the entire assembly was positioned in the solenoid that provided the magnetic focusing field.

Interaction between the beam and helix-wave components was observed by operating the tube either as a forward-wave or, backward-wave amplifier. The helix voltage was swept at 60 cps about some fixed center voltage, and the power output as a function of helix voltage was observed on an oscilloscope. The various components observed were identified by comparison with theory, and by their characteristic patterns: the sine wave-shaped dip and gain peak for forward waves, and the broad shallow dip and high

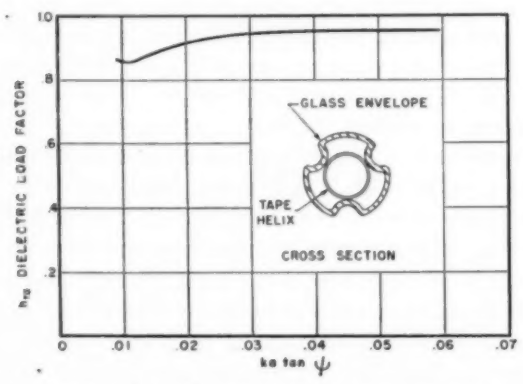

FIG. 7. Dielectric loading factor of the h_{t0} fundamental component *vs* ka tanψ. This is the ratio of the observed wave velocity to that calculated by using the sheath model; it is less than unity because of the dielectric effect of the glass envelope.

narrow gain spike for backward waves. Typical patterns are shown in Fig. 4.

Phase-velocity curves of components over a frequency range from 750 to 8250 Mc/sec are presented in Fig. 5. The components of the h_{t0} and h_{t1}' modes were observed to agree quantitatively with Sensiper's analysis. Only very weak interaction with the $h_{t0}(+1)$ component was observed; interaction with the other components was relatively strong at low beam currents. In making observations, it was necessary to keep the beam current below the level at which backward-wave oscillations on $h_{t0}(-1)$ began. The sharply dispersive component shown at the lowest frequencies is not predicted by any analysis, and remains for the

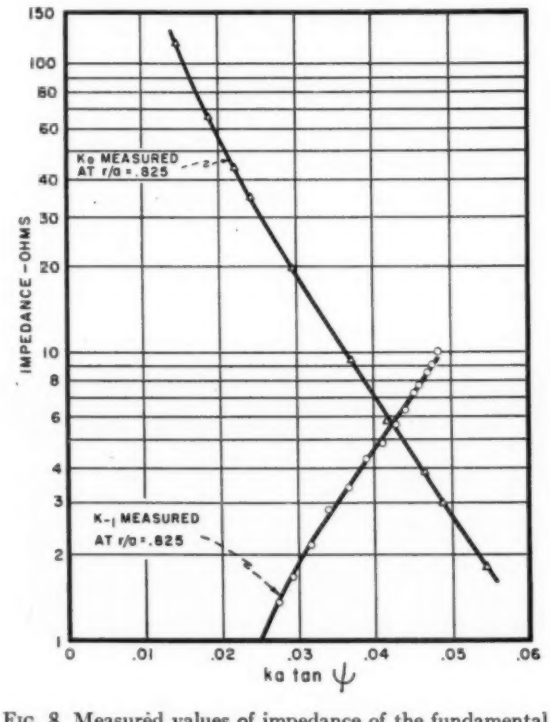

FIG. 8. Measured values of impedance of the fundamental and (-1) components of the h_{t0} mode at the electron beam position. Tan $\psi = 0.0944$.

present unexplained. It is a backward wave. If the observed wave is taken to be the fundamental, its $(+1)$ component lies somewhat above the first forbidden region, and all other components lie below it.

The observed component shown at the highest frequencies is identified as the (-2) space harmonic of the $h_t'1$ mode. Phase-velocity curves for the (-1) space harmonic and the fundamental of this mode, calculated from the observed component, are shown in Fig. 6. The fundamental lies just below the first forbidden region.

Figure 7 shows the ratio of the observed phase velocity of the h_{t0} fundamental to the phase velocity of the corresponding wave on a sheath helix. The glass configuration illustrated was used in order to minimize

the dielectric loading effect of the tube envelope on the wave propagation.

Measurements were made of K_0 and K_{-1}, the impedances of the h_{t0} fundamental and $h_{t0}(-1)$ component, respectively, over the frequency ranges 1000 to 4500 Mc/sec for K_0 and 2000 to 4000 Mc/sec for K_{-1}. As previously said, the impedances at the beam were derived from measurements of electron velocity and beam current at the cancellation point for K_0 and at the start-oscillation point for K_{-1}. The effect of circuit loss was taken into account, and the effect of space charge was negligible. The impedances were translated from the beam radius to the helix by using Eq. (5). Measured values of K_0 and K_{-1} at the beam radius are shown in Fig. 8. The reduction factor (observed impedance of tape helix divided by theoretical impedance of sheath helix) for K_0 is shown in Fig. 9, together with the value of the reduction factor calculated from Tien.[6] In Fig. 10

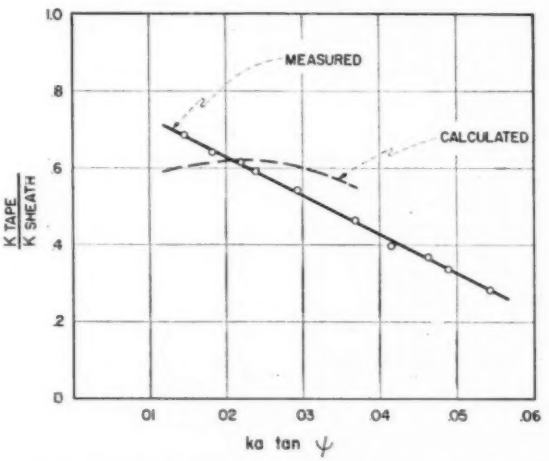

FIG. 9. Ratio of the observed h_{t0} (fund) impedance to the impedance calculated for the sheath model. Tanψ=0.0944; δ/p=0.444. The broken line is the ratio as calculated from Tien's analysis, which takes into account the effect of the dielectric on the impedance.

the measured value of K_{-1} at the helix is compared with the value computed from the measured K_0 by using Eq. (8).

BACKWARD-WAVE OSCILLATIONS

The tube operated as a continuously voltage-tuned backward-wave oscillator over the frequency range 1500 to 4300 Mc/sec, the helix voltage being varied from 100 to 5000 v. Oscillation at intermittent lower frequencies to 1200 Mc/sec was obtained, depending on the manner in which the helix was terminated. The highest frequency obtained was limited primarily by the power supply voltages available.

Plots of helix voltage and start-oscillation current as functions of frequency are shown in Fig. 11. Near 3600 Mc/sec the phase velocities of the $h_{t0}(-1)$ and fundamental components become equal in magnitude, and it is possible for the electron beam to interact

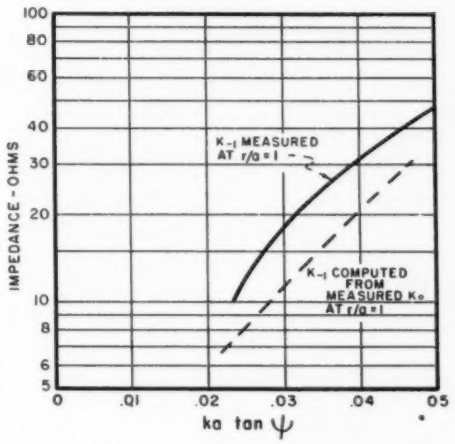

FIG. 10. Measured value of the $h_{t0}(-1)$ impedance compared with that calculated from the measured value of h_{t0} (fund) impedance using Eq. (8).

simultaneously with the fundamental of an h_{t0} mode traveling in one direction and the (-1) component of an h_{t0} mode traveling in the opposite direction. The sharp anomolies in the starting current near 3600 Mc/sec are attributed to interference effects between these two modes. These effects were sharply reduced by terminating the helix in a good match at both ends.

The frequency of oscillation was extremely stable when the helix voltage was well regulated, varying considerably less than one part in 10^4 over a 15-min period. The frequency decreased slightly with increasing beam current, but was independent of magnetic field strength above 600 gauss, the value necessary to focus the beam well. Variation in frequency with change in load impedance was small: oscillation frequency was constant to within 3 Mc/sec for any load impedance from perfect match to dead short. In the range 2900 to 3100 Mc/sec, the power output at a beam current of 2500 amp was approximately 25 mw, varying by $\pm\frac{1}{2}$ db over the band, with a beam efficiency of 1 percent.

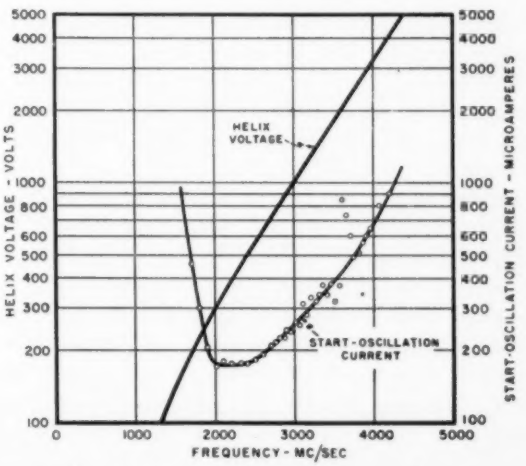

FIG. 11. Start-oscillation current and voltage *vs* frequency for the helix tester used as a backward-wave oscillator.

CONCLUSIONS

The existence of the forbidden regions deduced by Sensiper is verified by the experimental results. Two of the modes (h_{10} and h_{11}') of Sensiper's analysis were observed, together with an unidentified mode so far unexplained. The measured value of the impedance of the h_{10} fundamental agrees very roughly with Tien's calculation, but the check is not all one would desire. Some extrapolation was necessary in using Tein's results so that there is no necessary indication that his calculations are in error. The finite thickness of the tape used for the experimental helix would be expected to lower the impedance somewhat.

The observation of the h_{11}' mode suggests that it may have some possible uses either for dispersive (voltage-tuned) amplifiers or for amplifiers and backward-wave oscillators designed to operate at higher frequencies. It seems likely that the fast wave observed by Cutler[3] and nearly everyone else who has worked with a helix was in reality the h_{11}' mode. At low frequencies ($ka<1$), the group and phase velocities of the (-1) component for this mode are close to the velocity of light.

The experimental tube was built by J. J. Roberts and A. M. Anderson with assistance from other members of our Engineering Section.

JOURNAL OF APPLIED PHYSICS VOLUME 24, NUMBER 7 JULY, 1953

Consolidation Around Pore Pressure Meters

G. DE JOSSELIN DE JONG
Laboratorium voor Grondmechanica, Oostplantsoen 25, Delft, The Netherlands
(Received March 26, 1953)

Response of pore pressure meter on variations in loading conditions of surrounding soil is retarded by the necessity that pore water has to enter the instrument. This property is introduced as an instruments coefficient influencing the boundary conditions. With regard to the surface of the instrument, two types are considered: a rigid type and a cavernous type. At $t=0$ for unit step loading, consolidation has not yet started and the response of the instrument depends on shear modulus of soil only. Calculation of response as a function of time involves three-dimensional consolidation theory and is established with the aid of spherical solutions for simple harmonic and unit step loading conditions.

1. INTRODUCTION

THE newest type of pore pressure meter in use with the Delft Soil Mechanics Laboratory* consists of a cylindrical instrument of about 20 cm in length and 3.6 cm in diameter embedded in the soil mass. The body of the instrument contains a diaphragm-type pressure transducer connected by a coaxial flexible cable with the measuring apparatus above soil surface.

The response time of previous nonelectronic types amounted to several days, because of the compliance of the diaphragm and the very great flow resistance encountered in the soil by the water that has to actuate the manometer. By constructing the diaphragm as rigid as practically feasible the response time was reduced to 15 minutes.

A further reduction of the response time to a fraction of a second was obtained by a device resulting from an analysis of pore-water movement and soil deformation. This study forms the subject of this paper.

We shall treat the influence of simple harmonic loading conditions of the surrounding soil mass and by integration over the whole range of frequencies, using Fourier's integral, obtain the influence of unit step loading.

* Capacitive pressure-transducer and electronic circuitry developed by S. L. Boersma, Consulting Engineer, Delft, The Netherlands.

To simplify the mathematical treatment the instrument is idealized and instead of cylindrical symmetry a spherical symmetry is assumed. If idealized in this way, the pore pressure meter consists of a sphere with radius r_0 (cm). The following two types will be considered.

1.1 The Rigid Type

Here the diaphragm is in contact with a water volume enclosed in a rigid chamber. Holes in the wall form the connection between this water volume and the water in the pores of the soil.

We shall represent this schematically as a rigid, pervious sphere (Fig. 1a).

1.2 The Cavernous Type

Here the diaphragm is in contact with a water volume that fills a cavity in the soil. The connection between this water volume and the pore water is direct.

We shall represent this schematically as a spherical cavity (Fig. 1b).

Indicating by ΔV (cm³) the quantity of water necessary to account for the deformation of the diaphragm under water pressure, we introduce analogous to the compressibility coefficient a of the soil (see Sec. 5.1) a coefficient b (cm²/kg) for the instrument in such a

way that

$$\Delta V/(\tfrac{4}{3})\pi r_0^3 = bw_0, \qquad (1.1)$$

in which w_0 (kg/cm²) indicates the pressure in the water enclosed in the sphere.

When the surrounding soil mass is loaded, water pressures are generated in the pore water and in order that the pore pressure meter may register this, a volume of water ΔV must enter the chamber.

For the rigid type the volume of water enters by percolation through the holes in the wall. This water can only be supplied by the pore water squeezed out of the surrounding soil mass. For the cavernous type the volume ΔV arises principally from the deformation of the cavity, while an additional part is furnished by pore water coming out of the surrounding soil.

We shall proceed to formulate this action mathematically by first establishing the boundary conditions.

2. BOUNDARY CONDITIONS AT $r=r_0$

2.1 Water pressure at $r=r_0$

The *rigid type*. If we may apply Darcy's law of percolation. The water volume Q_1 cm³ entering through the pervious wall with a surface area $4\pi r_0^2$ is related to the pressure gradient in the pore water $\partial w/\partial r$ in the soil at $r=r_0$, by the expression:

$$\gamma_w(\partial Q_1/\partial t) = k4\pi r_0^2(\partial w/\partial r), \qquad (2.1.1)$$

in which γ_w (kg/cm³) denotes the density of water and k (cm/sec) the permeability of the soil (the permeability of the wall of the pore pressure meter is considered large in comparison with k of the soil).

Since for the rigid type $\Delta V = Q_1$, we obtain by using (1.1)

$$\tfrac{1}{3}br_0(\partial w/\partial t) = (k/\gamma_w)(\partial w/\partial r) \quad \text{at} \quad r=r_0. \qquad (2.1.2)$$

It is assumed here that w_0, the pressure in the meter, is equal to w, the pore pressure in the soil directly surrounding the meter, $w_0(r=r_0-0)=w(r=r_0+0)$.

The *cavernous type*. Here the water amount ΔV is the sum of Q_1 and the volume change produced by the deformation of the cavity Q_2. If we introduce the displacement u_r (cm) of the surface of the cavity in a radial direction, this volume is given by $Q_2 = -4\pi r_0^2 u_r$. Thus we obtain

$$\tfrac{1}{3}br_0(\partial w/\partial t) = (k/\gamma_w)(\partial w/\partial r) - (\partial u_r/\partial t) \quad \text{at} \quad r=r_0. \qquad (2.1.3)$$

These expressions relate to the spherically symmetrical case.

In the case when the variables w and u_r are axially symmetrical and are functions of ψ (Fig. 2) the second member of Eqs. (2.1.2) and (2.1.3) must be integrated over the range $0<\psi<\pi$. (See Sec. 4.)

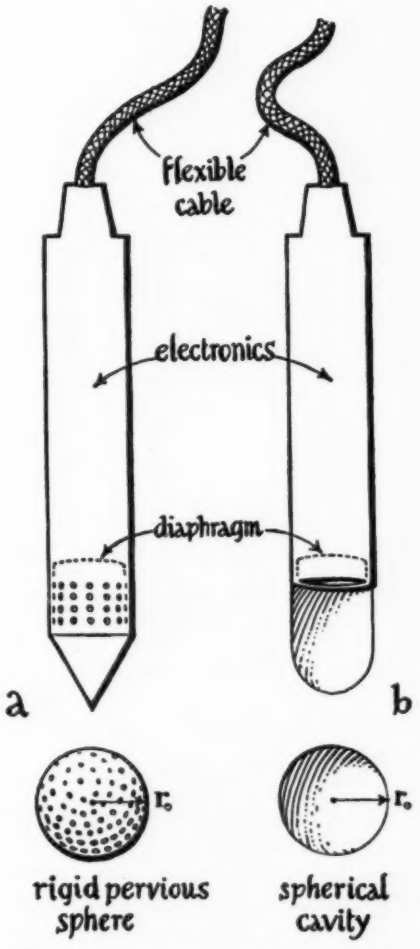

FIG. 1. Pore pressure meters of two different types.

2.2 Soil skeleton at $r=r_0$

In the *rigid type* the boundary condition at $r=r_0$ is imposed on the soil skeleton by the rigidity of the sphere:

$$u_r = 0 \quad \text{at} \quad r=r_0. \qquad (2.2.1)$$

In the *cavernous type* the wall of the cavity can displace itself freely and the stresses are determined by the condition that there is equilibrium between the water pressure w_0 in the cavity and the radial stress in the soil mass σ_r^* (negative sign for compression).

$$\left.\begin{aligned} w_0 &= -\sigma_r^* \\ 0 &= \tau_{r\psi}^* \end{aligned}\right\} \quad \text{at} \quad r=r_0. \qquad (2.2.2)$$

Here $-\sigma_r^*$ indicates the total radial stress acting on the soil skeleton and water combined, so we can divide $-\sigma_r^*$ into $-\sigma_r$, the radial stress on the grains only, and w the water pressure in the pores† by putting

$$-\sigma_r^* = -\sigma_r + w. \qquad (2.2.3)$$

These stresses act in the soil, that is to say for $r>r_0$, while w_0 is the water pressure in the cavity $r<r_0$.

† We shall use an asterisk to denote stresses and elastic constants associated with the combined system, water and soil skeleton, and omit it in the case of the grain skeleton alone.

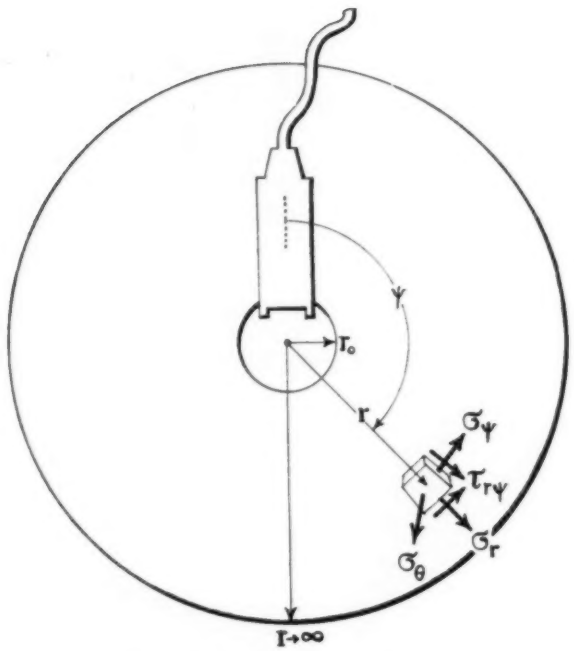

FIG. 2. Definitions of symbols used.

It follows from (2.2.2) and (2.2.3) that

$$w_0(r_0-0)=-\sigma_r+w(r_0+0). \tag{2.2.4}$$

Normally there is no difference between $w(r_0-0)$ and $w(r_0+0)$, except when the loading conditions are discontinuous with regard to time, as for instance at the moment $t=0$ for unit step loading. We shall treat this special situation in Sec. 4 and use condition (2.2.2) then. For the case of continuous loading conditions $w(r_0-0)$ equals $w(r_0+0)$ and the boundary stress condition becomes

$$\sigma_r=\tau_{r\psi}=0 \quad \text{at} \quad r=r_0. \tag{2.2.5}$$

3. BOUNDARY CONDITIONS AT $r\to\infty$

We shall assume that the dimensions of the pore pressure meter are so small in comparison with the distance to the boundary of the soil mass wherein it is embedded that we may consider the stress conditions of the soil as homogeneous. To simplify the formulas we shall also suppose that this homogeneous stress condition holds up to $r\to\infty$. As the disturbing effect diminishes proportional to r^{-3} the errors introduced by these assumptions are negligible.

In addition we shall suppose that in the surrounding soil mass the rate of squeezing out of pore water is slow in comparison with the response studied here. We may therefore simplify the condition for $r\to\infty$ to an impermeable coat, upon which the exterior loads act. Thus, we may write

$$\partial w/\partial r=0 \quad \text{at} \quad r\to\infty. \tag{3.1}$$

Regarding the stresses on the boundary at $r\to\infty$ we must consider the general case where there are three principal stresses of unequal magnitude: S_1, S_2, S_3. If we know the influence of one principal stress we may obtain by superposition their combined influence. Taking the principal stress S in the direction $\psi=0$, π we obtain as boundary condition:

$$\left.\begin{aligned} &\sigma_r^*=-S\cos^2\psi \qquad \sigma_\psi^*=-S\sin^2\psi \qquad \sigma_\theta^*=0 \\ &\tau_{r\psi}^*=S\sin\psi\cos\psi \qquad \tau_{r\theta}^*=\tau_{\theta\psi}^*=0. \end{aligned}\right\}$$

$$\text{at} \quad r\to\infty. \tag{3.2}$$

Because of the simpler treatment involved we shall finally derive a solution to the case where a uniform pressure P acts in all directions. In such a case we have

$$\sigma_r^*=\sigma_\theta^*=\sigma_\psi^*=-P, \quad \tau_{r\psi}^*=\tau_{r\theta}^*=\tau_{\theta\psi}^*=0,$$

$$\text{at} \quad r\to\infty. \tag{3.3}$$

The conditions (2.1.2), (2.1.3), (2.2.1), (2.2.2), (2.2.5), (3.1), (3.2), and (3.3) are necessary and sufficient to determine the solution to the problem explicitly in the different cases indicated.

4. SITUATION AT $t=+0$ FOR UNIT STEP LOADING

Because of its elucidatory character we shall first determine the response of the pore pressure meter to unit step loading at the moment of loading ($t=+0$). This is very simply feasible by virtue of the following considerations.

By neglecting mass acceleration and viscous retardation, we shall suppose, as is usual in the literature on consolidation, that any loading increases instantaneously the stresses in the soil mass, generating elastically the deformations that are therefore instantaneous too.

Assuming that in comparison with the compressibility of the grain skeleton of the soil the pore water is incompressible, at the instant of loading no volume change of the soil will take place. This may be expressed by putting

$$\nu^*=\tfrac{1}{2} \quad \text{for} \quad t=+0, \tag{4.1}$$

where ν^* is the Poisson's ratio of the combined system, water and soil skeleton. As the water is gradually expelled from an element at any point in the loaded soil, the Poisson's ratio ν^* at this point decreases and tends to the value of ν, where $\nu(<\tfrac{1}{2})$ is the value of the Poisson's ratio of the grain skeleton alone.

A result of some importance concerning the value of E^* may be derived in the following way. The water enclosed in the pores can prevent volume changes from occurring, but not shearing strains. This implies that shear stress in the combined system is carried by the grain skeleton alone. It follows directly that $\tau^*=\tau$, and hence that the shear moduli G^* and G are equal. Then by a well-known relation in elasticity theory,

$$G^*=E^*/2(1+\nu^*)=E/2(1+\nu)=G \quad \text{at all times,} \tag{4.2}$$

and in particular

$$\tfrac{2}{3}E^*=E/(1+\nu) \quad \text{at} \quad t=+0. \tag{4.3}$$

The relations (4.1) and (4.3) enable us to describe the condition at $t=+0$ as a function of the elasticity constants of the grain skeleton E and ν.

The relations between the stresses in the combined system and grain skeleton only, which have already been stated, may be condensed to

$$-\sigma^*=-\sigma+w \quad \text{and} \quad \tau^*=\tau. \tag{4.4}$$

By adding the normal stresses in three perpendicular directions we obtain

$$-(\sigma_1^*+\sigma_2^*+\sigma_3^*)=-(\sigma_1+\sigma_2+\sigma_3)+3w.$$

As the volume dilatation ϵ, which is known to be equal to

$$\epsilon=(1-2\nu)(\sigma_1+\sigma_2+\sigma_3)/E, \tag{4.5}$$

is zero at $t=+0$, we obtain, by virtue of the fact that $\nu\neq\frac{1}{2}$,

$$-(\sigma_1^*+\sigma_2^*+\sigma_3^*)=3w=-(\sigma_I^*+\sigma_{II}^*+\sigma_{III}^*) \quad \text{at} \quad t=+0. \tag{4.6}$$

in which σ_1^* etc., indicate the *principal* stresses in the combined system.

With the aid of these general considerations we shall proceed to determine the conditions at $t=+0$ in our special case.

Under the influence of the stress system (3.2) and the boundary condition for the cavity (2.2.5), the stress distribution in the soil can be determined by the aid of stress functions.[1] We shall not enlarge on these computations because they are easy to carry out and by applying the following expression for the radial displacement as derived from a stress function, Φ:

$$u_r=\frac{1+\nu^*}{E^*}\left\{2(1-\nu^*)\cos\psi\nabla^2\Phi - \frac{\partial}{\partial r}\left[\cos\psi\frac{\partial\Phi}{\partial r}-\sin\psi\frac{1}{r}\frac{\partial\Phi}{\partial r}\right]\right\}, \tag{4.7}$$

the reader may verify that u_r is given by

$$u_r=\frac{1+\nu^*}{E^*}r_0\left\{\left[\frac{\nu^*}{1+\nu^*}-\cos\psi\right]S+\tfrac{1}{2}w_0\left(\frac{r_0}{r}\right)^2+\frac{[(6-5\nu^*)+5(4\nu^*-5)\cos^2\psi](r_0/r)^2-[3-9\cos^2\psi](r_0/r)^4}{2(7-5\nu^*)}S\right\}. \tag{4.8}$$

In this expression w_0 is the pressure in the water contained in the cavity and caused by the volume change ΔV, which is, in turn, caused by the displacement of the wall of the cavity. We may obtain ΔV by integration over the surface of the sphere

$$-\Delta V=\int_\pi^0 2\pi r_0\sin\psi\cdot u_r r_0 d\psi. \tag{4.9}$$

$$-\Delta V=\{[(1+\nu^*)/2E^*](-\tfrac{1}{3}S+w_0) -[(1-2\nu^*)/3E^*]S\}4\pi r_0^3. \tag{4.10}$$

By the use of (4.1) and (4.2) it follows that

$$-\Delta V=4\pi r_0^3[-\tfrac{1}{3}S+w_0]/4G^* =4\pi r_0^3[-\tfrac{1}{3}S+w_0]/4G. \tag{4.11}$$

However, we have a relation (1.1) between ΔV and w_0, by which we may eliminate ΔV obtaining:

$$w_0=\tfrac{1}{3}S/\{1+\tfrac{4}{3}bG\}. \tag{4.12}$$

This result indicates that the cavernous pore pressure meter registers a pressure of nearly $\frac{1}{3}S$ so long as b is small in comparison with $1/G$. As in the newest type b is of the order of $1/100G$, where G is the shear modulus of the stiffest clay we have to deal with, the error involved is less than 1 or 2 percent.

We have shown in (4.6) that the water pressure in the pores of the soil is one-third of the sum of the principal stresses. Therefore, neglecting the influence of the denominator of (4.12), it follows that the water pressure, as measured by the cavernous type meter, is effectively the actual water pressure *in* the pores of the soil.

In the case of spherically symmetrical stress P at infinity all expressions have a simpler form, and it is easy to verify that the boundary conditions (2.2.2) and (3.3) are satisfied, together with those of equilibrium and compatibility, by taking

$$u_r=-[(1+\nu^*)/2E^*](P-w_0)(r_0^3/r^2) -[(1-2\nu^*)/E^*]Pr=-(P-w_0)r_0^3/4Gr^2, \tag{4.13}$$

$$\sigma_r^*=-P+(P-w_0)(r_0/r)^3, \tag{4.14}$$

$$\sigma_\theta^*=-P-\tfrac{1}{2}(P-w_0)(r_0/r)^3. \tag{4.15}$$

By virtue of the identity of (4.10) and (4.13) the resulting water pressure w_0 in the instrument is the same as given by (4.12) with $P=\frac{1}{3}S$.

The water pressure in the soil mass itself is $w=-\frac{1}{3}(\sigma_r^*+2\sigma_\theta^*)=P$. There is therefore a jump in the water pressure at $r=r_0$ with a magnitude of $\frac{4}{3}PbG$. It follows therefore that, the water gradient $\partial w/\partial r$ is infinite at that surface and percolation starts with infinite velocity giving a vertical slope of the water pressure registered by the meter as a function of time. The same effect occurs in the rigid type, but in this case the starting point for the water pressure at $t=+0$ is zero, because no increase of water pressure has been possible before water entered the holes by percolation. In Fig. 3 an account is given of the stresses around the instruments in the different cases.

[1] S. Timoshenko, *Theory of Elasticity* (McGraw-Hill Book Company, Inc., New York, 1934), p. 326.

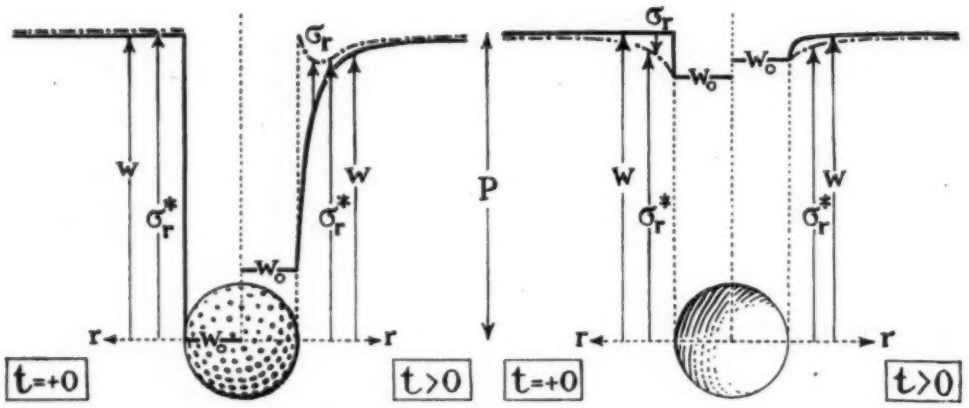

FIG. 3. Stresses and water pressure around pervious sphere and spherical cavity (arrow pointing upwards indicates compression).

5. DETERMINATION OF THE CONSOLIDATION PROCESS AROUND THE PORE PRESSURE METER

To determine the water pressure registered by the meter as a function of time we need a consolidation theory in 3 dimensions. Such a theory has been developed by Biot.[2] For the case of saturated soil the basic equation is derived in the form

$$(k/a\gamma_w)\nabla^2\epsilon=\partial\epsilon/\partial t, \tag{5.1}$$

where

a = compressibility coefficient $=(1-2\nu)(1+\nu)/(1-\nu)E$ (cm²/kg,)
k = permeability (cm/sec), γ_w = density of water (kg/cm³),
ϵ = volume dilatation of grain skeleton, and t = time.

The physical meaning of this result may be appreciated if we consider the well-known relation from elasticity[3] in which equilibrium and compatibility conditions are taken into account,

$$(1/a)\nabla^2\epsilon+(\partial X/\partial x)+(\partial Y/\partial y)+(\partial Z/\partial z)=0. \tag{5.2}$$

The body forces X, Y, Z in our case are furnished by the water gradients $X=-\partial w/\partial x$ etc., so that

$$(1/a)\nabla^2\epsilon=\nabla^2 w. \tag{5.3}$$

Now, by extending Darcy's law of percolation to the case of 3 dimensions it is easy to deduce that the rate of increase of volume $\partial\epsilon/\partial t$ necessary to store the excess of water at a certain point is given by

$$\partial\epsilon/\partial t=(k/\gamma_w)\nabla^2 w. \tag{5.4}$$

A combination of (5.3) and (5.4) gives the basic equation (5.1).

In order to obtain an agreeable treatment of the problem we shall consider simple harmonic loading conditions for $r\to\infty$.

$$P=\bar{P}\exp(i\omega t) \text{ in cond. (3.3).}$$

All variables influenced by this harmonic effect as for instance ϵ, will be written $\epsilon=\bar{\epsilon}\exp(i\omega t)$. So we can divide all expressions throughout by $\exp(i\omega t)$ and retain the overdashed characters. We get for (5.1) in the case of axially symmetrical stress distribution

$$\nabla^2\bar{\epsilon}=\frac{1}{r^2}\left[\frac{\partial}{\partial r}\left(r^2\frac{\partial}{\partial r}\right)+\frac{1}{\sin\psi}\frac{\partial}{\partial\psi}\left(\sin\psi\frac{\partial}{\partial\psi}\right)\right]\bar{\epsilon}=q^2\bar{\epsilon}, \tag{5.5}$$

where

$$q^2=i\omega\left(\frac{a\gamma_w}{k}\right),$$

which has the solutions

$$\bar{\epsilon}=r^{-\frac{1}{2}}[A_1J_{n+\frac{1}{2}}(iqr)+A_2N_{n+\frac{1}{2}}(iqr)]\Psi_n, \tag{5.6}$$

where J and N denote, respectively, Bessel and Neumanns functions,[4] and Ψ Legendres polynomials.[5] To fit this solution to the purpose of our problem we need such a combination of J and N that for $r\to\infty$ the expression vanishes. From the theory of Bessel functions it is known that this is accomplished if $A_2=iA_1$. We then obtain from (5.6)

$$\bar{\epsilon}=A_1i^{(3-n)}[\tfrac{1}{2}\pi iq]^{-\frac{1}{2}}r^{-1}\exp(-qr)S_{n+\frac{1}{2}}(2qr)\Psi_n, \tag{5.7}$$

in which S are polynomials in $(1/qr)$.[6]

This equation for $\bar{\epsilon}$ permits us to compute the solution to the axial symmetrical problem that arises when introducing the true form of boundary conditions. For instance location of the holes on rigid type, upper part of the cavity formed by the instrument, etc. Computation would then require a treatment with many stress functions Φ derived from (5.7) by

$$\bar{\epsilon}=[(1-2\nu)(1+\nu)/E]\{\cos\psi\partial/\partial r-\sin\psi r^{-1}\partial/\partial\psi\}\nabla^2\Phi. \tag{5.8}$$

[2] M. Biot, J. Appl. Phys. **12**, 155 (1941).
[3] See reference 1, p. 198.
[4] Jahnke and Emde, *Tables of Functions* (Dover Publications, New York, 1945), pp. 144, 146.
[5] See reference 4, p. 107.
[6] See reference 4, p. 136.

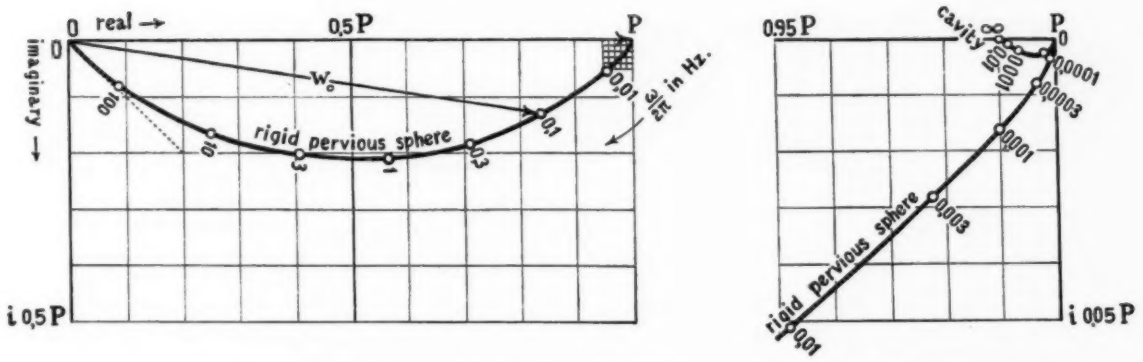

FIG. 4. Graphical representation of formula (6.6): response of pore pressure meter on simple harmonic loading. Assumptions: $b/3a=10^{-2}$, $r_0=1$ cm, $a\gamma_w/k=10^{-3}$ sec/cm², $\nu=\frac{1}{3}$.

In general: in all cases, where the solution of stress distribution under static loading is known as derived from stress functions, the consolidation problem is solved by replacing the dilatation-stress functions which satisfy $\nabla^2\nabla^2\Phi=0$ by corresponding functions of the form (5.7). The functions $\nabla^2\Phi=0$ need no alterations, because $\tilde{\epsilon}=0$ also satisfies (5.5), neither the rotation-stress-functions.

We shall limit ourselves, however, to the solution of complete spherical symmetry, because this leads to a simplification in the treatment. The same solution for w_0 as a function of time is then obtained for 3 equal stresses ($P=\frac{1}{3}S$) at $r\to\infty$ as well as for 1 principal stress (S) there. This conclusion has already been proved for the situation at $t=+0$ for unit loading (see the identity of (4.10) and (4.13)) and that it holds here may be accepted without proof.

6. SPHERICAL SYMMETRY

The solution needed is that of order $n=0$

$$\tilde{\epsilon}=\tilde{A}r^{-1}\exp(-qr). \tag{6.1}$$

We shall not use a stress function now, but u_r as basic variable as all stresses and boundary conditions can be written as functions of u_r by virtue of the symmetry. For instance $\tilde{\epsilon}=r^{-2}\partial/\partial r(\tilde{u}_r r^2)$, which gives after integration:

$$\tilde{u}_r=-\tilde{A}[(qr)^{-1}+(qr)^{-2}]\exp(-qr)-\tilde{B}r^{-2}. \tag{6.2}$$

In order to describe the boundary conditions with $\tilde{u}_r$ we must firstly dispose of $\tilde{w}$. This is simple by virtue of (5.3) which can be written $(1/a)\partial^2/\partial r^2(\tilde{\epsilon}r)=\partial^2/\partial r^2(\tilde{w}r)$, and which after integration becomes $(1/a)\tilde{\epsilon}=\tilde{w}-C_1-C_2r^{-1}$. We may omit the term C_2r^{-1}, which contributes a water-flow radiating from a point source at the origin and is irrelevant here. Therefore, it follows that

$$(1/a)\tilde{\epsilon}=\tilde{w}-\tilde{C} \quad \text{or} \quad \tilde{w}=\tilde{C}+(1/a)r^{-2}\partial/\partial r(\tilde{u}_r r^2). \tag{6.3}$$

Also $\tilde{\sigma}_r$ and $\tilde{\sigma}_r{}^*$ may be written in terms of $\tilde{u}_r$ in the following way:

$$\tilde{\sigma}_r{}^*=\tilde{\sigma}_r-\tilde{w}=E/(1+\nu)[\partial\tilde{u}_r/\partial r+\tilde{\epsilon}\nu/(1-2\nu)]-\tilde{w}. \tag{6.4}$$

We can now express the boundary conditions in terms of $\tilde{u}_r$. For the rigid type we need: (2.1.2), (2.2.1), (3.1), and (3.3). For the cavernous type: (2.1.3), (2.2.5), (3.1), and (3.3). The condition (3.1) is already satisfied by making $A_2=iA_1$, in (5.6). There then remain three conditions to be satisfied for each type. The integration constants to adjust are $\tilde{A}$ and $\tilde{B}$ in (6.2), and $\tilde{C}$ in (6.3). It can be verified that their values are

$$\begin{aligned}&\tilde{A}=-\tilde{P}\tfrac{1}{3}bq^2r_0{}^3\exp(qr_0)/N,\\ &\tilde{B}=\tilde{P}\tfrac{1}{3}br_0{}^3[(\mu_2-\mu_1)(qr_0)^2+(qr_0)+1]/N,\\ &\tilde{C}=\tilde{P} \quad \text{with} \quad N=[\mu(qr_0)^2+(qr_0)+1],\end{aligned} \tag{6.5}$$

where

$\mu=\mu_1$ for rigid type $=b/3a$,
$\mu=\mu_2$ for cavernous type $=b/3a+[(1-\nu)/2(1-2\nu)]$.

With these values we obtain finally for the water pressure $\tilde{w}_0$ at $r=r_0$ (that is the pressure registered by the meter)

$$\tilde{w}_0=\tilde{P}\{1-(b/3a)(qr_0)^2/N\}. \tag{6.6}$$

The complex value of q [see (5.5)] leads to a complex value of $\tilde{w}_0$, $\tilde{w}_0$ being out of phase with $\tilde{P}$. In Fig. 4 is shown the relation between $\tilde{P}$ and $\tilde{w}_0$ in the complex plane as a function of the frequency $\omega/2\pi$. The range of frequencies where the rigid type can be used is from 10^{-2} Herz down to zero, while the cavernous type can be used for all frequencies.

The response of the pore pressure meter on unit step loading is obtained by using the Fourier integral

$$w_0=\frac{1}{2\pi i}\int_{-\infty}^{+\infty}\tilde{w}_0\frac{\exp(i\omega t)}{\omega}d\omega. \tag{6.7}$$

Putting $\tilde{w}_0$ in a more manageable form

$$\begin{aligned}\tilde{w}_0&=\tilde{P}\left\{1-\frac{b}{3a}\frac{q^2}{\mu}\frac{1}{(q+\alpha)(q+\beta)}\right\}\\ &=\tilde{P}\left\{1-\frac{b}{3a}\frac{q^2}{\mu}\frac{1}{(\alpha-\beta)}\left[\frac{1}{(q+\beta)}-\frac{1}{(q+\alpha)}\right]\right\},\end{aligned} \tag{6.8}$$

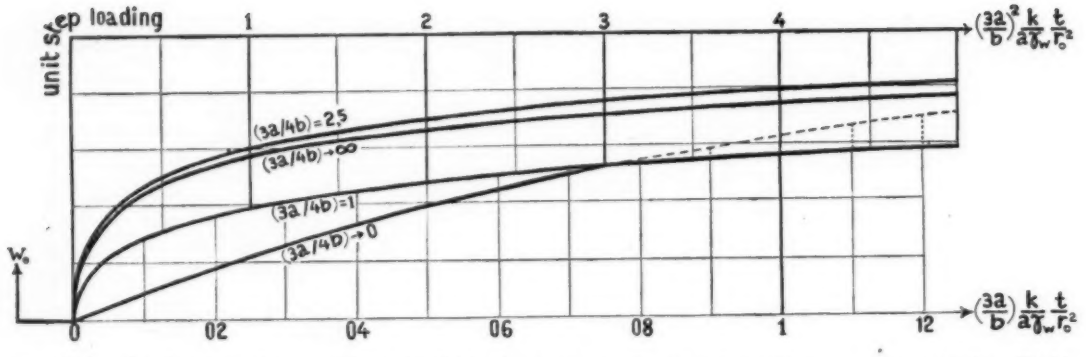

FIG. 5. Graphical representation of formula (6.9). Response of pore pressure meter on unit step loading. Rigid pervious type with some typical values of (3a/4b).

the integral may be expressed in terms of tabulated functions in the form (see Fig. 5):

$$w_0 = P\{1-(b/3a)r_0(1-4\mu)^{-\frac{1}{2}}[\alpha \exp(\alpha^2\kappa t)\ \mathrm{erfc}(\alpha^2\kappa t)^{\frac{1}{2}} - \beta \exp(\beta^2\kappa t)\ \mathrm{erfc}(\beta^2\kappa t)^{\frac{1}{2}}]\}, \quad (6.9)$$

which is valid for all $t>0$,

where P = value of step loading at $r\to\infty$

$$\alpha=[1+(1-4\mu)^{\frac{1}{2}}]/2\mu r_0,$$

$$\beta=[1-(1-4\mu)^{\frac{1}{2}}]/2\mu r_0,$$

$$\mathrm{erfc}\,\xi = 2\pi^{-\frac{1}{2}}\int_{\xi}^{\infty} \exp(-\lambda^2)d\lambda,$$

$$\kappa = k/a\gamma_w \text{ (see (5.1))}.$$

For the definition of μ see (6.5) and of $b/3a$ see (1.1) and (5.1).

Putting $\mu=\mu_2$ and $t=0$ the expression (6.9) reduces to (4.12). Since b is small in comparison with $3a$ the expression (6.9) for the rigid type becomes approximately

$$w_0 = P\{1-\exp(\gamma^2\kappa t)\ \mathrm{erfc}(\gamma^2\kappa t)^{\frac{1}{2}}\}$$

with

$$\gamma = (3a/br_0). \quad (6.10)$$

Reflection of Sound in the Ocean from Temperature Changes*

RICHARD R. CARHART
Rand Corporation, Santa Monica, California
(Received March 30, 1953)

When the temperature of the ocean changes with depth within a horizontal layer, it is accompanied by a change in the velocity of sound. The reflection of sound from such a transition layer depends on the incident angle and wavelength of the sound, the thickness of the layer, the manner in which the velocity changes, and the total amount of the change. The usual formula for reflection assumes a transition layer of negligible thickness. The reflection coefficient then depends only on the incident angle and the total velocity change. This case is treated and numerical values are given for the reflection coefficient under conditions of practical interest. It is then shown that for a gradual velocity change which corresponds to certain temperature data, the reflection coefficient for small glancing angles of incidence changes gradually with increasing layer thickness and may be approximated very closely by the usual formula. Quantitative comparison of the cases is made and the general applicability of the approximation is discussed.

I. INTRODUCTION

RATHER abrupt changes in the temperature of the ocean with depth are observed.[1] These changes cause a corresponding variation in the velocity of sound, and it is of interest to inquire as to the reflection of sound from strata in which such changes occur.

The usual treatment of reflection assumes a discontinuous velocity-depth function at the interface of two media of different indices of refraction. This is certainly a good approximation to a continuous change, provided it takes place within a distance which is small compared to the wavelength of the sound. In the ocean, however, there are indications of temperature and sound velocity changes occurring over an interval of several inches. Since the wavelength of 24-kc sound used in echo-ranging is about 2.4 inches, the above approximation is no longer justified without further study.

It is therefore convenient to treat the problem of reflection in two parts according to whether the velocity change is "sharp" or "smooth." The term "sharp" will be used to indicate the case in which the layer of velocity change has negligible thickness. A "smooth" change will denote a velocity change in a layer whose thickness is not negligible. The meaning of "negligible" in this connection will be discussed below. The fraction of incident energy which is reflected in the two cases will be called the sharp and smooth reflection coefficients and designated by r and r', respectively. It is seen that the sharp reflection coefficient is the usual reflection coefficient associated with a discontinuous $\rho_0 c$ change (ρ_0 being the density and c the sound velocity) and is given by the usual elementary calculation, but that the second requires a treatment which recognizes the wave nature of sound.

The analogous problem of reflection of electrons from a region in which their velocity changes (i.e., a potential barrier) has been treated by Eckart.[2] By a change of notation these results can be applied immediately to give the smooth reflection coefficient for sound, as has been shown by comparison with a paper by Epstein.[3] After a brief examination of the reflection from a sharp change, the results for the smooth case will be given and the smooth reflection coefficient r' will be shown to depend in a simple way on the sharp reflection coefficient r, and on a parameter u defined below.

II. REFLECTION FROM A SHARP VELOCITY CHANGE

A discontinuous change in the sound velocity will be assumed at the boundary between two semi-infinite media, the velocity being c in the first and $c'(=c+\Delta c)$ in the second, with θ and θ' the glancing angles of incidence and refraction (Fig. 1).

Snell's law is

$$c' \cos\theta = c \cos\theta' \tag{1}$$

for any ray, and the amplitude reflection coefficient is

$$s = \frac{c' \sin\theta - c \sin\theta'}{c' \sin\theta + c \sin\theta'}, \tag{2}$$

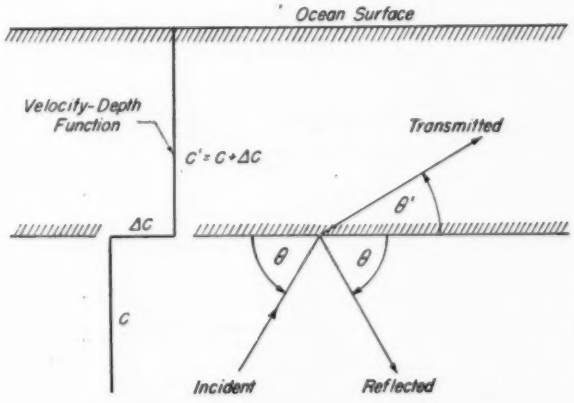

FIG. 1. Sound at a sharp velocity change.

* This work was performed in 1943 while the author was on the staff of the University of California Division of War Research, supported by OSRD under Contract OEMsr-30, and by the Bureau of Ships, Navy Department under Contract NObs 2074. Contribution from the Scripps Institution of Oceanography, New Series, No. 647.

[1] *Principles of Underwater Sound*, NDRC Summary Technical Reports, Chapter 2, Fig. 5, p. 12.

[2] Carl Eckart, Phys. Rev. **35**, 1303–1309 (1930).

[3] Paul S. Epstein, "Effect of the Thermocline on the Propagation of Sound," UCDWR, No. 5 (March 19, 1942).

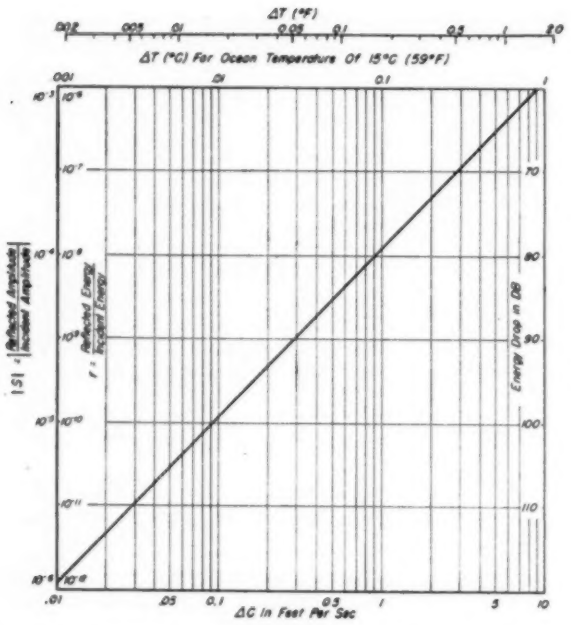

FIG. 2. Fraction of energy reflected at normal incidence from a sharp velocity change (increase or decrease) of Δc.

provided the densities of the two media are assumed to be equal, a justifiable approximation in considering the ocean. The sign of s is the same as that of Δc (i.e., positive for an increase in sound velocity along the incident ray and negative for a decrease). To a sufficient approximation, the energy reflection coefficient is $r=s^2$. Replacing c' by $c+\Delta c$ and assuming normal incidence ($\theta=\theta'=90°$), Eq. (2) reduces to $s=\Delta c/2c$ and the energy reflection coefficient becomes

$$r=(\Delta c/2c)^2 \tag{3}$$

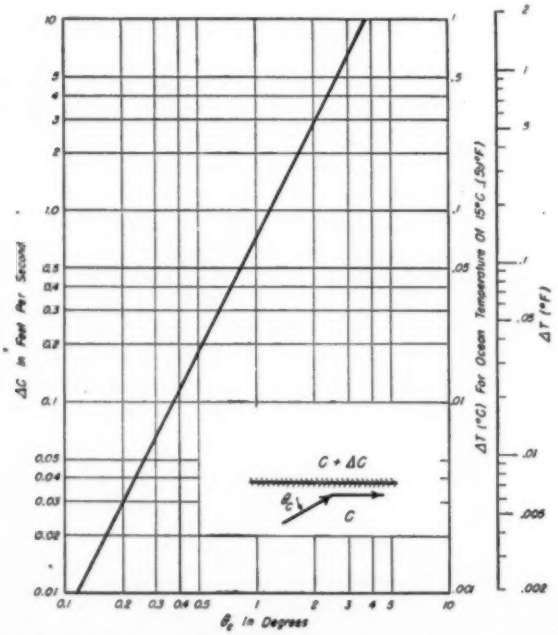

FIG. 3. Critical angle θ_c for various values of Δc and ΔT.

for normal incidence and is plotted in Fig. 2. The corresponding temperature change ΔT is also shown, and the reflected energy is seen to be down 60 or 80 db for ordinary values of ΔT.

It is convenient to give the following formulas in terms of radians rather than degrees. For small values of θ, Eq. (1) becomes approximately

$$\theta'=[\theta^2-(2\Delta c/c)]^{\frac{1}{2}}, \tag{1'}$$

and the critical angle is given by $\theta'=0$ or

$$\theta_c=(2\Delta c/c)^{\frac{1}{2}}, \tag{4}$$

which is shown in Fig. 3. Using Eq. (4), the angle of refraction θ' may be conveniently written

$$\theta'^2=\theta^2-\theta_c^2 \tag{1''}$$

and is plotted in Fig. 4. The value of the reflection

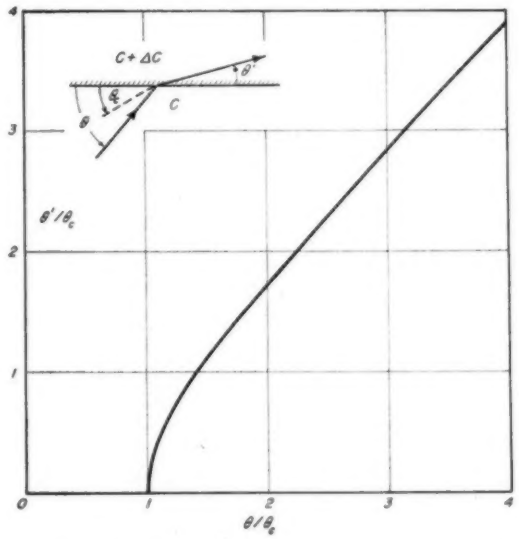

FIG. 4. Relation between incident, refracted, and critical angles.

coefficient is then approximately

$$r=(\theta-\theta')^2/(\theta+\theta')^2 \tag{5}$$

for small glancing angles.

The curves in Figs. 5 and 6 show how r changes with the angle θ for various values of Δc. Figure 5 is drawn for a velocity increase. For a given Δc, it is seen that for θ less than the critical angle the reflection is perfect. Within several degrees of the critical angle the reflected energy drops off rapidly to very small values. In Fig. 6 the reflection takes place at a velocity decrease, and there is no critical angle. The reflection is perfect only at grazing incidence ($\theta=0°$) and drops rapidly to small values (1 percent or less) as the glancing angle increases to 4° or 5°.

It should be mentioned that the reciprocity theorem holds; i.e., the reflection coefficient is independent of the direction of propagation along a given path. Thus, suppose sound from below to be incident on a stratum

at an angle of 3° with the horizontal, with the transmitted ray emerging above at 4°, then the theorem states that the reflected energy will be the same fraction of the incident energy as if the sound were incident from above at 4°, with the transmitted sound emerging below at 3°.

It may be concluded that good reflection from strata with sharp temperature changes occurs only when the ray angle with the horizontal is very near the grazing angle on the high velocity side and less than or equal to the critical angle on the low velocity side.

III. REFLECTION FROM A SMOOTH VELOCITY CHANGE

In general, it may be assumed that the velocity of sound changes somewhat as shown at the left of Fig. 7.

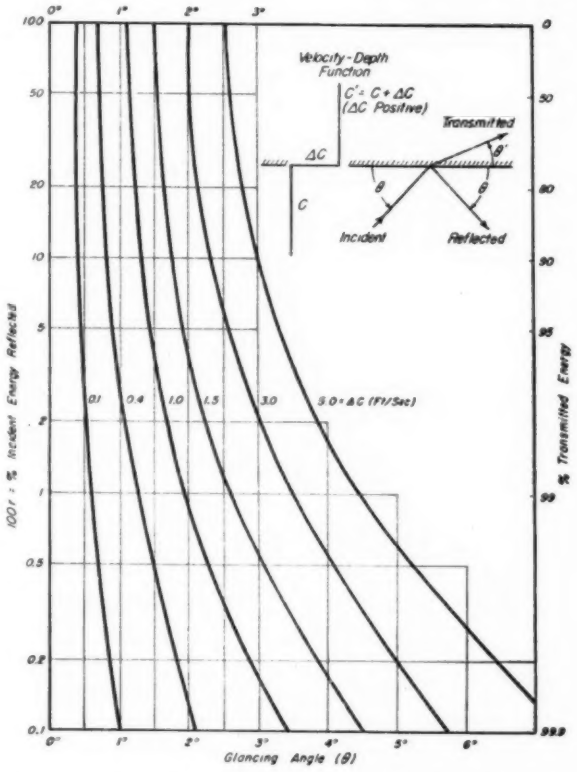

FIG. 5. Percent reflected energy from sharp velocity increase.

Sound of a single frequency rises from $z=-\infty$ through the layer of velocity change $v(z)$ (whose thickness is $2d$) towards the surface and $z=+\infty$. The velocity-depth function shown is given by

$$v^{-2}=(c+\Delta c)^{-2}+2\Delta c\{c^3[1+\exp(2\pi z/d)]\}^{-1}. \quad (6)$$

The coordinate z is measured upward from the center of the layer. Outside this layer the velocity approaches the limiting values c and $c'(=c+\Delta c)$ very rapidly. The situation, therefore, approximates the assumption of relatively constant velocity in each of two semi-infinite media which are separated by a stratum of changing sound velocity.

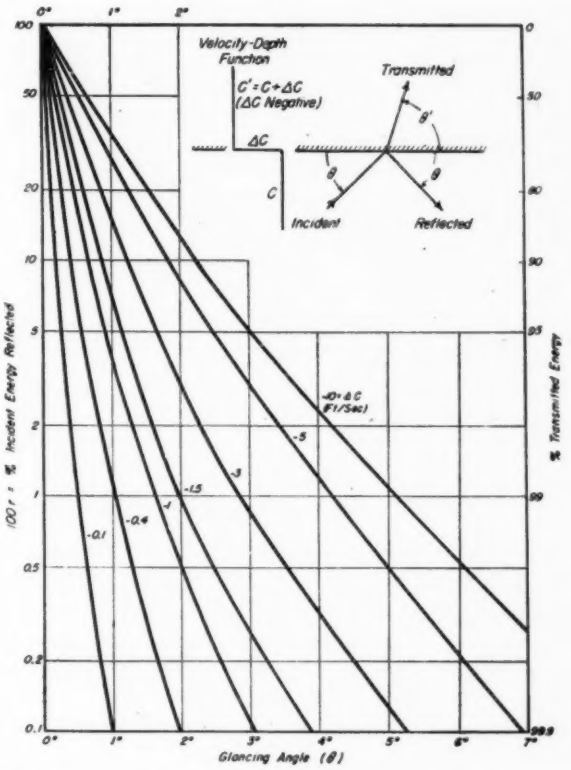

FIG. 6. Percent reflected energy from sharp velocity decrease.

The smooth amplitude reflection coefficient s' is then a function of the sharp reflection coefficient s (associated with the same Δc and θ) and of the variable

$$u=(2\pi d/\lambda)\sin\theta,$$

λ being the wavelength of the sound. (The differences in wavelength in the two media may be ignored for present purposes.) The energy reflection coefficients are then

$$r=s^2 \quad \text{and} \quad r'=s'^2. \quad (7)$$

With these definitions

$$s'=\sinh[us/(1+s)]/\sinh[u/(1+s)], \quad (8)$$

and has the same sign as s.

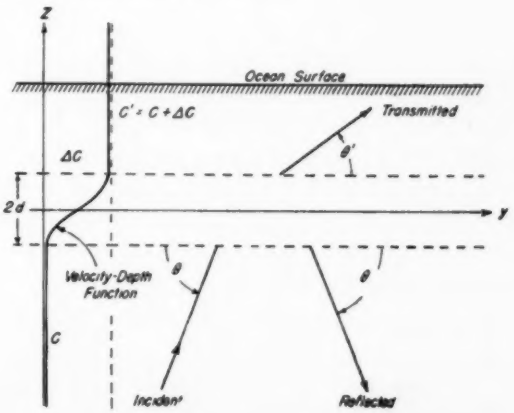

FIG. 7. Sound at a smooth velocity change.

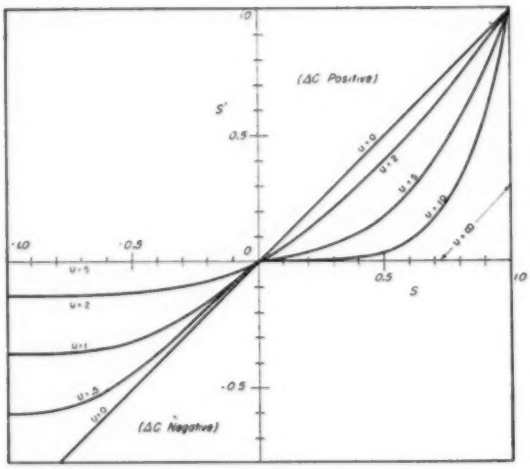

FIG. 8. Sharp and smooth amplitude reflection coefficients.

Figure 8 is a graphic presentation of Eq. (8), showing s' as a function of s for various values of u. All of the curves pass through the origin, and $s'=1$ corresponds to $s=1$ for all values of u. In general, an increase in u produces a decrease in s', this decrease being markedly greater for negative values of s than for positive values. This asymmetry does not imply a departure from the reciprocity principle, since the value of u is partially determined by the angle of incidence, but is independent of the angle of refraction.

In Fig. 9, r' is shown at a velocity increase for two values of $2d/\lambda$ (the layer thickness in wavelengths), with curves for the sharp reflection coefficient (r) repeated from Fig. 5 for comparison. Figure 10 shows the corresponding r' and r curves for a velocity decrease.

The variable u has a simple significance. If A is a point at the center of the transition layer and B a point vertically above (or below) A at the distance d, then u is the phase difference (in radians) of the sound wave at A and at B. Hence, the layer can be considered as an abrupt change whenever this phase difference is small, but it must be treated as a smooth change when this difference is large.

It will be seen that when $s=+1$, corresponding to perfect reflection at a sharp velocity increase, the sinh arguments become equal in Eq. (8), giving a smooth reflection coefficient of one. At a sharp velocity decrease the reflection is perfect ($s=-1$) at grazing incidence ($\theta=0$), making $u=0$ and again giving a smooth reflection coefficient of one. Thus, whenever the sharp reflection becomes perfect the smooth reflection also becomes perfect. Two results are thus reached for the smooth velocity change:

1. At grazing incidence the reflection is perfect.
2. At any velocity increase (Δc) of the form of Eq. (6), there will exist a critical angle which is identical with the critical angle associated with an equal discontinuous velocity change.

It can be shown that if a ray has a smaller glancing angle of incidence than this critical value, it will have a vertex within the stratum of change and the ray will curve back. The existence of a critical angle for reflection at a smooth velocity change is therefore consistent with refraction theory.

The calculation of r' is simplified by using the various graphs given above. From Fig. 3, the value of θ_c can be obtained for a given ΔT or Δc. Figure 4 simplifies the calculation of θ' from θ and θ_c, whereupon

$$s=(\theta-\theta')/(\theta+\theta'). \tag{9}$$

Knowing the value of u and s, s' can be obtained from Fig. 8. The accuracy thus obtained is sufficient for

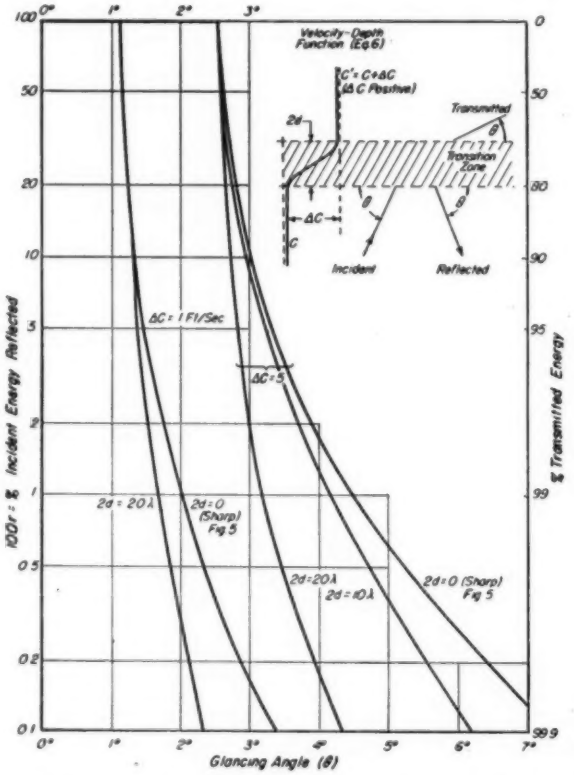

FIG. 9. Percent reflected energy from smooth velocity increase.

most purposes, except when s is very small. In this case, Eq. (8) reduces to

$$s'=us/\sinh u. \tag{10}$$

The function $u/\sinh u$ decreases very rapidly with increasing u, and is given in Table I. It is seen that s' and s have the same order of magnitude only for small values of u.

IV. APPLICATION AND GENERALITY OF RESULTS

The glancing angles usually encountered in echo ranging are less than 5°; small values of θ are therefore of primary interest. It can be seen at once from Figs. 5, 6, 9, and 10 that the reflection for such angles may be far from negligible.

Reflection from a Single Layer

To illustrate the magnitude of the smooth reflection from a single layer, two typical examples involving upward and downward refraction were calculated (Figs. 11 and 12).

In Example 1 the projector is in an isothermal layer extending from the surface to a depth of 50 ft. Owing to pressure the velocity increases with depth in this layer, being 0.9 ft/sec greater at 50 ft than at the surface and giving rise to mild upward refraction of the sound field. The various rays are incident upon a layer in which the velocity decreases according to Eq. (6). The reflection coefficient for 24-kc sound is calculated for several layer thicknesses and for two values of Δc (-10 ft/sec and -1 ft/sec) corresponding to a temperature decrease of about 2°F and 0.2°F, respectively. An isovelocity layer lies below the reflecting layer. The reflection coefficient increases with range from very low values at short ranges until it reaches one for the ray which is tangent to the top of the reflecting layer at D (Fig. 11).

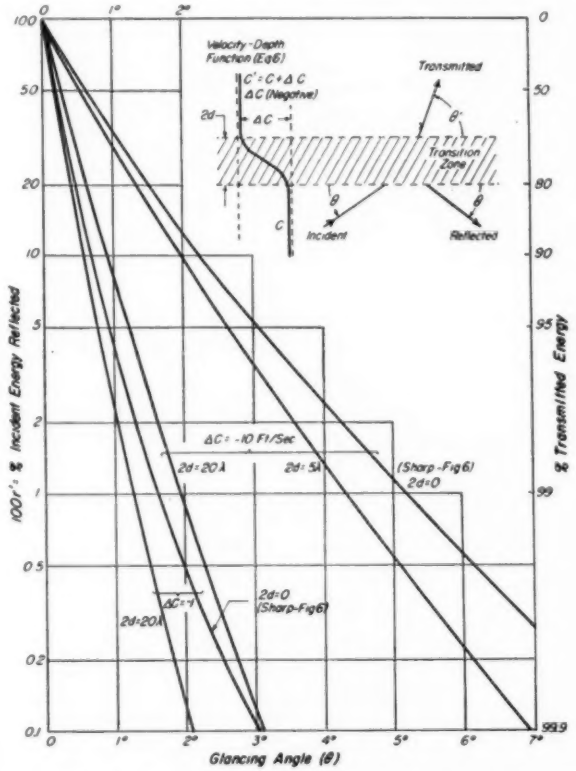

FIG. 10. Percent reflected energy from smooth velocity decrease.

In the second example (Fig. 12) a negative velocity gradient causes downward refraction in the top layer and, at a depth of 30 ft, the sound (again 24 kc) is reflected from the layer of change. The same values of Δc and $2d$ were used. Here it will be seen that the best reflection occurs at B for sound traveling along the axial ray (which leaves the projector horizontally), since this ray has the smallest glancing angle of incidence. Beyond the point B, the reflection drops off with increasing range until it reaches a small value at D for the limiting ray which is tangent to the surface. Inside the axial ray the reflection decreases more rapidly and drops to extremely small values for short ranges.

In general the reflection will be greater for upward refraction than for downward refraction and also greater at a velocity increase than at a velocity decrease as assumed in the two examples. It should also be remembered that the same reflection coefficient will again act on a returning echo from a target below the reflecting layer, so that the echo intensity will be lowered by a factor of $(1-r')^2$ from the value to be expected if the reflection is ignored.

Reflection from Many Layers

If the velocity depth curve is a series of steps randomly spaced and consisting of n alternate high and low gradient layers, the reflection coefficient is ρ, where

$$\rho/(1-\rho)=\sum_{k=1}^{n} r_k/(1-r_k), \tag{11}$$

r_k being the reflection coefficient at the top of the kth layer. If r_k is small compared to one, Eq. (11) becomes approximately

$$\rho=\sum_{k=1}^{n} r_k. \tag{12}$$

As the sound traverses the layers, the glancing angle of incidence increases and the reflection coefficient decreases rapidly. In general, therefore, only the first few layers need be considered in summing Eq. (12).

Generality of Results

In Fig. 13 three velocity-depth functions are shown:

1. The first ("exponential") is the form given by Eq. (6), used in calculating the smooth reflection coefficient.
2. The second ("observed") has the form indicated by certain temperature data.
3. The third ("hyperbolic") is a more gradual change than either of the others.

TABLE I. Values of $u/\sinh u$.

u	$u/\sinh u$
0.0	1.0
1.0	0.85
2.0	0.55
3.0	0.30
4.0	0.15
5.0	0.067
7.0	0.013
10.0	0.001

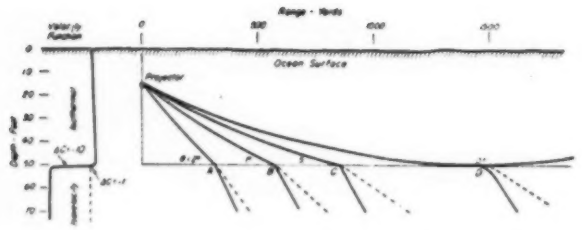

SMOOTH REFLECTION COEFFICIENT (r')

	A	B	C	D
ΔC = -10 Ft/Sec 2a = 1 Ft	0.10	0.32	0.55	1.0
ΔC = -10 Ft/Sec 2a = 5 Ft	0.0035	0.059	0.24	1.0
ΔC = -10 Ft/Sec 2a = 10 Ft	0.000046	0.0035	0.063	1.0
ΔC = -1 Ft Sec 2a = 1 Ft	0.005	0.042	0.20	1.0

FIG. 11. Example 1—Reflection with upward refraction for 24-kc sound.

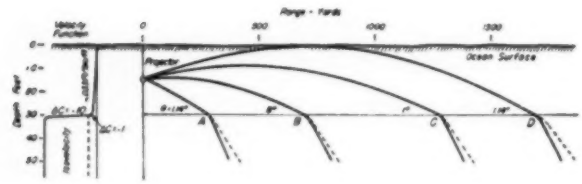

SMOOTH REFLECTION COEFFICIENT (r')

	A	B	C	D
ΔC = -10 Ft/Sec 2a = 1 Ft	0.25	0.40	0.32	0.25
ΔC = -10 Ft/Sec 2a = 5 Ft	0.040	0.11	0.088	0.040
ΔC = -10 Ft/Sec 2a = 10 Ft	0.0015	0.011	0.0035	0.0015
ΔC = -1 Ft/Sec 2a = 1 Ft	0.085	0.072	0.042	0.025

FIG. 12. Example 2—Reflection with downward refraction for 24-kc sound.

The main difference in the first and last forms lies in their asymptotic approach to the constant values c and c'. The first is exponential, and the third is approximately hyperbolic in form. There are theoretical reasons for believing that the latter is much less effective in reflection. However, it is evident that the exponential is the better approximation to the observed form, since the data indicate an abrupt rather than a gradual change from low to high gradient. It is, therefore, reasonable to believe that the calculated reflection from the assumed exponential is a conservative estimate of reflection to be expected from the observed change.

V. CONCLUSIONS

The principal results may be summarized as follows:

1. For normal incidence the reflection is very small and depends only on the total velocity change. It is independent of whether the velocity is increasing or decreasing. For a layer thickness up to a third of a wavelength the reflected energy is 60 db below the incident energy for a velocity change of 10 ft/sec (corresponding to a temperature change of about 1°C); it is 80 db down for 1 ft/sec (0.1°C) and 100 db for 0.1 ft/sec (0.01°C). The reflection then drops very rapidly with increasing thickness, being about one-tenth the values above for a thickness of one wavelength and about one-hundredth for a thickness of two wavelengths.

2. When the incident sound encounters a velocity decrease the reflection becomes perfect as the glancing angle of incidence decreases to zero. The reflection drops very sharply for increasing glancing angle.

3. At a velocity increase the familiar critical angle exists, and its value depends only on the total velocity change, not on the wavelength or layer thickness. For glancing angles less than the critical angle (which is of the order of 1° for commonly found temperature changes), the reflection is perfect, regardless of wavelength and layer thickness. As the glancing angle increases a degree or two above the critical values, the reflection drops very sharply (from 100 percent to 1 percent).

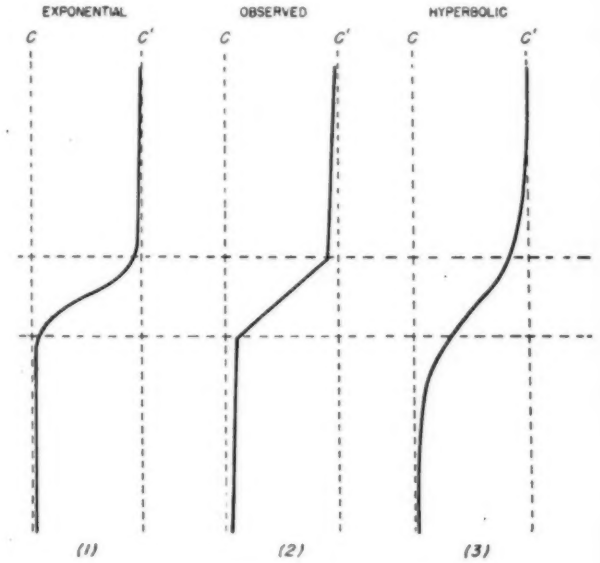

FIG. 13. Various velocity depth functions.

4. In general, for either of the above cases, the reflection drops off gradually with decrease in wavelength and increase in layer thickness.

5. In general, a velocity change can be considered as abrupt whenever the phase difference of the sound at two points vertically above each other and on opposite sides of the layer is less than one radian. A formula is given which is valid when this phase difference is greater than one radian.

6. In echo-ranging with 24-kc sound, changes of temperature occurring in horizontal layers less than 4 ft thick may usually be treated as abrupt since the sound rays generally approach the layers at small glancing angles of incidence.

On the Statistical Theory of Detection of a Randomly Modulated Carrier

W. M. STONE
Boeing Airplane Company, Seattle, Washington, and Oregon State College, Corvallis, Oregon
(Received April 30, 1953)*

A method is outlined for estimating the probability of detection for a pulsed radar, assuming a randomly modulated carrier. For a square law detector closed forms for the moments of the distribution of the envelope are presented in terms of three different choices of the distribution of carrier amplitude, thus leading to an Edgeworth series representation of the desired probability. At least one choice of distribution of the carrier amplitude leads to closed forms for the moments for the case of a linear detector. Curves of probability of detection *vs* signal-to-noise power ratio are constructed and cross checked by a method of numerical integration.

I. INTRODUCTION

RECENT papers by Marcum[1] and Kaplan and McFall[2] have discussed the statistical effect of receiver noise applied to radar range performance, assuming a constant amplitude carrier. The purpose of this paper is to extend the theory to include the case of a randomly modulated carrier. There are two simple mathematical procedures involved, the expansion of a bounded function by the asymptotic Edgeworth series and the numerical evaluation of a certain definite integral by the Simpson process.

A voltage consisting of a sinusoidal wave plus random normal noise may be represented as

$$V(t)=A\cos \mathrm{wt}+V_N(t). \tag{1}$$

Rice[3] has shown that for A constant the probability density function associated with the envelope R is

$$f(R)=\begin{cases}\psi_0^{-1}R\exp\left(-\dfrac{R^2+A^2}{2\psi_0}\right)I_0\left(\dfrac{RA}{\psi_0}\right), & R\geq 0,\\ 0, & R<0,\end{cases} \tag{2}$$

where ψ_0 is the noise power admitted by the filter of the system, I_0 is the modified Bessel function of the first kind, zero order. It is understood that (2) applies for the case of the narrow filter; usually it is required that the width of the filter be approximately equal to the reciprocal of the pulse duration time. The pulsing is considered to be a sampling of the continuous random variable R, the interval between pulses taken large enough for the successive values of R to be independent.

A more elaborate analysis by Middleton[4] has shown that (2) holds true for the general case where A is a function of time, random or nonrandom, provided the average is taken over all possible values of A. The case where $A(t)$ is random is, of course, of greatest interest in the radar problem. It is necessary to assume several logical (and elementary) forms of the probability density function associated with $A(t)$, say $p(A)$. In terms of the dimensionless variables,

$$y=A/\psi_0^{\frac{1}{2}},\quad x=R/\psi_0^{\frac{1}{2}},\quad 0\leq x,y<\infty,$$

the formal representation of the probability density of the envelope of a randomly modulated carrier in the presence of normally distributed receiver noise is

$$f(x)=x\exp(-x^2/2)\int_0^\infty p(y)\exp(-y^2/2)I_0(xy)dy. \tag{3}$$

The criterion of system performance is equivalent to those defined by Marcum, Kaplan, and McFall. That is, a signal is said to be detected at the instant of a pulse return if the received envelope of signal and noise exceeds a predetermined bias level, say x_0. Hence the probability of detection of a single pulse is

$$\begin{aligned}P(M_1,\sigma_1,x_0)&=\int_{x_0}^\infty f(x)dx\\ &=\int_{x_0}^\infty x\exp(-x^2/2)\int_0^\infty p(M_1,\sigma_1,y)\\ &\quad\times\exp(-y^2/2)I_0(xy)dydx,\end{aligned} \tag{4}$$

where the M_1 and the σ_1 are the mean and the standard deviation associated with the probability density function $p(y)$. The choice of x_0 depends on the prescribed false alarm time, the average time interval between false target indications in the absence of signal. Mathematically, the no signal case corresponds to the limiting case

$$\lim_{M_1,\sigma_1\to 0}p(M_1,\sigma_1,y)=\delta(y), \tag{5}$$

where $\delta(y)$ is the well-known Dirac delta-function. The criterion of choice of bias propounded by Kaplan and McFall is, therefore,

$$\begin{aligned}\lim_{M_1,\sigma_1\to 0}P(M_1,\sigma_1,x_0)&\\ =\int_{x_0}^\infty x\exp(-x^2/2)dx&=\frac{1}{\Delta f t_s f_n},\end{aligned} \tag{6}$$

* The original unrevised manuscript was received October 27, 1952.

[1] J. I. Marcum, *A Statistical Theory of Target Detection by Pulsed Radar: Mathematical Appendix* (Rand Corporation, RM-753, 1948).

[2] S. M. Kaplan and R. W. McFall, Proc. Inst. Radio Engrs. **39**, 56–60 (1951).

[3] S. O. Rice, Bell System Tech. J. **23**, 282–332 (1944); **24**, 46–156 (1945).

[4] D. Middleton, Quart. Appl. Math. **5**, 445–498 (1948).

where Δf is the filter band width, t_f is the false alarm time, f_a is the fraction of time between successive pulses that the receiver is gated on. The corresponding criterion of Marcum is only slightly different.

The evaluation of the probability of detection for a given set of parameters depends on carrying out the integration in (4). Cramér[5] has thoroughly discussed the problem of the most advantageous representation of a function of probability density type and the corresponding distribution function. Let $g(t)$ be any probability density function of the standardized variable $t=(x-M)/\sigma$, which has zero mean and unit standard deviation. The Gram-Charlier orthogonal function expansion is

$$g(t)=\sum_{n=0}^{\infty}\frac{c_n}{n!}\varphi^{(n)}(t), \tag{7}$$

where

$$\varphi(t)=(2\pi)^{-\frac{1}{2}}\exp(-t^2/2),$$
$$\varphi^{(n)}(t)=\frac{d^n}{dt^n}\varphi(t)=(-1)^nH_n(t)\varphi(t). \tag{8}$$

The $H_n(t)$ are the Hermite polynomials, orthogonal with respect to the weight function $\varphi(t)$. By repeated integration by parts

$$\int_{-\infty}^{\infty}H_n(t)H_m(t)\varphi(t)dt=\begin{cases}n!, & m=n,\\ 0, & m\neq n,\end{cases} \tag{9}$$

so the coefficients in (7) are determined by

$$c_n=(-1)^n\int_{-\infty}^{\infty}H_n(t)g(t)dt. \tag{10}$$

This means that each c_n is a linear combination of the central standard moments β_n of $g(x)$, with, in particular, c_1 and $c_2=0$. In practice, for any $g(x)$ it is usually necessary to first find the moments α_n and the central moments μ_n:

$$\alpha_n=E(x^n)=\int x^ng(x)dx,$$
$$\mu_n=E(x-\alpha_1)^n=\int(x-\alpha_1)^ng(x)dx, \tag{11}$$
$$\mu_2^{\frac{1}{2}n}\beta_n=\mu_n=\sum_{k=0}^{n}(-1)^k\binom{n}{k}\alpha_{n-k}\alpha_1^k,$$

where $M=\alpha_1$ and $\sigma=\mu_2^{\frac{1}{2}}$. The integration in (11) is understood to be over the entire range of x.

In spite of the simplicity of the above Gram-Charlier A series expansion, Cramér points out that an asymptotic series development due to Edgeworth requires less calculation for expansion of $g(x)$ to a given order of magnitude. This new series is a rearrangement of the terms in (7),

$$g(t)=\varphi(t)-\frac{1}{3!}\beta_3\varphi^{(3)}(t)+\frac{1}{4!}(\beta_4-3)\varphi^{(4)}(t)+\frac{10}{6!}\beta_3^2\varphi^{(6)}(t)$$
$$-\frac{1}{5!}(\beta_5-10\beta_3)\varphi^{(5)}(t)-\frac{35}{7!}\beta_3(\beta_4-3)\varphi^{(7)}(t)-\frac{280}{9!}\beta_3^3\varphi^{(9)}(t), \tag{12}$$

. . . . . .

where the terms in each line are the same order of magnitude. It is usually better not to go beyond the third line in (12).

Returning to (4) the probability of detection takes the form

$$P(M_1,\sigma_1,x_0)=\int_{x_0}^{\infty}f(x)dx$$
$$=0.5-\varphi^{(-1)}(t_0)-\sum_{n=3}^{\infty}\frac{c_n}{n!}\varphi^{(n-1)}(t_0), \tag{13}$$

where $t_0=(x_0-M)/\sigma$ and the c_n are defined in terms of the central standard moments according to (12). Here $\varphi^{(-1)}(t)$ is the error function; volume 23 of the *Annals of the Computation Laboratory of Harvard University*, "Tables of the Error Function and of Its First Twenty Derivatives," is quite sufficient for all possible calculations. Once the moments for single pulse detection are found, it is easy to obtain the corresponding $\bar{\beta}_n$ for the detection of N integrated pulses. Let $\bar{x}$ be a new random variable,

$$\bar{x}=\sum_{i=1}^{N}x_i, \tag{14}$$

where each x_i is independent and distributed according to (3) with mean α_1 and standard deviation $\mu_2^{\frac{1}{2}}$. The moments corresponding to the new variable are

$$\bar{\alpha}_1=E(\bar{x})=\sum_{i=1}^{N}E(x_i)=N\alpha_1, \tag{15}$$

$$\bar{\mu}_n=E(\bar{x}-\bar{\alpha}_1)^n=E\Big[\sum_{i=1}^{N}(x_i-\alpha_1)\Big]^n. \tag{16}$$

Bearing in mind that any difference $x_i-\alpha_1$ has a mean of zero,

$$\bar{\mu}_2=\sum_{i=1}^{N}E(x_i-\alpha_1)^2=N\mu_2, \tag{17}$$

$$\bar{\mu}_3=\sum_{i=1}^{N}E(x_i-\alpha_1)^3=N\mu_3, \tag{18}$$

[5] H. Cramér, *Mathematical Methods of Statistics* (Princeton University Press, Princeton, 1946).

but

$$\bar{\mu}_4=\sum_{i=1}^{N} E(x_i-\alpha_1)^4+6E[(x_1-\alpha_1)^2(x_2-\alpha_1)^2+\cdots + (x_{N-1}-\alpha_1)^2(x_N-\alpha_1)^2] =N\mu_4+6\binom{N}{2}\mu_2^2. \quad (19)$$

Hence, the Edgeworth coefficients for $\bar{x}$ would be obtained from

$$\bar{\beta}_3=N^{-\frac{1}{2}}\beta_3, \quad \bar{\beta}_4=N^{-1}\beta_4+3(1-N^{-1}). \quad (20)$$

Marcum discusses several methods for the evaluation of bias level for this case.

II. SQUARE LAW DETECTOR

A choice of square law detector leads to quite simple closed forms of the α_n. The substitution $u=x^2/2$ changes (3) to the form

$$f(u)=\exp(-u)\int_0^\infty p(y)\exp(-y^2/2)I_0(y(2u)^{\frac{1}{2}})dy. \quad (21)$$

The easiest method for obtaining the α_n is to apply the Laplace transformation:

$$F(s)=\int_0^\infty \exp(-su)f(u)du=(s+1)^{-1}\int_0^\infty p(y)\times\exp\left(-\frac{sy^2}{2(s+1)}\right)dy, \quad s\geq 0, \quad (22)$$

where

$$\alpha_n=E(u^n)=(-1)^nF^{(n)}(0). \quad (23)$$

The interchange of the order of integration in (22) and the evaluation of $F^{(n)}(s)$ for $s=0$ in (23) are justified since $f(u)$ is by definition a probability density function. Rather than to evaluate the nth derivative of $F(s)$, it is better to expand $F(s)$ in a Taylor series,

$$F(s)=\sum_{n=0}^{\infty}\frac{a_n s^n}{n!}, \quad (24)$$

where

$$a_n=(-1)^n\alpha_n. \quad (25)$$

Straightforward algebraic manipulation leads to a general formula,

$$\alpha_n=n!\int_0^\infty p(y)\sum_{k=0}^{n}\binom{n}{k}\frac{y^{2k}}{2^k k!}dy. \quad (26)$$

A. Normal Law

Further progress requires definite assumptions about $p(y)$, the probability density function associated with the carrier amplitude. For the normal law case

$$p(y)=B\exp\left(-\frac{(y-y_0)^2}{2a^2}\right), \quad (27)$$

$$Ba(\pi/2)^{\frac{1}{2}}[1+2\varphi^{(-1)}(y_0/a)]=1.$$

This is an example of a truncated distribution, necessary because the amplitude of the carrier is essentially positive. After an obvious change of variable, $r=a/y_0$,

$$\alpha_n=n!Ba\left\{\int_0^{1/r}\exp(-x^2/2)\sum_{k=0}^{n}\binom{n}{k}\frac{y_0^{2k}}{2^k k!}(1-rx)^{2k}dx + \int_0^\infty \exp(-x^2/2)\sum_{k=0}^{n}\binom{n}{k}\frac{y_0^{2k}}{2^k k!}(1+rx)^{2k}dx\right\}. \quad (28)$$

The integration is simple but tedious:

$$\alpha_n=n!\sum_{k=0}^{n}\binom{n}{k}\frac{y_0^{2k}}{2^k k!}[Q_{2k}(r) + Ba\exp(-1/2r^2)S_{2k-1}(r)], \quad (29)$$

where

$$Q_{2k}(r)=\sum_{i=0}^{k}\frac{(2k)!r^{2i}}{2^i i!(2k-2i)!}, \quad (30)$$

$$S^{-1}(r)=0, \quad (31)$$

$$S_{2k-1}(r)=r+r\sum_{i=1}\left[\binom{2k}{2i+1}\times\sum_{j=1}^{i}(2i)(2i-2)\cdots(2i+2-2j)r^{2i} -\binom{2k}{2i+2}\sum_{j=1}^{i}(2i+1)\times(2i-1)\cdots(2i+3-2j)r^{2i}\right], \quad k=1, 2, \cdots, n. \quad (32)$$

Note that $Q_{2k}(r)=(-1)^k r^{2k}H_{2k}(i/r)$. The second part of the α_n would be quite negligible for small values of r. Given specific values of the bias level u_0 $(=x_0^2/2)$ and the parameter r, the probability of detection could be obtained from (13) as a function of the signal to noise power ratio z.

It is interesting to note that since

$$\lim_{a\to 0} B\exp\left(-\frac{(y-y_0)^2}{2a^2}\right)=\delta(y-y_0), \quad (33)$$

the Marcum formulas for the moments of the constant amplitude carrier follow at once from (26). A similar result is possible for the other two forms of $p(y)$ discussed below.

B. Gamma Distribution

A choice of

$$p(y)=\frac{y^{m-1}\exp(-y/b)}{b^m\Gamma(m)}, \quad 0\leq y<\infty, \quad 0<m, \quad (34)$$

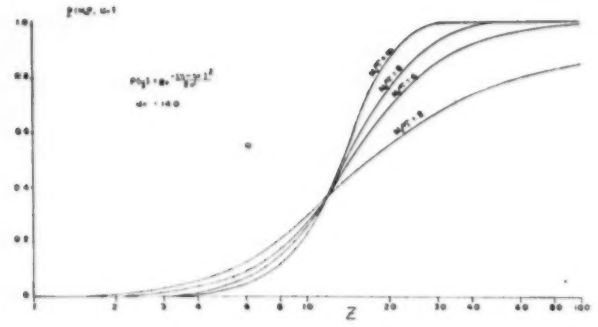

FIG. 1.

leads at once to

$$\alpha_n=\frac{n!}{\Gamma(m)}\sum_{k=0}^{n}\binom{n}{k}\frac{\Gamma(2k+m)}{2^k k!}b^{2k}, \quad (35)$$

where

$$z=E(y^2/2)=m(m+1)b^2/2. \quad (36)$$

C. Square Root of the Sum of Squares Distribution

Cramér (reference 5, p. 236) has shown that the distribution in question is defined by

$$p(y)=\frac{2y^{q-1}\exp(-y^2/2c^2)}{2^{q/2}c^q\Gamma(q/2)}, \quad 0\leq y<\infty, \quad 0<q. \quad (37)$$

This choice of $p(y)$ leads to

$$\alpha_n=\frac{n!}{\Gamma(q/2)}\sum_{k=0}^{n}\binom{n}{k}\frac{\Gamma(k+q/2)}{k!}c^{2k}, \quad (38)$$

where

$$z=E(y^2/2)=qc^2/2. \quad (39)$$

III. NUMERICAL EVALUATION

As indicated by (4) the probability of detection is a function of the bias level x_0 and the mean M_1 and standard deviation σ_1 of the probability density function $p(y)$. If the ratio M_1/σ_1 is taken constant the straightforward application of the Edgeworth expansion of (13) yields curves of the probability of detection *vs* signal-to-noise power ratio z. It was found that for the ratio $M_1/\sigma_1=2,4,6$, and $u_0=14$ the resulting curves of $P(z, u_0)$, $0\leq z\leq 100$, are very insensitive to the choice of $p(y)$. Hence in Fig. 1 only the normal form of $p(y)$ is included. The case $M_1/\sigma_1=\infty$ is, of course, the Marcum or Kaplan and McFall case:

$$\lim_{\sigma_1\to 0}P(M_1, \sigma_1, x_0)=\exp(-y_0^2/2)\times\int_{x_0}^{\infty}x\exp(-x^2/2)I_0(xy_0)dx$$
$$=1-F(u_0, v_0), \quad (40)$$

where $v_0=y_0^2/2$ and

$$F(x, y)=\exp(-y)\int_0^x\exp(-t)I_0(2(yt)^{\frac{1}{2}})dt, \quad (41)$$

which has been extensively tabulated by the U. S. Bureau of Mines.[6]

An alternative procedure is the straightforward use of numerical integration to evaluate

$$P(M_1, \sigma_1, u_0)=1-\int_0^{\infty}p(y)F(u_0, y^2/2)dy. \quad (42)$$

In all cases considered there was excellent agreement between the Edgeworth series and numerical integration results. At least for $M_1/\sigma_1=2$ it was essential that the asymptotic series be cut off with the $\varphi^6(t)$ term.

IV. LINEAR DETECTOR

In general there seems to be no simple form for the moments in the case of a linear detector. The results of Rice and Marcum are quickly extended to the randomly modulated carrier case:

$$\alpha_n=2^{n/2}\Gamma(1+n/2)\times\int_0^{\infty}p(y)\,{}_1F_1(-n/2; 1; -y^2/2)dy, \quad (43)$$

and, in particular,

$$\alpha_1=(\pi/8)^{\frac{1}{2}}\int_0^{\infty}p(y)\exp(-y^2/4)\times[(y^2+2)I_0(y^2/4)+y^2I_1(y^2/4)]dy. \quad (44)$$

The hypergeometric function is defined by the series,

$${}_1F_1(a; b; x)=\sum_{n=0}^{\infty}\frac{(a)_n}{(b)_n}\frac{x^n}{n!},$$
$$(a)_n=a(a+1)\cdots(a+n-1), \quad (a)_0=1. \quad (45)$$

Note that ${}_1F_1(-n/2; 1; -y^2/2)$ is a finite polynominal if n is a positive even integer, and that for n otherwise the series converges for all values of y. Use of the first four lines of the Edgeworth series (12) requires that n in (43) take values from 1 to 5. For the three choices of $p(y)$ the even moments are easily found in closed form, but the odd moments may require numerical evaluation of the integrals in (44), (46), and (47):

$$\alpha_3=3(\pi/8)^{\frac{1}{2}}\int_0^{\infty}p(y)[y^2\,{}_1F_1(-1/2; 2; -y^2/2)+2\,{}_1F_1(-1/2; 1; -y^2/2)]dy$$
$$=(\pi/8)^{\frac{1}{2}}\int_0^{\infty}p(y)\exp(-y^2/4)[(y^4+6y^2+6)I_0(y^2/4)+y^2(y^2+4)I_1(y^2/4)]dy, \quad (46)$$

[6] Brinkely, Edwards, and Smith, *Table of the Temperature Distribution Function for Heat Exchange Between a Fluid and a Porous Solid* (U. S. Bureau of Mines, Pittsburgh).

and

$$\alpha_5=\frac{15}{8}(\pi/2)^{\frac{1}{2}}\int_0^\infty p(y)[y^4{}_1F_1(-1/2;3;-y^2/2)$$
$$+8y^2{}_1F_1(-1/2;2;-y^2/2)$$
$$+8{}_1F_1(-1/2;1;-y^2/2)]dy$$
$$=(\pi/8)^{\frac{1}{2}}\int_0^\infty p(y)\exp(-y^2/4)$$
$$\times[(y^6+14y^4+45y^2+30)I_0(y^2/4)$$
$$+(y^6+12y^4+23y^2)I_1(y^2/4)]dy. \quad (47)$$

Middleton and Johnson[7] have tabulated the hypergeometric functions above, while the Bessel functions are tabulated in Watson.[8]

This numerical procedure would be mandatory for all α_n in the case where $p(y)$ is obtained only in tabular form. For $p(y)$ in analytic form there seems to be no closed formula for the odd moments, except for the case (*C*) in Sec. II. After an obvious change of variable the square root of the sum of squares form of $p(y)$ would yield

$$\alpha_n=\frac{2^{n/2}\Gamma(1+n/2)}{c^q\Gamma(q/2)}\int_0^\infty u^{\frac{1}{2}q-1}$$
$$\times\exp(-u/c^2){}_1F_1(-n/2;1;-u)du. \quad (48)$$

Use of the Laplace transform pair of Van der Pol and Bremmer[9] (p. 399) leads to

$$\alpha_n=2^{n/2}\Gamma(1+n/2){}_2F_1(-n/2,q/2;1;-c^2),$$
$$0\leq c^2<1, \quad (49)$$

where

$${}_2F_1(a,b;c;x)=\sum_{n=0}^{\infty}\frac{(a)_n(b)_n}{(c)_n}\frac{x^n}{n!}, \quad |x|<1. \quad (50)$$

Since c^2 may exceed unity for large values of signal-to-noise power ratio it may be necessary to use the analytic extension form of Whittaker and Watson[10] (p. 289):

$${}_2F_1(-n/2,q/2;1;-c^2)$$
$$=\frac{\Gamma\left(-\frac{n+q}{2}\right)}{\Gamma(q/2)\Gamma\left(-\frac{n+2}{2}\right)}$$
$$\times c^n{}_2F_1\left(-n/2,-n/2;1-\frac{n+q}{2};-1/c^2\right)$$
$$+\frac{\Gamma\left(\frac{n+q}{2}\right)}{\Gamma(-n/2)\Gamma\left(\frac{q-2}{2}\right)}$$
$$\times c^{-q}{}_2F_1\left(q/2,q/2;1+\frac{n+q}{2};-1/c^2\right).$$

V. CONCLUSIONS

From Fig. 1 it appears that the random nature of signal amplitude may have an important effect on the probability of detection by a single pulse. This effect is exaggarated if the over-all criterion of detection is such that only one pulse return out of many must exceed the bias level. Admittedly, there has been little information published about the nature of the distribution of amplitude of signal return from a target, but the calculations described above seem to show that the probability of detection is quite insensitive to the form of the distribution.

ACKNOWLEDGMENT

The research described in this paper has been supported by the United States Air Force. The author wishes to thank the referee for several valuable suggestions as to the organization of the paper. Thanks are also due the Rand Corporation for permission to quote the paper by Marcum, and to Mary Ellen Russell and Gladys Williams for the graphical and numerical work involved.

[7] D. Middleton and V. Johnson, Cruft Laboratory Tech. Report No. 140, Harvard University, 1952.
[8] G. N. Watson, *A Treatise on the Theory of Bessel Functions* (Cambridge University Press, Cambridge, 1950).
[9] B. Van der Pol and H. Bremmer, *Operational Calculus* (Cambridge University Press, Cambridge, 1950).
[10] E. T. Whittaker and G. N. Watson, *A Course of Modern Analysis* (Cambridge University Press, Cambridge, 1946).

A New Method for Continuous Viscosity Measurement. General Theory of the Ultra-Viscoson*

WILFRED ROTH AND STANLEY R. RICH
Rich-Roth Laboratories, Hartford, Connecticut
(Received April 9, 1953)

A new continuous ultrasonic viscometer employing a pulsed resonant exponentially damped magnetostrictive strip is described and treated theoretically. Properties of viscoelastic materials affecting the propagation of transverse elastic waves are derived and are related to the response of the viscometer. Typical applications of the use of the ultrasonic viscometer are presented.

I. INTRODUCTION

CONTINUOUS viscosity measurement has long been a neglected but highly desirable instrumentational objective. In research and development, untold hours have been spent in measuring viscosity using point-by-point methods while following temporal viscosity functions during change of temperature, pressure, the composition of the materials being measured, etc. In production, many processes have been controlled on a temperature/time basis rather than a preferred viscosity basis owing to the lack of a suitable continuous viscometer. An even more serious production limitation has been the necessity for using batch techniques when continuous flow methods could have been utilized if a satisfactory continuous viscometer had been available.

For high precision in the laboratory, flow through capillaries, flow through calibrated orifices, velocity of falling weights, drag forces on rotating or linearly moving elements, and the like are all methods which have been used to measure viscosity. When single measurements of high accuracy are desired, these techniques have often proved satisfactory. For use with non-Newtonian materials,[1] even these elementary forms of viscometers must be used with caution since the gross macroscopic motions which are inherent in all these methods affect the properties of the materials being measured.

Thus, the need for specification of flow velocities, orifice sizes, angular velocities of rotating members, etc., i.e., the need for specification of rate of shear or velocity gradient imparted to the material being measured by the measuring instrument, itself, has been found to be an essential characteristic of such viscometers.

For most production control requirements, the high accuracy and precision that are often essential in the laboratory when making single measurements can be relaxed somewhat if an automatic and continuous method is available. The few such viscometers employed in the past included elements such as rotating members, orifices, capillaries, and moving plungers. Over limited ranges of temperature and pressure and simple applications with materials that do not clog the elements of these instruments or in which the disturbing influences of the viscometers themselves are unimportant, these methods have been useful. For the greater number of production control and research problems, however, the many practical difficulties involved here obviate the use of such techniques.

A new continuous ultrasonic viscometer[2] that utilizes the interaction of ultrasonic elastic waves with the materials in question to measure viscosity has been evaluated over the past two years by many industrial firms and research institutions.

It has proved to be satisfactory for a large number of different applications ranging from the control of polymerization in the plastics industry to the quantitive study of blood coagulation for medical research and clinical use.[3]

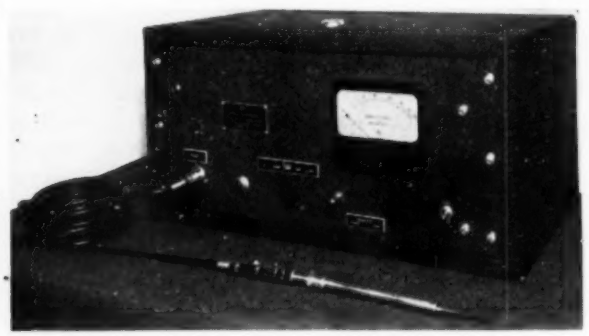

FIG. 1. The ultrasonic viscometer showing probe and electronic computer.

II. DESCRIPTION OF THE ULTRASONIC VISCOMETER

The ultrasonic viscometer comprises a small probe, an electronic computer and a connecting cable as shown in Fig. 1. This photograph illustrates the standard laboratory model. The basic probe is about the size of a

* Presented at the Annual Meeting of the Society of Rheology, Franklin Institute, October 30–31, 1952.

[1] In this paper, a non-Newtonian material is one for which rate of shear is not directly proportional to shear stress as the magnitude and/or the frequency of the shear stress is varied. Effects of frequency are included in this definition, since some materials showing no measurable non-Newtonianism owing to variations in magnitude of shear stress do exhibit change in viscosity as frequency of shear varies. Some silicone oils behave in this way.

[2] Ultra-Viscoson, developed by the Rich-Roth Laboratories, Hartford, Connecticut, manufactured by Cincinnati Division, Bendix Aviation Corporation, Cincinnati, Ohio.

[3] Yesner, Hurwitz, Rich, Roth, and Gordon, Yale J. Biol. and Med. 24, No. 3 (December, 1951); Hurwitz, Yesner, and Cooke, Lab. Investigation 1, No. 4 (January, 1953).

fountain pen, although both smaller and larger units are constructed to meet specific requirements. A stainless steel tube is the housing for a magnetostrictive transducer. Ultrasonic vibrations are excited by an electrical signal from the computer in a strip of special magnetostrictive alloy projecting from the end of the hermetically sealed tube. When the probe is immersed in a liquid, the metal strip acts as a source of transverse or shear elastic vibrations which radiate into the liquid. As will be seen in the succeeding sections, the vibrations in the strip are damped in accordance with the elastic and dissipative properties of the material being measured.

The probe is connected to the electronic computer by a cable which can be as long as one mile. The computer is an analog type in contrast to the digital, and its function is to produce an electrical output which is a function of viscosity × density.

The characteristics of the ultrasonic viscometer that lead to its wide applicability are listed below. These are

(1) Automatic, continuous—no moving parts.
(2) All metal—hermetically-sealed probe.
(3) Continuous operation from −190° to +650°F.
(4) Continuous operation from vacuum to 1000 psi; Special probes can be constructed for any pressure.
(5) Standard full-scale ranges are 0–1 to 0–50 000 cps×g/cc.
(6) Probe and computer can be separated by as much as one mile.
(7) Full reading obtained with 2 cc sample or larger.
(8) Once fully immersed, additional immersion does not affect reading.
(9) Not affected by flow of material or mechanical vibration, unless properties of material are affected by such treatment.
(10) Accuracy better than ±2 percent of full scale below 1000 better than ±5 percent of full scale above 1000.
(11) Reproducibility better than ±1 percent of full scale over all ranges.
(12) Response time less than 1 second.
(13) Probe is passive element—ultrasonic energy does not affect material since peak displacement amplitude is less than ½ micron.
(14) Probe readily installed in kettles, pipe lines, reactors, etc. or used with laboratory glassware.
(15) High corrosion resistance.
(16) Output dc millivoltage provided for actuating recorder/controllers.
(17) Multiplicity of probes can be used with one computer.
(18) Temperature compensation to correct for viscosity change caused by temperature variation is readily accomplished.
(19) Can be used to measure properties of films as well as material in bulk.

III. GENERAL THEORY OF THE PROBE

The most important element of the complete ultrasonic viscometer system so far as the theory is concerned is the thin narrow rectangular metal strip which can be seen in Fig. 1 projecting from the cylindrical barrel of the probe. In all models, both dimensions of the cross section of the strip are very much smaller than the length. The thickness and width of the strip are very much less than one wavelength of the elastic vibration which is excited by an impulsive signal from the computer. Consequently, if the strip is in a vacuum (or air)

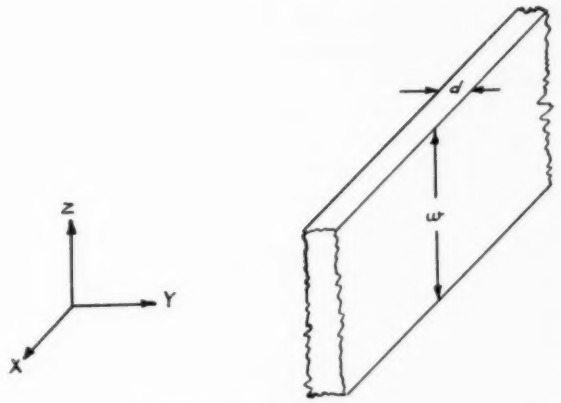

FIG. 2. Section of probe blade.

so that the movement of its surface is unimpeded, once an elastic disturbance is established, it will propagate along the strip with a velocity of propagation equal to the so-called "long bar" velocity.[4] If internal losses are negligible, the disturbance will propagate along the strip without suffering any attenuation. If this same strip is now immersed in a viscous liquid, its surfaces are no longer unimpeded—the velocity will be reduced, and the elastic disturbances will be attenuated as it propagates along the strip. The viscometer operates by measuring the attenuation of an elastic wave which is magnetostrictively induced in the metal strip of the probe as a function of time. The relations between the characteristics of the viscoelastic medium and the probe output are derived in the following sections.

We consider a section of a rigid strip dimensioned as shown in Fig. 2. We wish to obtain expressions for the amplitude of particle vibration for a compressional[5] plane wave traveling in the x direction that is impulsively excited as functions of the boundary conditions at the surfaces of the strip consistent with the condition that $d \ll \omega$. This latter fact immediately simplifies the problem since we need only concern ourselves with boundary loading effects on the two flat surfaces parallel to the xz plane—the ends and edges of the strip have negligible area compared to these, so will affect the results to a negligible degree.

With the strip in a vacuum, for a compressional plane wave in a rigid medium and for an infinitesimal volume of material, we can write

$$\rho_m \frac{\partial^2 \xi}{\partial t^2} = \frac{\partial X_x}{\partial x} \tag{1}$$

and

$$X_x = E \frac{\partial \xi}{\partial x}, \tag{2}$$

[4] Velocity of propagation of compressional elastic wave in a wire in which the diameter is very much less than one wavelength.

[5] The Ultra-Viscoson will operate with transverse waves polarized in the plane of the strip or with torsional waves if a round rod is used instead of a strip. The analysis is similar in these other cases, so only the compressional mode, which is the case of most immediate importance, is discussed here.

where ρ_m = density of strip, ξ = particle displacement in x direction, and E = Young's modulus. Obviously, the equation of motion, Eq. (1), must be modified to take care of general surface conditions other than vacuum loading, for if the strip is immersed in a medium other than vacuum, it will experience surface retarding or drag forces due to the reaction of the medium back on the strip.

We will make the assumption that no slip or amplitude discontinuity exists at the interface between the strip and the viscoelastic medium.[6] In this case, the surface loading is completely specified if we know the driving point impedance of the medium, i.e., the ratio of stress to particle velocity in the medium at the surface of the probe. Thus,

$$Z_0=\frac{Y_x}{\partial\xi/\partial t}, \tag{3}$$

where Y_x = shear stress in x direction on area normal to y axis. If we now consider an infinitesimal length of strip of unit cross-sectional area, by Newton's first law and Eq. (3), we have

$$X_{x+dx}-X_x-2\frac{Z_0}{d}dx\frac{\partial\xi}{\partial t}=\rho_m dx\frac{\partial^2\xi}{\partial t^2},$$

where d = thickness of strip (see Fig. 2).

The factor 2 is required to take account of immersion of both flat surfaces of the strip. By introducing Eq. (2) and noting that $X_{x+dx}=X_x+\frac{\partial x_x}{\partial x}dx$ for small displacements, we obtain the revised wave equation,

$$\frac{\partial^2\xi}{\partial t^2}+2k\frac{\partial\xi}{\partial t}=c_m{}^2\frac{\partial^2\xi}{\partial x^2},$$

where

$$k=Z_0/\rho_m d$$

and

$$c_m{}^2=E/\rho_m.$$

This wave equation includes all effects due to the material in which the strip is immersed in the complex constant k.

In order to solve this wave equation for the particle displacement, the actual boundary conditions that are imposed on the strip must be introduced. For many practical reasons beyond the scope of this paper, the strip is rigidly held at its center and only one-half of its length L is immersed in the material to be measured. (The solution for the many other possible boundary conditions are readily obtained by following a procedure similar to that used here.) Since the strip is held at its mid-point, only solutions having a node at the center are permitted. The condition that only half the strip is immersed is readily handled by including only half the damping term in the wave equation. This is an approximation that is strictly correct for small damping, but it introduces negligible error throughout the operating range of the present instrument. We, therefore, must solve the wave equation

$$\frac{\partial^2\xi}{\partial t^2}+k\frac{\partial\xi}{\partial t}=c_m{}^2\frac{\partial^2\xi}{\partial x^2} \tag{4}$$

for impulsive excitation consistent with the stated boundary conditions.

The complete solution of Eq. (4) in terms of the real and imaginary parts of k is involved but straightforward so it is not given here. The final result, the particle displacement at any point along the strip as a function of time, becomes

$$\xi(x,t)=\xi_0 e^{-(\alpha-j\beta)t}\sin\frac{n\pi x}{L},\quad n=1,3,\cdots \tag{5}$$

where

$$\alpha=\frac{R_0}{2\rho_m d}-\left[\tfrac{1}{2}(\{A^2+B^2\}^{\frac{1}{2}}-A)\right]^{\frac{1}{2}}$$

$$\beta=-\frac{x_0}{2\rho_m d}+\left[\tfrac{1}{2}(\{A^2+B^2\}^{\frac{1}{2}}+A)\right]^{\frac{1}{2}}$$

$$Z_0=R_0+jX_0=\rho_m dk,$$

and

$$A=\left(\frac{n\pi c_m}{L}\right)^2+\left(\frac{X_0}{2\rho_m d}\right)^2-\left(\frac{R_0}{2\rho_m d}\right)^2$$

$$B=\frac{R_0X_0}{2\rho_m{}^2d^2}.$$

These are the general equations for the response of the probe in terms of the driving point impedance of the material in which it is immersed. The amplitude is seen to comprise a sinusoidal oscillation of frequency which decays exponentially with time. The amplitude of the damped oscillation is distributed sinusoidally along the strip with a maximum at the free end and a zero at the center.

IV. DRIVING POINT IMPEDANCE OF VISCOELASTIC MATERIAL

We are concerned in this section with the general relationships that govern the driving point impedance of a viscoelastic material that exhibits both viscosity and rigidity so that the probe performance Eq. (5) can be solved for any given material.

Since little is known about the true viscoelastic behavior of the huge number of industrially important non-Newtonian materials including emulsions, colloids, suspensions, slurries, high polymers, and the like, particularly as regards the variations of rheological characteristics over a wide frequency spectrum, a viewpoint must be adopted that will enable us to proceed despite our limited understanding of the constitution of the materials to be measured. In all the work

[6] This assumption has proved to be true in all materials experimentally examined, including even mercury.

that follows, we will consider the problem from a phenomenological point of view. We arbitrarily will interpret all strains in the material that are in time phase with the applied stress as resulting from a single over-all rigidity coefficient function, and all strains that are 90° out of time phase with the applied stress as resulting from a single over-all viscosity coefficient function. Because any steady-state alternating strain can be resolved into these two time phase components, this approach does not reduce the generality of the analysis.

In the general case, the particular rigidity and viscosity coefficients that can be used to describe the behavior of a viscoelastic material at one frequency differ from those at any other frequency. It follows, therefore, that the coefficients we will be using are functions of frequency. As we will treat operation over a limited frequency range, in order to simplify notation, indication of this functional dependence on frequency will in general be omitted. It is important to note that with non-Newtonian materials, the ultrasonic viscometer measures frequency dependent dynamic viscosity rather than simple zero frequency unidirectional flow viscosity. The synthesis of these frequency functions in terms of frequency invariant rheological constants is beyond the scope of this present paper, although it has been the subject of many earlier papers.[7]

A. Wave Equation and Properties of its Solution

In accordance with this point of view, the shear stress, Y_x, produced in a viscoelastic medium by a transverse elastic wave of frequency ω traveling in the y direction is related to the shear strain by

$$Y_x = g\frac{\partial \xi}{\partial y} + \eta\frac{\partial^2 \xi}{\partial t \partial y},$$

where $g = g(\omega)$ = shear rigidity coefficient function, $\eta = \eta(\omega)$ = shear viscosity coefficient function, and ξ = particle displacement in x direction. Since

$$\rho\frac{\partial^2 \xi}{\partial t^2} = \frac{\partial Y_x}{\partial y},$$

where ρ is the density of the viscoelastic material, we obtain the wave equation governing shear wave propagation in a general viscoelastic material

$$\rho\frac{\partial^2 \xi}{\partial t^2} = g\frac{\partial^2 \xi}{\partial y^2} + \eta\frac{\partial^3 \xi}{\partial t \partial y^2}. \tag{6}$$

In order to solve this equation for the particle displacement corresponding to a particular frequency of particle vibration, we assume in the usual way $\xi(y, t) = e^{\Gamma y} e^{j\omega t}$, where Γ is the propagation function. It follows by straightforward substitution that

$$\Gamma = \pm\left[\frac{j\omega\rho}{\eta + g/j\omega}\right]^{\frac{1}{2}} \tag{7}$$

$$\xi = [Ae^{-\Gamma y} + Be^{\Gamma y}]e^{j\omega t} \tag{8}$$

and

$$Y_x = \Gamma(g + j\omega\eta)[-Ae^{-\Gamma y} + Be^{\Gamma y}]e^{j\omega t}. \tag{9}$$

Here the displacement ξ is represented as the summation of a wave traveling in the positive y direction and one traveling in the negative y direction with amplitude coefficients A and B, respectively.

If no discontinuities are present in the medium so that waves, once excited, propagate outward from the source without being reflected, Eq. (8) becomes,

$$\xi = \xi_0 e^{-\Gamma y} e^{j\omega t}, \tag{10}$$

where ξ_0 is the displacement amplitude at $y = 0$.

Many of the important operating characteristics of the Ultra-Viscoson result from the nature of the propagation function, Γ. By resolving Γ into its real and imaginary components, Eq. (10) becomes

$$\xi = \xi_0 \exp\left\{-\left(\frac{\omega^4\rho^2}{g^2+\omega^2\eta^2}\right)^{\frac{1}{4}} \sin\left(\frac{\tan^{-1}\omega\eta/g}{2}\right)y\right\}$$

$$\times \exp\left\{j\omega\left[t - \left(\frac{\rho^2}{g^2+\omega^2\eta^2}\right)^{\frac{1}{4}} \cos\left(\frac{\tan^{-1}\omega\eta/g}{2}\right)\right]y\right\}. \tag{11}$$

When written in this form, the first exponential factor, the attenuation term, clearly shows the frequency dependence of the attenuation, while the second factor shows the dispersive phase velocity when viscosity is present—velocity being a function of frequency. An important quantity which we will use later, is the skin depth δ of the shear wave. We define δ as the path length for the amplitude to fall to $1/e$ (36.8 percent) of its initial value—it thus becomes analogous to a similar quantity widely used in electromagnetic theory. In the general case,

$$\delta = \left[\frac{g^2+\omega^2\eta^2}{\omega^4\rho^2}\right]^{\frac{1}{4}} \csc\left[\frac{\tan^{-1}(\omega\eta/g)}{2}\right].$$

The phase velocity c can also be readily obtained from Eq. (11). We have

$$c = \left[\frac{g^2+\omega^2\eta^2}{\rho^2}\right]^{\frac{1}{4}} \sec\left[\frac{\tan^{-1}(\omega\eta/g)}{2}\right].$$

In purely rigid materials $\eta = 0$, these expressions reduce to the simple form,

$$\delta_0 = \infty$$

$$c_0 = (g/\rho)^{\frac{1}{2}}.$$

[7] W. P. Mason, *Piezoelectric Crystals and Ultrasonics* (D. Van Nostrand Company, Inc., New York, 1950), chap. 14; Smith, Ferry, and Schremp, J. Appl. Phys. **20**, 144 (1949); J. D. Ferry, J. Am. Chem. Soc. **64**, 1323 (1942); Ferry, Sawyer, and Ashworth, J. Polymer, Sci. **2**, 593 (1947); T. Alfrey, and P. Doty, J. Appl. Phys. **16**, 700 (1945); W. Philippoff, Physik. Z. **35**, 884, 900 (1934).

These will be recognized as the familiar expressions for propagation of plane shear waves in rigid solids. Similarly, for purely viscous materials $g=0$, we obtain,

$$\delta_\eta=\left(\frac{2\eta}{\omega\rho}\right)^{\frac{1}{2}}$$

$$c_\eta=\left(\frac{2\omega\eta}{\rho}\right)^{\frac{1}{2}}=\omega\delta_\eta.$$

This special solution for viscous liquids was first studied by Rayleigh.[8]

The wavelength for these two special cases is simply obtained by use of the general relation $\lambda=2\pi c/\omega$.

$$\lambda_g=\frac{2\pi}{\omega}(g/\rho)^{\frac{1}{2}},$$

and

$$\lambda_\eta=2\pi(2\eta/\omega\rho)^{\frac{1}{2}}=2\pi\delta_\eta.$$

For the viscous case, the extremely rapid attenuation per wavelength can be seen from the last result. Only 0.187 percent of the initial amplitude remains one wavelength from the source of excitation. It follows also that all particle vibration of any significant amplitude takes place well within $\frac{1}{2}$ wavelength from the source of excitation and phase shifts greater than 180° are of no practical importance.

B. Wave Impedance—General

An important quantity termed the characteristic acoustic wave impedance z_0 is the ratio of stress to particle velocity when either an outgoing wave or an incoming wave is considered acting alone. By letting $B=0$ and $A=0$ in turn in Eqs. (8) and (9) and by differentiating Eq. (8), we have[9]

$$z_0=\frac{-Y_x}{\partial\xi/\partial t}=\pm\left[j\omega\rho\left(\eta+\frac{g}{j\omega}\right)\right]^{\frac{1}{2}}, \tag{12}$$

where the positive sign is to be chosen for propagation in the positive direction, and the negative sign for propagation in the negative direction. For rigid materials, this reduces to the familiar expression,

$$z_{0g}=\pm(\rho g)^{\frac{1}{2}}=\pm\rho c_g, \tag{12a}$$

while for viscous materials, we obtain

$$z_{0\eta}=\pm(\omega\rho\eta/2)^{\frac{1}{2}}(1+j). \tag{12b}$$

We note that for rigid materials the characteristic impedance is real and independent of frequency, so that the particle velocity is always in phase with the stress for a wave propagating either outward or inward. In viscous materials, the phase shift between these two components is 45°, while the magnitude increases as the $\frac{1}{2}$ power of the frequency. In the general viscoelastic medium, the phase shift can have any value between zero and 45° depending on the ratio $\omega\eta/g$.

The effect that the liquid has on the probe for any general conditions can be wholly described if the acoustic impedance of the material at $y=0$ is known for the conditions assumed. If we terminate a given quantity of material by some arbitrary impedance Z_R, located at $y=l$, by using Eqs. (8), (9), and (12), we can write

$$Z_l=Z_R=\frac{z_0[Ae^{-\Gamma l}-Be^{\Gamma l}]}{[Ae^{-\Gamma l}+Be^{\Gamma l}]}.$$

Solving for the ratio B/A, we obtain,

$$\frac{B}{A}=\left[\frac{z_0-Z_R}{z_0+Z_R}\right]e^{-2\Gamma l}. \tag{13}$$

In general, the impedance at any point of the medium is given by

$$Z_y=z_0\left[\frac{Ae^{-\Gamma y}-Be^{\Gamma y}}{Ae^{-\Gamma y}+Be^{\Gamma y}}\right].$$

Since we are particularly concerned with the impedance at $y=0$, the so-called driving point impedance Z_0, we set $y=0$, and by substituting Eq. (13), after some trigonometric manipulation we find,

$$Z_0=z_0\left[\frac{1+(z_0/Z_R)\tanh\Gamma l}{(z_0/Z_R)+\tanh\Gamma l}\right]. \tag{14}$$

This expression completely describes the driving point impedance as seen by the probe in terms of the characteristic impedance of the medium, the impedance of any

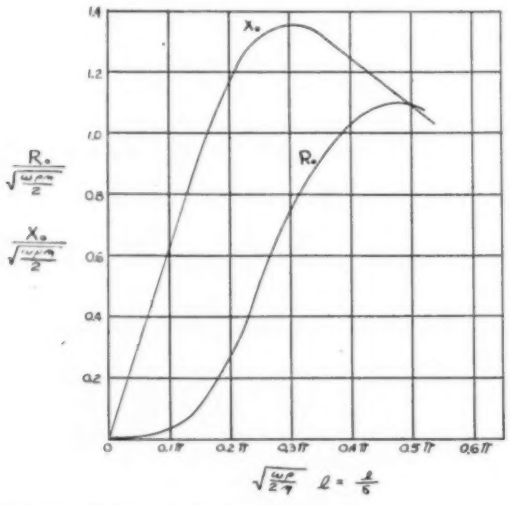

FIG. 3. Driving point impedance of viscous film *vs* thickness in skin depths: $g=0$.

[8] Lord Rayleigh, *Theory of Sound* Vol. II, p. 317 (Dover Publications, New York, 1945).

[9] The negative sign is introduced since acoustic wave impedance is usually employed with pressure rather than stress and, in accordance with usual sign conventions, a positive pressure is equivalent to a negative stress.

termination, and the position of this termination. This result is completely analogous to a similar well-known expression used in long line electrical transmission theory,[10] and therefore its solution for particular cases is greatly facilitated by employing graphical representations such as impedance charts and circle diagrams long used in the communications field.

C. Driving Point Impedance in Special Cases

The response of the probe under some particular conditions will be discussed in a later section. In order to evaluate the operation of the probe, however, in accordance with Eq. (5), it is necessary to know the driving point impedance of the viscoelastic material in each case. In general, the probe is either immersed in an unbounded or infinite volume (several cc usually suffices for this purpose), or else it is employed to measure properties of bounded volumes or thin films. For the latter case, the bounding medium is usually air, so we can derive the driving point impedance for this case by setting $Z_R=0$ in Eq. (14). Thus, the general expression for impedance when a gas or vacuum is the bounding medium becomes

$$Z_0=R_0+jX_0=z_0\tanh\Gamma l, \tag{15}$$

where R_0=real part of impedance and X_0=imaginary part of impedance.

Case I: Z_0 of Rigid Material

For an ideal rigid material having no viscosity, from Eqs. (12a), (7), and (15), we have,

$$R_0=0$$

and

$$X_0=(\rho g)^{\frac{1}{2}}\tan[\omega l(\rho/g)^{\frac{1}{2}}].$$

The resistance is always zero and the reactance function goes through excursions from $+\infty$ through zero to $-\infty$ as the argument of the tangent function goes through odd $\pi/4$ values. The poles correspond to path lengths equal to odd values of $\lambda_s/4$, while the zeros occur for path lengths equal to multiples of $\lambda_s/2$. This is a simple case of resonance. Of course, for infinite path lengths, the resonances do not occur and we have

$$R_0=(\rho g)^{\frac{1}{2}}=\rho c_s$$

and

$$X_0=0.$$

Case II: Z_0 of Viscous Material

For a viscous material, from Eqs. (12b) and (7), we have,

$$R_0=\frac{1}{2}\left(\frac{\omega\rho\eta}{2}\right)^{\frac{1}{2}}\left[\frac{\sinh 2\theta-\sin 2\theta}{\cos^2\theta+\sinh^2\theta}\right]$$

$$X_0=\frac{1}{2}\left(\frac{\omega\rho\eta}{2}\right)^{\frac{1}{2}}\left[\frac{\sinh 2\theta+\sin 2\theta}{\cos^2\theta+\sinh^2\theta}\right],$$

[10] J. C. Slater, *Microwave Transmission* (McGraw-Hill Book Company, Inc., New York, 1942), chap. 1.

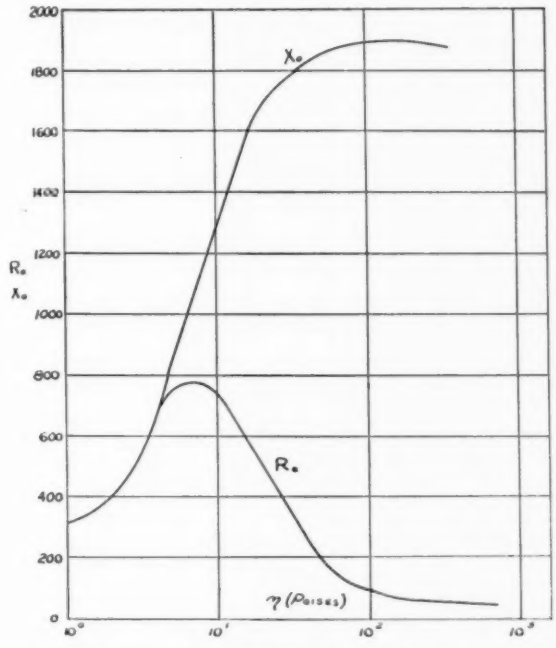

FIG. 4. Driving point impedance of viscous liquid *vs* viscosity: $l=0.01$ cm, $\rho=1.0$ g/cc, $\omega_0=1.88\times10^5$ rad/sec, $g=0$.

where

$$\theta=\left(\frac{\omega\rho}{2\eta}\right)^{\frac{1}{2}}l.$$

These functions are plotted in Fig. 3. For constant η, these graphs can be used to determine the value of l required for simulation of an unbounded or infinite medium. For large values of l, corresponding to the unbounded case, the components of the impedance (which is z_0 by definition) become,

$$R_0=X_0=(\omega\rho\eta/2)^{\frac{1}{2}},$$

which equals unity on the normalized ordinate scale employed. For very small values of l,

$$R_0=0,$$
$$X_0=\omega\rho l.$$

Of greater importance in practice, however, is the case in which l is constant but the properties of the materials vary. Figure 4 illustrates this for assumed $l=0.01$ cm, $\rho=1.0$, and $\omega=2\pi(30\times10^3)$.

Case III: Z_0 of Viscoelastic Material

Following a similar procedure we find

$$R_0=\frac{1}{2}\left(\frac{\omega\rho\eta}{2}\right)^{\frac{1}{2}}\left[4.49\left(\frac{\sinh 2x}{\cos^2 y+\sinh^2 x}\right)\right.$$
$$\left.-0.223\left(\frac{\sin 2y}{\cos^2 y+\sinh^2 x}\right)\right]$$

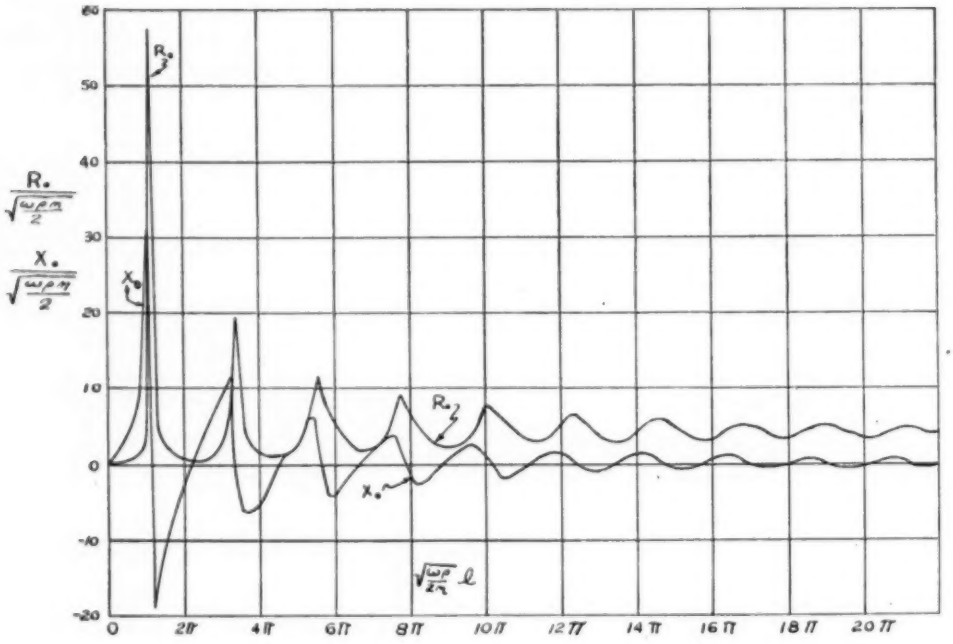

FIG. 5. Driving point impedance of viscoelastic film vs thickness in skin depth: $g/\omega\eta=10$.

$$X_0=\frac{1}{2}\left(\frac{\omega\rho\eta}{2}\right)^{\frac{1}{2}}\left[0.223\left(\frac{\sinh 2x}{\cos^2 y+\sinh^2 x}\right)+4.49\left(\frac{\sin 2y}{\cos^2 y+\sinh^2 x}\right)\right],$$

where

$$x=\left(\frac{\omega\rho}{2\eta}\right)^{\frac{1}{2}}(0.0222l)$$

and

$$y=\left(\frac{\omega\rho}{2\eta}\right)^{\frac{1}{2}}(0.446l).$$

These functions are plotted in Figs. 5 and 6 as functions of θl and viscosity, respectively. The oscillations are explained in Sec. VI.

V. PROBE RESPONSE IN UNBOUNDED VOLUMES

General explicit solutions for the ultrasonic viscometer response, i.e., α and β of Eq. (5) cannot be obtained because transcendental functions are involved. In this section, we will consider the response of the instrument when the probe is immersed in volumes of material sufficiently large so that no reflections from outer boundaries of the liquid are possible; this is termed the infinite volume case. The amount of material required for this to be true is usually only several cubic centimeters because of the enormous attenuation in liquids which prevents propagation of transverse waves to any appreciable distance in the ultrasonic frequency range under discussion.

By substituting the characteristic impedance Eq. (12) of a general viscoelastic material in Eq. (5), we obtain general expressions for α and β for the infinite medium case. These are,

$$\alpha=\frac{\rho^{\frac{1}{2}}}{2\rho_m d}\left(\frac{1}{2}\{g^2+\beta^2\eta^2\}^{\frac{1}{2}}+\frac{g}{2}\right)^{\frac{1}{2}}-\left\{\frac{1}{2}\left[\left\{\omega_0^2-\frac{\rho g}{4\rho_m^2 d^2}\right\}^2+\left\{\frac{\rho\beta\eta}{4\rho_m^2 d^2}\right\}^2\right]^{\frac{1}{2}}-\left\{\frac{\omega_0^2-\frac{\rho g}{4\rho_m^2 d^2}}{2}\right\}\right\}^{\frac{1}{2}}$$

$$\beta=\frac{-(\rho)^{\frac{1}{2}}}{2\rho_m d}\left(\frac{1}{2}\{g^2+\beta^2\eta^2\}^{\frac{1}{2}}-\frac{g}{2}\right)^{\frac{1}{2}}+\left\{\frac{1}{2}\left[\left\{\omega_0^2-\frac{\rho g}{4\rho_m^2 d^2}\right\}^2+\left\{\frac{\rho\beta\eta}{4\rho_m^2 d^2}\right\}^2\right]^{\frac{1}{2}}+\left\{\frac{\omega_0^2-\frac{\rho g}{4\rho_m^2 d^2}}{2}\right\}\right\}^{\frac{1}{2}}. \tag{16}$$

These equations are formidable, but fortunately throughout the major part of the operating range of the instrument

$$\rho\beta\eta/4\rho_m^2 d^2\ll\omega_0^2$$

and

$$\rho g/4\rho_m^2 d^2\ll\omega_0^2.$$

When these inequalities are employed, the general equations simplify to

$$\alpha=\frac{(\rho)^{\frac{1}{2}}}{2\rho_m d}\left(\frac{1}{2}\{g^2+\beta^2\eta^2\}^{\frac{1}{2}}+\frac{g}{2}\right)^{\frac{1}{2}}$$

and (17)

$$\beta=\frac{n\pi c_m}{L}=\omega_0,\quad n=1, 3, \cdots.$$

We can further simplify these relations for the two limiting viscoelastic conditions; purely rigid and purely viscous materials. For the rigid materials we have

$$\alpha_g=\left(\frac{\rho g}{4\rho_m{}^2 d^2}\right)^{\frac{1}{3}}, \tag{17a}$$

while for the viscous case we find

$$\alpha_\eta=\left(\frac{n\pi c_m\rho\eta}{8L\rho_m{}^2 d^2}\right)^{\frac{1}{3}}, \quad n=1, 3, \cdots. \tag{17b}$$

In both instances, the frequency is essentially equal to the undamped frequency throughout the range of operation—the frequency falling by less than 10 percent as α increases by many orders of magnitude.

VI. PROBE RESPONSE IN BOUNDED VOLUMES

The previous section relates to the boundary conditions met most frequently. This section concerns the response of the probe when immersed in bounded volumes that produce reflections between the surfaces of the strip and the bounding medium. These reflections in turn, lead to standing wave systems in the material being measured, and we find that the probe response becomes a function of the properties of both the material and those of the bounding medium. Since attenuation of shear waves is so high, the cases presented here pertain to thin films of viscous materials and rigid materials of somewhat greater thickness.

The response of the probe when thin films are being measured can be obtained from the general equations derived above, Eq. (5). The method employs the following steps:

(1) From the properties of the material and the thickness of the film, we obtain R_0 and X_0 as in Sec. V.

(2) A and B of Eq. (5) then follow directly by straight-forward manipulation.

(3) α and β of Eq. (5) are directly obtained by calculation using results of steps 1 and 2.

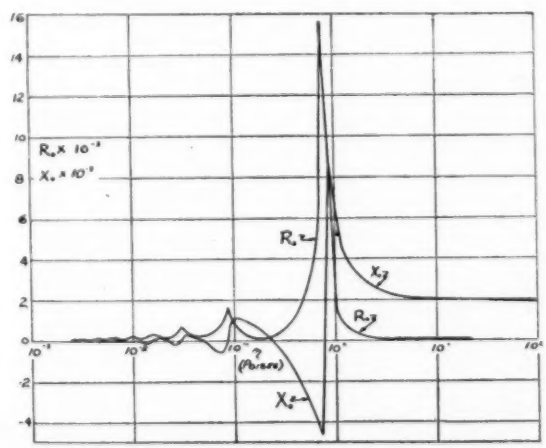

FIG. 6. Driving point impedance of viscoelastic liquid *vs* viscosity: $l=0.01$ cm, $\rho=1.0$ g/cc, $\omega_0=1.88\times10^5$ rad/sec, $g/\omega\eta=10$.

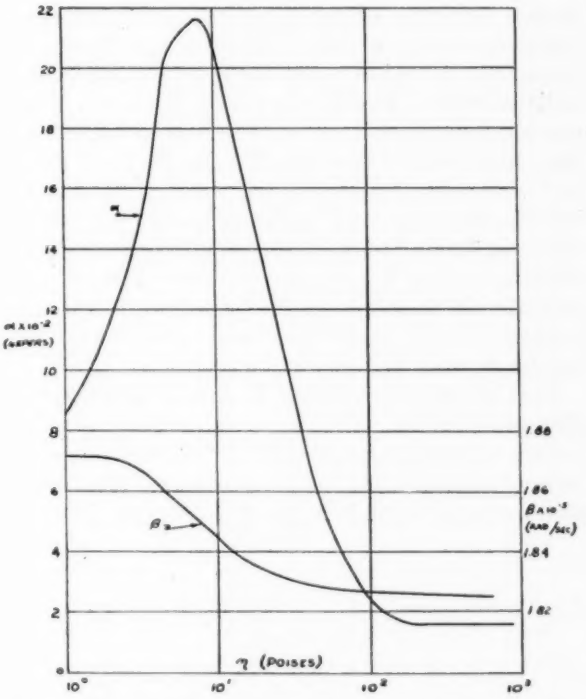

FIG. 7. Attenuation and frequency *vs* viscosity of viscous film: $l=0.01$ cm, $\rho=1.0$ g/cc, $\omega_0=1.88\times10^5$ rad/sec, $g=0$.

This procedure was followed in the preparation of Figs. 7 and 8 which show α and β as functions of viscosity for a purely viscous film and a viscoelastic film in which it is assumed that the ratio $g/\omega\eta=10$ is invariant. These two figures should be compared to the corresponding impedance graphs of Figs. 4 and 6.

Figure 7 for a viscous film is physically explained quite simply. At low viscosity, the thin film represents an infinite medium, and α is proportional to the $\frac{1}{3}$ power of η, while $\beta=\omega_0$, a constant. As η increases, the film is no longer thick enough to simulate an infinite volume, and energy is reflected back to the probe from the air boundary. In order that any appreciable energy be returned to the probe, the film must be much less

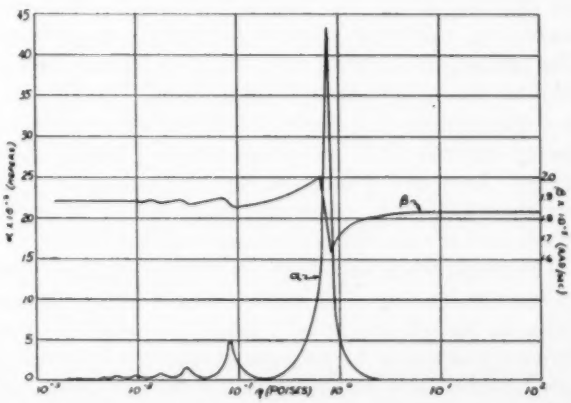

FIG. 8. Attenuation and frequency *vs* viscosity of viscoelastic film: $l=0.01$ cm, $\rho=1.0$ g/cc, $\omega_0=1.88\times10^5$ rad/sec, $g/\omega\eta=10$.

than $\lambda/2$ since, as discussed earlier, the attenuation per wavelength is enormous. Therefore, the energy is returned to the probe substantially in phase with the radiated energy. This results in a net reduction of damping and a decrease in α. As the viscosity increases further, more and more energy is reflected back in phase and α is reduced slowly toward zero as η approaches infinity. Since, in any practical case, η approaches a finite maximum limiting value, α approaches a limiting minimum value. The frequency β shows a small percent reduction in the region of the peak in α, followed by a leveling to a constant minimum value insensitive to further increase in viscosity.

For a viscoelastic film, Fig. 8, α and β show a radically different behavior. The case plotted is for a material having a high degree of rigidity so that propagation without appreciable damping can occur. The alternate minima and maxima in α as η increases from low values

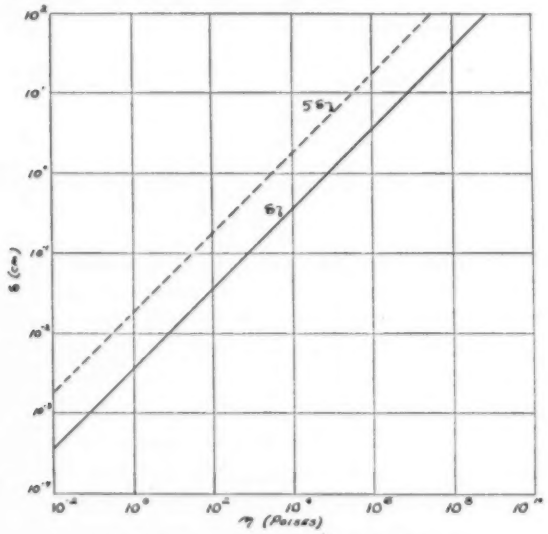

FIG. 9. Skin depth *vs* viscosity: $f=28$ kc/sec.

are produced by in-phase and out-of-phase superposition of the reflected and radiated energy. The phase relationship shifts continuously as η and g increase since the constant actual thickness film assumes continuously decreasing thickness when expressed in wavelengths. The peaks in α occur for odd $\lambda/4$ thicknesses, while the minima occur for even $\lambda/4$ thicknesses. The final peak in α occurs when the film is $\lambda/4$ thick, and the reflected energy returns 180° out of phase with the radiated energy. As η and g increase further leading to a film less than $\lambda/4$ thick, more and more energy returns in phase, and α continually decreases as shown.

The frequency β also shows sensitivity to the multiple resonances. In Fig. 7 β never exceeds the undamped value ω_0, but in this present case it is possible for the frequency actually to increase above ω_0. This will be noted particularly in the region of the last peak in α. This unusual behavior is produced by the presence of rigidity. At a thickness around $\lambda/4$, the metal strip of

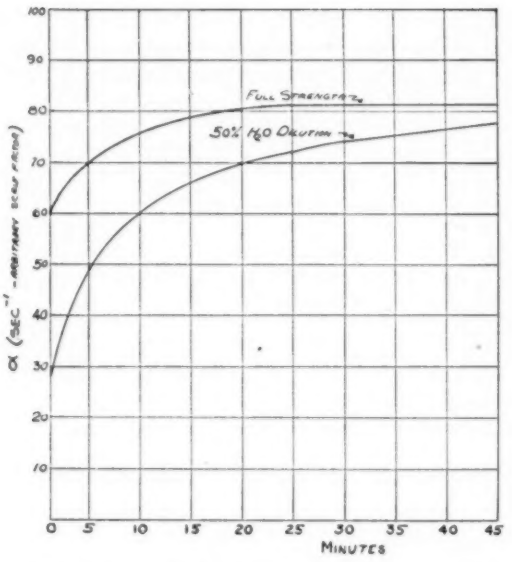

FIG. 10. Viscosity of colloidal Bentonite *vs* time: no agitation.

the probe is surrounded by a sheath of material that acts like a material having a rigidity coefficient approaching infinity. This rigid sheath effectively increases the apparent Young's modulus of the strip, thus increasing the resonant frequency of the probe. Once the region of $\lambda/4$ is exceeded, β falls quickly and then approaches a limiting value slightly less than ω_0 as in the previous case.

VII. FUNCTION OF ELECTRONIC COMPUTER

The electronic computer is an important part of the ultrasonic viscometer for convenient practical utilization of the probe, since it generates the impulse that sets the probe into vibration and it produces an electrical output proportional to α. The computer is an analog computer because it solves for the damping

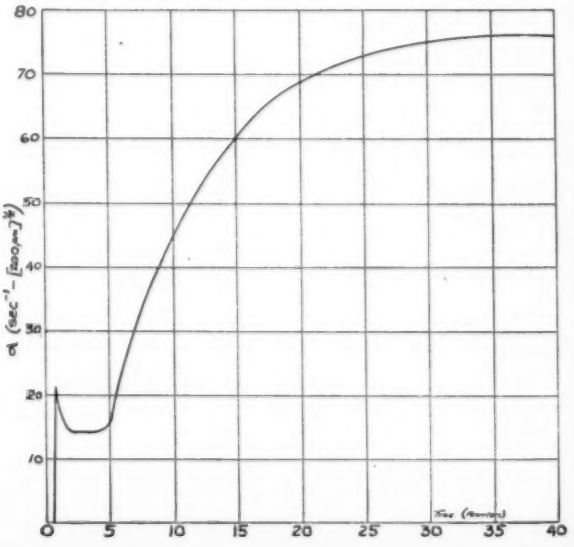

FIG. 11. Viscosity of whole human blood *vs* time during clotting.

coefficient α, which is a mechanical quantity, by establishing an electrical analog of the probe vibrations and operating upon it rather than upon the actual mechanical vibrations. Both the electrical analog which is established by the computer and the probe have the same α and β, but it is more convenient to employ electric automatic computing elements to measure these quantities than to employ mechanical elements

The computer produces both a current and a voltage proportional to α as given by Eq. (5). The current actuates a microammeter for direct reading, while the voltage is made available for actuating auxilary recorder/controllers. For the largest number of applications, the ultrasonic viscometer is used under conditions corresponding to the infinite volume case of Sec. V. In these applications, Eq. (17) with $g=0$ is such an excellent approximation that a parabolic scale can be employed on the output current meter to square all terms. The meter reading therefore becomes, from Eq. (17b),

$$\begin{aligned} \text{meter reading} &= K_1\alpha_\eta, \\ \text{meter reading} &= K_2\rho\eta, \end{aligned} \tag{18}$$

where K_1 and K_2 are system constants determined by the specific design of both the probe and the electronic circuitry. The instrument thus becomes direct reading in units of viscosity $\times$ density. Cgs units have been chosen; the output meter is calibrated to read centipoises$\times$grams/cc directly.

For Newtonian liquids, the standard instrument is direct reading in absolute units over a range of 4 decades. For all other viscoelastic materials, the ultrasonic viscometer reads an apparent viscosity—that is, it indicates the true viscosity of a Newtonian liquid that would damp the probe to the same extent as the non-Newtonian material in which it is actually immersed. It can be seen from Eq. (17) that if g is about the same order of magnitude or greater than $\beta\eta$, α will be affected by the rigidity of the material. With the standard unit, for g to affect α under the condition of infinite volume, g must exceed 10^5 or 10^6 dynes/cm^2 at the measuring frequency employed. It is rare, therefore, for rigidity to affect the measurements to any extent in other than unusual high polymeric materials, because rigidity values of liquids and semisolids do not ordinarily attain such high values. In the treatment of bounded volumes, however, we have seen that rigidity can markedly affect the results, because standing wave resonances can be set up in the material.

VIII. OPERATING CHARACTERISTICS AND DATA

The standard ultrasonic viscometer operates at about 28 kc/sec, although special units have been constructed for use in the range from 10 to 150 kc/sec. Figure 9 is a plot of the skin depth δ as a function of η at 28 kc/sec. Since δ is the path length for the amplitude to fall to e^{-1} or 36.8 percent of its value at the surface of the probe, it can be assumed that a path length of, say, 5δ where the amplitude will be only 0.7 percent of its initial value is equivalent to a medium of infinite extent. This locus is shown dotted in Fig. 9. It is clear, therefore, that the instrument measures the viscosity of extremely thin

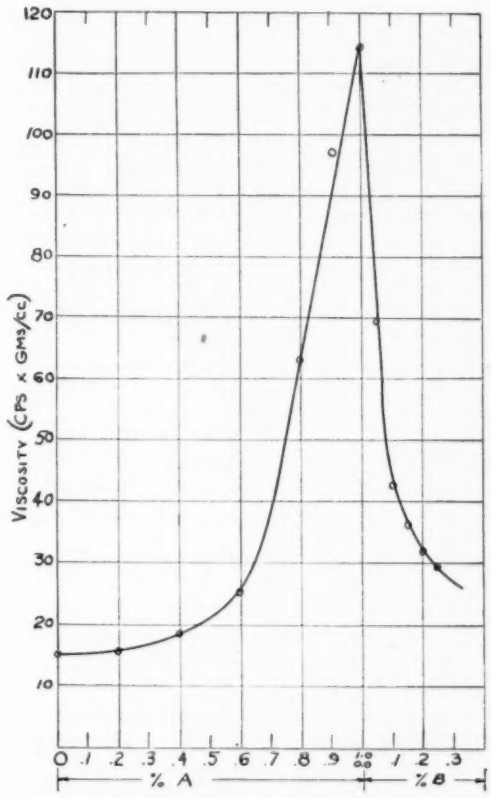

FIG. 12. Viscosity of ceramic glaze *vs* percent addition of thickener and thinner.

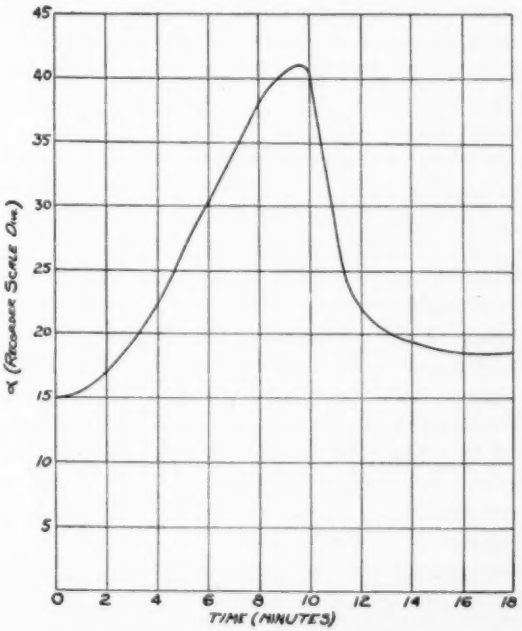

FIG. 13. Viscosity of rubber latex film *vs* time: thickness=0.05 cm.

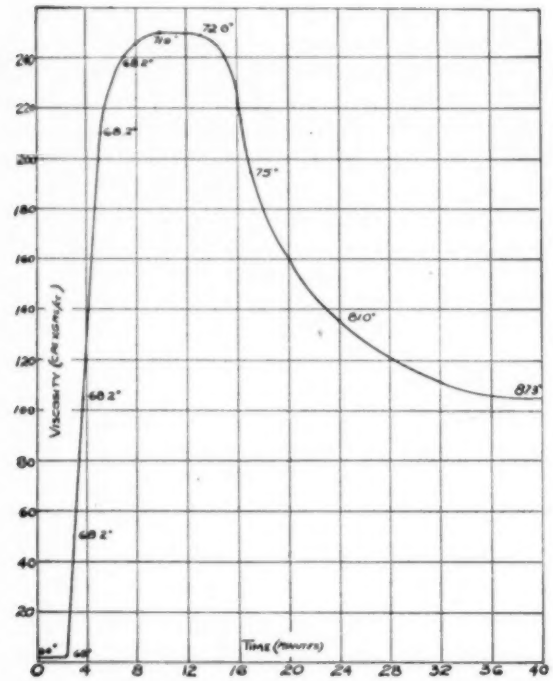

FIG. 14. Viscosity of thin boiling starch *vs* time during conversion: 290 g starch, 750 cc water, temperature in °C.

layers without affecting, or being affected by, liquid outside this immediate region.

The maximum amplitude of motion of the vibrating strip occurs at the instant following application of the exciting impulse. This peak amplitude is less than $\frac{1}{2}$ micron and it decays to zero at a rate proportional to e^{-at}. Thus, the ultrasonic energy radiated by the probe is so minute that no disturbance of material in which the probe has been immersed has ever been observed. The probe, as such, does affect some materials, but this phenomenon is not related to the presence of ultrasonic energy. Since this effect is useful, it warrants brief discussion here.

A well-known thermodynamic principle first set forth by Gibbs states that any substance present in a liquid that reduces surface or interfacial tension will migrate to surfaces or interfaces that may be present. Thus, if colloidal clay particles are placed in a beaker of water and thoroughly mixed, after several minutes the concentration of clay along the walls of the beaker and at the air-liquid interface will be higher than that in interior regions since the clay particles reduce interfacial tension. If agitation is present, of course, this migration cannot take place. With such materials, if the probe is immersed, the reading will start at a low initial value and increase exponentially to reach a final stable value in the order of 5–10 minutes.

The explanation of this behavior is that clay particles migrate to the water-metal interfaces of the probe and coat the probe with a higher concentration of clay. Since a layer only several microns thick approximates an infinite volume in this type of material, the measured viscosity increases to a maximum as determined by the higher clay concentration and remains there. If agitation is introduced, the viscosity reading will immediately fall to the initial value until agitation is stopped, after which it will again climb. This effect, which is shown in Fig. 10, has been found in colloids, adhesives containing volatile solvents, drilling muds, clay slips, printing inks, slurries, and the like and can be used as an additional means for studying the properties of this most complex class of materials. In solutions or mixtures containing substances that lower surface tension but have a lower viscosity than the principal constituent, the viscosity will have an exponential decrease rather

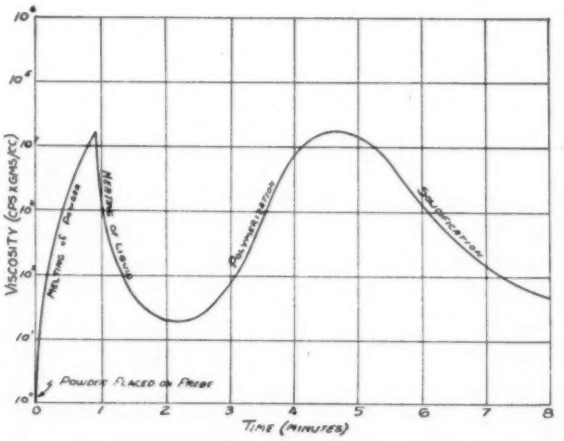

FIG. 15. Viscosity of thermosetting resin film *vs* time: Temperature = 300°F.

than increase as in the above case. This is shown by the initial peak and subsequent decline found in curves of blood coagulation (see Fig. 11). This effect of particle migration has been shown to be independent of the ultrasonic vibration of the probe itself, by removing the electrical exciting impulses for timed intervals. Upon reconnection, the readings immediately assume the identical values on the exponential curve as were previously obtained with no interruption of probe vibration.

Typical data taken with the ultrasonic viscometer on non-Newtonian systems are presented in Figs. 12 through 15. On Newtonian systems the viscometer indicates classical flow viscosity. It is interesting to compare Fig. 13 with the theoretical curve for a thin film, Fig. 7. The close correlation indicates that the viscosity of the rubber latex film changed logarithmically with time during the drying period.

Letters to the Editor

Comments on "The Dirac Delta Function and the Summation of Fourier Series"*

ERICH R. BERGER
Vienna University of Technology, Karlsplatz 13, Wien IV, Austria
(Received April 9, 1953)

AS I consider the mentioned paper to be a very important one for the treatment of Fourier series, I wish to point out some errors, which could trouble anyone using the given formulas.

(1) According to the definition (1),

$$\int_{-\pi}^{+\pi} F(x)\delta(x)dx=F(0);$$

and as $\delta(x)$ is an even function, we get

$$\int_0^{\pi} F(x)\delta(x)dx=\tfrac{1}{2}F(0)$$

only. For this reason, Eq. (4) yields

$$a_k=\frac{2}{\pi}\int_0^{\pi}\delta(x)\cos kx dx=\frac{1}{\pi},$$

and (7) yields

$$\tfrac{1}{2}+\sum_1^{\infty}\cos nx=\pi\cdot\delta(x),$$

not $(\pi/2)\delta(x)$, as stated.

By the same reason, in Eq. (15) we have to put

$$\int_0^{\infty} e^{-st}\delta(2t)dt=\tfrac{1}{2}\int_0^{\infty} e^{-st/2}\delta(t)dt=\tfrac{1}{4},$$

not $\frac{1}{2}$. But these two mistakes in (7) and (15) cancel each other and had no influence upon the result.

(2) The function

$$\frac{1}{\pi}[\tfrac{1}{2}+\sum_1^{\infty}\cos nx]=\delta(x)$$

is not exactly the Dirac delta function, but a periodically repeated δ function with the period 2π. On the contrary, in Eq. (15), $\pi/4$ is the Laplace transform of the normal δ function, not the repeated one. Anyway, that difference does not matter if we consider the interval $0<x<\pi$ only.

To avoid mistakes, I should propose for the repeated δ function the notation

$$(1/\pi)[\tfrac{1}{2}+\sum_1^{\infty}\cos nx]=\sum_{-\infty}^{+\infty}\delta(x-2n\pi).$$

(3) In example 2, there is an error in Eq. (27),

$$Y(x)=[Y(0)-\tfrac{1}{2}]\cosh x-(\pi/2)|\sinh x|+\tfrac{1}{2},$$

and also in Eq. (29),

$$\int_{-\pi}^{+\pi} Y(x)dx=2\pi.$$

That yields

$$Y(0)=\tfrac{1}{2}+(\pi/2)\operatorname{ctgh}\pi.$$

So we get the result

$$Y(x)=\tfrac{1}{2}+\frac{\pi}{2}\cdot\frac{\cosh(\pi-x)}{\sinh\pi}\quad(0<x<\pi),$$

according to the formula given by Kneser,[1] with $\alpha=\pi-x$ and $\mu=1$.

(4) In example 1, Y' is discontinuous at zero; thus $Y'(+0)\neq 0$, and zero is only the mean value of the right-side and the left-side limits. So one might be puzzled by the fact that in the Laplace transformation one has to start with $Y'=0$ and not with the right-side limit. The reason is that the impulse, represented by the δ function, is distributed equally on both sides of the axis. The left half changes Y' from the left-side limit to zero, the right half changes it from zero to the right-side limit. Thus, zero is really the correct value for Y' to begin with.

(5) The use of the Laplace transformation is not essential for this method. It is also possible, and sometimes easier, to solve the differential equation by the normal way, and to calculate the integration constants by means of the boundary conditions.

For example, in example 1, the differential equation is

$$(15):\quad Y''+Y=\tfrac{1}{2}-(\pi/2)[\delta(t)+\delta(t-\pi)]$$

with the general solution

$$Y(t)=A\cos t+B\sin t+\tfrac{1}{2}\quad(0<t<\pi).$$

Integration of Eq. (15) between $-\epsilon$ and $+\epsilon$ yields

$$Y'\Big|_{-\epsilon}^{+\epsilon}+\int_{-\epsilon}^{+\epsilon} Y dt=\epsilon-(\pi/2)$$

and with $\epsilon\to 0$

$$Y'\Big|_{-0}^{+0}=-\pi/2.$$

As $Y'(-0)=-Y'(+0)$, we obtain $Y'(+0)=-\pi/4$ and therefore $B=-\pi/4$. As the period of Y is π, $Y(0)=Y(\pi)$, and thus $A=0$. So we get the result

$$Y(t)=\tfrac{1}{2}-\frac{\pi}{4}\sin t\quad(0<t<\pi),$$

according to the result of the Laplace transform method.

* M. R. Spiegel, J. Appl. Phys. **23**, 906 (1952).
[1] Kneser, *Integralgleichungen* (1922), second edition, p. 157, Eq. (1).

Measurements of Stacking Faults in Cold-Worked Alpha Brass*

B. E. WARREN AND E. P. WAREKOIS
Massachusetts Institute of Technology, Cambridge, Massachusetts
(Received April 20, 1953)

BARRETT[1] has suggested that stacking faults on the (111) planes should contribute to the broadening of the x-ray reflections from a cold-worked face-centered cubic metal. Paterson's[2] recent treatment of this problem predicts peak shifts as a result of stacking faults and hence gives a method for uniquely proving their existence and measuring the probability of occurrence. The (111) reflection moves toward large angle and the (200) reflection toward small angle, so that the separation of these two peaks decreases as a result of stacking faults. For the (222)–(400) pair the opposite effect is predicted.

Filings of 70–30 brass were pressed into flat briquets and the reflections recorded on a Norelco spectrometer using Co $K\alpha$. To minimize positioning errors of the sample, all peaks were recorded on a single run, and measurements were made only of the distance between the centers of gravity of the neighboring lines (111)–(200) and (222)–(400). Figure 1 shows the measured peak separations for a cold-worked sample given subsequent one-hour anneals at various temperatures. The left-hand side corresponds to the cold-worked filings, and the right-hand side to well-annealed material. The effect of cold work in the sample is to decrease the (111)–(200) separation by 0.15° and to increase the (222)–(400) separation by about 0.34°.

From Paterson's theory, stacking faults produce a peak shift $\Delta h_3=\pm 3\sqrt{3}\alpha/4\pi$, where α is the stacking fault probability. In spectrometer coordinates, the shift in degrees is

$$\Delta(2\theta^\circ)=\pm\frac{\tan\theta\cos^2\varphi 270\sqrt{3}\alpha}{h_3\pi^2},\qquad(1)$$

where φ is the angle between the normal to the diffracting planes and the normal to the (111) planes on which the stacking faults exist. Allowing for the fact that stacking faults on a particular set of (111) planes will produce shifts on only $\frac{1}{4}$ of the (111) powder pattern reflections, the change in the (111)–(200) peak separation for 70–30 brass and Co $K\alpha$ is given by $\Delta(2\theta)_{(111)-(200)}=6.0\alpha$. For

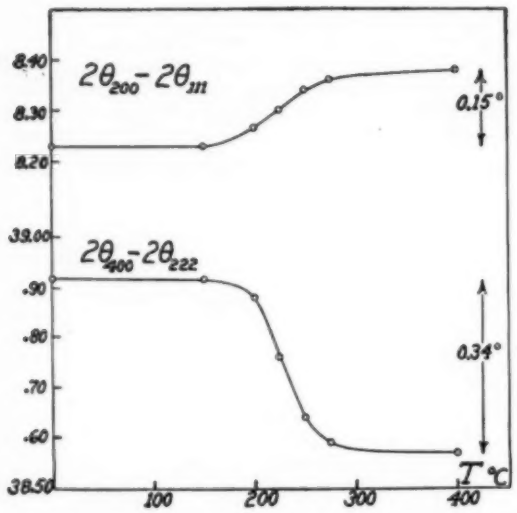

FIG. 1. Peak separations (111)–(200) and (222)–(400) for cold-worked 70–30 brass filings given subsequent 1-hour anneals at various temperatures until well annealed. Radiation Co$K\alpha$.

the cold-worked brass filings represented by Fig. 1, the reciprocal of the stacking fault probability is then $1/\alpha=6.0/0.15=40$. On the average there is a stacking fault once every 40(111) planes.

Using log plots[3] of the Fourier coefficients to separate particle size and distortion broadening, average particle size dimensions of about $\langle L_{100}\rangle=80$A and $\langle L_{111}\rangle=180$A are obtained. It turns out that most of this apparent particle size broadening results directly from the stacking faults, and there is very little true particle size or fragmentation broadening. In cold-worked brass there is both particle size and distortion broadening, but the major part of the particle size broadening results from stacking faults. For the high angle reflections the broadening is due mostly to distortion (a root mean square strain $(\langle\epsilon^2\rangle)^{\frac{1}{2}}=0.008$), and for the low angle reflections it is due mostly to stacking faults. If slip occurs on (111) by a series of half-dislocations, an odd number produces a stacking fault and an even number leaves the proper sequence of planes. If the probabilities are equal, a stacking fault on the average every 40(111) planes means slip on the average every 20 planes.

* Research sponsored by the U. S. Atomic Energy Commission.
[1] C. S. Barrett, *Imperfections in Nearly Perfect Crystals* (John Wiley and Sons, Inc., New York, 1952), Chap. III.
[2] M. S. Paterson, J. Appl. Phys. **23**, 805 (1952).
[3] B. E. Warren and B. L. Averbach, J. Appl. Phys. **23**, 497 (1952).

A Limitation of the Reversion Method

W. J. CUNNINGHAM
Yale University, New Haven, Connecticut
(Received March 9, 1953)

DURING the past year two papers[1,2] have appeared concerning the so-called reversion method of obtaining an approximate solution for certain kinds of nonlinear differential equations. The method is applicable to equations of the form

$$Z_1x+Z_2x^2+\cdots+Z_nx^n=\lambda f(t), \tag{1}$$

where $Z_1, \cdots, Z_n$ are differential operators involving the independent variable t, $f(t)$ is a forcing function, and λ is a parameter introduced to facilitate the solution. Ultimately λ is allowed to become unity. An approximate solution for Eq. (1) is found as

$$x=\lambda x_1+\lambda^2x_2+\lambda^3x_3+\cdots, \tag{2}$$

where $x_1, x_2, \cdots$ are functions of t, with each x_i being determined from a linear equation dependent only upon functions found previously. Formulas are given allowing the direct calculation of each x_i.

The reversion method of solution is quite similar to the perturbation method.[3] This latter method is applicable to nonlinear equations in which the nonlinear term appears multiplied by a small parameter, say α. An approximate solution is obtained as a power series in the small parameter, as

$$x=x_0+\alpha x_1+\alpha^2x_2+\cdots. \tag{3}$$

The similarity between Eqs. (2) and (3) is evident.

A difficulty may arise in applying the perturbation method if the differential equation is one having an oscillatory solution, as for example,

$$d^2x/dt^2+\omega_0^2x+\alpha x^3=0. \tag{4}$$

If the series of Eq. (3) is substituted into Eq. (4) and an attempt made to evaluate each x_i, so-called secular terms appear with amplitudes growing without bound. In order to remove these terms, it is necessary to allow the frequency of the solution to differ from ω_0, as

$$\omega^2=\omega_0^2+\alpha b_1+\alpha^2b_2+\cdots. \tag{5}$$

Functions $b_1, b_2, \cdots$ are chosen during the analysis so as to remove the secular terms as they arise.

It would appear that if an attempt is made to use the reversion method with an equation similar to Eq. (4), so that operator $Z_1=(d^2/dt^2+\omega_0^2)$, the elaborate formulas for $x_1, x_2, \cdots$, developed in the references, will not yield correct results. Besides the assumption of Eq. (2), some condition such as Eq. (5) must be used simultaneously. This additional condition has not been employed.

It would seem that the difficulty of the appearance of secular terms has been overlooked in the references and that this difficulty should be pointed out. Examples given in the references involve only equations in which secular terms do not arise. For such equations, the formulas of the reversion method are applicable and solutions are simply and readily obtained.

[1] L. A. Pipes, J. Appl. Phys. **23**, 202 (1952).
[2] G. I. Cohn and B. Saltzberg, J. Appl. Phys. **24**, 180 (1953).
[3] N. W. McLachlan, *Ordinary Nonlinear Differential Equations* (Oxford University Press, London, 1950), p. 43.

Crossed Electron Beam Technique for Displaying Short Pulses*

PAUL D. COLEMAN AND MURRAY D. SIRKIS
Electrical Engineering Department, University of Illinois, Urbana, Illinois
(Received April 21, 1953)

THE principal problem in producing submillimeter waves by Doppler radiation oscillators[1–3] is that of obtaining a tightly space bunched, high-energy, electron beam. An experimental study of the bunching problem requires a method capable of measuring 1–5 Mev electron beams with "effective" pulse times of less than one micromicrosecond. A crossed electron beam scheme[4] under investigation in the Electrical Engineering Research Laboratory of the University of Illinois shows promise of meeting the

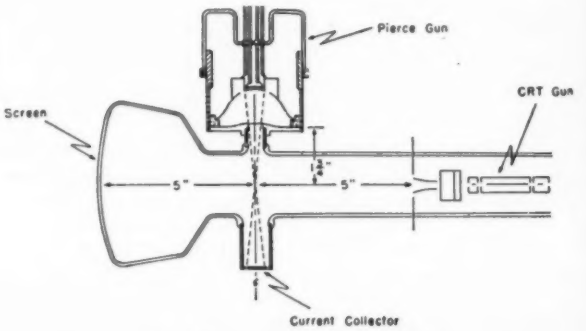

FIG. 1. Crossed electron beam tube.

above requirements. A verification of the basic idea at low voltage (8 kv) has been obtained and is briefly presented in this letter.

The low voltage device is shown in Fig. 1. An 8-kv, 0.115-ma, pulsed (2-μsec) Pierce gun is used for the test beam. This pulsed beam is collected and passed through a noninductive resistor, the resulting pulse being displayed on a synchroscope. A 1.45-kv CRT gun, powered by a second synchroscope, is used to probe the test beam, the resulting Coulomb scattering pattern being displayed on a fluorescent screen as indicated.

If l is the space distance over which the pulsed beam (space length d, velocity v) is scattering the swept probe beam (sweep speed v_s), then by equating corresponding times

$$l/v_s=(l-d)/v. \tag{1}$$

It is seen that the length of the pedestal on the screen will be

$$l=\frac{v_s}{v_s-v}d\leq\text{sweep length}. \tag{2}$$

As a first approximation for long pulsed beams, it will be assumed that while the probe beam is crossing the pulsed beam, the scattering can be represented as that from an infinite line charge. In cylindrical coordinates ($r=1/u, \theta$), the equation of motion of a charge q is[5]

$$\frac{d^2u}{d\theta^2}+u=-\frac{q\sigma_0U_0^2}{2\pi\epsilon m_0v_0^2u}, \tag{3}$$

where $\sigma_0=I/v$ is the ratio of current to velocity of the pulsed beam, and v_0 is the charge velocity at closest distance of approach $1/U_0$ (at which point $\theta=\pi/2$)

The series solution of Eq. (3) is

$$u=U_0\left[\sin\theta-\frac{q\sigma_0}{4\pi\epsilon m_0v_0^2}\left(\frac{\pi}{2}-\theta\right)^2-\cdots\right]. \tag{4}$$

The semiscattering angle θ_0 is obtained by setting $u=0$.

The conservation of energy equation is obtained by integrating Eq. (3) once

$$v_0^2=v_g^2-\frac{q\sigma_0}{\pi\epsilon m_0v_0^2}\ln\frac{U_0}{u}, \tag{5}$$

where v_g is the probe beam velocity at position u.

Figure 2 shows a comparison of the trace obtained from the scattered beam and the current pulse trace measured by the synchroscope. The computed displacement is 0.18 inch, and the measured displacement is 0.19 inch. The corresponding times associated with the current pulse are given in Table I.

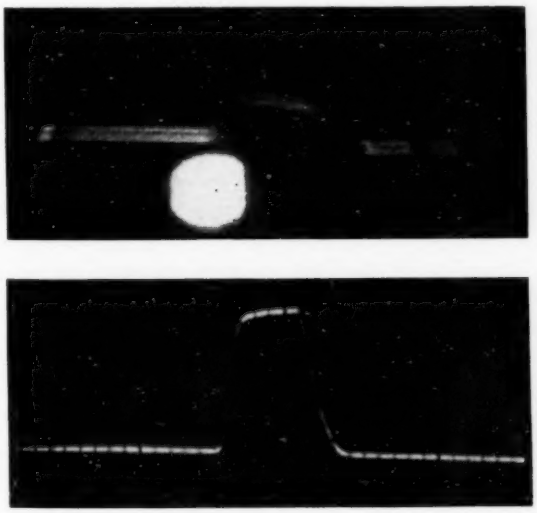

FIG. 2. Comparison of scattered beam trace with current trace. (a) Trace of scattered beam. (b) Current trace on synchroscope.

TABLE I.

	By scattering	By synchroscope
Top	2.32 μsec	2.13 μsec
Bottom	4.49 μsec	4.49 μsec

A Lecher wire[6] deflecting system with sweep velocities greater than the velocity of light is under investigation for measuring a 1.5-Mev bunched beam produced by a 10-cm microwave cavity accelerator[7] using the crossed beam technique.

* Work supported by Air Force Cambridge Research Center.

[1] Research Laboratory of Electronics Quarterly Reports, Massachusetts Institute of Technology, 1948.

[2] P. D. Coleman, "Theory of Generation of Submillimeter Waves by Accelerated Electrons," AF18(600)-23 Engineering Report No. 1.1, Electrical Engineering Research Laboratory, University of Illinois.

[3] H. Motz, J. Appl. Phys. **22**, 527 (1951).

[4] Quarterly Report Nos. 1 and 2 on Contract AF19(604)-524, Electrical Engineering Research Laboratory, University of Illinois.

[5] See, for example, Whittaker, *Analytical Dynamics* (Dover Publications, New York, 1944), p. 80.

[6] H. Von Foerster, "Beam Analyzer," Technical Reports Nos. 5-2 and 5-3, N6-ori-71 Task XIX, Electrical Engineering Research Laboratory, University of Illinois.

[7] P. D. Coleman, "Electron Acceleration and Bunching with a Single Microwave Cavity to Energies of 1–1.5 Mev," AF18(600)-23 Engineering Report No. 2, Electrical Engineering Research Laboratory, University of Illinois.

On Damage to Specimens by Shadowing Bombardment.* I. Experiment

K. TOKUYASU

Laboratory of Electron Microscopy, Kyushu University, Fukuoka, Japan

(Received April 6, 1953)

ELECTRON microscopical studies of polyvinyl acetate particles shadowed singly or doubly from opposite directions revealed such distorted figures as shown [Fig. 1(b) and (c)], differing from the original sphere forms of unshadowed particles [Fig. 1(a)]. The distortion indicates that the shadowing bombardment may result in damage to such spheres. This material softens easily by heating as is well known. If heated before shadowing, the heated particles show flattened images [Fig. 1(d)]. But once shadowed, the particles have a strong resistance to flattening by the heating. This fact indicates at least that the surfaces of the particles may be made more rigid by the shadowing bombardment. As the shadowing bombardment may consist of the direct bombardment by the shadowing ray and the effect of the radiation from the filament, it will be necessary to decide whether the former or the latter is more effective than other. For this purpose the particles exposed only to the radiation from the filament were examined, and it was concluded that the damage by the radiation alone is negligible. Thus, it is reasonable to attribute the change in the particles to the direct bombardment of the shadowing ray.

When the particles were mounted on a collodion film, of thickness about 20 mμ, and the opposite surface of the film was shadowed vertically with a reasonable weight of Cr, the particles were not noticeably damaged. This suggests that the damage by the bombardment may not be able to penetrate even such a thin film and, accordingly, it may be able to damage only the surface in the case where samples themselves are shadowed.

For studying the strength of the pressure that may be caused by the bombardment, carbon black particles shadowed obliquely after just being shadowed vertically were taken off the supporting film by repeated shakings, and patterns drawn by Cr on the supporting film were examined. Such examinations revealed that the particles were not moved at all by the oblique shadowing and that the pressure caused by the bombardment might be negligibly small.

In Part II,[1] it is shown that the pressure caused by the bombardment seems to be negligible but that the damage given to the thin layers of sample surfaces does not appear to be so small.

Though the explanation of actual distortion forms produced by shadowing are omitted here, the possibility that surface thin

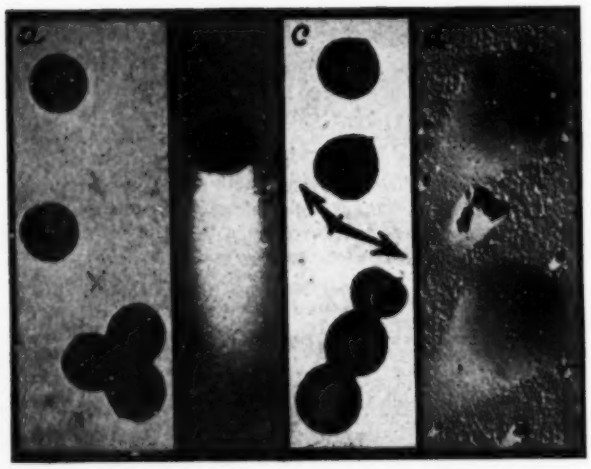

FIG. 1. Various figures of polyvinyl acetate particles: (a) unshadowed; (b) by single shadowing with 15 mg of Cr; (c) by double shadowings, of which directions are indicated by arrows, with 5 mg and 7 mg, lightly printed; and (d) heated before the shadowing. Prints of positive. ×22 000.

layers of organic or biological samples may be denaturated in general by the shadowing bombardment seems to be important since such damage may be one of the causes for the difference between sizes of shadowed and unshadowed samples.[2-4] In fact, thin surface layers of such samples seemed to be denaturated by the shadowing bombardment in the experiments in our laboratory. For instance, the shadowed surface layers of the silkworm polyhedra, which are the crystal-like inclusion bodies of the silkworm virus disease and are soluble in a dilute alkali, showed a strong resistance to the alkaline treatment, and it was possible to observe the films of the surface thin layers of the polyhedra.[5]

* This paper was presented, in part, at the meeting of the Electron Microscope Society of Japan held in Kyoto, December, 1951.
[1] K. Tokuyasu, J. Appl. Phys. **24**, 954 (1953).
[2] S. F. Kern and R. A. Kern, J. Appl. Phys. **21**, 705 (1950).
[3] S. G. Ellis, J. Appl. Phys. **23**, 728 (1952).
[4] H. Kahler and B. J. Lloyd, Jr., J. Appl. Phys. **21**, 699 (1950).
[5] K. Tokuyasu (to be published).

On Damage to Specimens by Shadowing Bombardment.* II. Calculation

K. TOKUYASU
Laboratory of Electron Microscopy, Kyushu University, Fukuoka, Japan
(Received April 6, 1953)

IF a small quantity of Cr at 0°C is heated to the boiling point in the filament, it would gain roughly the energy E,

$$E=mc_1 t \text{ cal}, \tag{1}$$

where m is the weight of Cr in g, c_1 is the specific heat of Cr in cal/°C g, and t is the boiling point of Cr in °C. The quantity of Cr seems not to lose its energy E to the shadowing ray during the process of evaporation, because there is nothing around it with which it can interact, except the filament, and it may not be able to give any part of its energy to the filament having a higher temperature than itself. And also, if we suppose that the vacuum is so high that the mean free path of the Cr ray is much longer than the distance between the filament and the sample surfaces and if the energy radiated from Cr in space during transit is negligible, the energy E may not be lost during the transit process of the Cr ray.

Thus if the solid-angular distribution of the shadowing ray is uniform and, accordingly, the distribution of the energy carried by the ray is uniform, the energy brought by the ray to the sample surface $a^{m\mu}\times a^{m\mu}$ will be approximately given by

$$\frac{mc_1 ta^2}{4\pi R^2\cdot 10^{14}} \text{ cal}, \tag{2}$$

where R is the distance from the filament to the plane in cm.

As described in Part I,[1] the thickness of the damaged part by the bombardment may be so thin that only one sheet of the collodion film can protect the sample from the damages. Though such thickness may vary according to various kinds of samples, we assume, at first sight, that the thickness d is 30 mμ. If the volume $a^{m\mu}\times a^{m\mu}\times d^{m\mu}$ and the weight $(ma^2)/(4\pi R^2\cdot 10^{14})$ g of Cr that arrived to the area $a^{m\mu}\times a^{m\mu}$ were assumed to be heated uniformly by the energy (2), the temperature increment s would be

$$s=\frac{mc_1 t}{4\pi R^2}\Big/\left(\frac{c_2\rho d}{10^7}+\frac{c_1 m}{4\pi R^2}\right)^{\circ}\text{C}, \tag{3}$$

where c_2 is the specific heat of the sample in cal/°C g and ρ is the density of the sample in g/cm³. If we take $R=10$ cm, $m=10$ mg, $c_1=0.1$ cal/°C g, $t=2200$°C, $c_2=0.5$ cal/°C g, and $\rho=1$ g/cm³,

$$s=\text{about } 760^{\circ}\text{C} \tag{4}$$

is obtained from Eq. (3). But in truth the energy seems to be used in various ways besides heating; the breaking of the chemical bonds in the sample, the interaction between Cr molecules and constituent molecules in the sample, recrystallization of Cr film, and so on. Accordingly it appears that the energy of the shadowing ray may be released locally to the outermost layers and, as a consequence, the damage suffered by these layers can be relatively great even though the energy of the shadowing ray itself may be small. The calculations described above are not thoroughly accurate but seem to be sufficient to understand the phenomenon qualitatively.

If the sample is assumed to be a perfect elastic body, the rough value of the velocity of the shadowing ray is calculated from the energy E assuming that the whole energy appears as kinetic energy and the quantity of Cr,m, is assumed to be evaporated during 1 second, the pressure p caused by the bombardment will be calculated as follows:

$$p=m(2c_1 t)^{\frac{1}{2}}/2\pi R^2 \text{ dyne/cm}^2. \tag{5}$$

We take the same values as the ones of m, c_1, and R in the calculation (4) and obtain $p=\text{about } 3.3\times 10^{-4}$ dyne/cm². Though the calculation is rough, it may be enough to suppose that the pressure is negligibly small. It seems to be noticeable that the percentage error based on the damage may be bigger on the measurement of the dimension of the smaller sample.

* This paper was presented, in part, at the meeting of the Electron Microscope Society of Japan held in Kyoto, December, 1951.
[1] K. Tokuyasu, J. Appl. Phys. **24**, 953 (1953).

X-Ray Transmission Studies of Large Imperfect Crystals*

GEORGE L. ROGOSA AND GUENTER SCHWARZ
Department of Physics, Florida State University, Tallahassee, Florida
(Received March 16, 1953)

STUDIES of the transmission of x-rays in the Laue diffraction case have been made mainly for calcite and quartz crystals which approach perfection.[1-3] In those studies it has been found that the transmitted intensity may undergo large changes as the crystal is rotated through a diffracting position. The intensity change may be an increase, decrease, or a combination increase-decrease depending on the thickness of the crystal and the wavelength of the radiation. These three cases have been classified, respectively, as anomalous transmission, extinction, and asymmetrical transmission. The cases may also be classified according to the product $\mu_0 t$, where μ_0 is the ordinary linear absorption coefficient and t is the crystal thickness.[4] For $\mu_0 t\gg 1$, one has the

case of anomalous transmission, while $\mu_0 l \ll 1$ gives extinction. Asymmetrical transmission corresponds to $\mu_0 l \sim 1$.

Using the experimental set-up described earlier[3] reflection and transmission curves for LiF crystals at Mo $K\alpha_1$, and Cu $K\alpha_1$ wavelengths have been recorded. Figure 1 shows the diffracted and transmitted intensity for a LiF crystal of 10-mm thickness

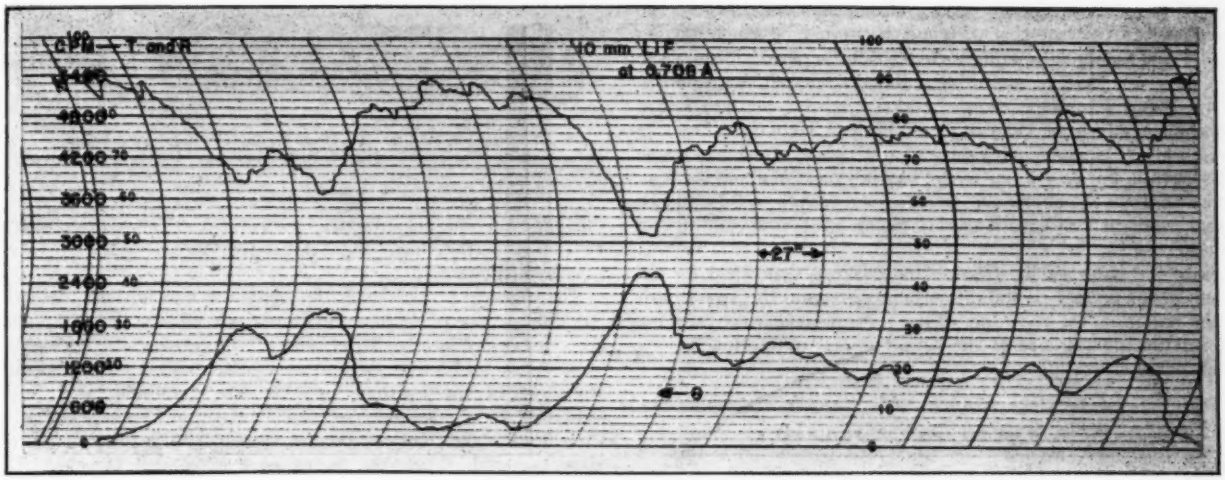

FIG. 1. Transmitted and reflected intensities for a LiF crystal showing extinction.

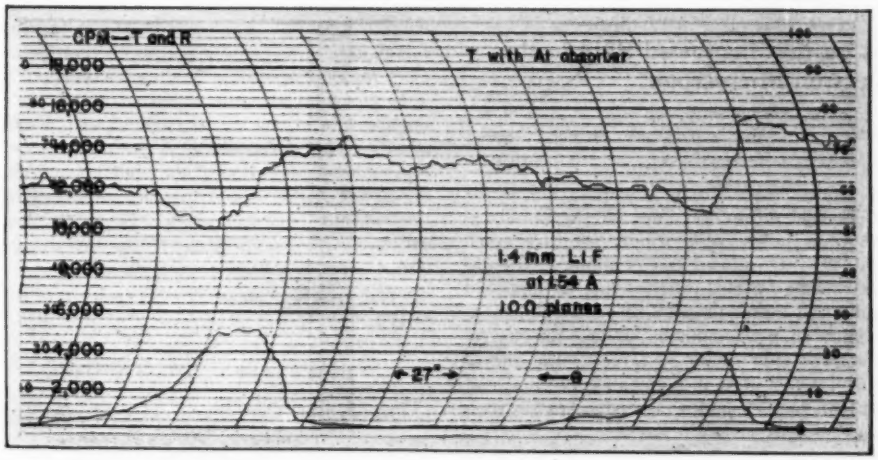

FIG. 2. Transmitted and reflected intensities for a LiF crystal showing asymmetrical transmission.

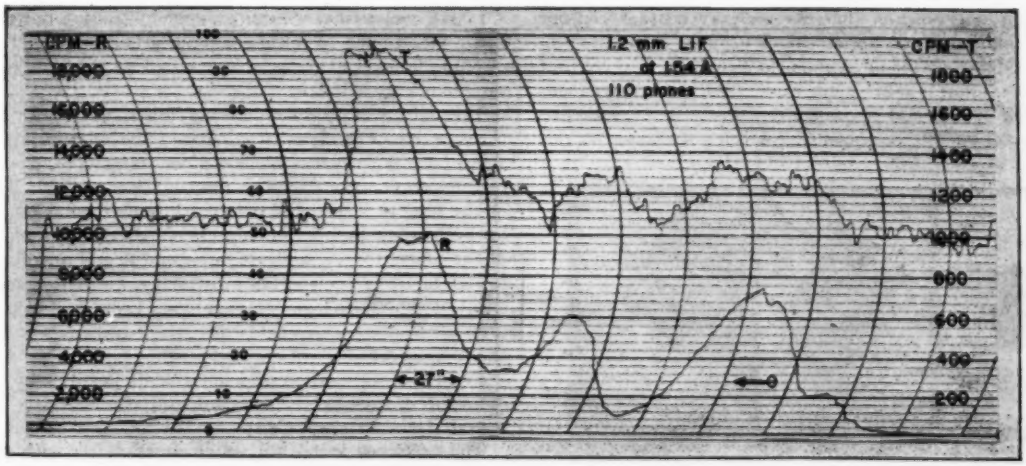

FIG. 3. Transmitted and reflected intensities for a LiF crystal showing anomalous transmission.

and at a wavelength of 0.708A. The numerous diffraction peaks indicate that the large crystal is made up of smaller crystals with slightly different angular orientations. The shape of the transmitted curve classifies the various crystal diffracting regions as belonging in the extinction class. This means that $\mu_0 l \ll 1$, and since $\mu_0 = 2.5$ cm^{-1} at this wavelength, l must be much smaller than 4 mm for the diffracting regions. $\mu_0 l$ for a perfect 10-mm LiF crystal would be 2.5, giving an entirely different transmission curve. Figure 2 shows a recorded curve at a wavelength of 1.54A, where μ_0 for LiF has a value of about 30 cm^{-1}. Here the diffracting regions are of large enough extent to give the asymmetrical transmission case. For $\mu_0 l = 1$, one would have a l value of about 0.3 mm. Figure 3 shows the anomalous transmission case for a 1.2-mm LiF crystal again at 1.54A, with the 110 planes used for the diffracting planes.

Since the shape of the transmitted curve is dependent on the extent of the perfect crystal diffracting region and the wavelength of the radiation, the recording of the transmission curve can give information on the size of the single crystal diffracting regions inside large crystal pieces.

* This work has been supported by a grant from the National Science Foundation.

[1] G. Borrman, Physik. Z. **43**, 157 (1941); Z. Physik **127**, 297 (1950).
[2] H. N. Campbell, Acta Cryst. **4**, 180 (1951); J. Appl. Phys. **22**, 1139 (1951).
[3] G. L. Rogosa and G. Schwarz, Phys. Rev. **87**, 995 (1952).
[4] W. H. Zachariasen, Proc. Natl. Acad. Sci. **38**, 378 (1952) and private communication.

Contour Lines on the Shadowed Side in the Electron Microscope*

K. TOKUYASU
Laboratory of Electron Microscopy, Kyushu University, Fukuoka, Japan
(Received April 6, 1953)

KERN and Kern[1] reported that "there is a difference in the position of the Fresnel diffraction lines on the shadowed and unshadowed side of a polystyrene sphere for any given setting of the objective lens." If the negative charging of the unshadowed side was responsible for this phenomenon as supposed by them, electric conductive materials such as carbon black or flakes of Cr would not show such phenomenon because the electric potential of the unshadowed side would be same as the one of the shadowed side. And further, if such nonconductive material as Fe_2O_3 was used as a material for shadowing instead of Cr, such phenomenon might not be found.

Nevertheless, in our experiments such phenomena were found on the images of shadowed specimens without relation to whether the specimens and the material for shadowing are conductive or nonconductive (Figs. 1 and 2). Furthermore, a more accurate description of the phenomenon than Kern's may be that contour lines on the shadowed side appear more vaguely than those on the unshadowed side, since our examinations revealed that contour lines on the shadowed side are more vague both in the over-focus of the unshadowed side and in the under-focus (Fig. 2). Thus the charging does not seem to be responsible (even if it exists), for this

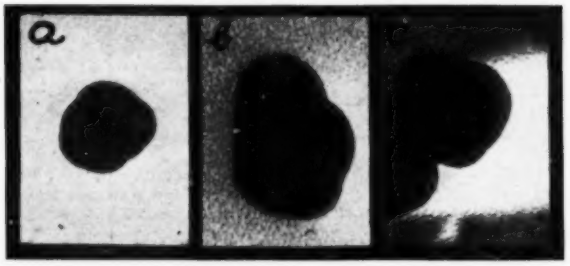

FIG. 1. Positive images of carbon black particles in over-focus. (a) unshadowed, (b) shadowed with Cr, and (c) with Fe_2O_3. ×45 000.

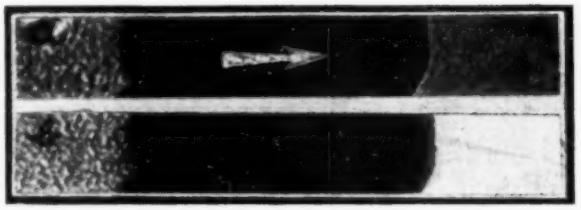

FIG. 2. Positive images of a portion of Cr flake in (a) under- and (b) over-focus. Shadowed with Cr. Arrow indicates direction of shadowing. ×65 000.

phenomenon and, accordingly, "a difference in the position of the Fresnel diffraction lines" seems not to be evidence for the existence of specimen charging.

The physical properties of the shadowed and unshadowed side will differ at the point that the former side has the metal cap and the portion of the supporting film of the former side is covered with the metal film. If the existence of the metal cap causes the vanishing of the contour lines on the shadowed side, both shadowed and unshadowed sides of the flakes of Cr shadowed with Cr will not show clear contour lines because both sides consist of same material. When the flakes were examined, however, the contour lines were visible only on the unshadowed side (Fig. 2). Further, when unshadowed specimens were mounted on the collodion films covered with metal films having various thickness and were examined, it was observed that the appearance of the contour lines dulls gradually in proportion to the thickness of the metal film. This evidence suggests that the metal cap is not the chief reason responsible to the phenomenon.

In the final analysis, whether or not the portion of the supporting film of one side is covered with a metal film seems to be most probably responsible. In other words, it may be the most reasonable explanation of the phenomenon that when the scattering power of the supporting film for the electron beams is small, the contour lines are visible; but if the power becomes bigger owing to the superposition of the metal film on the supporting film, the contour lines become obscure.

* This paper was presented at the meeting of the Electron Microscope Society of Japan held in Tokyo, June, 1952.
[1] S. F. Kern and R. A. Kern, J. Appl. Phys. **21**, 707 (1950).

Dielectric Constant Measurements at 8.6-mm Wavelength

PAUL HERTEL, JR., A. W. STRAITON, AND C. W. TOLBERT
University of Texas, Austin, Texas
(Received April 24, 1953)

THE dielectric constants and conductivity reported here were determined by measuring the attenuation and phase shift of 8.6 millimeter electromagnetic waves as they passed through a sample of the dielectric.

The output of an 8.6-millimeter klystron oscillator was split in a magic tee. The signal from one of the tee outputs went to a small horn on which a flat container was placed. Small amounts of the sample were added to the container to vary the thickness of the sample. The signal passing through the sample was picked up by another horn antenna and compared to the second output of the magic tee. A calibrated attenuator and a calibrated phase shifter in this reference line provided a means of measuring the effect of the added amount of sample. From graphs of the measured attenuation and phase shift *versus* thickness of the sample, the propagation factors were obtained.

From the attenuation and phase shift per unit of length thus obtained, the dielectric constant and conductivity were determined. These values are given in Table I.

The measured values for water agree closely with those which may be calculated using the work of Saxton and Lane.[1] Their theoretical values are given in Table II.

TABLE I.

Dielectric	Temperature °C	Dielectric constant	Conductivity mhos/meter
Distilled water	30	21	60
Distilled water	23.5	23	55
Saturated salt water (6.2 normal solution)	25	21	53
Tap water	24	24	56
Ethyl alcohol	24	3.6	3.2
Dry soil (as found)	24	3.0	0.51

TABLE II.

Dielectric	Temperature °C	Dielectric constant	Conductivity mhos/meter
Distilled water	30	24.4	62.1
Distilled water	20	18.6	54.7
Saturated salt water (2.0 normal solution)	30	20.6	57.6

The ethyl alcohol measurements are in close agreement with the values calculated from absorption coefficient and index of refraction data obtained by Lane and Saxton.[2] Their values are given in Table III.

TABLE III.

Wavelength	Temperature °C	Dielectric constant	Conductivity mhos/meter
0.62 cm	20	3.45	2.10
1.24 cm	20	4.21	3.01

The dielectric constant for the soil sample agree closely with the value of 2.8 previously reported (3) for measurements made on a soil sample taken at the Off Campus Research Center of The University of Texas. No comparison can be made for the conductivity since the water content was not determined.

[1] J. A. Saxton and J. A. Lane, Wireless Engr. **29**, 269–275 (1952).
[2] J. A. Lane and J. A. Saxton, Proc. Roy. Soc. (London) **213**, 400–408 (1952).
[3] A. W. Straiton and C. W. Tolbert, J. Franklin Inst. **246**, No. 1, 13–20 (1948).

Effect of Biaxial Orientation on the Ultimate Strength and Crazing of Linear Polymers*

C. C. HSIAO and J. A. SAUER
The Pennsylvania State College, State College, Pennsylvania
(Received March 23, 1953)

ONE of the most important properties of a material, from either a theoretical or a practical standpoint, is the ultimate strength. Until now, little useful knowledge has been obtained in connection with the breaking strength of materials and their related properties.[1,2] The general difficulties are mathematical as well as experimental. This is particularly true for high polymers.

Recently, however, the understanding of the effect of uniaxial orientation on the ultimate strength of linear high polymers has been advanced through the development of a theory which permits calculation of strength as a function of orientation in terms of strain change.[3] Experimental results[4,5] are found to agree fairly well with theoretical calculations.

By extending the theory to the case of biaxial orientation, the strength is found to be related with strains in the following manner:

$$S_{\epsilon_x}=\frac{4}{\pi}\left((1+\epsilon_x)^{\frac{1}{2}}\int_0^{\pi/2}\frac{d\phi}{(1+\epsilon_x)^{\frac{1}{2}}+[\sin^2\phi+(1+\epsilon_y)^3\cos^2\phi]^{\frac{1}{2}}}\right)S_0,$$

where S_{ϵ_x} is the ultimate breaking strength in the X direction at a state of biaxial orientation corresponding to strain changes of ϵ_x and ϵ_y, in X and Y directions, respectively, and S_0 is the strength of this linear polymer without any preferred orientation.

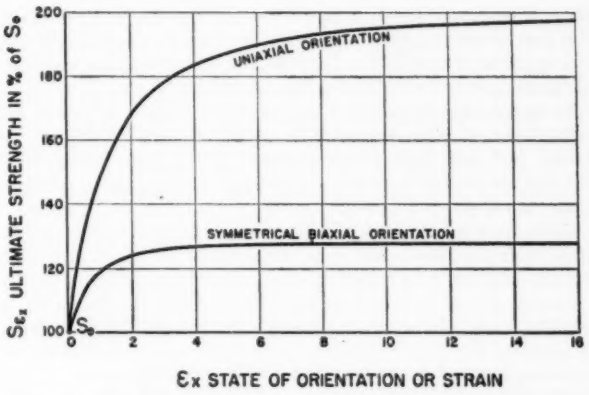

FIG. 1. Effect of orientation on ultimate strength of linear polymers.

Using graphical solution for the case of a symmetrical biaxial orientation, i.e., $\epsilon_x=\epsilon_y$, the result is plotted as shown in Fig. 1. For comparison, the effect of uniaxial orientation on the ultimate strength of linear high polymers measured in the direction of orientation, is also shown in the same figure. This latter curve can also be represented by the following formula:[3]

$$S_{\epsilon_x}=2\frac{(1+\epsilon_x)^{\frac{1}{2}}}{1+(1+\epsilon_x)^{\frac{1}{2}}}S_0,$$

where S_{ϵ_x} is the ultimate strength in the X direction of uniaxial orientation at a state of orientation corresponding to a strain change of ϵ_x in that direction, and S_0 is again the strength of this material without any preferred orientation.

For large specimens, experimental agreement has been found of laminated Polyflex sheets with approximately 300 percent orientation in each of the two, say X and Y, perpendicular biaxial directions. As predicted by the theory, the actual ultimate strength was found to be about 6800 psi, which is just about 26 percent higher than its amorphous strength of 5400 psi. A more thorough experimental investigation is being carried out, and it is hoped that a detailed report will be made in the future.

This statistical theory analyzes the effect of orientation of linear polymeric molecules on strength by considering the microstrength, as it may be called, of each fundamental unit and its particular direction of orientation. By introducing the assumption that there remains no change in volume after the material is oriented, various consequences of the assumed model can be worked out. It should be pointed out that some of the influential factors such as the structure and the molecular weight, as well as the stress concentration of the material, are automatically taken care of. However, other factors such as the temperature and the rate of testing will

FIG. 2. Fracture surface of biaxially oriented polystyrene.

have to be controlled, if a significant comparison is to be made. The size of the specimen seems to be surprisingly important in this type of investigation, as the ultimate breaking strength increases rapidly as the size of the specimen reduces.

An interesting phenomenon is observed of the biaxially oriented polystyrene relative to crazing,[6,7] as can be predicted from the theory, just described. Figure 2 shows the fracture surfaces of a 300 percent biaxially oriented polystyrene tested at a constant strain rate of about 2×10^{-4} per sec. A clear crazed fracture surface is shown as a result of the biaxial orientation that numerous long chain molecules are being lined up in parallel with the fracture surface, whereas an unoriented specimen will not show any sign of crazing at the same testing rate. This phenomenon of crazing can easily be demonstrated by subjecting biaxially oriented polystyrene film under tension, in one direction, until suddenly numerous crazing cracks are observed perpendicular to this one of the biaxial directions.

* This work was made possible through the assistance of the National Science Foundation Grant NSF-G100.

[1] A. A. Griffith, Trans. Roy. Soc. (London) **A221** (1921).
[2] T. Alfrey, Jr., *Mechanical Behavior of High Polymers* (Interscience Publishers, Inc., New York), 1948.
[3] C. C. Hsiao, J. Appl. Phys. **23**, 1189 (1952).
[4] J. Bailey, India Rubber World **118**, 225 (1948).
[5] M. S. Sapuppo, "The Effect of Molecular Orientation on the Tensile Properties of Polymethyl Methacrylate," thesis, Massachusetts Institute of Technology, 1952.
[6] C. C. Hsiao and J. A. Sauer, J. Appl. Phys. **21**, 1071 (1950).
[7] J. A. Sauer and C. C. Hsiao, "Stress Crazing of Plastics," presented at the Rubber and Plastics Division of the American Society of Mechanical Engineers Annual Meeting, December, 1952, New York (also published in the June, 1953 issue of India Rubber World).

A Method of Determining Electrical Resistivities at Low Temperatures

DAVID C. BAIRD AND WILLARD S. BOYLE
Royal Military College, Kingston, Ontario, Canada
(Received March 23, 1953)

IN order to correlate the thermal and electrical conductivities of certain copper specimens at liquid helium temperatures it was found that resistivity measurements had to be made on relatively thick samples. Because of the extremely low resistance (of the order of one micro-ohm) that had to be measured, it was difficult to obtain accurate results using conventional dc methods. It was found, however, that by forming the sample into a closed ring, the resistance could be easily determined from the decay time of a single induced current pulse. The principle of the method is not unlike that of the relaxation time technique used in setting lower limits to the resistivity of superconductors.

The copper sample, about 2 mm thick, was formed into a ring 4 cm in diameter. A coil consisting of about 200 turns of fine wire was mounted coaxially with and adjacent to the specimen and the output of this coil was taken directly to a wide band dc amplifier on the Y axis of an oscilloscope. The current pulse in the specimen was induced by breaking the current in a solenoid wound on the outside of the Dewar, thus eliminating the need for heavy current leads running into the helium bath. The self-inductance of a single circular loop of wire can be calculated from

$$L=0.01257a(\log_e 16a/d-2+\delta),$$

where a is the radius of the loop, d the diameter of the wire, and δ a factor to take account of skin effect, which, since the time constants involved were about 1/50 sec, can be neglected. The time constant of the loop is then L/R so that a measurement of the decay time leads directly to the resistance of the loop. This decay time could be determined to within 1.0 percent by placing millisecond brightening pulses on the oscilloscope trace and using a recurrent sweep so that the decay extended over six or more complete sweeps (see Fig. 1). Systematic errors which might arise from the finite time constant of the exciting circuit and damping effects due to coupling between the specimen and other circuits are well below one percent.

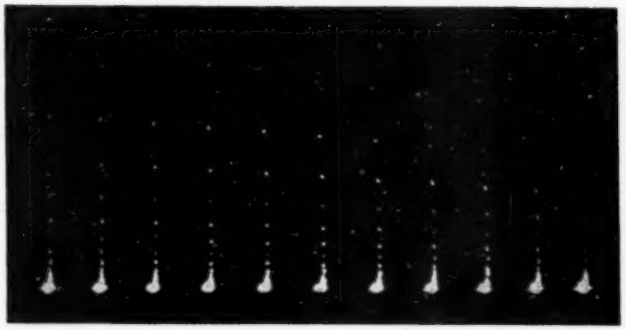

FIG. 1. Oscillograph trace of decaying current pulse with millisecond marker pulses.

Figure 1 shows a photograph typical of a series from which the resistivity of an annealed sample of Johnson and Matthey H.S. brand copper (quoted as 99.999 percent pure) was calculated for the temperature range from 1.5° to 4.2°K. The results presented in Fig. 2 indicate that the resistivity is effectively constant over

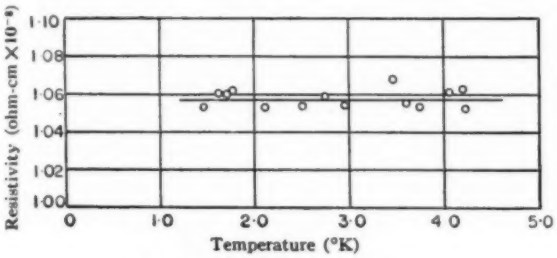

FIG. 2. Resistivity of annealed copper.

this range. This is in agreement with the results obtained by MacDonald[1] and others for samples of comparable purity.

It should be noted that in forming the ring a certain amount of work hardening is introduced into the sample. For the particular specimen used this increased the residual resistance by about 5 percent above the annealed value. This, of course, may be removed by re-annealing. Apart from its application to low resistance measurements, the method has the advantage of the very short time required for any particular observation.

The authors wish to acknowledge assistance obtained in discussion with Dr. J. B. Brown and Dr. J. Reekie.

[1] D. K. C. MacDonald, Phys. Rev. **88**, 148 (1952).

The Radiation Fields of a Horizontal Dipole in a Semi-Infinite Dissipative Medium

JAMES R. WAIT
Radio Physics Laboratory, Defense Research Board, Ottawa, Canada
(Received February 27, 1953)

IN a recent interesting paper[1] Roy Harold Lien derives expressions for the electric fields of an oscillating horizontal dipole placed in a semi-infinite dissipative medium. As stated in the paper, the final formulas hold only at low frequencies. Lien tacitly neglects the displacement currents in the insulating medium, thus ruling out the possibility of a surface wave along the interface. Apparently his results are valid only when the distance from dipole to observer is a small fraction of the free space wavelength. A much more optimistic picture of the situation is obtained by including the effects of the displacement currents in the insulating medium as outlined below.

In the cylindrical coordinate system ρ, ϕ, z, the dissipative medium μ, ϵ, σ and the insulating medium μ, ϵ_0 occupy the half-

spaces $z>0$ and $z<0$, respectively. The dipole of moment p is placed normal to the z axis at $\rho=0$, $z=h$, and ϕ is measured from its axis. The square of the refractive index n is $\kappa-j\sigma/\omega\epsilon_0$ where κ is ϵ/ϵ_0. The expressions for the field components are given by Lien's Eqs. (25), (26), and (27) in terms of the direct and image fields plus two functions U and V. The main difficulty is the evaluation of the infinite integral for V which appears in Eq. (28). Lien writes n^2l for n^2l+m in the denominator of this integral which gives a result [Eq. (38)], valid when $|n^2|\gg1$, in terms of modified Bessel functions. Another approximation is found by writing jnk for m where k is the wave number. The result, which holds when $|n^2|\gg1$ and $\rho\gg z+h$, is the integral

$$V\approx 2\int_0^\infty \frac{J_0(\lambda\rho)\exp[-jnk(z+h)]\lambda d\lambda}{(\lambda^2-k^2)^{\frac{1}{2}}+jk/n}. \tag{1}$$

Essentially this is the same approximation made by Sommerfeld[2] in his analysis for dipoles situated in the insulating medium or interface. Using Sommerfeld's integration gives

$$V\approx 2e^{-jk\rho}\rho^{-1}F(p)e^{-jnk(z+h)}, \tag{2}$$

where $F(p)$ is the "attenuation factor" given by

$$F(p)=1-j(\pi p)^{\frac{1}{2}}e^{-p}\operatorname{erfc}(jp^{\frac{1}{2}}), \tag{3}$$

erfc is the complement of the error function, and p is the numerical distance $-\frac{1}{2}jk\rho n^{-2}$. $F(p)$ has been adequately tabulated by Norton.[3] U has the same form as (2) but with p replaced by $-\frac{1}{2}jk\rho n^2$.

When these values for U and V are substituted in Lien's Eqs. (25), (26), and (27) for the field components the results, if kp, $|jnkr_1|$, and $|jnkr_2|$ are all much greater than one, are

$$E_z\approx cn^{-1}k^2\cos\phi V, \tag{4}$$

$$E_\rho\approx -ck^2\cos\phi V, \tag{5}$$

$$E_\phi\approx -cjk\rho^{-1}\sin\phi V. \tag{6}$$

For frequencies so low that $p<1$, the E_z and E_ρ fields vary as the inverse distance because $F(p)$ is near unity. In all cases the attenuation depends mainly on the sum of the distances of the dipole and observer from the interface. The E_ϕ component varies as the inverse square of the distance for small numerical distances. Evidently the signal in the insulating medium propagates chiefly as a displacement current when the separation of dipole and observer is much greater than the sum of their distances from the surface.

[1] R. H. Lien, J. Appl. Phys. **24**, 1 (1953). The factor k on the right-hand side of Lien's Eqs. (39) and (40) should be omitted. A factor $\cos\phi$ should be added to the right side of Lien's Eq. (49).
[2] A. N. Sommerfeld, Ann. Physik **81**, 1135 (1926).
[3] K. A. Norton, Proc. Inst. Radio Engrs. **24**, 1367 (1936).

Deduction of the Maximum Torsional Stress in a Shaft with Notches

SENNOSUKE MOMMA
Institute of High Speed Mechanics, Tōhoku University, Sendai, Japan
(Received January 19, 1953)

IN this paper an approximate solution is derived for a twisted shaft with circumferential notches periodically situated along its length. The solution for the extreme case, where the dimensions of notches are infinitely small, has been obtained previously by Neuber.[1] The present solution, however, is of sufficient accuracy for practical use even in the range of moderate dimensions of notches.

As all stresses for the present problem vary periodically with z, we may take for the stress function the expression[2]

$$\phi=\frac{\theta}{4}r^4+r^2\sum_{n=1}^{\infty}A_nI_2\left(\frac{n\pi r}{a}\right)\cos\frac{n\pi z}{a}, \tag{1}$$

where $2a$ is the period of notches, and θ is the mean twist in a period. At the points where r is large as compared with a, we have the approximate relation

$$I_2\left(\frac{n\pi r}{a}\right)=\frac{a^{\frac{1}{2}}e^{n\pi r/a}}{\pi(2nr)^{\frac{1}{2}}}\left(1-\frac{15a}{8n\pi}\right),$$

where the minimum radius of the shaft is assumed as unity. Assuming that

$$A_n=\frac{2^{\frac{1}{2}}\pi(-1)^{n+1}Pe^{-n\pi r_0/a}}{(an)^{\frac{1}{2}}[1-(15a/8n\pi)]},$$

Eq. (1) reduces to

$$\phi=\frac{\theta}{4}r^4+Pr^{\frac{1}{2}}\log\left(1+\exp\frac{2\pi}{a}(r-r_0)+2\exp\frac{\pi}{a}(r-r_0)\cos\frac{\pi z}{a}\right). \tag{2}$$

Hence the contour of the axial section of the shaft is given by

$$\phi=C. \tag{3}$$

Equation (3) contains three arbitrary constants P, C, and r_0, so we can specify the pitch, depth, and radius of curvature of the notch. Taking for an example the pitch and depth of notches as 0.3 and 0.1, respectively, the forms of notches are obtained from Eq. (3) for various values of r_0. They are shown in Fig. 1. The

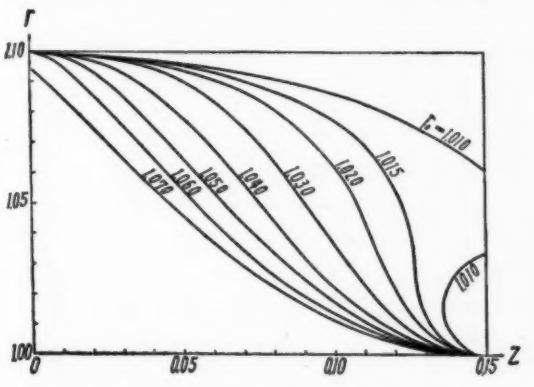

FIG. 1. Forms of notches, when $a=0.15$ and $h=0.1$.

corresponding values of radius of curvature are obtained from

$$\rho=\frac{a^2}{P\pi^2}\left\{1-\cosh\frac{\pi}{a}(1-r_0)\right\}\left\{\theta+3P\log\left(1-\exp\frac{\pi}{a}(1-r_0)\right)\right\}+\frac{a}{\pi}\left(1-\exp\frac{\pi}{a}(1-r_0)\right). \tag{4}$$

The maximum stress is readily obtained from Eqs. (1) or (2), as

$$\frac{\tau_{\max}}{2T/\pi(1+h)^3}=\frac{(1+h)^3\theta}{4C}\left\{1+\frac{3P}{\theta}\log\left(1-\exp\frac{\pi}{a}(1-r_0)\right)-\frac{2\pi P\exp\frac{\pi}{a}(1-r_0)}{a\theta\left(1-\exp\frac{\pi}{a}(1-r_0)\right)}\right\}, \tag{5}$$

where h is the depth of notches and T is the torque acting on the shaft. The maximum stress is calculated from Eq. (5) for the notches shown in Fig. 1, and its relation to ρ is shown in Fig. 2, together with the corresponding ones for a single notch, calculated by two different formulas, previously obtained by Sonntag and Ōkubo, respectively.[3] It may be seen from the figure that the stress concentration deduces perceptively when notches are situated in a row. For smaller value of ρ/h we find a considerable discrepancy between the two formulas for a single notch of the previous writers. The discrepancy is too large even for practical use, while theoretical justification for the two is not so easy, since these formulas are approximate ones, derived from somewhat different assumptions. The data obtained in this paper,

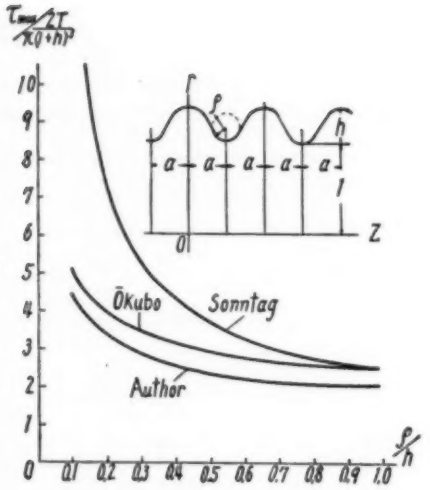

FIG. 2. Relation between the maximum stress and the radius of curvature, when $a=0.15$ and $h=0.1$.

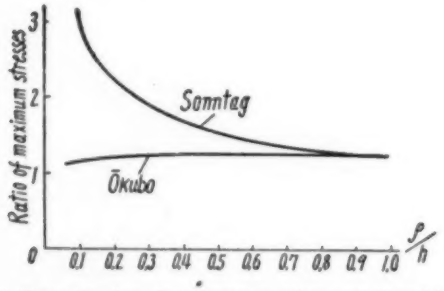

FIG. 3. The ratio of maximum stresses, when $a=0.15$ and $h=0.1$.

however, will be a good reference for the justification of the two formulas, since the ratio of maximum stress for a single notch to that for multiple notches may not be affected perceptively by ρ/h, considering the known fact that the ratio is independent of ρ/h if notches be sharp and infinitely small.[1] From the curves in Fig. 2 this ratio is obtained using the results by Sonntag and Ökubo, respectively, and it is shown in Fig. 3.

In conclusion, the writer wishes to express his hearty thanks to Professor H. Ökubo for his kind suggestions in this study.

[1] H. Neuber, *Kerbspannungslehre* (Verlag Julius Springer, Berlin, 1937), p. 140.
[2] S. Timoshenko and J. N. Goodier, *Theory of Elasticity* (McGraw-Hill Book Company, Inc., New York, 1951), p. 304.
[3] R. Sonntag, Z. angew. Math. Mech. **9**, 3 (1929). H. Ökubo, J. Appl. Mech. **19**, 16 (1952).

Polystyrene and Lucite Rod Antennas

GISWALT VON TRENTINI
Laboratorio de Electronica, Fabricaciones Militares, Buenos Aires, Argentina
(Received March 16, 1953)

WHEN designing antennas of dielectric rods excited in the dominant mode, one depends mainly on experimental measurements.

With decreasing diameter the power guided externally along the rod increases, and thus the radiation also increases. By suitable tapering of the cross section along the rod, the field distribution (amplitude and phase velocity) can be influenced, and an end-fire antenna with an appropriate directivity can be constructed.[1,2]

Apart from the length, cross section, and dielectric constant, the loss in the dielectric material is an essential parameter. This

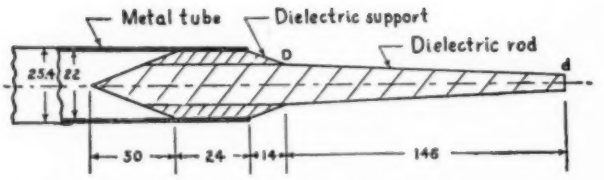

FIG. 1. Experimental arrangement of the dielectric rod antenna in a circular wave guide. Wavelength = 3.21 cm. All dimensions are in millimeters.

causes not only absorption by line losses but also a changed field distribution along the rod, i.e., a modified radiation pattern. Therefore results with rods of material having the same dielectric constant but different loss will not be equivalent.

Horton and McKinney[3] published various experimental series showing the marked differences between polystyrene and Lucite antennas. The rods used by these authors had a diameter of $0.87\lambda_0$ at the end of the wave guide and were tapered slightly or not at all. Since the influence of the losses is greatly reduced in thinner rods, it is necessary to compare these forms.

Various rods with circular cross section and gradual taper were fitted snugly in a circular wave guide of 22-mm inside diameter. They were tested in the TE_{11} mode at free space wavelength of $\lambda_0=3.21$ cm. The directional patterns were measured using the dielectric rod antennas as a receiver. The dielectric rod was tapered in the interior of the wave guide to avoid strong reflections. The external dielectric rod length was in all tests $5\lambda_0$.

A polystyrene and a Lucite rod of identical dimensions (see Fig. 1) with $D=12.5$ mm ($=0.39\lambda_0$) and $d=8.5$ mm ($=0.265\lambda_0$) showed almost the same results and high efficiency. The difference in gain was only 0.4 db. In each case the rod support was constructed of foam material of low loss and dielectric constant 1.05. If the foam support is replaced by one of polystyrene or Lucite, only a moderate change resulted. Finally the rod and support were made in one piece, and the following results were obtained:

Polystyrene antenna: gain approximately 16.1 db; half-power beam width 31.9° (H plane) and 30.1° (E plane); side lobe −14 db (H plane) and −13 db (E plane).

Lucite antenna: gain approximately 15.3 db; half-power beam width 30.4° (H plane) and 28.3° (E plane); side lobes −13 db.

Hence the difference in gain was 0.8 db and the radiation patterns were almost similar.

The largest gain of approximately 16.8 db was obtained with a slightly thicker polystyrene rod with $D=16$ mm, $d=8.5$ mm (see

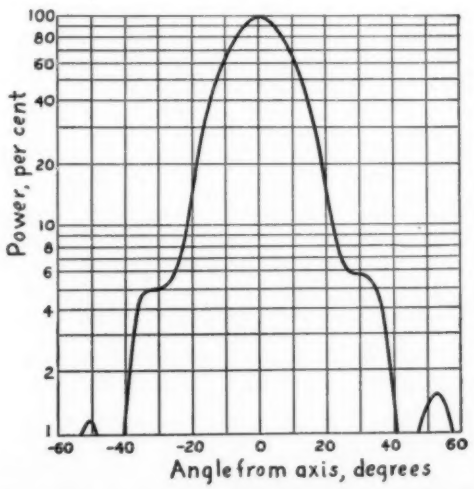

FIG. 2. Directional pattern of the polystyrene rod antenna in the H plane.

Fig. 1). The radiation was strongly symmetrical about the principal axis of the rod and the H-plane pattern is shown in Fig. 2. An identical Lucite rod already had a 1.8-db decrease in gain and a slightly different radiation pattern.

The fundamental difference compared to thicker rods could be proved by placing a metal disk (25-mm diameter) near the end of the rod. With the thin rod (Fig. 1) the received power decreased by approximately one-half, whereas with a thicker rod of unchanged cross section ($0.7\lambda_0$ diameter) and equal length the power fell below $\frac{1}{10}$. In the first case the reception occurs along the side; in the second case, however, mainly at the plain end of the rod.

Conclusion: The absolute gain of a thinner, twice linearly-tapered rod, is somewhat increased and the losses of the dielectric are less accentuated compared to other forms of construction.

[1] G. E. Mueller and W. A. Tyrrell, Bell System Tech. J. **16**, 837 (1947).
[2] P. Mallach, Fernmeldetech. Z. **2**, 33 (1949).
[3] C. W. Horton and C. M. McKinney, J. Appl. Phys. **22**, 1246 (1951).

Surface Wave Propagation over a Coated Conductor with Small Cylindrical Curvature in Direction of Travel

KAZUO HORIUCHI
Laboratory of Communication Instruments, Waseda University, Tokyo, Japan
(Received March 20, 1953)

WE have already some knowledge of the various properties of Harms-Goubau's surface-wave propagation. But the theoretical analysis of field in the neighborhood of the bend of the surface wave line is difficult. Such rigorous analysis must be made in the coordinate system of ring-type, but the outline of such field can be suggested in the system of plane conductor as by Attwood.[1]

This letter shows the deviation of his TM wave over the coated plane conductor caused by a small curvature σ in the direction of travel.

Adopt the coordinate system whose line element ds is defined as

$$ds^2=dx^2+dy^2+(1+\sigma y)^2d\zeta^2, \quad \sigma y\ll 1$$

as in Fig. 1, then the field whose components E_x, H_y, and H_ζ vanish and whose ζ, t factor is $\exp j(\omega t-\beta\zeta)$ is expressed in general by H_x which satisfies the equation

$$\frac{\partial^2 H_x}{\partial y^2}+\sigma\frac{\partial H_x}{\partial y}+(-k^2+2\beta^2\sigma y)H_x=0, \quad k^2=\beta^2-\omega^2\mu\epsilon$$

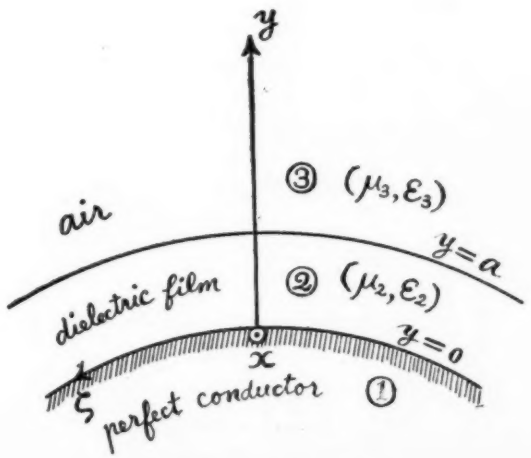

FIG. 1. Geometry for the problem.

and by the following E_y and E_ζ:

$$E_y=-\frac{\beta}{\omega\epsilon(1+\sigma y)}H_x,$$

$$E_\zeta=-\frac{1}{j\omega\epsilon}\frac{\partial H_x}{\partial y}.$$

Now, consider the dielectric film with the thickness a over a perfect conductor surface having a small curvature σ in the

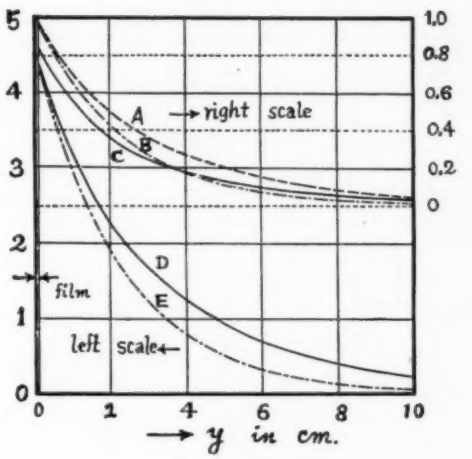

FIG. 2. Field distribution in y direction. Curves A, C, and D denote the distributions of H_{x3}, $E_{\zeta 3}$ and E_{y3}, respectively. Curves B and E denote the corresponding exponential distributions.

ζ direction only, as in Fig. 1. Then the fields in the region 2 are expressed as follows:

$$H_{x2}=-\frac{\omega\epsilon_2}{h_2}A_2\Big[\cos(h_2y)+\sigma\Big\{-\frac{\beta^2}{2h_2}y^2\sin(h_2y)-\frac{1}{2}\Big(\frac{\beta^2}{h_2^2}+1\Big)y\cos(h_2y)+\frac{1}{h_2}\Big(\frac{\beta^2}{h_2^2}+1\Big)\sin(h_2y)+j\frac{1}{h_2}\Big(\frac{\beta^2}{h_2^2}+1\Big)\cos(h_2y)\Big\}\Big],$$

$$E_{y2}=\frac{\beta}{h_2}A_2\Big[\cos(h_2y)+\sigma\Big\{-\frac{\beta^2}{2h_2}y^2\sin(h_2y)-\frac{1}{2}\Big(\frac{\beta^2}{h_2^2}+3\Big)y\cos(h_2y)+\frac{1}{h_2}\Big(\frac{\beta^2}{h_2^2}+1\Big)\sin(h_2y)+j\frac{1}{h_2}\Big(\frac{\beta^2}{h_2^2}+1\Big)\cos(h_2y)\Big\}\Big],$$

$$E_{\zeta 2}=jA_2\Big[\sin(h_2y)+\sigma\Big\{\frac{\beta^2}{2h_2}y^2\cos(h_2y)+\frac{1}{2}\Big(\frac{\beta^2}{h_2^2}-1\Big)y\sin(h_2y)+\frac{1}{2h_2}\Big(\frac{\beta^2}{h_2^2}+1\Big)\cos(h_2y)-\frac{1}{h_2}\Big(\frac{\beta^2}{h_2^2}+1\Big)\sin(h_2y)-j\frac{1}{h_2}\Big(\frac{\beta^2}{h_2^2}+1\Big)\cos(h_2y)\Big\}\Big],$$

where $h_2^2=\omega^2\mu_2\epsilon_2-\beta^2>0$ and ζ, t factors are omitted. In the region 3 the fields are

$$H_{x3}=-\frac{\omega\epsilon_3}{k_3}A_3\exp(-k_3y)\Big[1+\sigma\Big\{\frac{\beta^2}{2k_3}y^2+\frac{1}{2}\Big(\frac{\beta^2}{k_3^2}-1\Big)y\Big\}\Big],$$

$$E_{y3}=\frac{\beta}{k_3}A_3\exp(-k_3y)\Big[1+\sigma\Big\{\frac{\beta^2}{2k_3}y^2+\frac{1}{2}\Big(\frac{\beta^2}{k_3^2}-3\Big)y\Big\}\Big],$$

$$E_{\zeta 3}=jA_3\exp(-k_3y)\Big[1+\sigma\Big\{\frac{\beta^2}{2k_3}y^2-\frac{1}{2}\Big(\frac{\beta^2}{k_3^2}+1\Big)y-\frac{1}{2k_3}\Big(\frac{\beta^2}{k_3^2}-1\Big)\Big\}\Big],$$

where $k_3^2=\beta^2-\omega^2\mu_3\epsilon_3>0$, ζ, t factors are omitted and

$$A_3=A_2\exp(k_{30}a)\left[\sin(h_{20}a)+\sigma\left\{\left[\frac{\beta^2a^2}{2h_2}+\frac{1}{2h_2}\left(\frac{\beta^2}{h_2^2}+1\right)-j\frac{1}{h_2}\left(\frac{\beta^2}{h_2^2}+1\right)\right]\cos(h_{20}a)+\left[-\frac{\beta^2a^2}{2k_3}+\frac{\beta^2a}{2}\left(\frac{1}{h_2^2}+\frac{1}{k_3^2}\right)-\frac{1}{h_2}\left(\frac{\beta^2}{h_2^2}+1\right)+\frac{1}{2k_3}\left(\frac{\beta^2}{k_3^2}-1\right)\right]\sin(h_{20}a)\right\}\right].$$

Figure 2 shows the distribution of this field in the region 3 for the case of $a=0.001$ meter, $\sigma=0.5$ and $f=10\,000$ mc, where electric and magnetic field are normalized to make, respectively, the A_3 and $(\omega\epsilon_3/k_3)A_3$ unity.

Using β_0, h_0 and k_0 which are given by Attwood and satisfy the equations

$$\frac{h_{20}}{\epsilon_2}\tan(h_{20}a)=\frac{k_{30}}{\epsilon_3},\quad k_0^2=\beta_0^2-\omega^2\mu\epsilon=-h_0^2,$$

the phase constant β' and induced attenuation constant α are determined as follows from the continuity of the y direction impedance at the boundary $y=a$:

$$\beta'=\beta_0+\frac{\sigma}{\beta_0}\left\{\frac{\beta_0^2a^2}{2h_{20}}\left[\frac{k_{30}\epsilon_2}{h_{20}\epsilon_3}+\frac{h_{20}\epsilon_3}{k_{30}\epsilon_2}\right]+\beta_0^2a\left[\frac{1}{h_{20}^2}+\frac{1}{k_{30}^2}\right]+\frac{1}{2k_{30}}\left[\frac{\epsilon_3}{\epsilon_2}\left(\frac{\beta_0^2}{h_{20}^2}+1\right)+\left(\frac{\beta_0^2}{k_{30}^2}-1\right)\right]-\frac{1}{h_{20}}\left(\frac{\beta_0^2}{h_{20}^2}+1\right)\times\left(1+\frac{k_{30}\epsilon_2}{h_{20}\epsilon_3}\right)\right\}\Big/\left\{\frac{1}{h_{20}^2}+\frac{1}{k_{30}^2}+\frac{2a}{h_{20}\sin(2h_{20}a)}\right\},$$

$$\alpha=\frac{\sigma}{\beta_0h_{20}}\left(\frac{\beta_0^2}{h_{20}^2}+1\right)\left(1+\frac{h_{20}\epsilon_3}{k_{30}\epsilon_2}\right)\Big/\left\{\frac{1}{h_{20}^2}+\frac{1}{k_{30}^2}+\frac{2a}{h_{20}\sin(2h_{20}a)}\right\}.$$

Moreover, the average power radiated in the y direction per unit area of x, ζ surface is given as

$$\bar{P}_{y3}=A_3A_3^*\frac{\beta_0\alpha\omega\epsilon_3}{2k_{30}^3}\sin^2(h_{20}a)\cdot\exp[2k_{30}(a-y)]$$

for $y\geqslant a$. In addition, lines of electric force in the region 3 are expressed by the formula

$$C\sin(\omega t-\beta\zeta)=\exp(k_3y)\left[1-\sigma\left\{\frac{\beta^2}{2k_3}y^2+\frac{1}{2}\left(\frac{\beta^2}{k_3^2}-1\right)y\right\}\right),$$

where C is a parameter.

From the above formulas it is suggested that a bend in this sort of transmission line produces attenuation and the field intensity around the line is intensified on the outside of the bend. These results have been verified by Dr. Mastumoto in experiments concerning the bend of the Goubau line, in particular the coated strip line.

[1] S. S. Attwood, J. Appl. Phys. **22**, 504 (1951).

Effect of Particle Size on Magnetic Loss Tangent of Obstacle Type Artificial Dielectrics

J. M. Kelly and J. O. Stenoien
Boeing Airplane Company, Physical Research Unit
(Received April 29, 1953)

ARTIFICIAL dielectrics consisting of a metal powder suspended in a dielectric binder have been shown to possess a magnetic loss tangent. In a recent publication[1] it was suggested that the magnitude of this loss tangent for particles of a particular shape and composition should depend on the average size of the particles.

Experimental verification of this phenomenon has been obtained. With paraffin wax as the dielectric binder, wave-guide samples were made using two commercially available aluminum powders—Alcoa No. 322 standard varnish powder and Alcoa No. 422 extra fine lining powder. Both these powders consisted of

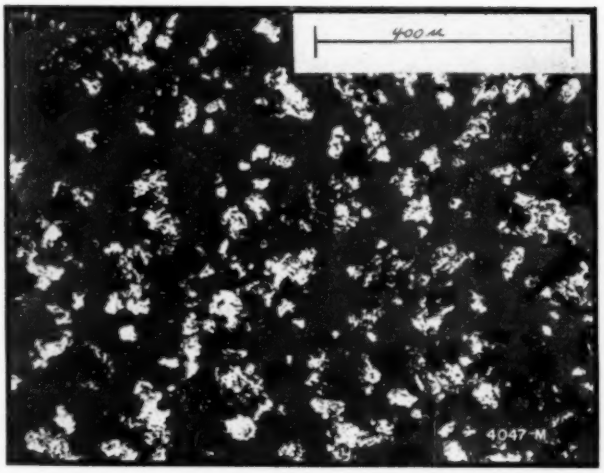

Fig. 1. Photomicrograph of Alcoa aluminum powder No. 322.

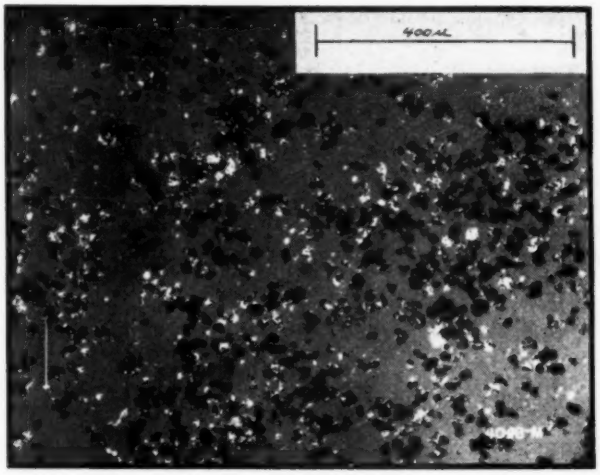

Fig. 2. Photomicrograph of Alcoa aluminum powder No. 422.

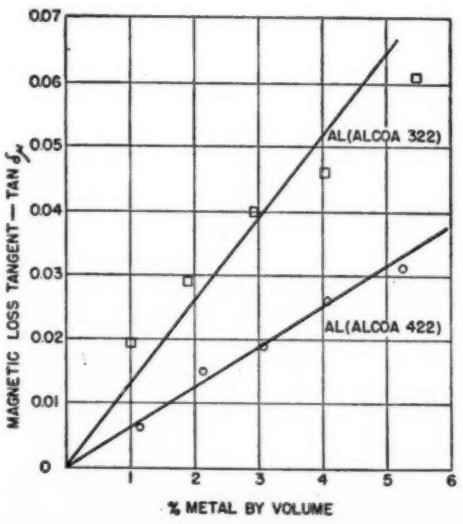

Fig. 3. Magnetic loss tangent as a function of volume concentration of metal in paraffin wax for two sizes of aluminum flakes.

aluminum flakes together with approximately 3 percent stearic acid. The average particle size is apparent from the photographs.

The graph shows clearly that the smaller particle yields an artificial dielectric with smaller magnetic loss. The dielectric loss for both powders was negligible. Also indicated is the linear relation between magnetic loss tangent and powder concentration. The index of refraction for the 5 percent mixture is 3.3.

[1] Kelly, Stenoien, and Isbell, J. Appl. Phys. **24**, 258 (1953).

The Effect of Neutron Bombardment Upon the Magnetic Susceptibility of Several Pure Oxides

J. D. McClelland and J. J. Donoghue
North American Aviation, Inc., Atomic Energy Research Department, Downey, California
(Received April 24, 1953)

NEUTRON bombardment has been found to produce an increase in the paramagnetism of several pure oxides. The specific susceptibility of the oxides were measured by the Faraday method using fields which ranged from 8000 gauss to 16 000 gauss. An experimental error of one percent is assigned to the values reported below. The irradiations took place in a Hanford reactor at 30°C with integrated neutron fluxes, 0.51×10^{19} nvt and 3.76×10^{19} nvt where the nvt's refer to neutrons with energies in excess of 500 kev. Table I gives the experimental results.

All of the oxides studied are diamagnetic. Neutron irradiation produces lattice defects which could give rise to a spin paramagnetism. If it may be assumed that a spin of $\frac{1}{2}$ be associated with each defect, as would be the case for a trapped electron, it is possible to estimate the number of such defects from the decrease in the diamagnetic susceptibility. Such an assumption leads, in the case of the long exposure, to an apparent defect concentration of 3.2×10^{-3} defects per molecule for crystalline SiO_2, 2.1×10^{-3} for the fused SiO_2, 2.4×10^{-3} for the alumina, and 0.5×10^{-3} for the MgO. No measurable change occurred in the case of the sapphire Al_2O_3 or the spinel $MgO\cdot3.5\,Al_2O_3$.

Table I.

Material	Specific susceptibility $\times10^6$		
	No irradiation	0.52×10^{19} nvt	3.76×10^{19} nvt
SiO_2 (fused)	−0.430	−0.402	−0.390
SiO_2 (crystalline)	−0.434	−0.390	−0.374
Al_2O_3 (alumina)	−0.353	−0.337	−0.329
Al_2O_3 (sapphire)	−0.375	−0.375	−0.373
$MgO\cdot3.5Al_2O_3$ (spinel)	−0.338	−0.338	−0.340
MgO	−0.253	−0.249	−0.235

Erratum: Growth of Cadmium Sulfide Crystals

[J. Appl. Phys. **24**, 660–661 (1953)]
M. E. Bishop and S. H. Liebson
Naval Research Laboratory, Washington, D. C.

IN the fourth paragraph, fourth line, the words "of sulfur" should be deleted.

In the sixth paragraph, the third line, the word "sulfide" should be deleted.

Announcements

On September 9, 1953, a three-day **Conference on Nuclear Engineering** will convene at the University of California, Berkeley. It is presented by the University's Departments of Engineering at Berkeley and Los Angeles, in cooperation with Northern California sections of the A.I.Ch.E., A.I.E.E., and A.S.M.; Southern California sections of the A.S.M.E., A.I.Ch.E., and A.S.M.; and the Committee on Atomic Energy Education of the A.S.E.E. The major purpose of the Conference is to provide a high-level technical program of contributed papers by and for personnel working in nuclear engineering and closely related fields.

On August 19–21; **WESCON (Western Electronic Show and Convention),** jointly sponsored by IRE (7th Region) and WCEMA (West Coast Electronic Manufacturers' Association), will be held in the Municipal Auditorium, San Francisco. Technical sessions will feature 25 sessions on antennas, propagation, electron devices, circuits, computers, airborne electronics, microwave techniques, servos and telemetering, instrumentation, transistors, nuclear-radiation measurements, and medical electronics. Booth exhibits will feature products of 275 manufacturers, and special field trips and social events are planned for both delegates and their wives.

Five new members have been appointed to the staff of the **National Science Foundation.**

The new staff members, their position with the Foundation, and their previous positions, are:

Harry Alpert, study director for social science research, Program Analysis Office, from the Bureau of the Budget.

James W. Cole, Jr., program director for scientific manpower, Division of Scientific Personnel and Education, from the University of Virginia.

Walter R. Kirner, program director for chemistry, from the National Research Council.

Raymond W. Mayhew, physical science administrator, Division of Scientific Personnel and Education, from the U. S. Navy.

H. Kirk Stephenson, program director for earth sciences, from Los Alamos Scientific Laboratory.

Karl Hilding Beij, acting chief of the Hydraulics section of the **National Bureau of Standards,** retired April 30, 1953, after more than 32 years of distinguished service at the Bureau.

George A. Hornbeck has joined the Combustion Section of the Missile Development Division at the **National Bureau of Standards** where he will engage in research on molecular spectroscopy.

Dr. Abraham S. Friedman has joined the Thermodynamics Section of the **National Bureau of Standards,** where he is heading a group of scientists investigating the properties of various deuterium compounds.

Shirley A. Johnson Jr., (CQ) one of the region and nation's foremost young research administrators, has been named permanent director of the **Denver Research Institute** of the University of Denver.

Dr. James J. Brophy has been promoted to supervisor of the physics of solids section at **Armour Research Foundation of Illinois Institute of Technology.**

Dr. Elmer H. Schulz to director of research and **Dr. Maurice J. Day** to assistant director for program development at Armour Research Foundation of Illinois Institute of Technology.